DOCTOR OF PHILOSOPHY

Solar thermal collectors for use in hybrid solar-biomass power plants in India

Jonathan Nixon

2012

Aston University

Solar thermal collectors for use in hybrid solar-biomass power plants in India

Jonathan Daniel Nixon

Doctor of Philosophy

ASTON UNIVERSITY

December 2012

Aston University

Solar thermal collectors for use in hybrid solar-biomass power plants in India

Jonathan Daniel Nixon

Doctor of Philosophy

June 2012

This thesis examined solar thermal collectors for use in alternative hybrid solar-biomass power plant applications in Gujarat, India. Following a preliminary review, the cost-effective selection and design of the solar thermal field were identified as critical factors underlying the success of hybrid plants. Consequently, the existing solar thermal technologies were reviewed and ranked for use in India by means of a multi-criteria decision-making method, the Analytical Hierarchy Process (AHP). Informed by the outcome of the AHP, the thesis went on to pursue the Linear Fresnel Reflector (LFR), the design of which was optimised with the help of ray-tracing. To further enhance collector performance, LFR concepts incorporating novel mirror spacing and drive mechanisms were evaluated. Subsequently, a new variant, termed the Elevation Linear Fresnel Reflector (ELFR) was designed, constructed and tested at Aston University, UK, therefore allowing theoretical models for the performance of a solar thermal field to be verified.

Based on the resulting characteristics of the LFR, and data gathered for the other hybrid system components, models of hybrid LFR- and ELFR-biomass power plants were developed and analysed in TRNSYS®. The techno-economic and environmental consequences of varying the size of the solar field in relation to the total plant capacity were modelled for a series of case studies to evaluate different applications: tri-generation (electricity, ice and heat), electricity-only generation, and process heat. The case studies also encompassed varying site locations, capacities, operational conditions and financial situations. In the case of a hybrid tri-generation plant in Gujarat, it was recommended to use an LFR solar thermal field of 14,000 m^2 aperture with a 3 tonne biomass boiler, generating 815 MWh per annum of electricity for nearby villages and 12,450 tonnes of ice per annum for local fisheries and food industries. However, at the expense of a 0.3 ¢/kWh increase in levelised energy costs, the ELFR increased saving of biomass (100 t/a) and land (9 ha/a). For solar thermal applications in areas with high land cost, the ELFR reduced levelised energy costs. It was determined that off-grid hybrid plants for tri-generation were the most feasible application in India. Whereas biomass-only plants were found to be more economically viable, it was concluded that hybrid systems will soon become cost competitive and can considerably improve current energy security and biomass supply chain issues in India.

Keywords: Concentrating solar thermal power (CSP); linear Fresnel reflector (LFR); multi-criteria decision-making (MCDM); analytical hierarchy process (AHP); exergy.

Acknowledgements

I would like to firstly express my sincere gratitude towards Dr. Philip Davies for his continuous and outstanding supervision. I also thank my associate supervisor Dr. Prasanta Dey for all his guidance and the rest of my Science Bridge team colleagues, who through meetings and interactions have contributed towards my studies. In particular I would like to thank Rohintan, Cyrus and Zaraan Engineer (Industrial Boilers Ltd), and Professors Padma and Pradeep Sen (Indian Institute of Technology, Delhi), who were kind enough to accommodate me during my visits to India.

Furthermore, I acknowledge the assistance of the Solar Energy Centre (MNRE), Delhi, in hosting the expert workshop, the contribution of anonymous referees during paper publications, and the financial support under the Science Bridge project financed by Research Councils UK (EP/G039992/1) and Department of Science and Technology, India.

The technicians and Estates department at Aston University are also acknowledged for their contribution in helping me during the constructions of a solar thermal collector on the roof of Aston University. I thank Opus Ngoye for his assistance in developing the electronics for the solar collector and acknowledge the data provided by the company Siemens and by my colleague Vimal Eswarlal. I wish to also give my gratitude towards my friends, especially Tom Drew, Joe Davies, Ben Coldrick and Alec Kingsnorth who have made my time completing my PhD thoroughly enjoyable, and thank them for all their input.

Lastly I would like to thank my family, in particular my father John Nixon, for consistently reviewing my work, and my beautiful wife Ene Nixon, for all her love and support.

List of contents **Page**

Chapter 7: Conclusions

Appendix

Figures

Tables

Nomenclature

ΔT	Fluid temperature rise (K)
a	CPC aperture width (m)
A	Reference area of an object perpendicular to wind direction (m^2)
a'	Target width of receiver (m)
A_a	Effective mirror aperture area of n^{th} element (m^2)
A_{an}	Effective mirror aperture area (m^2)
A_{cg}	Surface area of cover glazing (m^2)
A_m	Total mirror area (m^2)
A_r	Area of receiver (m^2)
A_{RT}	Surface area of per unit depth of CPC (m^2)
A_{SF}	Aperture area of solar field (m^2)
a_T	Truncated CPC aperture width (m)
B_{saved}	Biomass saved (tonnes/a)
c_{bio}	Cost of biomass feedstock ($/a)
c_{boiler}	Cost of boiler ($)
$C_{capital}$	Capital cost ($)
c_{chill}	Cost of chiller ($)
Cd	Drag coefficient (-)
c_{elec}	Cost of electricity ($)
C_i	CPC concentration ratio
c_{ins}	Annual insurance costs ($/a)
c_{land}	Cost of land ($)
$C_{O\&M}$	Operations and maintenance cost ($/a)
C_p	Specific capacity of heat transfer fluid (kJ/kg.K)
C_{pa}	Specific capacity of air (kJ/kg.K)
C_{pb}	Cost of rest of power block ($)
$C_{pel,b}$	Cost per exergy loss of boiler ($/GJ/a)
$C_{pel,c}$	Cost per exergy loss of collector (solar field) ($/GJ/a)
$C_{pel,hc}$	Cost per exergy loss of heat cycle ($/GJ/a)
$C_{pel,os}$	Cost per exergy loss of overall system (hybrid plant) ($/GJ/a)
C_{pi}	Specific heat capacity of ice (kJ/kgK)
C_{ps}	Specific heat capacity of steam (kJ/kgK)
C_{pw}	Specific heat capacity of water (kJ/kgK)
c_{sf}	Cost of solar field ($)
c_{spare}	Annual replacement costs ($/a)
c_{staff}	Cost of employees ($/a)
c_{turb}	Cost of turbine ($)
c_{water}	Cost of water ($/a)
D	Daylight saving (1 when in effect)
d	Depth of CPC (m)
d_c	Depth of cavity (m)
D_i	Inside diameter of absorber pipe (m)
d_n	Width of shade on n^{th} mirror element (m)

D_o	Outside diameter of absorber pipe (m)
d_T	Truncated depth of CPC (m)
eb_n	Elevation required to remove blocking of an n^{th} element (m)
e^{CH}	Chemical exergy of biomass (MJ/kg)
E_{el}	Electricity produced (MWh_e/a)
$E_{el,\%bio}$	Percentage of electricity from biomass input
$E_{el,\%sol}$	Percentage of electricity from solar input
$E_{el,aux}$	Auxiliary electrical requirement (MWh_e/a)
$E_{el,val}$	Value of saleable electricity ($/a)
es_n	Elevation required to remove shadowing of an n^{th} element (m)
$E_{x,out}$	Exergy per total mirror area (maximum available power output) (W/m^2)
Ex_b	Exergy received by boiler (GJ/a)
Ex_c	Exergy received by collector (solar field) (GJ/a)
Ex_{hc}	Exergy received by heat cycle (GJ/a)
Ex_{os}	Exergy received by overall system (hybrid plant) (GJ/a)
Exu_b	Exergy delivered by boiler (GJ/a)
Exu_c	Exergy delivered by collector (solar field) (GJ/a)
F'	Collector efficiency factor (-)
F''	Collector flow factor (-)
$Fccw$	Force counterclockwise (N)
FCR	Fixed charge rate (-)
Fcw	Force clockwise (N)
F_d	Drag force (N)
f_m	Final overall weighting (-)
$f_{PBstaff}$	Number of employees for power block (-)
F_R	Heat removal factor (-)
FS	Solar share - Fraction of total useful energy from solar input (%)
$f_{SFstaff}$	Number of employees for solar field (-)
F_T	Tipping force (N)
g	Acceleration due to gravity (m^2/s)
Gen_{eff}	Generator efficiency (%)
g_m	Customer requirement importance (-)
Gr	Grashof number (-)
h	Receiver height (m)
h_{co}	Convection heat transfer coefficient from outer cover glazing (W/m^2K)
h_{cp}	Convection heat transfer coefficient from absorber pipe (W/m^2K)
h_{fi}	Heat transfer coefficient inside absorber pipe (W/m^2K)
h_{ro}	Radiation heat transfer coefficient from outer cover glazing (W/m^2K)
h_{rp}	Radiation heat transfer coefficient from absorber pipe (W/m^2K)
Is_{eff}	Turbine isentropic efficiency (%)
I_{val}	Value of Ice ($/a)
k_a	Thermal conductivity of air (W/m.K)
k_d	Interest rate on debt (%)
k_{gw}	Thermal conductivity of insulation (W/m.K)
k_{pipe}	Thermal conductivity of absorber pipe (W/m.K)

L	Length of collector (m)
L_c	Longitude correction (hrs)
Lco	Length of outer cover glazing (m)
L_{ew}	Latent heat of evaporation for water (kJ/kg)
L_{fw}	Latent heat of fusion for water (kJ/kg)
L_{saved}	Land saved (ha/a)
m	Matrix size (-)
M_{bio}	Mass of biomass (tonnes)
M_{ice}	Mass of ice (tonnes)
m_{sol}	Mass flow in solar field (kg/s)
m_{turb}	Mass flow in turbine (kg/s)
M_{water}	Mass of water (tonnes)
N	Day of the year (-)
n_i	Number of internal reflections in a CPC
Nu_{co}	Nusselt number for convection from outer cover glazing (-)
Nu_{cp}	Nusselt number for convection between absorber and cover glazing (-)
P_{ar}	Profits after capital repayments ($/a)
P_{exit}	Turbine exit pressure (bar)
P_{inlet}	Turbine inlet pressure (bar)
P_n	Pitch (m)
PP_{cap}	Capital cost payback period (years)
PP_{sol}	Solar investment payback period (years)
Pr_{co}	Prandtl number for heat transfer from outer cover (-)
Pr_{cp}	Prandtl number for heat transfer between absorber and cover glazing (-)
P_{wr}	Profits with capital repayments ($/a)
Q	Net heat transfer to receiver's absorbing target (W)
Q_{boiler}	Useful energy from boiler (GJ/a)
Q_e	Heat absorbed by chiller (GJ/a)
Q_{in}	Heat transferred in (W)
Q_{in}^*	Solar radiation rate on collector (GJ/a)
Q_{loss}	Heat loss (W)
Q_n	Distance of an n^{th} mirror element from receiver (m)
$Q_{reject,h}$	High grade reject heat from solar field (GJ/a)
$Q_{reject,l}$	Low grade reject heat from chiller (GJ/a)
Q_u	Useful energy gained from solar field (GJ/a)
Q^{year}	Annual solar insolation ($GJ/m^2/a$)
r_c	Central band of illumination (m)
Re	Reynold number (-)
r_l	Left band of illumination (m)
r_{mn}	Technical and customer requirement relationship score (-)
r_n	Width of illumination (m)
r_r	Right band of illumination (m)
S_n	Shift or gap between mirror elements (m)
T_1	Turbine inlet temperature (°C)
T_2	Turbine exit temperature (°C)

T_a	Ambient temperature (K)
TA_{SF}	Total land usage of solar field (K)
T_{avg}	Average temperature of absorber (K)
T_c	Average temperature of cover glazing (K)
T_{exit}	Exit fluid temperature from receiver (K)
T_{ice}	Temperature of ice (K)
T_{in}	Inlet fluid temperature to receiver (K)
T_{local}	Local standard time (hrs)
t_n	Technical priority (-)
T_p	Surface temperature of receiver's absorbing pipe (K)
$T_{r,max}$	Stagnation temperature (maximum temperature of receiver) (K)
$T_{r,opt}$	Optimum temperature of receiver (K)
T_s	Temperature of steam available to heat cycle (K)
T_{sol}	Apparent black body temperature of the sun (K)
T_{solar}	Solar time (hrs)
U_L	Heat transfer coefficient ($W/m^2.K$)
U_{L1}	Heat loss through convection and radiation ($W/m^2.K$)
U_{L2}	Heat loss through conduction ($W/m^2.K$)
u_m	Improvement factor (-)
U_o	Overall heat loss coefficient ($W/m^2.K$)
ve	air velocity (m^2/s)
W	Width of mirror elements (m)
W_{net}	Net work of hybrid plant (GJ/a)
W_{turb}	Work at turbine (GJ/a)

Greek Symbols

α	Absorption
α_s	Solar altitude angle
β	Expansion coefficient of air (1/K)
β_n	Ray angle from n^{th} mirror element to receiver tower in transversal plane
γ_s	Solar azimuth angle from the south
δ	Declination
ε_c	Emissivity of cover glazing
ε_p	Emissivity of absorber pipe
η_c	Solar collector efficiency
η_{Carnot}	Carnot efficiency
$\eta_{endloss}$	Collector end loss efficiency
ηI_b	Energy efficiency of biomass boiler
ηI_c	Energy efficiency of solar field
ηI_{hc}	Energy efficiency of heat cycle
ηI_{os}	Energy efficiency of overall cycle
ηII_b	Exergetic efficiency of biomass boiler
ηII_c	Exergetic efficiency of solar field
ηII_{hc}	Exergetic efficiency of heat cycle
ηII_{os}	Exergetic efficiency of overall cycle

η_o	Optical efficiency
$\eta_{o(0=\theta)}$	Optical efficiency at normal incidence
η_{Shadow}	Shadow efficiency
$\eta_{thermal}$	Thermal efficiency
θ	Angle of incidence
θ_c	Half acceptance angle
θ_l	Angle in the longitudinal plane
θ_n	Slope angle of an n^{th} mirror element
θ_p	Profile angle of the sun
θ_t	Angle in the transversal plane
θ_z	Zenith angle
λ	Intercept factor
λ_{max}	Sum of priority vectors multiplied by totalled pair-wise matrix column
μ	Dynamic viscosity of air (kg/m s)
ν	Kinematic viscosity (m^2/s)
ρ	Density of air (kg/m^3)
ρ_r	Reflectance
σ	Stefan–Boltzman constant, 5.67×10^{-8} ($W/m^2/K^4$)
τ	Transmittance
φ	Latitude
ω	Solar hour angle

Abbreviations

AHP	Analytical hierarchy process
CI	Consistency index
CPC	Compound parabolic concentrator
CR	Consistency ratio
CSP	Concentrating solar thermal power
DNI	Direct-normal irradiance (W/m^2)
DSG	Direct steam generation
ELFR	Elevation linear Fresnel reflector
EOT	Equation of time
H-constant	Horizontal-constant mirror spacing arrangement
HFC	Heliostat field collector (power tower)
HoQ	House of quality
HTF	Heat transfer fluid
H-variable	Horizontal-variable mirror spacing arrangement
IAM	Incident angle modifier
LCOE	Levelised cost of electricity (¢/kWh)
LEC	Levelised energy cost (¢/kWh)
LFR	Linear Fresnel reflector
LHV	Lower heating value (kJ/kg)
MCDM	Multi-criteria decision-making
PDR	Parabolic dish reflector (dish engine)
PTC	Parabolic trough collector

QFD	Quality function deployment
RI	Random consistency index
TMY	Typical meteorological year

Chapter 1

Introduction

1.1 Problem statement: energy issues in India

According to the 2011 census, 69% of India's population lived in the countryside and was sustained primarily by agriculture and small local industries [1]. As of 2008, 47.5% of India's population living in rural areas did not have access to electricity [2]. Just fewer than 24,500 out of 112,401 villages in India without electricity were classified as being in remote and inaccessible areas [3]. The financial viability of extending the electricity grid to these areas is poor due to a dispersed population with a low peak power demand. Currently, the grid already suffers from high transmission and distribution losses, blackouts and power theft. Progress to improve the grid has been slow due to India's rapidly growing energy demand and population. In 2008, India used 0.84 million GWh of electricity, demonstrating a tremendous growth in electrical energy usage in the past decade (see Figure 1.1). In comparison, countries such as the UK have maintained a relatively stable electricity usage [4].

On top of India's national energy problems, fossil fuel prices are rising globally and international pressure to use ever more sustainable energy sources is increasing, due to concerns about global warming. Thus, governments in India and the rest of the world have aims to increase the contribution of renewable energy sources to the total energy mix. As a result, organisations and researchers are constantly seeking to improve and develop innovative solutions of providing electricity and other energy services.

Figure 1.1: Electricity usage in India and the UK, as provided by the United Nations Statistics Division [5].

1.2 Status of solar energy in India

Since the Indian Independence Act in 1947, India has increased its electrical generation capacity from 1.4 to 205 GW, but has largely neglected its solar resource [5]. The primary energy consumption mix, in 2010, consisted of 52.96% coal, 29.66% oil, 10.63% natural gas, 4.81 hydro-electric, 0.99% nuclear and 0.95% from other renewable resources [6]. As of 2009, grid connected solar generation capacity was a mere 2 MW [7].

India receives a high level of Direct Normal Irradiance (DNI), 4–7 kWh/m^2 per day. Thus, there is a vast potential for off-grid decentralised solar energy applications. To take advantage of this resource, one option that is currently of much interest is Concentrating Solar thermal Power (CSP) technologies, also known as solar thermal collectors. The Jawaharlal Nehru National Solar Mission was established in 2010 to encourage solar energy technology market penetration in India. The National Solar Mission is one of several initiatives as part of the Indian Government's National Action Plan on Climate Change to tackle issues of energy security and encourage renewable energy growth. With the objective of establishing India as a global leader in solar energy, a number of targets have been specified, most notably, to achieve 20 GW of solar power by 2022 [8].

The first phase, up to 2013, of the Solar Mission aims to support off-grid systems, such as hybrid CSP plants generating electricity, heat and cooling, to empower people at the working class level [9, 10]. India's Solar Mission also proposed demonstration plants for Research and Development (R&D) into various CSP technologies, including 100–150 MW of solar hybridisation with coal, gas and biomass [8]. CSP technologies are currently expensive; thus the Indian government plans to provide support in the form of capital subsidies and soft loans. This is to help achieve grid parity by 2022, another objective of the Solar Mission [10].

Solar thermal technologies have been successfully implemented in locations such as California and Spain, and are being vigorously promoted for schemes to provide Europe with electrical power from the Sahara. Detailed feasibility studies for such schemes have been prepared [11, 12]. In India, the uptake of solar thermal electricity has so far been limited to demonstrations, though solar thermal collectors are currently used in at least two locations to provide heat for milk pasteurisation processing and cooking [13, 14]. Proposals have also been made for a number of power plants in the regions of Rajasthan

and Gujarat, encouraged by incentives such as feed-in-tariffs. However, currently, most projects are still only at the planning phase.

1.3 Status of biomass energy in India

The potential for biomass boilers in India is vast with over 370 million tonnes of biomass being produced every year [15]. Biomass is available from agricultural wastes, direct harvesting and as a by-product from industries such as rice mills, sugar mills and saw mills. Biomass is estimated to contribute 46% to the total energy consumption in India and 80% in rural areas [16]. In industry, 40% of the fuel for boilers is supplied from biomass. However, due to problems with infrastructure and the seasonal variability of biomass in India, consumers are struggling to obtain a consistent fuel supply [17]. Furthermore, while biomass is still competitive, prices have increased considerably in recent years [18, 19].

The upstream activities required to use biomass as a feedstock for direct combustion include farming, harvesting, handling, storing, transporting and processing; storage is a critical issue in the biomass feedstock supply chain. A consequence of insufficient storage capabilities can be low biomass feedstock availability, particularly during India's monsoon season [20], which results in fluctuating prices [7]. Storage can be at the farm, an intermediate site or at the power plant. Storage is expensive and, depending upon moisture content, drying is often required; otherwise quality degradation, material loss, spores, fungal growth and fire are a problem. Labourers can also suffer from breathing problems as a result of handling husk and sawdust. Therefore, due to these heath risks labour availability is characteristically low during peak crop seasons in India. Costs from transportation and handling activities typically form a large percentage (20 – 50%) of the total cost for biomass feedstock [17]. Land requirements depend on crop yield but are significant in comparison to the energy output per land usage of alternative energy sources, such as solar [21].

1.4 The context of the Science Bridges programme

This PhD project was carried out in the context of the Science Bridges programme funded by Research Councils (UK) and Department of Science and Technology (DST, India). This programme was initiated to: 'Enhance linkages with USA, China and India through provision of a limited number of Science Bridges between research organisations, to raise the impact and profile of collaborative activity between the UK and these countries and to facilitate innovation from existing research' [22]. In this case, the Science Bridge was

between Aston University, in Birmingham, and the Indian Institute of Technology, Delhi (IIT Delhi). The title of this Science Bridge project was: 'Bio-energy: technology and business solutions for UK and India'. The overall aim of the project was 'to implement, in the UK and India, efficient decentralised bio-energy systems to carry out research needed to assist widespread adoption of these systems' [23]. The project involved 4 workpackages which included activities in both countries:

1. Resource assessment with regard to the use of wasteland and wastewater for energy crops.
2. Design and proof of concept of a Combined Heat and Power (CHP) plant in UK based on pyrolysis.
3. Implement a steam-powered tri-generation plant in India.
4. Design and implementation of a hybrid solar-biomass power plant (2–5 MW thermal) in Gujarat, producing electricity, ice, and thermal energy for various processes.

The author was appointed to carry out his PhD project to contribute towards the 4th workpackage: the hybrid solar-biomass power plant. A number of stakeholders and collaborators have been involved in the project; in particular the School of Engineering and Applied Science and Aston Business School (Aston University), Department of Applied Mechanics (IIT Delhi), and Industrial Boilers Ltd (IBL), Vapi, India.

Hybridisation of solar thermal with biomass combines two energy sources that complement each other, both seasonally and diurnally, to overcome their individual drawbacks. During the day the sun's rays can be harnessed by solar collectors and biomass feedstock can be burnt as a supplementary fuel to achieve constant base load operation. Generated steam can drive a turbine with exhaust steam used for heating and/or cooling. This is particularly practical in food-processing facilities where thermal energy and ice are potentially more of a requirement than electricity. India currently loses 20–40% of its vegetable and fruit food production before it reaches the consumer due to high temperatures and coinciding harvests [24]. There is therefore a need for ice in short and long term food preservation; and in certain areas of India, like Gujarat, this extends to fisheries and chemical plants. A hybrid solar-biomass plant can be designed according to a number of layouts. For the purpose of introduction, a typical layout for tri-generation is presented in Figure 1.2.

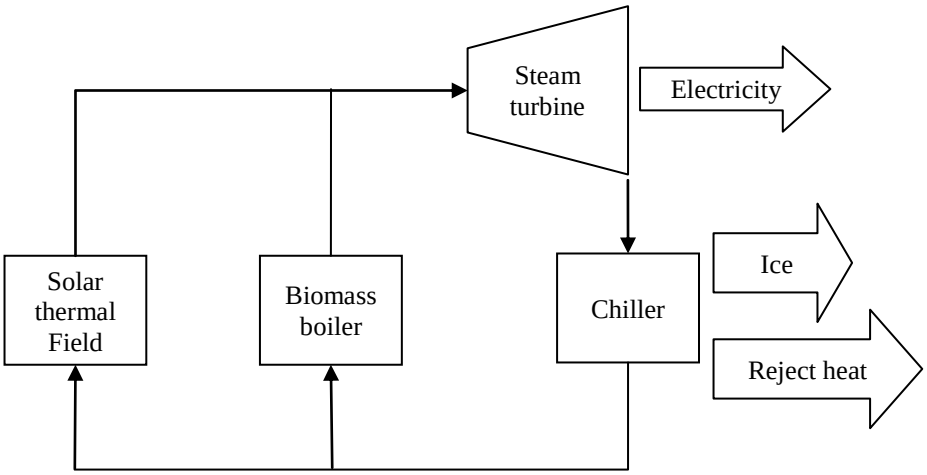

Figure 1.2: The main components of a hybrid solar-biomass power plant for tri-generation.

1.5 Hybrid solar-biomass energy

There are numerous approaches to hybridising solar and biomass energy. Space heating systems naturally use solar energy but are often balanced with biomass to provide any additional heat required. The European project SOLLET (European network strategy for combined solar and wood pellet heating systems for decentralised applications) has installed 10 hybrid solar-biomass heating systems as demonstration plants across Europe. These test facilities vary in size and operate with different solar-pellet combinations [25]. Another hybrid application, which is well documented in the literature, is the solar-biomass drier. Experimental studies of these hybrid types for the drying of agricultural products and foodstuffs have been performed in India, Thailand, and the Philippines [26, 27]. Small biomass boilers have also been hybridised with solar hot water panels for domestic heating by a number of companies, including Solar Focus and Treco. One recent proposal for a hybrid solar-biomass power plant has been made by the Government of China which has apparently agreed a deal to buy 2 GW of solar thermal technology from eSolar to supplement a biomass driven generator [28]. Another power generating system, designed by Electricité de Marseille, claims to use solar thermal and biomass co-generation for district heating, and compressed air technology for producing electricity [29]. A hybrid system has even been used in the creation of diesel. New Mexio-based Sundrop Fuels have created a refinery that utilises CSP technology to heat the biomass in the process of creating a synthetic gas that can be formed into fuel. They assert that 30 percent of the necessary heat in this process will come from the CSP technology, thus saving a third of the fuel that would have been required in this process otherwise [30].

While there are many alternative approaches to hybridising solar and biomass, the studies contained within this thesis focus on a hybrid power plant for electricity, ice and/or process heat generation. An overview of each component will now be given in order to introduce the aim and objectives of the project.

1.6 Overview of components of the hybrid solar-biomass power plant

1.6.1 Solar thermal field and solar thermal collector

Since initial attempts to convert solar energy for the purpose of steam generation in the mid 19th century [31], only comparatively recently has there been a renewed interest in CSP technologies. A solar thermal collector is formed from a concentrator and receiver assembly [32]. The concentrator usually comprises mirrors to focus captured solar energy onto a receiver. The receiver consists of an absorbing target to transfer concentrated energy, typically, to a Heat Transfer Fluid (HTF). A range of different solar collectors with varying concentrator and receiver configurations are available on the market today. A solar thermal field is formed from an array of solar collector units to capture a large amount of solar energy.

Solar collectors can either be linear or point focusing. Linear collectors require a single-axis tracking mechanisms to follow the traversing sun to increase energy capture. Collectors are typically aligned with one of the following: north–south horizontal axis with east-west tracking; east-west horizontal axis with north-south tracking or polar axis alignment with east-west tracking. A polar axis arrangement provides the highest annual energy capture, followed by a north-south axis alignment. An east-west axis results in the lowest energy capture, but provides the most constant energy capture through the whole year [33]. Point focusing collectors require a two-axis tracking mechanism. Whilst they are more complicated and expensive than a single-axis method, greater energy capture is achieved.

A range of operating temperatures is achievable from a solar thermal field due to the variety of collector designs and their geometrical concentration ratio. The concentration ratio is defined by the aperture area of the concentrator to the area of the receiver's absorbing target. A larger concentration ratio results in higher obtainable temperatures at which energy can be available to a coupled system. The theoretical maximum concentration ratio for a linear and point focusing collector is 212 and 45,000 suns

respectively. The solar collector types and solar thermal field are discussed in greater depth in the subsequent chapters.

1.6.2 Steam boilers

The steam boiler in its basic form consists of a container filled with water, with heat supplied to it to generate steam. The standard features of a boiler are: feed water, a combustion chamber for burning fuel, a draft system to supply air for the combustion process and a system for the collection and control of steam (see Figure 1.3). By placing a combustion chamber inside the boiler the heat exchange surface area is maximised improving boiler performance. The combustion chamber is crucial in the control of a boiler. The chamber regulates the fuel supply in proportion to the steam demand, the air supply, and the air-fuel ratio in order to achieve a stoichiometric mixture. The ratio between the fuel and air mixture is essential in trying to achieve complete combustion so that no smoke or soot is produced before the air is exhausted, termed the flue gas, typically to pre-heat the feed water [34].

Figure 1.3: Basic diagram of a steam boiler (left) and IBL's biomass fired boiler (right) [35].

Depending upon the fuel used in a boiler the fuel feed system varies. When oil is used, the oil is forced into the oil burner by fuel oil discharge lines. For solid fuels they can simply be shovelled into a firebox, however, this is inefficient, so a feed mechanism known as a stoker is commonly employed. Gas from city main lines can also be used, when mixed with air from a blower the gas is ignited in the firebox. Different boiler types exist to transfer heat from the combustion process to generate steam. The three basic approaches include: the fire tube boiler, heat passing through pipes surrounded by water in the container; the water tube boiler, water heated inside pipes by heat passing over them, and

the cast iron sectional boiler, large container sections heated externally. Steam generated is controlled and directed to its point of application through the use of vents, valves, headers, piping, etc. Boilers are warmed slowly upon start up; therefore, they are typically not taken off-line but banked to enable fast response times. Banking is achieved by the stoker coming online occasionally to keep the fire alive in the combustion chamber [*ibid*].

1.6.3 Steam turbines

The invention of the steam turbine is attributed to Sir Charles Parsons in 1884, and led to a revolution in power generation worldwide. The steam turbine is a mechanical device used to convert thermal energy, in the form of pressurised steam, into rotary motion, thus being particularly suited for driving electrical generators. The steam turbine, of which there are several modern variations, are used in the majority of power stations around the world. Steam turbines can either be connected directly to a generator or with a reduction coupling. As well as driving generators, steam turbines can also be used as mechanical drives. With a lower operating cost than using mains electricity, steam turbines are often considered for driving fans, compressors, pumps, etc., when steam is readily available. Different steam turbine types can be described in terms of their steam supply and exhaust condition [36].

The condensing turbine is favoured for most electrical power plants. Steam enters at a superheated state and then exits the turbine at a partially condensed or saturated state. The exit pressure is then below that of atmospheric, maximising the work output. The enthalpy or energy per kilogram of steam which flows through a steam turbine is a function of the pressure ratio, given by the inlet pressure to exhaust pressure. The higher the pressure ratio, the lower the steam flow rate required in order to produce power. Two other main classifications of steam turbines exist, non-condensing and extraction. These turbines are typically considered in combined heat and power applications.

The non-condensing (or back-pressure) turbine is used for applications which further process the steam for the use of its heat (see Figure 1.4). The exhaust pressure, which is above atmospheric, can be controlled through the use of regulating valves to meet the requirements of the process stream. The disadvantage is that power generation is significantly reduced.

Figure 1.4: IBL's BT-4 back pressure turbine [35].

In an extraction turbine, steam can be withdrawn through openings at an intermediate pressure for process heat. During periods of low thermal demands at the process heat stage more electricity can be generated. Additional steam can also be added to what are called induction or admission turbines. This type of operation can occur in large facilities using multiple boilers. In an induction turbine, steam is added at a point where the steam pressures are matched, increasing the flow through though the turbine, thus generating additional work. The induction steam is typically a by-product of some other process in the plant. At steam extraction and induction locations a governor controls steam flow. Exhaust steam from a high pressure can also be extracted and returned to the boiler for reheat before being passed to a second stage turbine operating at a lower pressure than the first. The design and geometry of each turbine stage can be classified by whether it is an impulse or reaction turbine [*ibid*].

In an impulse turbine, steam is accelerated through a set of stationary nozzles and directed into a set of rotating blades or buckets. In a single stage Rateau design turbine there is one row of buckets. For a Curtis design two buckets exist per stage and consists also of turning vanes separating the two buckets for redirecting the flow. In a multi-stage turbine a Rateau or Curtis design is used in the first stage followed by one or more Rateau stages. The total pressure drop is taken across the nozzles with the buckets being at static pressure. An impulse turbine controls speed and reduces steam enthalpy to a specified level. For a reaction turbine the rotor blades themselves form convergent nozzles moving due to a differential pressure between the front and back of the blades, with the steam directed by fixed vanes of a stator. A reaction turbine stage just receives steam from impulse blades. A

steam turbine is therefore rarely an impulse or reaction turbine only, rather an arrangement of the two. For example, one Curtis followed by several Rateau and finally a reaction row. In comparison to a multi-stage turbine, a single-stage turbine has a relatively lower capital cost but is also less efficient, therefore more steam is required to achieve the same power output [37].

The efficiency of a steam turbine ranges from potentially lower than 40% for a small low power single-stage turbine to as high as 90% for a high power multi-stage turbine. Part-load efficiencies, which vary with stage numbers, flow, and speed, can be estimated by assuming the power to vary as the cube of the rotational speed [38]. In a non-condensing turbine the efficiency is even further reduced for part loads. The efficiency of a turbine can be affected by several factors, including leakages, friction, bearing losses, throttle losses and degeneration.

Steam turbines can be damaged by steam condensing in the turbine leading to blade erosion. Thermal fatigue is also an issue. When starting a steam turbine gradual pre-heating is required before any loads are applied to reduce thermal stresses and strains. This can be particularly time consuming for large turbines, but relatively simple for smaller units. Cold and hot starts are experienced in practice depending on a turbine's state. Care is also required during the stopping and standing periods for a turbine. Extensive research has gone into the development of improved ferritic steels to minimise costs and reduce creep and fatigue. Currently, operating temperatures are limited to around 550–600 °C for small and large turbines respectively. However, with a push towards more powerful and efficient power plants, operators are looking towards using higher pressures and temperatures in the supercritical and ultra-super critical region. The result being improved thermal cycle efficiencies, with the drawback of increased material costs from the use of advanced alloys to handle temperatures in excess of 600 °C [39, 40].

Steam turbines can be controlled in a variety of ways to suit a given application. Speed is the primary control parameter and is crucial in any turbine; without it, safe operation cannot be maintained. Using a flow metering device, inlet steam is measured and controlled through governor valves. When generating electricity, a turbine typically runs at nearly constant speed to ensure a uniform voltage and frequency. With the speed fixed to match the frequency of the grid, a higher steam load will increase torque, rather than shaft rotational speed, thus the generator produces higher amperage. The steam load is often the

main consideration in a turbine's design. The other turbine parameters usually controlled are the inlet, extraction, induction and exhaust pressures; through set-point values and corrective signals, pressures are regulated so that they are stable. In mechanical drive applications the process parameters are also included into the control system [41].

The steam turbine, in comparison to a reciprocating steam engine, uses less floor space, foundations and lubricating oil. On a small scale, steam turbines can be as efficient and cost about the same as a steam engine, while on a large scale they have a greater capacity than any other prime mover [37], thus no other types of prime mover are considered in this thesis.

1.6.4 Chillers

Absorption chillers are thermally driven machines to achieve cooling, and can replace the more conventional mechanical vapour compressor system. Absorption chillers utilise a liquid sorbent; however adsorption machines also exist which use a solid sorbent. Chillers are an efficient way to make use of waste heat from sources such as generators, engines, turbines and solar collectors. The hot fluid (steam) entering the chiller evaporates refrigerant, removing heat through the latent heat of vaporization from a chilled stream, typically water or brine. In an absorber stage, refrigerant vapour is absorbed and cooling water continuously removes the generated heat out of the system. The ammonia-water chiller was patented by Ferdinand Carre in 1859, and soon after similar machines were widely used for food storage and ice making [42]. Depending upon the grade of heat supplied (i.e. temperature and pressure) chillers can be single or double effect. A higher coefficient of performance is achieved from a double effect chiller; however, system costs and complexity are increased. To achieve temperatures required for making ice the refrigerant used is typically ammonia, chilling a brine solution [43].

Ice can be formed in a variety of ways through refrigeration. Blocks of ice can be made in metal cans submerged in refrigerated brine and removed once frozen. To form blocks of ice more rapidly, thinner blocks can be produced with refrigerant passed through tubes in direct contact with the ice. The ice then needs to be partially defrosted and harvested. Flakes of ice are produced from water being sprayed on a refrigerated drum and scraped off. Hollow cylindrical pieces of ice can be formed in refrigerated tubes, and large plates of ice can also be formed on refrigerated metal sheets with hot water passed on the other side for removal. Manufactured ice is typically further crushed or cut depending upon its

application. Ice making plants are usually run automatically and on a continuous cycle [44].

Solar cooling is considered a priority for developing countries in sunny locations due to the need of refrigeration for food and vaccines and the high availability of solar radiation [45]. This is reflected in the literature with numerous publications on solar powered ice makers using low grade heat from flat plate solar collectors and a carbon and methanol solid adsorbent pair [45-47]. A carbon ammonia pair has also been proposed by Critoph [48] for use in a solar/biomass powered adsorption system, using biomass to reduce the area of solar collector required as the solar collector forms the most expensive part of the system. The direct use of solar collectors for cooling/ice making in an adsorption system is however considered beyond the scope of this thesis.

1.7 Aim and objectives

The biomass boiler, steam turbine and chiller are well established technologies that are widely used in India. In contrast, electricity generation from solar thermal is a relatively new concept. The solar thermal technology was therefore considered the critical component for the successful implementation of a hybrid solar-biomass power plant. Thus, the primary research contained within this thesis contributes towards the selection and design of a solar thermal collector for India, with specific focus given to the Science Bridge's hybrid plant to be developed in Gujarat. Considering this the following aim and objectives were outlined.

The overall aim of this thesis is to specify the design details of a solar thermal collector and evaluate the feasibility of its application to hybrid solar-biomass power plants in India. This aim is to be achieved by completing the following three main objectives and corresponding sub-objectives.

1. **Select solar thermal collector technology for power generation in India**
   1.1. Review current solar thermal technology options
   1.2. Establish a method for evaluating and selecting a solar thermal collector for India
2. **Improve selected solar thermal collector for applications in India**
   2.1. Determine avenues of optimisation for the selected solar collector
   2.2. Investigate new concepts based on the selected solar collector technology to improve further its design

2.3. Describe a model to simulate the selected solar collector and build a prototype for experimental verification

3. Evaluate the feasibility of hybrid solar-biomass power plants in India

3.1. Perform a technical, financial and environmental study of alternative hybrid plant applications in India

3.2. Investigate the suitable sizing of a solar thermal field in hybrid operation with a biomass boiler for alternative applications, including the Gujarat hybrid plant

1.8 Structure of the thesis

This first chapter has given a broad overview of the energy situation in India. The potential for solar and biomass energy applications has also been outlined. The chapter has concluded with the overall aim and objectives for this thesis on solar thermal collectors for use in hybrid solar-biomass power plant applications. The subsequent chapters of this thesis address these objectives and are organised as follows:

Chapter 2: The different solar thermal technologies are reviewed and assessed for electricity generation in north-west India through a Multi-Criteria Decision-Making (MCDM) method: the Analytical Hierarchy Process (AHP). The solar thermal technology options are compared against a series of technical, financial and environmental criteria. Quantitative data is established through a literature review and qualitative data is collected through a workshop convening experts working within the field of solar energy. As a result, the Linear Fresnel Reflector (LFR) is recommended as one of the most appropriate solar technologies to pursue for India.

Chapter 3: A cost-exergy optimisation study of the LFR is performed to seek improvements in the LFR design. Optimisation is achieved through varying the mirror spacing arrangement to maximise the potential power output (exergy) and operational hours whilst minimising the capital cost. In addition, the ideal operating temperature of the collector is determined. The optimisation method is applied principally to a prototype LFR collector developed by project stakeholders and the author in India.

Chapter 4: Applying a multi-criteria decision-making methodology, novel LFR concepts are developed and compared that are not constrained by the boundaries of the conventional LFR design. A new design termed the Elevation Linear Fresnel Reflector (ELFR) is produced; subsequently a full scale prototype is developed in the UK. A final comparison

is made between the ELFR and a conventional LFR design by consideration of both technical and financial aspects. Design recommendations for LFR applications in India are provided.

Chapter 5: The development of the ELFR prototype and an experimental set-up is described in detail. Experimental procedures are outlined and performed to validate theoretical models presented for estimating the energy gained by an HTF (the fluid passing through the collector) in an LFR system. The validated models enable a solar thermal field – based on LFR technology – to be controlled and simulated. Further work and design improvements for the ELFR are discussed.

Chapter 6: The technical, financial and environmental feasibility of hybrid solar-biomass power plants is evaluated through a series of case studies, including the hybrid Gujarat power plant. The studies investigate alternative hybrid applications for tri-generation (electricity, ice and heat), electricity generation and process heat, and the sensitivity of variable factors such as plant size, location, control and financing. As a result, the ideal sizing of the solar thermal field for each case study is provided.

Chapter 7: The research outcomes of the thesis are discussed and the extent to which the original aim was met considered. The thesis concludes by highlighting the contributions to knowledge and the potential for future work.

Figure 1.5 presents the thesis structure diagrammatically. It shows how the technology selection process in Chapter 2 focused the studies performed in Chapters 3–5. A combination of these studies determined the model parameters for a series of alternative hybrid plant scenarios analysed in Chapter 6.

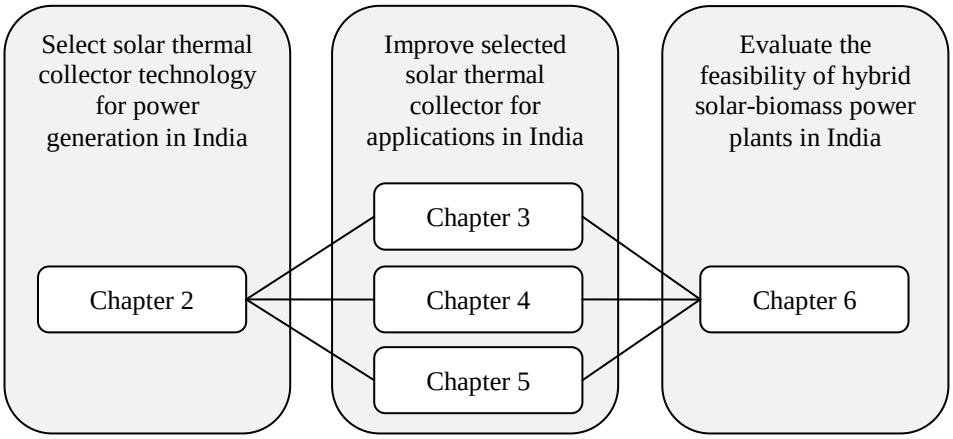

Figure 1.5: Thesis chapter structure. Chapters are listed under the three main objectives of section 1.7.

Chapter 2

Solar thermal collector selection: evaluation of options using the analytical hierarchy process

2.1 Introduction

This chapter addresses the selection of the solar collector technology for India. Elsewhere in the world the preferred choice has been the parabolic trough type, which is used in most of the large installed CSP plants in the US and Spain. Alternatives are being actively pursued, however, such as heliostat type concentrators with central tower receivers and parabolic dishes coupled to Stirling engines. As is frequently the case with energy technologies, there are numerous options, each with its advantages and drawbacks. Moreover, the best solution for India may not be the same as for the US or Europe, as the economic and technological environments are different.

The aim of this chapter was to review and evaluate the competing solar thermal collector technologies applicable to electricity generation in India with the help of a structured method. Specifically, the objective was to provide a recommendation about which technologies to pursue in the context of the current project in Gujarat and others that were expected to follow. The Analytical Hierarchy Process (AHP) was adopted because it is a decision-making tool well suited to multifaceted problems where a basic cost-benefit analysis is simplistic. It is a process that facilitates discussion among the designers and other stakeholders. Furthermore, it generates documentation thus lending transparency to the decision making rationale. The process is based both on mathematics and psychology to provide an overall answer and differs from other decision-making models by encompassing both known and unknown data. The essence of the process is that judgment is used to evaluate the problem as well as factual information and expert opinion. This is particularly useful in the case of evaluating solar collector technologies where the varying scale and prototype nature of some of these systems gives uncertainties when drawing a direct comparison between their operating characteristics [49].

Saaty, who originated AHP in the 1970s, described applications ranging from transportation planning to choosing a school for his son [50]. More recently, AHP and other Multi-Criteria Decision-Making (MCDM) methods have been applied to many issues in energy planning, as reviewed by Pohekar and Ramachandran [51], along with other

energy selection decisions including the assessment of oil pipeline inspections and energy resource allocation for households [52-54]. One paper from Marttunen and Hamalainen uses the AHP process to help assess the environmental impact of hydropower [55]. Bhattacharya and Dey use the AHP for power sector market selection in southern India [56]. Kaya and Kahraman use a combined Fuzzy and AHP approach for renewable energy planning in Istanbul [57]. The AHP is a tool that is being consistently used for the implementation and growth of technology throughout the energy sector [58]. In this sector, it is typical to find a large choice of technologies, surrounded by controversial issues and variations in expert opinion. This makes AHP a particularly valuable tool that can be used to help obtain a consensus. In essence, AHP simplifies a complex decision by decomposing the problem into a hierarchy of 'criteria' or sub problems to be analysed individually. To illustrate how the process works, a simple example is first provided based on the selection of a car.

2.2 The analytical hierarchy process: An example for car selection

Suppose that a car has to be selected from three alternatives, Car A, B, and C. This decision is tackled by breaking down the problem into a hierarchy of four more manageable sub-problems, called criteria, which can be analysed individually. Further sub-criteria can be developed to give a more accurate selection. Selection of a car in this example is made based on the criteria of speed, comfort, cost and fuel economy (MPG). Figure 2.1 shows the resulting hierarchy.

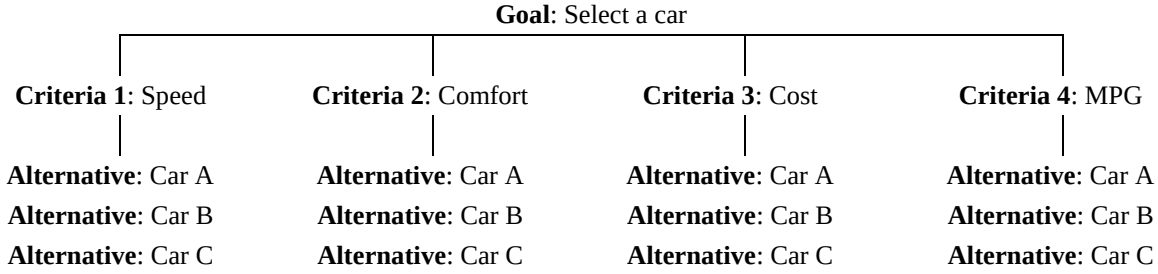

Figure 2.1: Simple hierarchy tree for the selection of a car.

The alternative cars are first compared against each criterion through a pair-wise comparison matrix. Using factual data or judgement, each alternative is scored on a scale of 1–9 (1-week, 9-strong) against the other alternatives to show their preference (see Table 2.1). If an alternative is worse, a reciprocal value is produced, e.g. 1/9. The matrix is then normalized by dividing a cell by its corresponding column total. The average of the row of

the normalized table provides a priority vector (i.e. the preference in comparison to the other alternatives) for each alternative for the criterion analysed. An example is given for the criterion speed, showing that Car A is the fastest, and therefore has the highest priority vector (see Table 2.2).

Table 2.1: Pair-wise comparison scale values for the level of preference to be used in the pair-wise comparison matrix.

Verbal Judgment of Preference	Numerical Rating
Extremely Preferred	9
Very strong to extremely	8
Very strongly preferred	7
Strongly to very strongly	6
Strongly preferred	5
Moderately to strongly	4
Moderately preferred	3
Equally to moderately	2
Equally preferred	1

Table 2.2: Normalized pair-wise comparison matrix for alternatives preference against the speed criterion.

	Car A	Car B	Car C		Normalized			Priority Vector
Car A	1	8	5		0.75	0.67	0.79	0.74
Car B	1/8	1	1/3	=	0.09	0.08	0.05	0.08
Car C	1/5	3	1		0.15	0.25	0.16	0.19
Total	1.33	12	6.33					

This process is repeated till a priority vector for each alternative is developed against every criterion. However, the importance of each criterion in relation to the other criteria is not specified. Thus, a final pair-wise comparison matrix is completed to develop a weighting vector for each criterion (see Table 2.3). This stage of an AHP is often subjective and a study can be improved by obtaining the opinion of experts in a relevant field. The hierarchy tree can be updated to show all alternative priority vectors and criteria weighting vectors (see Figure 2.2).

Table 2.3: Pair-wise matrix for the weighting preference of each criterion.

	Speed	Comfort	Cost	MPG		Normalized				Weighting Vector
Speed	1	1/4	1/7	1/5		0.06	0.08	0.03	0.10	0.07
Comfort	4	1	1/3	1/2	=	0.24	0.15	0.07	0.25	0.18
Cost	7	3	1	1/3		0.41	0.46	0.22	0.16	0.31
MPG	5	2	3	1		0.29	0.31	0.67	0.49	0.44
Total	17	6.5	4.48	2.03						

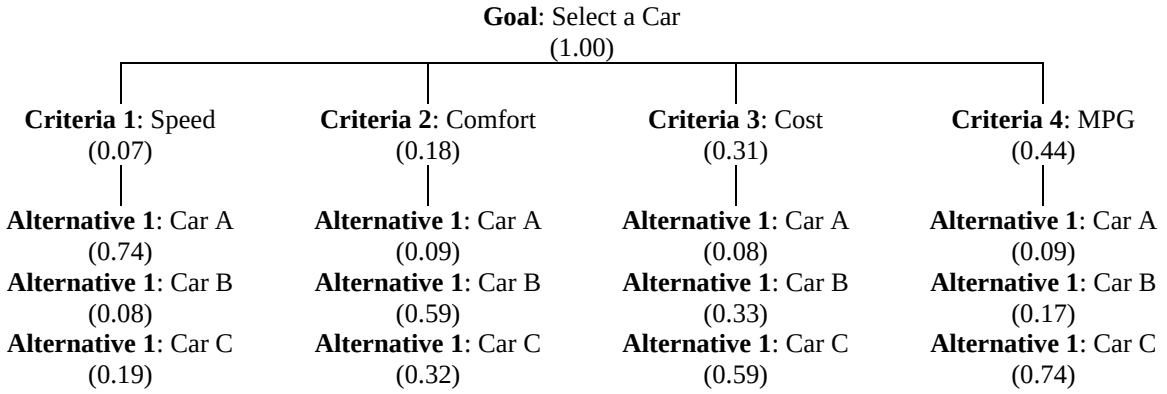

Figure 2.2: Updated hierarchy tree showing final priorities.

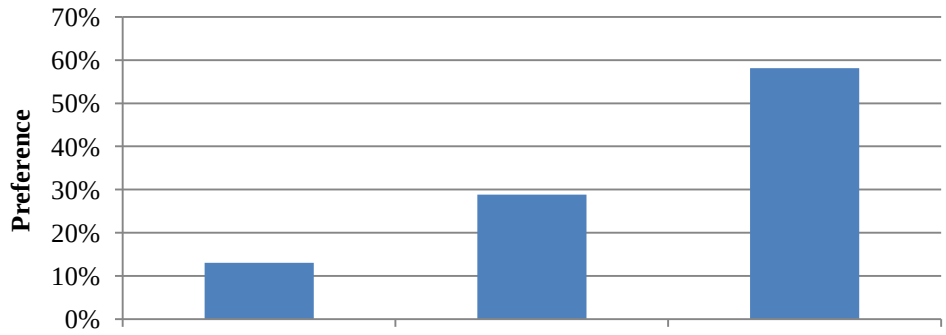

	Car A	Car B	Car C
Speed	0.049	0.005	0.012
Comfort	0.016	0.104	0.057
Cost	0.024	0.105	0.186
MPG	0.042	0.074	0.325
Total	13.1%	28.8%	58.1%

Figure 2.3: Preferential ranking for the AHP car selection study.

The final overall value for how much each technology is preferred, is calculated by multiplying each alternative's priority vector by the corresponding criterion's weighting vector and totalling the values for each alternative. The final ranking gives a relative value which can be expressed as a percentage of the preference. For the car selection example, alternative C is the preferred car (see Figure 2.3).

Finally, a consistency check can be performed to access the reliability of the results, and highlight any potential mistakes. For example, if Car A was ranked higher than Car B for speed and Car B was faster than Car C, Car C could not be preferred over Car A.

Saaty measured consistency by using the consistency ratio *CR*, which is calculated from a consistency index *CI* and random consistency index *RI*. Saaty determined that there is an acceptable level of inconsistency when the consistency ratio is less than or equal to 10%.

$$CI = \frac{\lambda_{max} - m}{m - 1} \tag{2.1}$$

Where λ_{max} is the sum of the priority vectors multiplied by the corresponding totalled value of the original pair-wise matrix column and *m* is the size of the matrix. For the speed criterion (Table 2.2), λ_{max} is given by, (1.33x0.74) + (0.08x12) + (6.33x0.19), which equals 3.08. The size of the matrix, *m*, is 3. The consistency ratio is finally calculated from,

$$CR = \frac{CI}{RI} \tag{2.2}$$

where the random consistency index, *RI*, is obtained from a standard table for the AHP (see Table 2.4). Therefore, for the speed criteria there is acceptable consistency of 0.0667 or 6.7%. Each criterion is evaluated and if all criteria have an acceptable consistency the AHP study is finished.

Table 2.4: Random consistency index (RI).

m	1	2	3	4	5	6	7	8	9	10
RI	0	0	0.58	0.9	1.12	1.24	1.32	1.41	1.45	1.49

2.3 Methodology

The methodology for utilising the AHP for the technology selection of a solar thermal collector for alternative case scenarios was outlined as follows (see Figure 2.4).

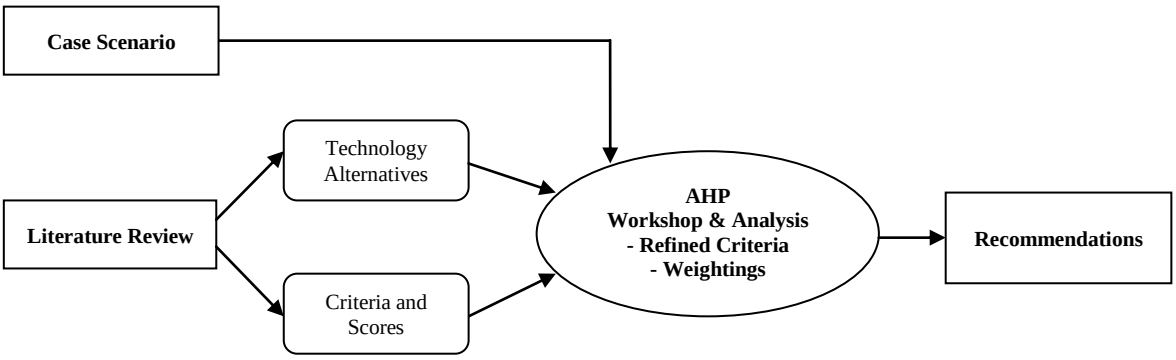

Figure 2.4: Flow diagram showing the methodology for the technology evaluation and selection based on the AHP.

i. A comparative literature review of solar thermal collectors was performed to compare the existing technologies. The output was a shortlist of technology alternatives and evaluation criteria. The criteria were categorised as technical, financial or environmental.

ii. These technology alternatives were scored against criteria through a pair-wise comparison, using a characteristic table of data produced from a literature review. In addition, thermodynamic calculations provide numerical values against certain criteria.

iii. A workshop was convened among solar energy experts in India, at which the technological alternatives and criteria were presented. The expert panel was invited to review the criteria and weight them for four case studies to produce a set of recommendations.

The choice of case studies encompassed the target location of Gujarat and three others: Southern Spain, California's Mojave Desert and the Sahara desert. These last three were included to broaden the frame of reference to include locations where CSP plants were already operational, or where advanced stages of planning have been carried out. The outcome was a recommendation of the best solar thermal collector technologies for each case scenario.

2.4 Solar thermal collectors: a literature review

With the goal of selecting the best CSP technology for a solar thermal power plant in India, technology alternatives and criteria for an AHP study were established through a literature review.

2.4.1 Parabolic trough collector (PTC)

The Parabolic Trough Collector (PTC) is the most established CSP used to date. Formed from a parabolic mirror, they use a single-axis tracking mechanism to track the sun and focus the solar rays onto a linear receiver positioned at the focal axis (see Figure 2.5). The receiver is an evacuated glass tube and absorbing pipe configuration, commonly used among CSP technologies due to low heat loss properties. Synthetic oil is commonly pumped through the absorber pipe to transfer heat to a heat exchanger to generate steam.

PTCs of this type can achieve concentration ratios in the range of 30 – 100, with working temperatures of around 400 ºC.

The largest solar thermal facility in the world currently is the nine Solar Energy Generating Systems (SEGS), built by Luz Industries in the Mojave Desert in California. Together the systems provide a total installed capacity of 354 MW [33]. Other large PTC facilities in Europe include Andasol 1 and 2 (Figure 2.5).

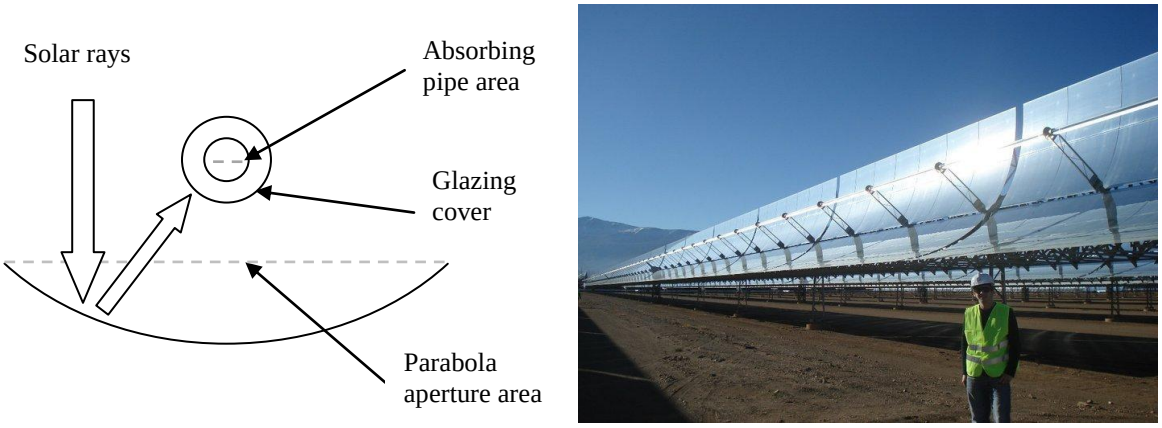

Figure 2.5: Cross section of a parabolic trough collector (left). PTCs and the author at Andasol 1, Spain, during a site visit (right).

A series of PTCs form a solar field which is usually orientated to a north-south axis alignment with careful consideration given to the distance between collector rows. This distance will determine the amount of land and piping used and therefore affects costs. It also affects fluid transport and optical shadowing losses which in turn affect the efficiencies of the system [59]. Optical efficiencies of 80% have been obtained at the SEGS, with a land usage of 3.2 m^2/MWh/year [33, 60]. The on-line parasitic or auxiliary electrical load of the SEGS VI system varies monthly, but is on average around 10% of the gross solar output [61]. The newer SEGS VI – VII increased the outlet temperature from the solar field from 320 – 390 ºC to raise the generated steam at the heat exchanger to a pressure of 100 bar. A useful technical detail for comparing solar collectors is the temperature obtained when the heat transfer fluid (HTF) flow is stopped and no more heat is entering the receiver, this is known as the stagnation temperature. For the parabolic trough collector stagnation temperatures greater than 600 ºC are typical [33].

While some types of tracking methods are more accurate than others, some collectors do not require as high a level as accuracy as others. The most suitable solar tracking method

for a collector depends upon a factor known as the acceptance angle or direct beam capture angle. The acceptance angle is the range of incidence angles or maximum error tolerance of the tracking device, where the efficiency factor changes by no more than 2%. This can be calculated by turning the tracking mechanism off and measuring the efficiency against the out of focus angle. This can be shown graphically with the efficiency at a normal incidence plotted against the efficiency at varying focal angles. The angle is often stated as a half-acceptance angle [31]. The half-acceptance angle for a PTC is around 0.5º [31, 62]. For the standard PTC, the projected total operational and maintenance cost is approximately 0.02 $/kWhe with a capital cost of 350 $/m^2 (275 €/m^2) [63, 64]. The SEGS VI plant in 1997 cost 3972 $/kW, projected costs for a similar system built now (2010 – 2020) are in range of 3000 $/kW [60].

Though synthetic oil has been used as the HTF in the absorbing tubes of most PTCs to date, this transfer medium limits the operating temperature to around 400 ºC. Molten salt has been suggested, but only prototype systems have been built due to the problems of the higher viscosity and high melting temperatures requiring trace heating. An actively pursued alternative is to have Direct Steam Generation (DSG) in the absorber tubes, thus avoiding the costs of expensive HTFs and heat exchangers [59]. The pumping requirements and thermal losses are also smaller as the field temperature can be reduced without affecting the steam temperature. The system is not without its technical challenges, with the risk of overheating tubes and potential flow instabilities. Sophisticated controls are required to accommodate the use of the two-phase flow of water and steam. Luz Industries, who planned to commercialize the technology, projected that efficiencies would be improved, with capital costs reduced to around 2100 – 2300 $/kW. It has also been conceived that in DSG systems, the solar field can act as an evaporation stage, with turbine exhaust gas used for superheating and preheating in a conventional gas turbine combined-cycle power plant. The overall cycle efficiencies are again expected to increase with higher working steam temperatures achieved for the same level of heat use [33].

The Plataforma Solar de Almería (PSA) in Spain has installed a 2 MW plant to carry out a number of experimental investigations into the behaviour of steady-state and transient flow in DSG parabolic troughs. The two-phase flow and stress on the receivers for different operating and process conditions are of particular interest. In DSG, there are three process methods typically considered, each with benefits and disadvantages. They are the once-through, the injection, and the recirculation process (see Figure 2.6) [65].

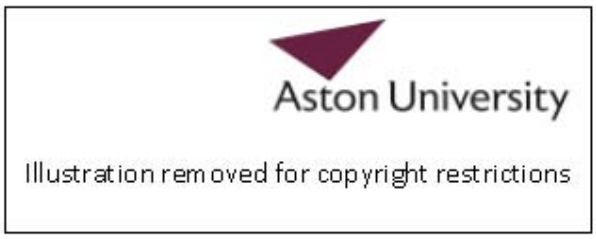

Figure 2.6: Methods for direct steam generation in parabolic trough collectors – redrawn from ref. [66].

The once through concept simply circulates water from inlet to outlet generating superheated steam at the field outlet. Control of the superheated steam parameters at the outlet have proved difficult. The injection method injects water at several places along the collector rows. Problems with the complexity of this system have resulted in further developments to be rejected. The recirculation mode uses a water steam separator located near the outlet. With too much water to be evaporated fed through the collector rows stratification of the water is prevented with a good wetting of the absorber pipes. Excess water is re-circulated at the separator while the steam is passed on to be superheated.

One of the greatest problems in DSG is the deformation and bending on the receivers during stratified two-phase flow. The separation of water and steam in steel pipes causes high thermal stresses which is difficult to overcome, if the pipe is wet all round the inside the heat is transferred more evenly. The insertion of copper can reduce these stresses and provide greater heat transfer; however the economics of this solution however are doubtful. Bimetallic copper-steel receivers have been proven to be superior to steel receivers particularly in low power applications (1 – 60 kWe), where stratification is unavoidable [67]. The recirculation method has been shown to have the greatest benefit in terms of stability and stress on the absorbers [68, 69]. Where tilted troughs have been used they have proved unsuccessful and unnecessary to achieve direct steam generation [70].

As well as engineering difficulties with DSG, the control system becomes more complicated. In typical PTCs using synthetic oil, the mass flow rate at the inlet to the field is controlled to maintain a target temperature [71]. In DSG systems, the pressure also needs to be regulated to match the specifications of the prime mover, e.g. a steam turbine. The quantity not the quality of steam being produced is then the only varying parameter with changes in solar irradiance. Valenzuela et al. have presented a proportional-integral control-based system for a DSG power plant operating with recirculation, finding that the system is more stable and easier to control at higher pressures [66]. DSG also enables higher process temperatures in comparison to thermal oils, however thermal storage is more complicated [72] .

Many of the environmental effects restricting the development of solar thermal power stations are similar to those of other conventional power plants. However, locations that are usually suited to solar applications, such as deserts and steppe areas, tend to be away from populated areas, with plenty of available land. Although the accessibility of water can be a problem which goes in hand with some of these places, solar thermal systems generally use less water in comparison with other conventional power stations. The water requirement is heavily dependent upon the entire plant cycle being used rather than the collector type alone. With the land and water availability being very dependent on the proposed location, the type of collector most suited for the implementation of a solar thermal plant may vary [59]. While collectors may typically use around only a third of the land covered, it is difficult to use the ground for anything else, unlike with wind turbines which can have crops growing among them. It is claimed however that the SEGS plant use no more land than conventional power plants when the full fuel cycle land requirements are considered [73].

2.4.2 Heliostat field collector (HFC)

A Heliostat Field Collector (HFC), also known as a power tower uses an array of mirrors, called heliostats, to redirect incoming solar rays to a receiver (Figure 2.7). The heliostats which can be flat or slightly concave use a two-axis tracking mechanism to focus rays to a single point at the central receiver. Typically, water-steam has been used at the receiver, but some more recent systems use a molten salt mixture of sodium and potassium nitrates. The benefit of the molten salt is that the solar receiver can be started quickly as it is a single phase fluid and the system is well suited to heat storage.

An oversized solar thermal system enables storage of excess heat in an auxiliary thermal unit. While solar collectors can only capture the sun's rays during daylight periods, stored heat can be used to extend the operational hours of the plant. The percentage of time a solar plant can operate at full load during a year is known as the capacity factor.

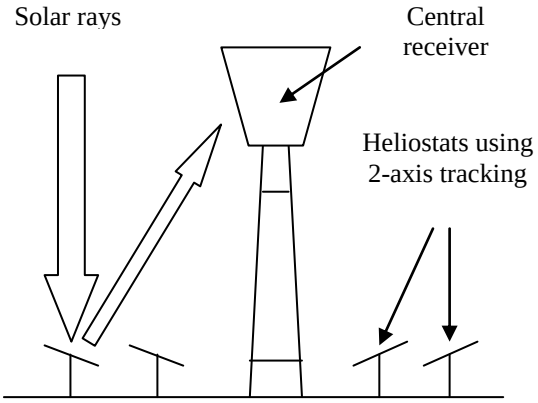

Figure 2.7: Schematics of a heliostat field collector (left). Solar 2 in the Mojave Desert, California (right) [74].

Gemasolar, a 19.9 MW_e solar power station commenced selling electricity to the grid in Spain, May 2011, and is the world's largest HFC using molten salt storage. The storage facility permits a remarkable 15 hours of operations with zero solar input. Gemasolar operates with an annual capacity factor of 74% [75]. However, the majority of data on HFCs come from the demonstration projects, Solar 1 and Solar 2, constructed in the Mojave Desert (Figure 2.7). The Solar Tres Tower in Andalusia, Spain, was a more recent development that aimed to build upon Solar 2. Spain is also home to the world's first commercial water-steam power tower PS10 and PS20. There are also several other pilot test facilities around the world have been built and remain in operation.

Such HFC systems are usually large at over 10 MW as they benefit from economies of scale. The use of a central receiver means that minimal thermal transport is required giving higher optimal temperatures of around 500 ºC [73], and a stagnation temperature in the region of 1750 ºC [31]. This can represent a technical challenge with thermal fatigue limiting the level of solar irradiance that can be sustained. The Solar 1 tower operated at 516 ºC with an outlet pressure of 105 bar, which are common operating parameters for HFCs [33]. Typical concentration ratios range between 300 – 1500 [31, 76]. With the higher temperatures, the result is that these systems have the capacity for greater efficiencies, giving more output than the more commonly employed parabolic trough. The

parasitic loads are estimated to be around 10% for a full scale system, with values being considerably higher in the non commercial Solar 2 plant, due to the lower capacity factor, at over 20% [77].

The capital cost of an HFC system is considerable at around 4000 \$/kW or 476 \$/m^2 and with operational and maintenance costs of 0.034 – 0.093 \$/kWh_e [33, 78]. As most of the cost comes from the expensive heliostats, significant effort has gone into reducing the cost of these components over the years, and by making them progressively larger, the cost has now fallen from approximately 1000 \$/m^2 to 150 \$/m^2. It is predicted that the cost for a large central receiver system could fall as low as 2500 \$/kW [33, 63, 79].

From an environmental perspective, the nature of a heliostat array layout requires a large amount of space and therefore HFCs use more land than any other CSP technology at around 4.6 m^2/MWh/year [78]. Depending upon the layout and location, factors such as the optical efficiency, capture efficiency and acceptance angle are variable [80]. The type of terrain available is also variable; whereas levelled ground is the common choice, hillsides have also been utilised [81].

The concept of using air as a heat transfer medium in an HFC's receiver has been conceived as well. In 1987 the CESA-1 tower at the Plataforma Solar de Almería in Spain used an air receiver with operating temperatures of up to 1000 ºC at 10 bar with the use of ceramic receivers [31, 33]. Problems arose from the ceramic receivers having to be 20 – 25 times larger than a molten salt receiver, making the system very expensive and subject to high heat loss. A newer idea is to create a three dimensional volume that came to be known as the volumetric air receiver. In spite of its theoretical advantages, technical limitations have, as yet, restricted any large scale developments of the technology. Solgate, erected in the CESA-1 tower, is one of the few volumetric air receiver pilot projects in existence and has achieved operating temperatures of over 1000 ºC with the direct drive of a gas turbine [59]. A comprehensive description of all the power tower projects and types of receivers has been presented by Goswami and Kreith [65].

2.4.3 Linear Fresnel reflector (LFR)

The Linear Fresnel Reflector (LFR), also referred to as the Linear Fresnel Collector (LFC), is considered to be particularly promising among CSP technologies as it benefits from a relatively simple and inexpensive design. In comparison to the PTC, which uses large parabolically shaped reflectors and a moving receiver, the LFR employs long, thin, low profile mirror elements, spaced horizontally and located close to the ground at vary distances from a central tower, thus minimising structural requirements and wind loads. Located at the top of the receiver tower is a fixed absorber, therefore removing the need for flexible high pressure pipe lines (see Figure 2.8). Yet, as the LFR has less energy capture per unit area than the PTC and HFC technologies, the need for improvements is still considered to be significant, particularly in raising the annual optical efficiency [64].

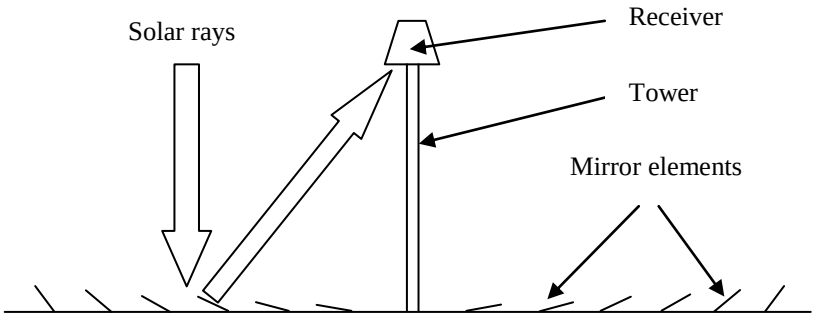

Figure 2.8: Linear Fresnel reflector with mirror elements focusing onto a horizontal receiver.

Several receiver designs exist, including configurations using simple pipes, plates, evacuated tubes and secondary concentrating devices [82]. Typically a horizontal type is favoured over a vertical or angled receiver [83, 84]. One particular design often utilised is the trapezoidal cavity receiver which comprises partially insulated absorber pipes with a reflector plate and cover glazing forming a cavity for the collection of rays and minimisation of heat losses [85, 86].

The LFR principle was first developed by Baum et al. in 1957, and later applied by Giorgio Francia in 1961, who designed both linear and two-axis tracking Fresnel reflectors [31, 87, 88]. In 1979 a large scale project was initiated by the U.S Department of Energy for a 10 MW_e and 100 MW_e power plant during the oil crisis, but these never came to fruition due to a lack of funding [89]. In 1991 the Israeli Paz company constructed a LFR at the Ben-Gurion Solar Electricity Technologies Test Centre; however, due to construction difficulties resulting optical efficiencies were very low [90]. A new variant of the LFR termed the Compact Linear Fresnel Reflector (CLFR) was initially proposed in 1993 at the

University of Sydney. It used interleaving mirrors to focus sunlight onto multiple receiver towers [70, 83]. In 2001 a Belgian company, Solarmundo, installed a 2500 m^2 LFR prototype in Liege [86]. Solarmundo later merged with the Solar Power Group, Germany, who constructed Fresdemo, a large pilot LFR system at the Plataforma Solar de Almería (PSA) in Spain, which was tested until 2008 [91-93]. Since 2005 several LFRs have been constructed for industrial process heat applications and solar cooling in various locations across the USA [94] and Europe, including the towns of Freiburg, Bergamo, Grombalia, and Sevilla [95]. Founded in 2006, Novatec Solar has recently development the world's first commercial LFR power plant, Puerto Errado 1 (PE 1), a 1.4 MW power plant that commenced selling power to the Spanish grid in March 2009. Puerto Errado 2, a 30 MW power plant has also begun construction in Murcia, Spain [96]. An extension of the CLFR design, termed 'etendue-matched', was proposed in 2010 [97]. Also in 2010 Industrial Solar, previously Mirroxx, built a 1408 m^2 aperture area LFR for cooling of a 500 seat showcase stadium for Qatar's 2022 FIFA World Cup bid [98]. In 2011 Novatec Solar and Avera claimed that superheated steam at 450 °C through DSG had been achieved in their LFR system [99, 100]. It has been reported that Avera has been contracted to build two 125 MW LFR power plants in Rajasthan, India [101].

The CLFR design claims to provide the most efficient use of land out of all the solar thermal technologies at around 1.6 hectares/MW or 1.8 m^2/MWh/year; however CLFR systems do require that the ground is level with a slope tolerance of less than 1 degree [102]. Moreover the high number of segmented mirrors means that a more complex control system is required to operate the large number of drives, which has been given as a reason that the system has not be used on a major scale [59]. However, a comparatively good half acceptance angle of 0.75º can be achieved, and the closeness of the structure to the ground makes construction and maintenance easier, along with reduced wind loads [83].

Due to optical, gap, and shadow losses, efficiencies are comparatively low in an LFR system, although the use of a compound parabolic collector (forming a secondary concentrator) at the receiver can improve overall peak optical efficiency to around 65 – 70 % [82] and the capture efficiency to 76% [103]. Small LFR systems are stated to operate at only 150 ºC [83], but with the use of a secondary concentrator temperatures of 300 ºC [82] at pressures of 80 bar [104] can be reached. The configuration of evacuated receivers with secondary concentrators can have a significant impact on the potential power achievable. The lower temperatures are attributed to the lower concentration ratio, which is in the

region of around 30 [104]. Receivers can also be protected more easily than the PTC receivers making them a practical alternative to linear PTCs with capital and maintenance cost significantly lower [82]. Capital costs of the system are approximately 234 $/m^2 [103]. It has been estimated that an LFR solar field, based on aperture area, must range between 100 – 285 $/m^2 to be competitive with other CSP technologies [105].

2.4.4 Parabolic dish reflectors (PDR)

The Parabolic Dish Reflector (PDR) or dish engine is a concave mirror that focuses sunlight onto a single point receiver (Figure 2.9). Mirrors can be facetted segmented surfaces or a single parabolically shaped surface made in some forming process. The mounting structure will then depend upon the type of mirrors used. The system requires continuous two-axis tracking as the concentrated solar rays are focused onto a receiver at the single focal point. Stirling engines are the most common receiver used; however Photovoltaic (PV) modules, heat pipes, micro turbine and other engines have been considered.

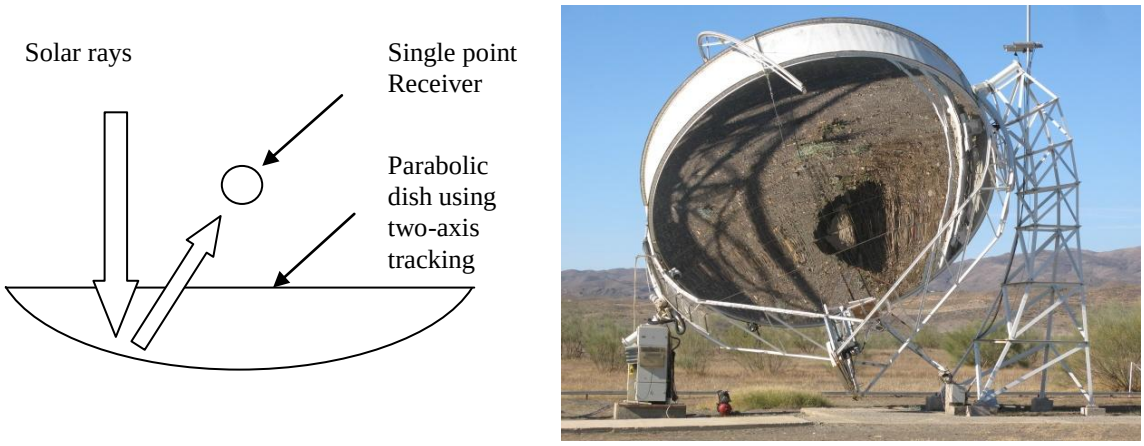

Figure 2.9: Schematic of a parabolic dish reflector (left). PDR at the Plataforma Solar de Almería, photographed by the author (right).

Technically, dish engines have the greatest potential, with the PDR holding the world record for solar thermal to electrical efficiency at 31.25% [106]. With a two-axis tracking mechanism dish engines can achieve optical efficiencies of up to 94% and concentration ratios ranging from 500 – 2000. For a concentration ratio of 500 the theoretical stagnation temperature would be in the region of 1285 ºC [31]. With the correct materials, temperatures of over a 1000 ºC can be reached in practise [73]. Common operating pressures for these temperatures would be between 40 – 200 bar [59]. One proprietor of a 25 kW Dish Engine claim that their system focuses around 60,000 kWh/year, and in a

good desert location can be situated with one dish for every 500 m^2 equating to an average power of 14 W/m^2 of land coverage [107].

Even though the dish system has the greatest potential efficiency, the problem remains of finding a reliable, inexpensive and efficient engine for the system. PDRs using a Stirling engine typically have had the highest cost of electrical production, and difficulties with hybridisation and heat storage. The capital costs of prototype dish systems have been as high as 12600 $/kW, with more recent designs costing 9000 $/kW; however large scale purchases could reduce the price to 2000 $/kW [108]. Dish engines do have the benefit of being modular in regards to having the capability to come in all sizes so can be useful in small and off-grid applications. Another benefit of the dish is that unlike other solar thermal systems, completely level ground is not a requirement [106].

Mirrors are a major contributor to the high expense of these systems, costing around 80 - 150 $\$/m^2$. An alternative method that has been used on some pilot projects is to use a stretched aluminium silvered polymer, which can be considerably cheaper at around 40 – 80 $\$/m^2$ [109].

2.4.5 Linear compound parabolic concentrator (CPC) and Fresnel lenses

The 2-dimensional linear Compound Parabolic Concentrator (CPC) is considered in this review. The CPC is a non-imaging concentrator. Compared to imaging concentrators such as the parabolic trough or dish, non-imaging concentrators accept radiation over a wider range of approaching angles for a given concentration ratio. A typical configuration has a lower circular portion and an upper parabolic section to form a trough with an absorber pipe located at the bottom [110]. However, this type of design tends to be large, hence truncated CPCs are often used instead; only a slight reduction in concentration results from a one-third decrease in height [111-113].

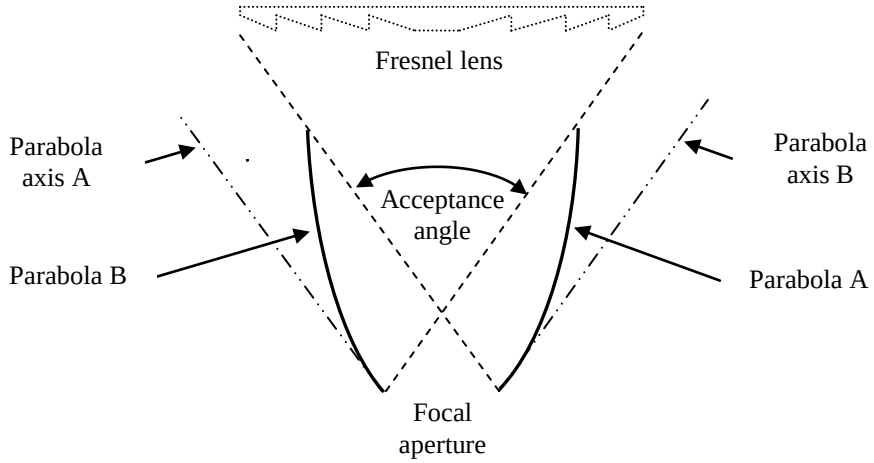

Figure 2.10: Cross section of a compound parabolic concentrator with or without Fresnel lens.

The key advantage of the CPC is that it can achieve some concentration without any form of tracking with half acceptance angles of over 20º; however this permits only a very low concentration ratio of around 3 [32]. The aim with solar thermal systems is to have a device that will operate at higher temperatures and efficiencies, which requires much higher concentration ratios than this. Due to the impractically large size of a conventional CPC for concentration ratios above 10, an alternative approach is to use a lens in front of the collector's aperture entrance. The lens and CPC are then referred to as primary and secondary concentrators respectively. To reduce the size and weight of the lens, a Fresnel lens, either linear or circular, would usually be selected [111] (see Figure 2.10). The advantage of refractive materials, such as polymethylmethacrylate which is often used to make Fresnel lenses, is that they are generally cheaper and have a longer lifespan than reflective materials used to make mirrors [114]. For the secondary concentrator again relatively cheap materials such as aluminium or glass can be used. Furthermore, if a material is chosen that has some flexibility, a less rigid frame is required to withstand wind loads without risk of fracture.

Lenses can be used in solar applications to create either an imaging or non-imaging system. Imaging systems require very accurate 2-axis tracking to create an exact image of the light source on a receiver. However, tracking inaccuracies and manufacturing process errors can make successful implementation difficult in solar collectors. Therefore non-imaging arrangements, using the CPC or similar types of non-imaging secondary, are often preferred and can be competitive with other types of collector [115].

For a linear Fresnel lens-CPC arrangement to achieve temperatures of up to 200 ºC, the half acceptance angle would have to be reduced significantly to around 3º as compared to static non-imaging CPCs. The benefit of this is that, although a tracking system would still have to be used, the comparatively wide tracking error margin means a simpler clock mechanism may suffice, rather than using sensors and/or a tracking algorithm. A flat Fresnel lens, with grooved side facing down and smooth surface up, is usually preferred by most designers. The lens protects the receiver from environmental damage without collecting dirt in its grooves making maintenance far easier. However, high surface reflection losses and large off-axis aberrations are found from this configuration. For these reasons curved linear Fresnel lenses are often considered which can help overcome these disadvantages through prism minimum deviation at each refractive surface [116]. Although only comparatively low operating temperatures are achievable with a concentration ratio of up to 20 with single axis tracking around a polar axis [117], and low capture efficiencies of up to 50% [118], and optical efficiencies of 60 – 65%, the capital and operational costs are reduced significantly compared to other solar thermal technologies. For a linear lens, tracking has to follow a north-south alignment due to the shortening of the focal length from off-meridian rays. For a linear lens with a two-axis tracking system, higher concentration ratios of up to 70 can be achieved. A single axis tracking CPC with focusing linear Fresnel lens is predicted to cost in a similar region to the CLFR at 260 $/m^2. For a lens-CPC solar collector to achieve working temperatures above 200 ºC, Colleras Pereira recommends that a circular lens be used; however these are beyond the scope of this review [111].

2.5 Output of literature review

The literature review identified the main technology alternatives and sub-alternatives to be the parabolic trough collector with synthetic oil or direct steam generation; the Heliostat field collector with either a water–steam, molten salt, or volumetric air receiver; the linear Fresnel reflector or compact linear Fresnel reflector; the parabolic dish reflector combined with a Stirling engine, and finally the compound parabolic concentrator with or without a linear Fresnel lens.

It also revealed the detailed criteria deemed necessary to compare the different technological alternatives, as summarised in Table 2.5 (units of US dollars are use for the financial values). Due to the prototype nature of some of these technologies and the lack of their establishment, some data have been unattainable; therefore, judgement has been used

as the AHP allows. Values have been listed under the three sections of technical, financial and environmental. Values for the ideal conversion and collector efficiency have also been included from an idealised thermodynamic analysis of the different collectors. Note that this analysis used the approach that will be given in Section 3.5; a detailed description is also available in the appendix of [119]. The criteria and alternatives in this table can be developed into a decision hierarchy tree (see Figure 2.11 a–d), which forms the first part of the AHP study. The tabulated values can then be used to complete the pair-wise comparison mathematical model and develop the priority vectors (see Appendix 1 for sample calculations and Appendix 2 for full workings). The weighting vectors for the criteria were not provided from this review, as they will vary depending upon the CSP application and site location. While judgement could have been used to calculate them, the approach chosen was to obtain the opinion of experts working within the field of solar energy.

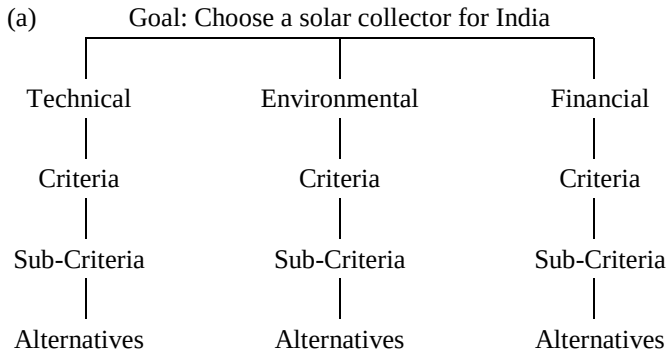

Figure 2.11a–d: Decision hierarchy tree for the selection of a suitable solar thermal collector for Gujarat (a) with the expanded hierarchy tree for the technical criteria (b), environmental criteria (c), and financial criteria (d), showing the technologies ordered on preference for each sub-criterion, using the characteristic values (Table 2.5) from the literature review.

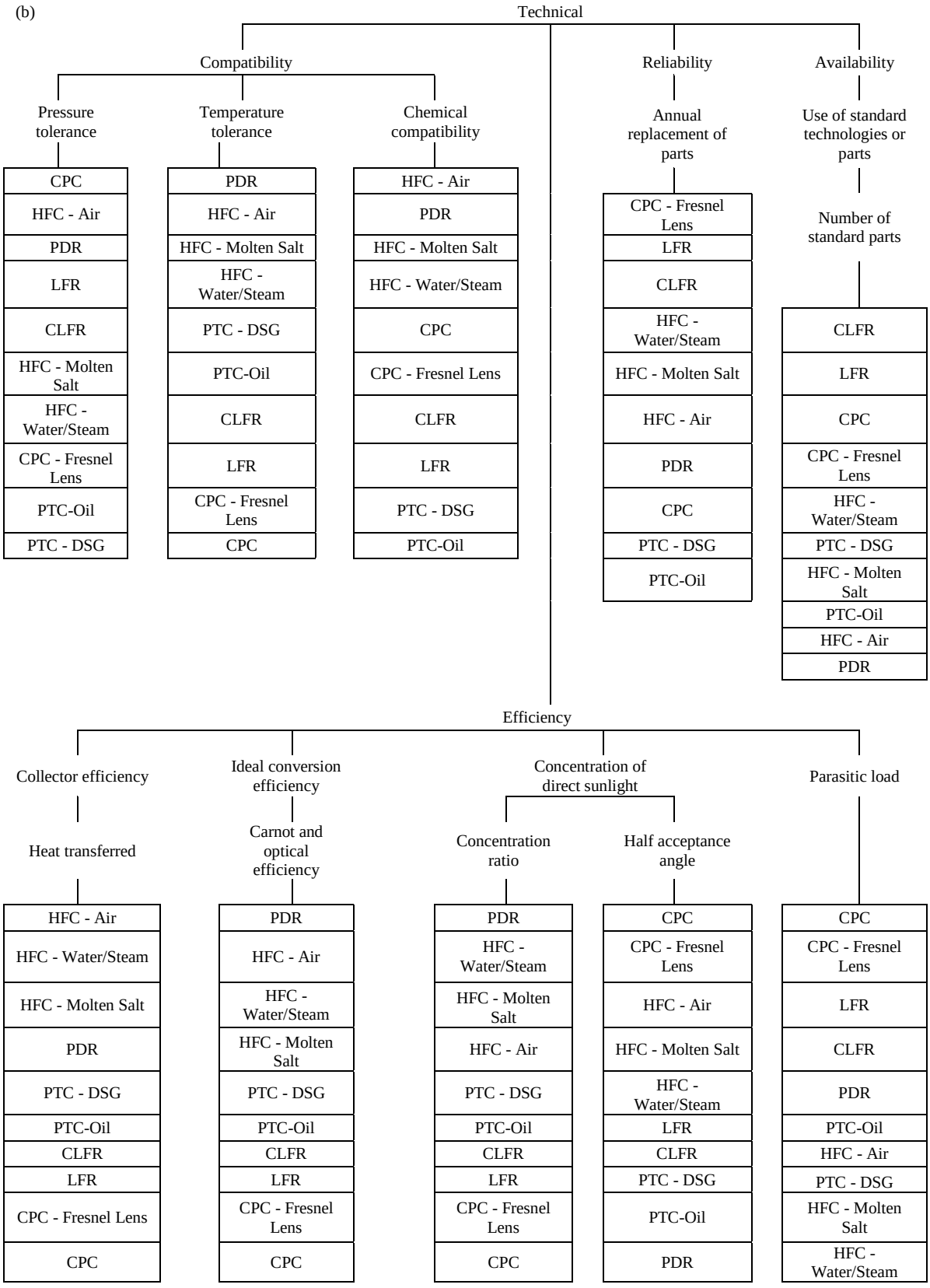

Figure 2.11: (*continued*).

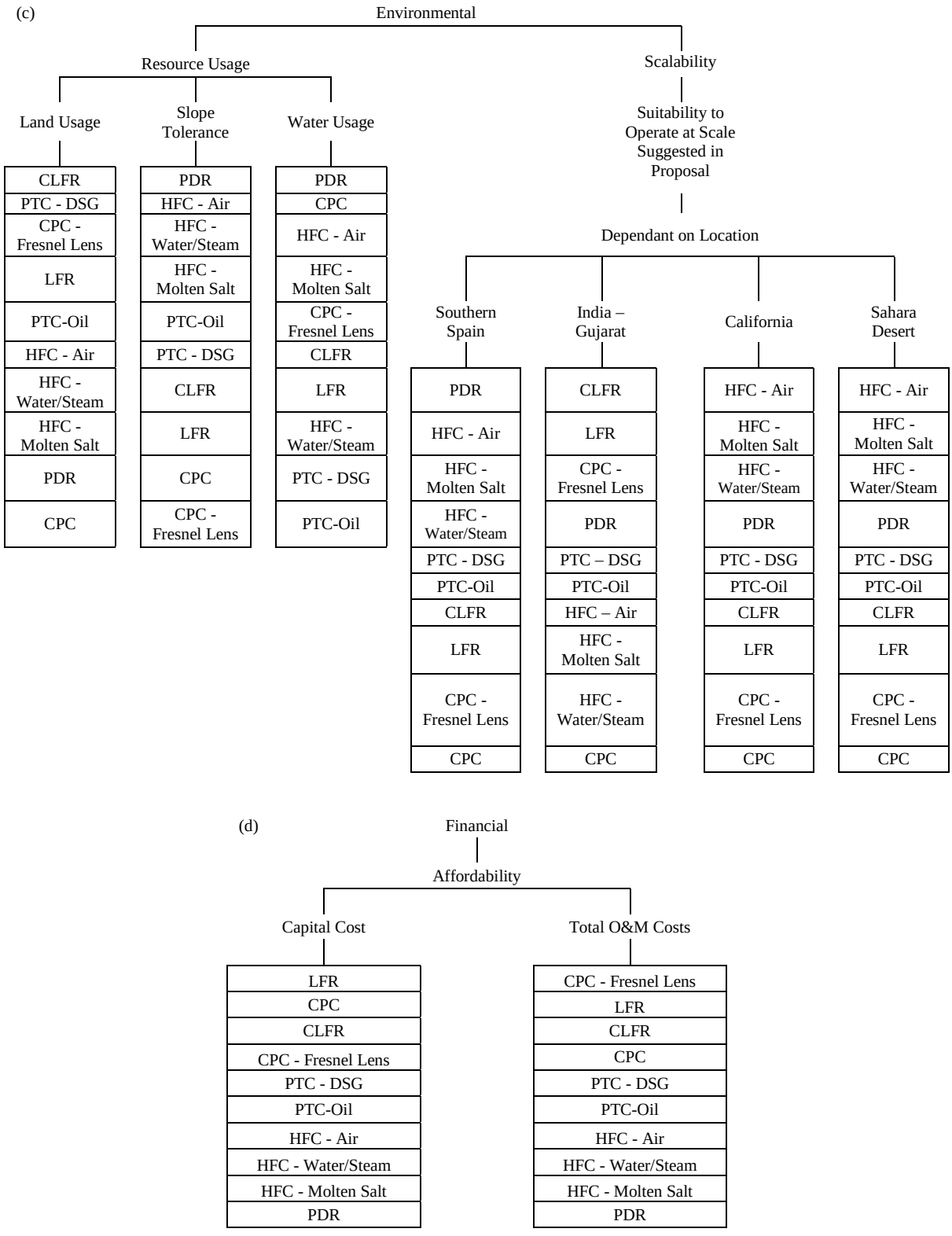

Figure 2.11: (*continued*).

Table 2.5: Characteristic values for solar thermal technologies and their alternatives, under the criteria of; technical, financial, and environmental, developed from the literature review.

					Alternatives	**Parabolic Trough**		**HFC**			**LFR**		**PDR**	**CPC**	
					Sub- Alternatives	Synthetic Oil	DSG	Salt Receiver	Water /Steam	Volumetric	CLFR	LFR	Glass	CPC	with Fresnel lens
	Criteria	**Sub criteria**	**Metric**	**Unit**	**Comment**										
Technical	**Efficiency**	Ideal conversion efficiency		%	Carnot and optical efficiency	33%	Higher	45%		Higher	25%	Lower	65%	Lower	22%
		Collector efficiency		%	Heat transferred based on the ideal system	63%		72%			36%		66%	36%	
		Stagnation temperature		°C		600	Higher	1750		*[a]	300 +		1200 +	*	*
		Optical efficiency		%	Ratio of sunlight capture to incident sunlight	80		Varied		73	67	Lower	94	*	60 - 65
		Concentration of direct sunlight	Concentration ratio	-		30 - 100		300 - 1500		Lower	30+		500 - 1500	3	10 to 20
			Capture efficiency	%		91		Varied		*	76	Lower	100	*	40 - 50
			Half Acceptance Angle	Degrees	Affects required tracking accuracy	0.5		*			0.75		0.4	20	3
		Parasitic load	Fraction of electrical output	%	E.g. for tracking, pumps, etc.	10	Higher	10 - 20		10	Higher	Low	4	Very low	2.3
	Compatibility with working fluid	Pressure tolerance		bar	Flexible hosing, fixed receiver	40 - 100		100+		10 -20	69		20	*	
		Temperature tolerance		°C		100 - 400	Higher	150 -800		1000+	100 - 300		500 - 1500	<100	< 200
		Chemical compatibility of heat transfer medium			Freezing, fire hazard, corrosion	Synthetic Oil	water	Molten Salt	Steam	Air	Water		Air	Water	
		2-phase flow			Are difficulties with 2-phase flow encountered	No	Yes	No	Yes	No	Yes		No	Yes	
	Reliability	Annual replacements of part		% /Prediction	Environmental resistance, Annual replacement of parts	5.5 - V.Low		Medium			Medium		Med - Low	Low	High
	Availability	Use of standard technologies or parts	Number of standard parts			Med - Low	Medium	Med - Low	Medium	Med - Low	High		Very low	High	Med - High
Financial	**Affordability**	Capital cost		Dollars/kW		3972	2300	4000+			-	Lower	12578	Lower	-
				Dollars/m^2		350	Lower	476			234	Lower	-	Lower	260
		Total O&M cost		Dollars/ kWh_e		0.012 - 0.02	Lower	0.034			Low	Lower	0.21	*	
Environmental	**Resource usage**	Land usage		m^2/MWh/ year	Land used per energy output	3.2	Lower	4.6			1.8	Higher	4.15	*	
		Slope tolerance		Degrees		<1		Flexible			<1		Flexible	level	
		Water usage	Dependant on System	m^3/MWh_e	Water cooled	3.07	*	2.27	Higher	*	*		None	*	
					Dry cooled	0.3	Higher	*	Higher	*	0.04		None	*	
				m^3/m^2/year	Water mirror washing	0.022		0.022			0.022		0.022	*	Lower?
	Scalability	Efficiency at different scales	At the scale suggested in the proposal		The proposal suggested in scenario	Better		Poor			Better		Better	Better	
		Suitable operating range	Electrical Range	MW		0.05-100		0.5-100			0.05-100		0.025-100	*	

[a] Due to the prototype nature of some of these systems were data is not currently widely available or known values are represented with a '*'.

2.6 AHP workshop analysis

Four case study scenarios for Gujarat, Southern Spain, Mojave Desert and the Sahara Desert were proposed to a panel of ten experts working in various fields within the Solar Energy Centre. Located at Gurgaon, Haryana, the Solar Energy Centre was built in 1991 to extend research into various solar technologies. It is recognised by India's Ministry of Non-conventional Energy Sources as a centre for the testing and evaluation of solar based devices [120]. Due to its nationally and internationally acknowledged expertise, the centre was chosen for this AHP workshop.

A presentation explaining the purpose of the AHP study was delivered followed by a synopsis for each of the different case scenarios. These synopses were presented to the panel in written form also. They included information about each region's climate and topography, along with the policy setting and government legislation that existed to promote renewable projects. Demographic factors were also mentioned, as was the probable scale of a solar thermal power plant in these areas (see Appendix 3).

Firstly, the experts were given the opportunity to expand or reduce the list of criteria that had been developed from the literature review given. However, in this case no sub-criteria were added or removed. The experts were then asked to score the criteria from 1 to 10, for each of the case studies. Taking an average of their scores, the pairwise comparison was then completed to determine the criteria weighting vectors (see Appendix 4). Thus the combination of the literature review (which gave the priority vectors) and the experts' opinions (giving the weightings) enabled the analysis to be completed following the standard AHP methodology [121].

2.7 Results and sensitivity analysis

The bar charts of Figure 2.12 a–d gives the results for the four cases studies, in terms of percentages which indicate relative levels of preference for each technology. For Gujarat, the preferred technology was the linear Fresnel lens-CPC which scored 11.9%. The compact linear Fresnel reflector at 11.5% and was a close second.

These results for Gujarat arose from the high weighting given by the panel to the criteria of good reliability, low cost and low ground usage for this location. For the other regions, the study gave very different recommendations. With a score of 13.5%, the parabolic dish reflector was preferred for the Sahara Desert. For the large scale implementation assumed

in this case study, the technical capabilities of the system were weighted as the most important criteria, thus favouring the PDR due to its superior technical efficiencies. Surprisingly, the PTC using synthetic oil received an unfavourable rating of only 5.9%. Another factor favouring the PDR was water usage, which for a system in a large desert such as the Sahara is crucial; the PDR with a Stirling engine has a very low water usage whereas the PTC with steam turbine has a high usage.

The Heliostat field collectors and PDR were highly favoured for both the Mojave Desert and Southern Spain. In the Mojave Desert the volumetric air receiver power tower was strongly favoured at 14.2%, with the PDR a close second at 13.9%. A similar result profile was found for southern Spain except with regard to the PTC which was less favoured than in the Mojave Desert.

For Gujarat, it was noted that the AHP study resulted in very close comparisons among alternatives. Therefore a sensitivity analysis was carried out to investigate the significance of the differences (see Figure 2.13). The three top-ranking criteria (collector efficiency, ideal conversion efficiency, and capital cost) were varied by adding or subtracting 1 to the experts scoring for each one, thus altering the weighting given from the pair-wise comparison matrix.

The effect of decreasing the top three weighted criteria re-ordered the criteria so that the importance of the maintenance costs, land usage, and reliability increased; meanwhile the ideal conversion efficiency and capital cost moved down the weighting order. This had the effect of increasing the percentage preferences of the Fresnel lens-CPC, CLFR and LFR to 12.9%, 12.1% and 11.3% respectively.

In contrast, increasing the weighting of the top three criteria did not change the criteria order, but it still had a substantial effect on the results. With the ideal conversion efficiency and collector efficiency weighting increased, the more technically efficient PDR became favoured against technologies like the linear Fresnel lens-CPC and CLFR.

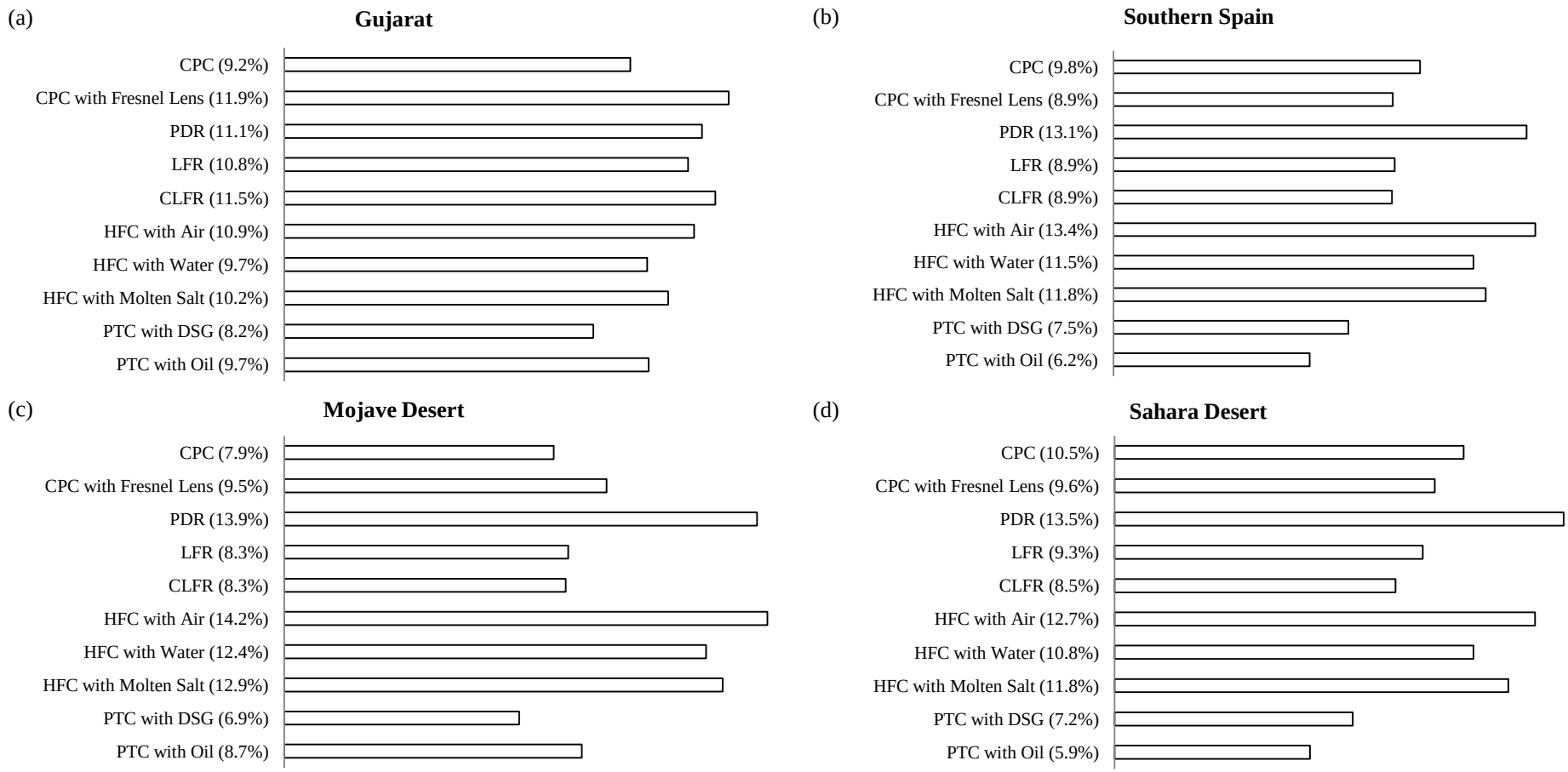

Figure 2.12a-d: Final results from the AHP study showing each solar thermal collector's percentage preference for Gujarat (a), Southern Spain (b), Mojave Desert (c) and the Sahara Desert (d).

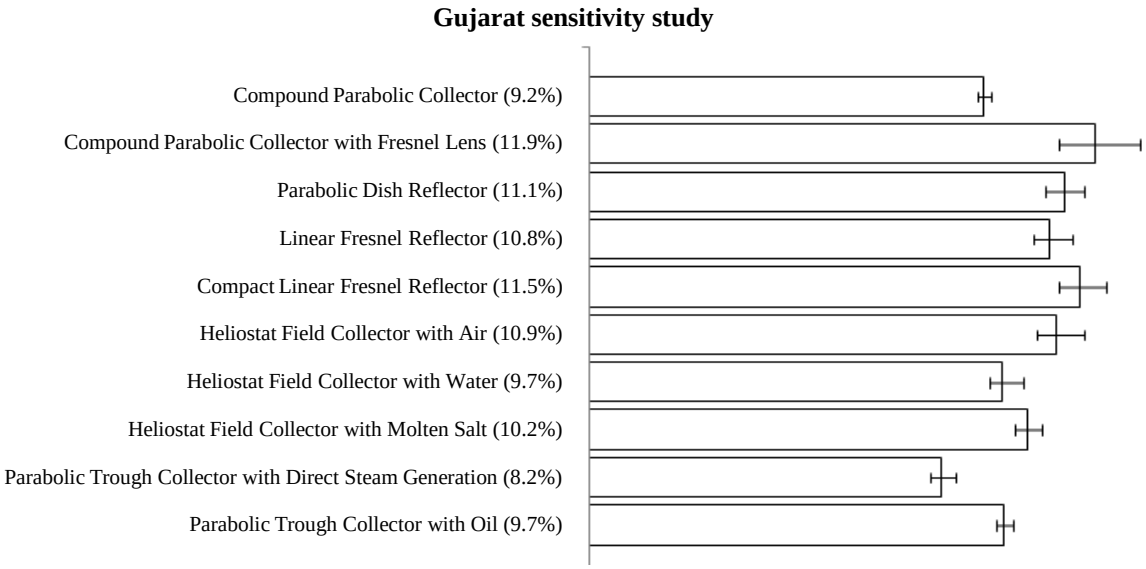

Figure 2.13: Sensitivity study for Gujarat showing the potential range of the percentage preference for each alternative.

2.8 Discussion

The variation in the results among the four regions merited further discussion about each technology. Aspects of how the study was conducted may have influenced the outcomes and it was therefore worth reviewing what has been learnt about the process in order to guide future studies of this kind.

The PTC, despite being the most widely adopted technology, was not especially strong against any of the criteria used in this study. On the other hand, the very fact that the PTC was well established could have distorted the results, because the data and opinions about them were the consequence of many years of operational experience; whereas for other technologies the information available sometimes had to be based on prototypes or theoretical estimates aimed at promoting the technology. Comparisons based on expected values stated for newer or yet-to-be-implemented systems had to be judged carefully.

The PDR fared very favourably in all four case studies. With the highest weightings for all four case studies given to the ideal conversion efficiency and collector efficiency, the PDR immediately gained an advantage with its greater operational efficiencies in comparison with the other technologies. Power towers have been pioneered in both Spain and California; however, the volumetric air receiver was a technology that has not been used as much as other types of receivers. Again this suggests that the model was biased towards operational capabilities rather than reliability and market establishment. While there was

danger of making over-optimistic assumptions about future technological advancements, it was also important not to model a scenario that would only ever produce well established existing technologies as the answer, as this might have resulted in technology choices that were too conservative.

The variability in the results for the different regions was attributed primarily to the importance given to the cost criterion for India, with the cheaper technologies, Fresnel lens-CPC and CLFR/LFR, ranking highly in the final group order. In comparison, the HFC ranked first for the economically developed countries of Europe and America due to its suitability for large commercial-scale deployment. The water usage in the Sahara desert governed that the PDR, which uses the smallest amount, ranked top. As a whole, greater confidence was given to the AHP results for Gujarat than for the other three regions due to the fact the panel consisted of Indian experts. For this reason, the background information provided on the other three case scenarios would have had a greater influence on the panel's decisions. Depending on an AHP's application, any background information provided to an expert panel should be carefully considered in order to avoid bias.

The number of experts consulted in this study was 10. With a panel of different size or make-up, the outcomes may have been different. This type of uncertainty applies to all AHP or similar decision-making processes. While no literature was known that defines the exact number of experts to consult, taking into account a greater amount of expert opinion will benefit the process. However, a larger panel will make workshop facilitation and resolution of conflicts more difficult. In practice, experience indicates that limiting the panel size stimulates participation and contribution, leading the group to a consensus [122]. Moreover, once an overall result has been produced the whole process can be examined and refined with further opinion taken into account.

The AHP process does suffer from several other known drawbacks: subjectivity can never be reduced to zero and the AHP does not necessarily highlight poor judgements [123, 124]. In addition, the AHP cannot guarantee the independence of the results with regard to the inclusion of an irrelevant alternative. An ideal decision-making process should be unaffected by such alternatives; however in practice this is often violated in AHP [125]. The consequence for this study was that the pre-selection process, whereby the experts were not presented with all possible technologies but a shortlist based on the judgement of the author, may in principle have affected the outcome. However, even the weakest

technology considered (the CPC without Fresnel lens, which ranked very poorly against certain criteria) did not rank poorly against all criteria; therefore there was no irrelevant alternative as such. Nevertheless, the fact that this technology was unlikely to be considered a viable choice by any expert led the author to believe that it would be better to exclude it from any re-run of the study.

Another area of improvement relates to the choice of criteria. Although the expert panel declined to change the criteria or alternatives chosen when given the opportunity to do so, the author considered that inclusion of 'market establishment' or 'internal rates of return' as explicit criteria would be an improvement to the model.

Despite the several well-researched challenges facing the AHP, it remains the most popular among MCDM techniques. The review by Pohekar and Ramachandran [51], of MCDM techniques applied to sustainable energy planning, demonstrates how AHP has been favoured over other MCDM methods based on the numbers of publications in each field. These methods include Preference Ranking Organization Method for Enrichment Evaluation (PROMETHEE), the Elimination and Choice Translating Reality (ELECTRE), Multi-Attribute Utility Theory (MAUT) and several other methods. Wallenius et al. provides evidence through publication history, that research using AHP has been greater than that using other MCDM techniques and other decision-making methods such as Multi-Objective Decision-Making (MODM). Between 2000 and 2004 there were nearly 450 publications relating to the AHP, MAUT had only 250. The use of MODM methods demonstrated considerable growth through Evolutionary Multi-objective Optimization (EMO) with 330 publications. Other MODM methods such as Goal Programming and Math Programming had substantially fewer with less than 250 and 150 publications respectively [126]. This trend in publication history indicates a significant preference towards AHP over other decision-making models. These different decision-making techniques are not necessarily in competition with each other, and integration of methods could be complementary as it would remove any shortcomings associated with each one. An integrated Goal Programming – AHP model has been recommended, particularly in the field of energy where quantitative and qualitative criteria are incorporated into the analysis [54]. Further work on the integration of MCDM and MODM techniques would be the next logical step for their application in the field of solar energy.

On a final note, it was worth observing that the results of the study may also be used to infer how much more people may be willing to pay for improvements in certain criteria. This could be obtained from the AHP weighting vectors, and the characteristic table of values, for the different alternatives. For example, the attributes and weightings for the LFR and PTC could be used to determine the value, in terms of the capital cost, for an improvement in the ideal conversion efficiency and concentration ratio. A swing from 36 to 63% for the LFR to the PTC was seen for the ideal conversion efficiency, implying a value of 116 $/m^2 for this increase, as these two criteria received equal weighting from the panel. However the value (in capital cost) for an improvement in the concentration ratio was worth less as seen from the different weightings given. With the capital cost receiving nearly twice the weight given to the concentration ratio, the increase in concentration ratio from the LFR to the PTC was worth only 67 $/m^2. In a future study these findings could be confirmed with the help of a separate questionnaire designed explicitly to enquire about the monetary values placed by the experts on such technical improvements.

2.9 Conclusion

The AHP study indicated that the preferred solar collector for the case of Gujarat in north-west India was the linear Fresnel lens with secondary CPC-type receiver. After a sensitivity analysis, in which criteria weightings were varied to reflect likely uncertainties in the selection process, several preferred technologies emerged, including the linear Fresnel reflector based solar collectors. For the other cases of southern Spain and the Mojave Desert in California, the study indicated the parabolic dish reflector; and for the Sahara Desert it indicated the heliostat field collector with the air receiver.

These findings for India were unexpected in that these are not the technologies used mostly to date. In particular, Fresnel lenses have hardly been used for solar thermal power, though they are used for photovoltaic solar power. Nevertheless, this could be for historical reasons. Though several technologies were closely ranked, the potential low cost and high reliability of the linear Fresnel lens and reflector technologies make them worthy of further investigation and development. It was therefore recommended that these solar collector types were pursued in the context of the current project in Gujarat following this study.

2.10 Chapter summary

This chapter evaluated the main existing concentrating solar thermal power technologies using the framework of the analytical hierarchy process. It encompassed parabolic troughs, heliostat fields, linear Fresnel reflectors, parabolic dishes, compound parabolic concentrators and linear Fresnel lenses. These technologies were compared based on technical, financial and environmental criteria. Within these three categories, numerous sub-criteria were identified; similarly sub-alternatives were considered for each technology. A literature review, thermodynamic calculations (see Section 3.5; a detailed description is also available in the appendix of [119]) and an expert workshop was used to arrive at quantitative and qualitative assessments. The methodology was applied principally to a case study for Gujarat in north-west India, though case studies based on the Sahara Desert, Southern Spain and California were included for comparison. A sensitivity analysis was carried out for Gujarat. The chapter concluded that the linear Fresnel lens with a secondary compound parabolic concentrator or the linear Fresnel reflector was the preferred technology for north-west India.

Chapter 3

Cost-exergy optimisation of the linear Fresnel reflector

3.1 Introduction

Provisional work was undertaken by the author and the Science Bridge project partners to further investigate the Fresnel lens-CPC and LFR technologies. While staying in India the author assisted in the design and construction of several prototype collectors at IBL and IIT Delhi. Even though the Fresnel lens-CPC technology was indicated as one of the preferred solar collectors for India, at an early stage it became evident that in-house manufacturing constraints restricted further development of the technology. Project partners were keen to source or manufacture components locally, thus avoiding expensive imports; however Fresnel lenses require high precision optical surface generation facilities that were unavailable. Therefore, the decision was made to focus on R&D for the LFR.

In the previous chapter the LFR was highlighted as a promising CSP technology, but one requiring improvements in performance and cost reduction. One significant drawback identified was that the LFR suffers from shading and blocking caused by adjacent mirrors. Increasing the spacing between mirror rows or the height of the receiver reduces these effects, but can increase cost because more land is required. Land usage may not be an important issue in some situations such as deserts and certain rural areas [31]. However, for solar process heat or solar thermal cooling applications roof installations may be used requiring compact footprint. The design of the width, shape, spacing, and number of mirror elements of the LFR has been studied by several authors and optimised for various applications [84, 85, 127, 128]. However, those authors chose the spacing arrangement of the mirror elements according to the method by Mathur et al. [129, 130]. This method (henceforth referred to concisely as ‘Mathur’s method’) calculates the appropriate value of the shift (i.e. the horizontal gap between adjacent mirror elements) such that shading and blocking of reflected rays are avoided at solar noon specifically, thus providing a technical (but not necessarily economic) design principle of the solar collector. Other authors have optimised the equidistant spacing of mirror elements for levelised electricity cost [105, 131]. Studies using ray-tracing have also been used to optimise the optical performance of an LFR with equidistant spacing [132, 133].

In this Chapter, the LFR was investigated using the principle of exergy to seek improvements in performance and cost. Exergy provides a means of analysing a collector's maximum available power, for given operating and ambient temperatures, without the need for a detailed specification of the plant to which the collector is coupled. Achievable performance can then be predicted for a collector with specified location, mirror field arrangement and tracking orientation. Exergy analyses of solar collectors have already been carried out by several authors. For example, Singh et al. studied the exergetic efficiencies of a solar thermal power plant having parabolic trough collectors coupled to a Rankine cycle, to show that the maximum heat losses occurred at the concentrator-receiver assembly [134]. Tyagi et al. have studied the exergetic performance of a collector as a function of the mass flow rate, concentration ratio and hourly solar irradiation [135]. Gupta and Kaushik investigated different feed water heaters for a direct steam generation solar thermal power plant [136]. Indeed, the exergy concept has been widely adopted for thermodynamic assessment of power generation systems within various fields of the renewable energy sector, ranging from wind power to geothermal power systems, and extended to comparisons of non-renewable energy sources [31, 137, 138].

The aim here was to present a method to optimise the mirror spacing arrangement of an LFR. The objective of the optimisation was to maximise exergy and operational hours and minimise cost. This was to be achieved through analysis of the optics for different non-equidistant spacing arrangements over an annual period, not just at solar noon. The resulting methodology was applied to a case study for an LFR prototype built at IBL, Vapi, India, shown in Figure 3.1.

Figure 3.1: An LFR prototype developed in Vapi, India.

3.2 Method of optimisation

The measure of cost to be minimised was the ratio of the capital cost per exergy. The cost estimate was calculated from the sum of the main components, namely the collector's frame ($/m^2), concentrator ($/m^2), receiver ($/m^2), and land costs ($/m^2). Running costs were neglected because these were considered equivalent among the design variations. Therefore the following expressions were used:

$$\frac{Cost}{Exergy} = \frac{Total\ Cost\ Estimate}{\left[DNI.A_m.\eta_{o(\theta=0)}.IAM - Q_{loss}\right]\eta_{Carnot}} \tag{3.1}$$

where

$$Total\ Cost = (Collector\ Area\ (Frame + Land)) + (A_m.Concentrator) + (A_r.Receiver) \tag{3.2}$$

Exergy was calculated from the Direct Normal Irradiance, DNI (W/m^2) on the collector's total mirror area, A_m, and the heat loss from the receiver, Q_{Loss}. The calculation took into account the terms $\eta_{0(\theta=0)}$, *IAM*, and η_{Carnot} representing the optical efficiency for normal incidence rays to the horizontal, the Incidence Angle Modifier (IAM), which accounts for the losses in the concentrator and receiver optics for varying ray incidence angles, and the Carnot efficiency respectively. Key to this investigation was the shadow efficiency, which was incorporated into the IAM, and depended upon the concentrator's mirror element spacing arrangement. The Carnot efficiency is an idealisation underlying the exergy analysis and was calculated on the assumption that the receiver operates at a constant or continuously optimised surface temperature. Since the focus was on the design of the collector, the variation in temperature of the heat transfer fluid inside the absorber tubes and over the solar field was not considered. This would require detailed assumptions about the plant design (e.g. piping layout, choice of heat transfer fluid, and flow rate) that were beyond the scope of this chapter.

For a range of different mirror element spacing arrangements, and operating temperatures, the above efficiencies and thus the corresponding exergies were calculated. The spacing arrangements were chosen such that the mirror elements were spaced for the onset of shadowing at a given height of the sun in the sky. This generally led to non-equidistant spacing with the mirrors further from the tower more widely spaced. The sun's height was

represented by the transversal angle which is the angle between the projection of the sun's rays onto a plane perpendicular to the tracking axis and the vertical.

The method comprised four main steps, which are listed below and described more fully subsequently.

i. **Determination of solar irradiation characteristics for target location:** Calculate typical characteristics of solar radiation for the target location based on a Typical Meteorological Year (TMY).

ii. **Determine mirror spacing designs and shadow efficiencies:** Develop a number of mirror spacing arrangements each for the onset of shadowing at a given transversal angle. Find corresponding hourly shadow efficiencies, for each design.

iii. **Performance of collector:** Analyse heat loss from the receiver. For each spacing arrangement, calculate optical efficiency at normal incidence and hourly values of variables: DNI, IAM (which accounts for shadowing, blocking of reflected rays, incidence cosine for each mirror element, and effective mirror aperture area), heat loss coefficient, receiver temperature, ambient temperature, Carnot efficiency and thus output exergy averaged over the year. The calculation was repeated for (a) different constant operating temperatures and (b) a continuously optimised operating temperature.

iv. **Application:** For each spacing arrangement determine cost per exergy using Eq.(3.1). Provide optimum design recommendations based on exergy, cost and operational hours.

To study the sensitivity of the optimised design to the input parameters for the Vapi prototype case study, upper and lower limits were applied to the costs of the mirror elements, the land, and the receiver. Four cost scenarios were considered. (i) a minimum baseline cost, (ii) a high component cost, (iii) a high land cost, and (iv) a high component and land cost.

3.3 Determination of solar irradiation characteristics for target location

Hourly DNI values were calculated for a TMY in Gujarat using the meteorological database, Meteonorm® [139]. The orientation considered in this study was a north-south horizontal axis with east-west tracking.

3.4 Determine mirror spacing designs and shadow efficiencies

The slope angle and distance from the receiver for each mirror element were determined for a given transversal angle. The amount of shadowing that was produced on an hourly basis for each design could then be found. Results for the shadow efficiency for a series of different spacing arrangements, for a typical day of each month, were then produced as a final output. A number of standard calculations relating to the sun-earth geometry from the literature are initially provided [140, 141].

3.4.1 Sun-earth geometry

The position of the sun relative to a given location on the earth's surface is required in a number of calculations for determining a solar collector's performance. Sun-earth geometry calculations require knowledge of the solar time, not the local standardised time which is a generalised clock time for large regions or countries. The solar time, T_{solar}, can be calculated from the local standard time, T_{Local}, longitude correction L_c and the equation of time EOT.

$$T_{Solar} = T_{Local} + \left(\frac{EOT}{60}\right) - L_c - D \tag{3.3}$$

where EOT is a conversion factor for which there are several approximations. One estimate, accurate to about 30 seconds, is given by [142],

$$EOT = 0.258cosx - 7.416sinx - 3.648cos2x - 9.228sin2x \tag{3.4}$$

and x is in degrees and dependant on the day of the year, N.

$$x = \frac{360(N-1)}{365.242} \tag{3.5}$$

Daylight saving, D, is also considered. Thus, D is equal to 1 when daylight saving is in effect. The longitude correction, L_c, is determined from,

$$L_c = \frac{(local\ longitude) - (longitude\ of\ standard\ time\ zone\ meridian)}{15} \tag{3.6}$$

The sun's position relative to the earth is first described by the earth's rotation about its polar axis. The angle from an observer seeing the sun traverse the sky creates the hour angle, ω , which changes 15° every hour and is zero at solar noon, (i.e. the highest point the sun reaches in the sky). The hour angle is simply calculated from,

$$\omega = 15(T_{solar} - 12) \tag{3.7}$$

The angle created between the earth's equatorial plane and the line formed between the centre of the sun and earth is known as the declination angle, and is another important variable in determining the sun's position. One approximation, is given by [32],

$$\delta = 23.45\, sin\left(360\frac{284 + N}{365}\right) \tag{3.8}$$

The latitude angle, ϕ, is the angle formed between the earth's equator and a line drawn from the centre of the earth to a position on the earth's surface (see Figure 3.2).

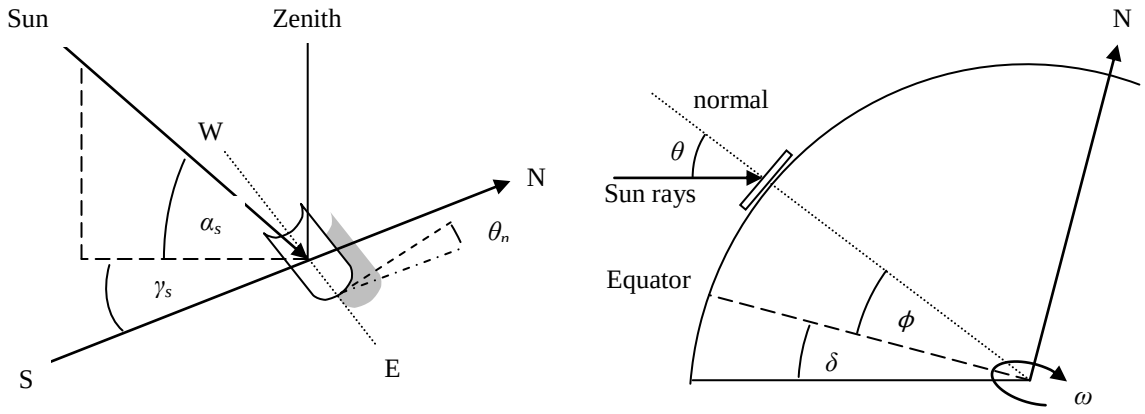

Figure 3.2: Sun-earth geometry angles.

Using the latitude, ϕ, hour, ω, and declination, δ, angle the sun's position, as seen from an observer about a known position on the earth's surface, can be defined via a series of additional angles: the solar altitude angle, α_s, defining the angular height of the sun in the sky (or zenith angle, θ_z, which is the opposite angle to the vertical plane rather than the horizontal) and the solar azimuth angle, γ_s, which is the angular displacement from the

south. The mathematical derivation of vector relations pointing to the sun's position are given in several sources of solar literature [140, 141].

$$\alpha_s = sin^{-1}(sin\delta sin\phi + cos\delta cos\omega cos\phi) \tag{3.9}$$

$$\gamma_s = cos^{-1}\left[\text{sign}(\omega)\left(\frac{\cos\theta_z sin\phi - \sin\delta}{\sin\theta_z \cos\phi}\right)\right] \tag{3.10}$$

Depending on the tracking method implemented for a solar collector, a beam from the centre of the sun will not always be normal to the collector's aperture plane. The angle to the normal is known as the angle of incidence, θ, and is important for calculating the amount of solar irradiance received on a concentrator element. The angle formed between the plane of aperture to the horizontal ground surface is referred to as the slope angle, θ_n.

3.4.2 Geometrical positioning of LFR mirror elements

The sun's position, relative to the axis of rotation of the LFR elements, was determined from the solar profile angle [32]. The profile angle, θ_p, in the transversal plane can be found for a north-south axis tracking orientation from,

$$tan\theta_p = \frac{tan\alpha_s}{\cos(90 - \gamma_s)} \tag{3.11}$$

The transversal angle, θ_t, is then the angle to the vertical i.e. the complement of the profile angle.

The projected angle into the longitudinal plane is given by,

$$tan\theta_l = \frac{tan\alpha_s}{\cos\gamma_s} \tag{3.12}$$

The slope angle, θ_n, for a mirror element located at a distance Q_n, from the receiver, can be determined for any profile angle from Eq.(3.13) (see Figure 3.3). The following equations in this section enable hourly slope angles to be determined for the purpose of specifying the shift distance required for the onset of shadowing at a particular solar profile angle.

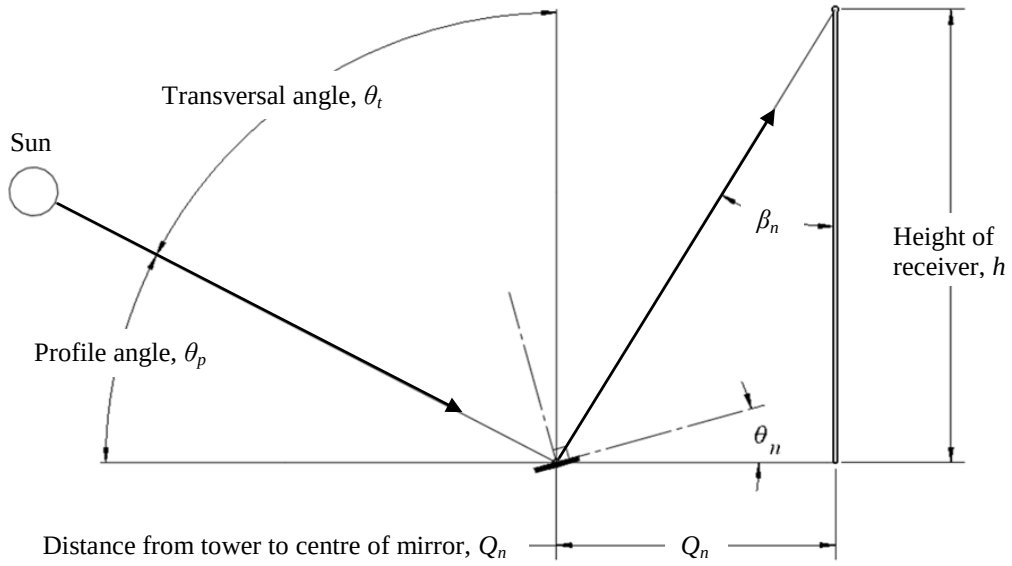

Figure 3.3: Sun's position relative to an LFR, showing the path of a single ray from a mirror element to a receiver tower.

$$\theta_n = \frac{90 - \theta_p - \beta_n}{2} \tag{3.13}$$

Where β_n, the angle subtended between the receiver tower and the projection onto the transversal plane of a ray reflected towards the receiver, is given by,

$$tan\beta_n = \frac{Q_n}{h} \tag{3.14}$$

The first mirror (starting from the centre and working out) was placed such that the receiver does not cast a shadow upon it at midday. The following mirrors were pitched with varying amounts of shift, S_n, for a given profile angle (see Figure 3.4).

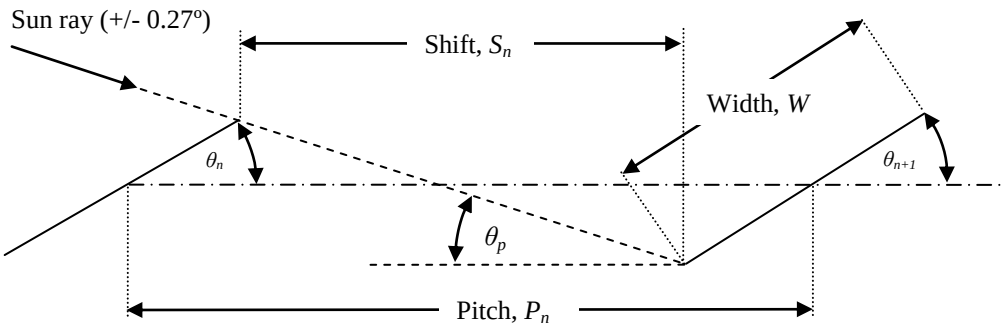

Figure 3.4: Shift distance between two consecutive mirror elements based on the sun's profile angle.

For a mirror element of width W and pitch P_n from its inward neighbour, the shift can be calculated from the following two equations,

$$S_n = P_n - \frac{W}{2}(cos\theta_n + cos\theta_{n+1}) \tag{3.15}$$

$$S_n = \frac{W[sin\theta_n + (sin\theta_{n+1} - sin\theta_n)]}{tan(\theta_p - 0.27)} \tag{3.16}$$

the simultaneous solution of which gives,

$$P_n = \frac{W[sin\theta_n + (sin\theta_{n+1} - sin\theta_n)]}{tan(\theta_p - 0.27)} + \frac{W}{2}(cos\theta_n + cos\theta_{n+1}) \tag{3.17}$$

Because the distance, Q_n, from a mirror element to the receiver tower changes for each newly selected value of shift, an iterative process was required to provide the final spacing for each mirror element. The effective area of aperture, A_a, of the mirror elements as encountered by approaching rays in the transversal plane can be calculated by,

$$A_a = \sum_{n=1}^{k} Wcos(\theta_t - \theta_n) \tag{3.18}$$

The incidence cosine for an nth mirror element in the transversal plane is therefore given by A_{an}/W.

3.4.3 Shadow on mirror elements

Until the sun's profile angle reaches that of the design profile angle and corresponding transversal angle used to specify the mirror spacing arrangement, a proportion of the mirror elements will be in the shade. For a spacing arrangement based upon a particular design transversal angle, the average shadowing on the collector system throughout the day can be calculated from the geometry shown in Figure 3.5.

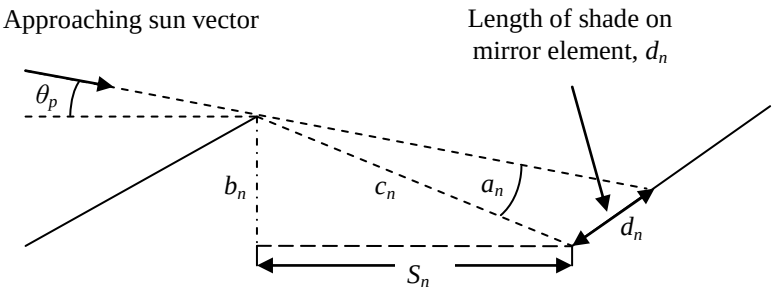

Figure 3.5: Shadow cast on a mirror element when the sun is lower than the design profile angle.

Using trigonometry, the following equations can be determined,

$$b_n = \frac{W}{2}(sin\theta_n + sin\theta_{n+1}) \tag{3.19}$$

$${c_n}^2 = {b_n}^2 + {S_n}^2 \tag{3.20}$$

$$a_n = 90 - tan^{-1}(S_n/b_n) - \theta_P \tag{3.21}$$

$$d_n = \frac{c_n \sin a_n}{sin(\theta_p + \theta_{n+1})} \tag{3.22}$$

Therefore the shadow efficiency, η_{Shadow}, throughout the day, for various spacing arrangements, each based on a different transversal angle, can be found from the amount of shade upon each mirror, d_n, and the overall width of the mirror element, W. The average shadowing on an LFR can therefore be calculated for any time of day.

$$\eta_{Shadow_n} = 1 - \frac{d_n}{W} \tag{3.23}$$

$$\eta_{Shadow} = \frac{\sum \eta_{Shadow_n}}{n} \tag{3.24}$$

3.4.4 Selection of spacing arrangements

Examples of spacing arrangements used for the optimisation are illustrated in Figure 3.6. Each is labelled S15°, S30°, etc., according to the corresponding transversal angle for the onset of shadowing. The corresponding approximate solar times for shadow free operation are also indicated, though note that these times refer specifically to Gujarat in April and will be different for other locations and times of year.

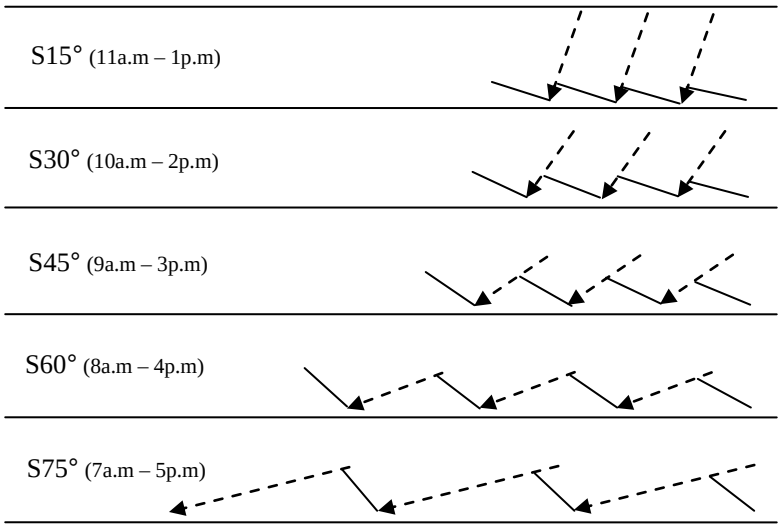

Figure 3.6: Spacing arrangements set for the onset of shadowing at various transversal angles. Hours of no shadowing are given for the Gujarat area in April.

3.5 Performance of collector

The exergy, i.e. maximum available power output in W/m^2 of the collector's total mirror area, for an LFR at a certain hour of the day can be calculated.

$$E_{x,out} = Q\left(1 - \frac{T_a}{T_r}\right) \tag{3.25}$$

Where Q, the heat transfer at the receiver at a temperature T_r (representing the temperature at the surface of the absorber tubes), is given by,

$$Q = Q_{in} - Q_{loss} \tag{3.26}$$

and Q_{in} is the product of the direct solar irradiance, total mirror area, optical efficiency at normal incidence and the incidence angle modifier, which includes the effective mirror aperture area and changing optics for ray incidence angles in the transversal and longitudinal planes.

$$Q_{in} = DNI.A_m\eta_{0(\theta=0)}.IAM \tag{3.27}$$

A thermodynamic study performed on the LFR with a horizontal absorber trapezoidal cavity receiver configuration (see Figure 3.7), was used to determine an approximation of

the heat loss Q_{loss}. Note that the cover glazing width was chosen such that a diverging edge ray of the widest mirror element was accepted.

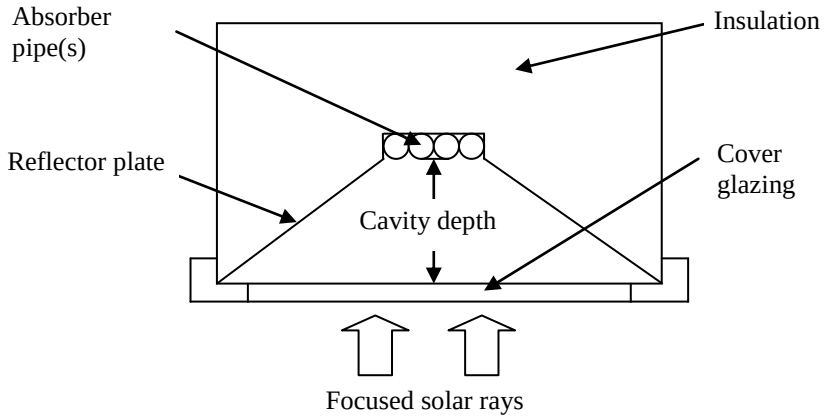

Figure 3.7: Schematics of a trapezoidal cavity receiver.

For a receiver of given characteristics, the heat loss coefficient, U_L, can be estimated by considering the heat loss from the bottom of the receiver through convection and radiation, and from the insulated sides of the receiver, as shown by Singh et al. in [143]. The example plot of Figure 3.8 shows that the heat loss coefficient increases significantly with temperature. The heat loss coefficient can be used to determine the stagnation temperature, $T_{r,max}$, which occurs when all incoming solar radiation is lost as ambient heat, meaning no more heat transfer can take place at the receiver. This will be discussed in detail in Chapter 5.

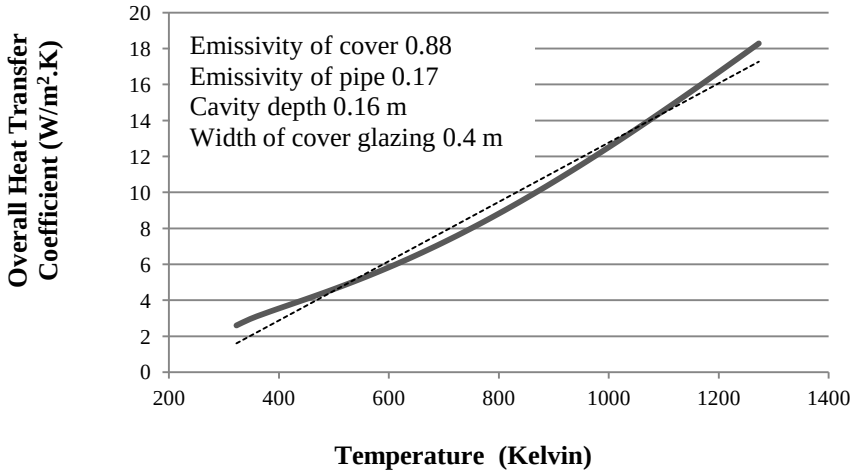

Figure 3.8: The heat loss coefficient increases with the trapezoidal cavity receiver temperature and may be approximated by a linear trend.

$$T_{r,max} = T_a + \frac{DNI.A_m\eta_{0(\theta=0)}.IAM}{U_L A_r} \tag{3.28}$$

Optical efficiency is an essential parameter for the calculation of exergy and stagnation temperature in any solar collector. The optical efficiency of the system includes factors such as the reflectance, ρ, the transmittance of the cover, τ, the absorbance, α, and the intercept factor, λ. The absorbed solar radiation is also decreased if shading and blocking is caused from adjacent mirror elements. Estimations can be made for the optical efficiency on an hourly basis using an incident angle modifier. Asymmetric solar collectors with translational symmetry show a bi-axial dependency with respect to the direct beam incidence angle [32]. A bi-axial incident angle modifier includes a transversal angle, θ_t, (for rays perpendicular to the rotation axis of the concentrator elements) and a longitudinal angle θ_l (for rays in a plane parallel to the rotation axis) [144]. The IAM is defined by the ratio of the collector output at a given incidence angle $\eta_0(\theta)$ and the collector output at normal incidence $\eta_0(\theta=0)$.

$$IAM(\theta) = \frac{\eta_0(\theta)}{\eta_0(\theta = 0)} \tag{3.29}$$

The approach taken in this study was to project the solar incidence angle onto the transversal and longitudinal plane to calculate a total optical efficiency based on a product of the IAM(θ_t) and IAM(θ_l). For an LFR, depending on the spacing arrangement of the mirror elements, the effective mirror aperture area, individual mirror incidence cosines, blocking of reflected rays and shadowing show a large dependency on θ_t. In the longitudinal plane the major effects are the transmittance of a cover or glazing, the intercept factor, and the absorption and reflectance of the collector in respect to a changing θ_l. Assuming the collector is of substantial length the end losses for rays with a shallow θ_l can be neglected.

Ray-tracing is commonly employed in the analysis of the optical efficiency for solar collectors and was used in this study. Due to the width of the solar disk, as observed from the collector, solar rays diverge with an angle of +/- 0.27°. Buie and Monger have studied circumsolar radiation and its effect on LFR optics [145]. The amount of circumsolar radiation varies considerably according to atmospheric conditions. For the sake of generality it was neglected in this analysis. Additional divergence from tracking inaccuracies and mirror shape surface errors were also not considered. The reflectivity of the mirrors was taken to be constant and the relationship between absorption and angle of

incidence was taken for nickel pigmented aluminium oxide (Ni-Al_2O_3), as reported by Tesfamichael and Wäckelgård [146].

Determination of the optical efficiency enabled the stagnation temperature to be calculated. A linear approximation of the heat loss coefficient (see Figure 3.8) was used to derive an expression for $T_{r,max}$, by substitution from Eq.(3.28). Therefore a solution for $T_{r,max}$ was obtained on an hourly basis. Furthermore, the optimum operating temperature of the receiver, $T_{r,opt}$, could be deduced [31].

$$T_{r,opt} = \sqrt{T_{r,max} T_a} \tag{3.30}$$

In reality constant temperature operation is more practical. If the stagnation temperature was below the target operational temperature it was assumed that any captured radiation was not utilised, as the irradiance level was not sufficient for the collector to operate.

3.6 Application to case study

The cost-exergy method was applied to the LFR prototype, operating with different spacing arrangements and a north-south tracking axis, in the Gujarat area. Research costs were gathered by the author during the prototype's construction in Vapi, Gujarat. To account for likely variations, four cost scenarios were considered (see section 3.2). Units of US dollars were used here, converted from Indian national rupees (INR/Rs.) at 2011 rates (1 Rs. = 0.02135 US$), see Table 3.1.

Table 3.1: Initial upper and lower cost estimates of a prototype LFR and land costs for Gujarat.

Horizontal Frame	Lower Concentrator	Upper Concentrator	Lower Land	Upper Land	Lower Receiver	Upper Receiver
750 Rs./m^2	2953 Rs./m^2	10000 Rs./m^2	720 Rs./m^2	10000 Rs./m^2	2000 Rs./m^2	8000 Rs./m^2
16 \$/m^2	63 \$/m^2	214 \$/m^2	15 \$/m^2	214 \$/m^2	43 \$/m^2	171 \$/m^2

The prototype LFR consisted of twenty eight 80 mm wide mirrors, and a 100 mm wide receiver fixed at a height of 2 metres. The receiver was formed from four 25 mm diameter copper tubes joined together, held in a 200 mm wide and 160 mm deep trapezoidal cavity. The design parameters of the different spacing arrangements for the collector are given in Table 3.2.

Table 3.2: Sizing parameters of each spacing arrangement for the prototype LFR.

Spacing arrangement	Area of receiver per unit length (A_r/L)	Area of mirror per unit length (A_m/L)	Total width of collector (m)	Area of cover glazing per unit length (A_{cg}/L)
Mathur	0.1	2.24	2.69	0.32
S15°	0.1	2.24	2.62	0.32
S30°	0.1	2.24	2.90	0.34
S45°	0.1	2.24	3.46	0.40
S60°	0.1	2.24	4.75	0.52
S75°	0.1	2.24	9.08	0.96

To obtain the optical efficiency at normal incidence ($\theta=0$) and the incident angle modifiers IAM(θ_t) and IAM(θ_l) for the collector, ray-tracing was performed using Optica, a software package developed within Mathematica®. The IAM(θ_t) and IAM(θ_l) for each spacing arrangement is shown in Figure 3.9. Mathur's method for determining the spacing arrangement of the mirror elements was also analysed to enable a comparison of the methods to be drawn.

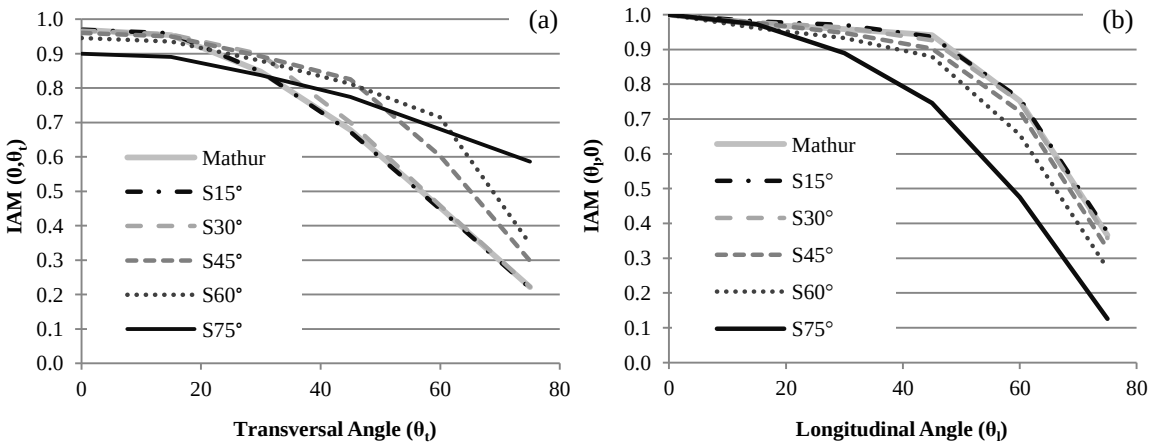

Figure 3.9a–b: IAMs for changing angles in the transversal plane (a) and longitudinal plane (b) for each spacing arrangement.

The exergy outputs per total mirror area (given as an hourly average over a TMY) at different operating temperatures for each spacing arrangement are shown in Figure 3.10. Maximum exergy of 50 W/m^2 was achieved with S52.5° (i.e. corresponding to a transversal angle of 52.5° for the onset of shadowing) and a constant operating temperature of 300 °C; the baseline cost per exergy at this temperature is also plotted in Figure 3.10. A continuously optimised temperature gave only slightly higher exergy of 52 W/m^2. As a spacing of S52.5° maximised exergy and was close to the optimum for minimum cost it was therefore also analysed in addition to those specified in Figure 3.6. Figure 3.11 shows

that for a constant operating temperature of 300 °C the operational hours were maximised at S45° and that for lower operating temperatures the number of operational hours per year were comparatively insensitive to the choice of spacing arrangement.

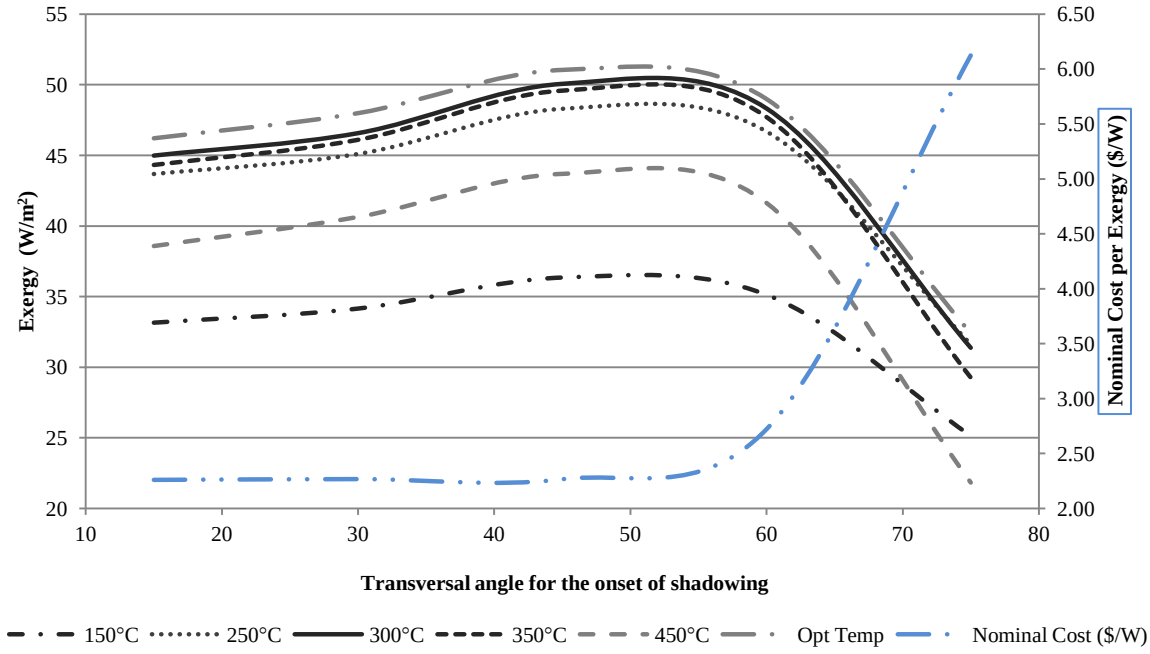

Figure 3.10: Exergy averaged over the TMY vs. spacing arrangement as specified by the transversal angle used for the onset of shadowing (Figure 3.6), for different operating temperatures and for the ideal case of continuously optimised temperature. The baseline cost per exergy for 300 °C operation is plotted on a secondary axis.

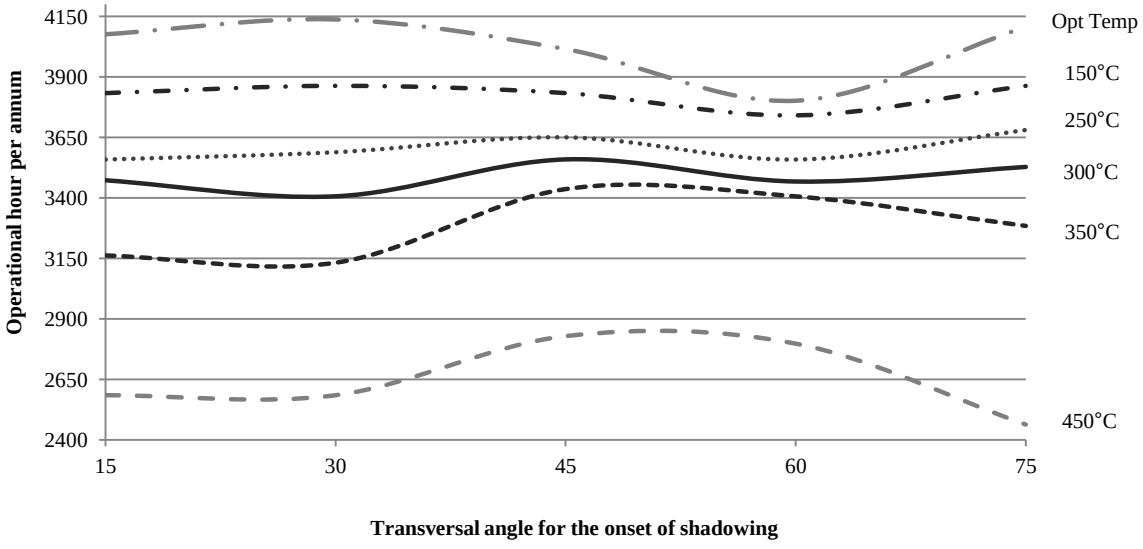

Figure 3.11: Operational hours per annum vs. spacing arrangement as specified by the transversal angle used for the onset of shadowing (Figure 3.6), for different operating temperatures and for the ideal case of continuously optimised temperature, $T_{r,opt}$.

To show the sensitivity to cost assumptions, Table 3.3 presents for each spacing arrangement the cost-exergy calculations for the four cost scenarios of the sensitivity analysis, at the preferred operating temperature of 300 °C. Included among the spacing arrangements were S52.5° and Mathur for comparison. Table 3.4 shows yearly exergy and net heat transfer to the receiver.

Table 3.3: Cost-exergy results for the four cost sensitivity scenarios for the different spacing arrangements, operating with a north-south axis tracking orientation.

Spacing arrangement	Optical efficiency $\eta(\theta=0)$	Exergy per total mirror area (W/m^2)	Operational hours per annum	Sensitivity Analysis ($/W)			
				Baseline cost	High component cost	High land cost	High component and land cost
Mathur	83.6%	45.9	3437	2.2	5.6	7.4	10.8
S15°	81.7%	45.0	3473	2.3	5.4	7.4	10.9
S30°	83.1%	46.6	3407	2.3	5.2	7.8	11.1
S45°	83.1%	50.1	3559	2.3	5.0	8.4	11.5
S52.5°	82.3%	50.1	3559	2.4	5.0	9.4	12.5
S60°	81.7%	48.3	3468	2.7	5.4	11.4	14.6
S75°	66.1%	31.4	3528	6.1	9.3	31.7	36.7

Table 3.4: Annual exergy produced and net heat transfer to receiver.

Spacing arrangement	Exergy per unit length	Exergy per total mirror area	Net heat transfer per unit length	Net heat transfer per total mirror area
	kWh/m a	kWh/m^2a	kWh/m a	kWh/m^2a
Mathur	901	402	1916	855
S15°	883	394	1878	838
S30°	914	408	1945	868
S45°	982	439	2090	933
S52.5°	983	439	2088	932
S60°	948	423	2017	900
S75°	616	275	1313	586

3.7 Discussion

Based on this case study for Vapi, Gujarat, the recommended spacing arrangement was that corresponding to an onset of shadowing at a transversal angle of 45°. Using this arrangement, the exergy, and number of operational hours per year were maximised, and the cost per exergy was kept at a minimum for all cost scenarios. In comparison to the method of Mathur et al., a 9% increase in exergy was achieved, resulting in an extra 122 hours of operation per annum at a receiver temperature of 300 °C. This was consistent with operating fluid temperatures claimed for commercial LFRs given that the temperature used in this study was the absorber tube surface temperature and therefore expected to be

slightly higher than the fluid temperatures [82, 96]. For different operating temperatures the exergy output and operational hours varied, yet the optimum spacing arrangement remained constant. A constant receiver temperature of 300 °C proved to be the most efficient operating temperature for the prototype LFR presented. If a coupled heat cycle could utilise a continuously changing optimum operating temperature the operational hours would be significantly increased by 13%; however, the exergy would not improve significantly compared to a constant operating temperature of 300 °C.

The sensitivity analysis established that the cost was relatively insensitive to spacing arrangements specified by a traversal angle of up to 52.5° for a baseline cost scenario. The optimum spacing arrangement for a high component cost was always the one giving maximum exergy, because this maximised the output from potentially expensive materials. A maximum saving of 11% in the cost per exergy was obtained under this scenario. On the other hand, the narrower spacing arrangements used less land and were thus favoured when land costs were high. Therefore, it is recommended that for a ground installation with plentiful land and an application requiring high operating temperatures for long periods of time, such as for electricity generation, the spacing arrangement giving maximum exergy should be selected. For an application with restricted space or high land cost, such as a roof installation, a narrower spacing arrangement, as given by Mathur's method, should be used.

The cost-exergy approach proved to be a more illuminating (albeit more complex) method compared to that of Mathur et al. when it came to specifying the spacing arrangement of the mirror elements in an LFR system. The new method can in fact be used to provide alternative recommendations for different LFR designs to reduce land usage, increase performance or minimise cost according to the priorities at hand. A potential drawback of the approach is that it leads to bespoke design recommendations according to location. Moreover, the non-uniform spacing may make the support frame more complex to design and manufacture. The improved performance should justify to some extent these additional investments, even if the cost advantages alone are not sufficient. Whereas it is unlikely that an LFR would be redesigned for each individual location, the flexibility of modern manufacturing techniques and the growth in demand for solar collectors should partially overcome these drawbacks and justify a number of design variants each optimised for a climatic or economic region.

Avoidance of excessive mirror reflector spacing in an LFR has been shown to be important so that optical performance is not compromised and cost from additional array structure and land usage does not become excessive. More factors could be considered in future studies, such as ground preparation, additional steam line length, thermal losses and additional optical effects (e.g. circumsolar radiation, tracking errors, and mirror shape surface errors). These factors could affect the results for the costs and ideal operating temperature. The effects of thermal storage on the potential work output and operational hours could also be considered. The optimisation method outlined in this chapter could even be extended to LFRs utilising different concentrator-receiver assembly configurations. For example, curved mirror elements, which reduce the flux distribution on the absorber and allow wider mirror elements, could be analysed. So could evacuated tube type collectors, which would reduce the heat loss coefficient, increasing the temperatures and hence exergy of the system. The higher cost of the evacuated tubes would tend to favour optimisation for performance as in the high component cost scenario considered above. A relatively new and exciting variant is the compact linear Fresnel reflector (CLFR), which should also be investigated by extension of the new method.

A limitation of the exergy approach is that it assumes the idealised Carnot engine. It does not take into account losses in real engines or losses associated with extracting the heat from the receiver field using a working fluid. Depending upon the heat cycle coupled to the system, the operational hours at full load would be significantly less than the total operational hours stated in this study. Nevertheless, the cost-exergy method enables general conclusions to be drawn without reference to specific applications. For real arrangements the optimum design is likely to be similar even if the overall power output is lower.

3.8 Conclusion

The cost exergy approach presented in this chapter successfully enabled the spacing arrangement in an LFR to be specified such that the exergy and operational hours were maximised over a typical meteorological year and costs were minimised. For the case study of the LFR situated in Gujarat, it was recommended to use a north-south tracking axis with a non-equidistant spacing arrangement chosen for the onset of shadowing at a transversal angle of 45°, operating at a constant receiver temperature of 300 °C, representing the temperature at the surface of the absorber tubes. This resulted in an additional 122 operational hours per annum being achievable at a baseline cost per exergy

of 2.3 $/W. However, the sensitivity analysis showed that an increase in the land cost favoured a narrower spacing arrangement, even though technical performance was reduced.

The new method for optimising mirror spacing arrangements can be applied to other locations and is expected to give similarly significant improvements in the value of the LFR for use in a variety of applications. Novel LFR concepts will need to be investigated to achieve a design that has compact footprint as well as high annual performance.

3.9. Chapter summary

This chapter presented a new method for the optimisation of the mirror element spacing arrangement and operating temperature of linear Fresnel reflectors. The specific objective was to maximise available power output (i.e. exergy) and operational hours whilst minimising cost. The method was described in detail and compared to an existing design method prominent in the literature. Results were given in terms of the exergy per total mirror area (W/m^2) and cost per exergy (US $/W). The new method was applied principally to the optimisation of an LFR prototype developed in Vapi, Gujarat, India, for which cost data was gathered. It was recommended to use a spacing arrangement such that the onset of shadowing among mirror elements occurred at a transversal angle of 45°. This resulted in a cost per exergy of 2.3 $/W. Compared to the existing design approach, the exergy averaged over the year was increased by 9% to 50 W/m^2 and an additional 122 hours of operation per year were predicted. The ideal operating temperature at the surface of the absorber tubes was found to be 300 °C. It was concluded that the new method is an improvement over existing techniques and a significant tool for any future design work on LFR systems.

Chapter 4

Design of a novel LFR using a multi-criteria decision-making methodology

4.1 Introduction

It has been shown in Chapter 3 that an LFR's mirror spacing arrangement can be optimised according to site location and application. However, with less energy capture than other CSP technologies, Fresnel collectors would benefit from an increase in annual optical efficiency. By considering novel LFR concepts, it was interesting to seek further improvements in customer and technical requirements for a solar collector in Gujarat and elsewhere. Particularly since the LFR principle has remained relatively unchanged since its conception in 1957. This chapter therefore differs from the previous one in that novel LFR concepts, which do not necessarily conform to the standard LFR design, were developed and compared.

To arrive at these novel concepts, structured design methods were used, in particular Quality Function Deployment (QFD). QFD was developed by Akao [147] in 1966 in Japan and since then has grown in popularity for use in a number of industries including automotive, software development, steel and electronics [148]. More recently QFD has been applied to the design of building integrated photovoltaic systems [149]. So far, however, there have been very few (if any) references to the use of QFD in the field of solar thermal energy.

The primary and most significant tool in QFD is the 'House of Quality' (HoQ), which translates the customer requirements into engineering characteristics i.e. technical requirements. A step-by-step illustrative application and example of the HoQ was given by Chan and Wu in [150]. These requirements are commonly obtained through interviews, surveys and multi-criteria decision-making methods. Approaches integrating QFD with decision-making methods such as the analytical hierarchy process, goal programming and the Analytic Network Process (ANP) have been demonstrated in areas such as product planning [151] and strategic marketing [152]. Other decision methodologies have also been integrated with QFD to further enhance concept selection. A joint US Air Force/NASA program to produce a heavy lift launch vehicle used the Pugh concept selection matrix with QFD for the selection of a new fuel turbo pump, comparing two different designs with a baseline concept [153]. QFD, AHP and Failure Modes and Effects Analysis (FMEA) were

also used by Hsiao in the development of a new musical toy [154]. A number of publications combining AHP and QFD for product design and selection were reviewed by Ho [155].

As indicated in Chapter 2, in the field of renewable energy, numerous publications have demonstrated MCDM tools for system assessment and selection: Lozano-Minguez et al. [156] used a MCDM technique to assess alternative support structures for offshore wind turbine installations; Lee et al. [157] applied an AHP model to the issue of site selection for wind farms; Nobre et al. [158] applied a multi-criteria analysis to determine the best location for a wave farm in Portugal; and Cavallaro [159] utilised PROMETHEE to assess and compare alternative CSP systems. Kosoric et al. [160] and Cavallaro [161] have used MCDM methods for design, development and technology selection of Photovoltaics. The QFD and Pugh methods are also well documented in the literature and were therefore used here without detailed background explanations [162].

The aim of this chapter was to develop a novel LFR and thus improve on the standard LFR design in response to customer (and not purely technical) requirements. The objectives to accomplish this were as follows:

1. Using a multi-criteria decision-making methodology (QFD, AHP and Pugh), develop and select a novel LFR concept based on requirements (i.e. criteria) arising in Gujarat, India. Analyse the technical performance of a detailed design of the selected concept and an equivalent standard LFR design for comparison.
2. Construct a prototype of the novel LFR design to establish monetary values for comparison to standard design.
3. Evaluate the benefits and drawbacks of the novel design compared to the standard design, with reference to original customer and technical requirements.
4. Evaluate the effectiveness of the decision-making method in terms of incorporating customer and technical requirements, thus improving total quality.

4.2 Methodology

The methodology used to reach these objectives will now be outlined.

(i) **Construction of the House of Quality:**

As in all QFD approaches, the customer requirements (WHATs i.e. what the customer wants) were collected for use in the HoQ. In this chapter results from the AHP study (Chapter 2) were used to generate WHATs and their importance. Technical requirements (HOWs) for how the WHATs will be satisfied were also determined. The main outputs from the completed HoQ were technical priorities (weightings) for each HOW for the design of a novel LFR. Technical targets, limits and difficulties were also specified to develop product specifications.

(ii) **Concept development and selection:**

Concepts for a novel LFR were developed. Through a Pugh matrix, integrated with the HoQ technical priorities, concepts were compared with reference to a standard LFR, and the 'best' concept was selected.

(iii) **Finalized design of selected concept:**

A detailed design of the selected novel LFR concept was developed, while targets and limits were maintained based on those specified in the HoQ.

(iv) **Detailed analysis of selected LFR with standard design:**

The novel design was analysed through the use of ray-tracing to enable annual performance to be predicted over a TMY for the region of Gujarat, India. Performance results included exergy per total mirror area, operational hours above a target operating temperature, net heat transfer to receiver and annual optical efficiency. The annual performances of two standard LFRs were also analysed for comparison. Financial results were determined through the construction of a prototype; and upper and lower land costs were researched for Gujarat. Capital costs and achievable cost per exergy among the final designs were evaluated and compared.

4.3 Construction of the House of Quality

The customer requirements were extracted from the importance weightings attributed by the expert panel convened for the AHP study, as described in Chapter 2 (see Appendix 4). The relevant criteria from the AHP study, and the corresponding weightings, were translated into WHATs, W_m, and their importance, g_m, rated with a low (1), medium (3), and high (9) score (Table 4.1). The technical requirements provided from the AHP results were expanded to include additional HOWs, H_n, deemed necessary for the design of a

novel solar collector for Gujarat. An additional input to the HoQ was included to reflect an improvement factor, u_m, given by the ratio of the 'future product' rating, a_m, to 'current product' rating, x_m. A standard LFR was scored against the customer requirements, and compared to a target score for a novel design. A final overall weighting, f_m, was formed from the product of the customer's importance score and the design improvement factor.

Table 4.1: Customer requirements and their importance for a solar collector in India, established from the AHP study (Chapter 2).

Customer Requirements	Customer importance
Ease of Operation/Set-up	3
High Quality of Heat	3
Reliability	9
Land Usage	9
Cost of O&M	9
Capital Cost	9

$$f_m = g_m . u_m \tag{4.1}$$

To complete the HoQ relationship matrix, each HOW was scored against each WHAT on whether there was a weak (1), medium (3), or strong (9) relationship. The correlation matrix was omitted for simplicity. The importance, t_n, of each technical requirement was established by multiplication of each value in the relationship matrix, r_{mn}, by the respective overall weighting and totalling the scores for each technical requirement [150]. A relative technical priority was established through normalisation. The completed HoQ included a target or limit and a technical difficulty for each HOW (see Figure 4.1).

$$t_n = \sum_{m=1}^{M} f_m . r_{mn} , \qquad n = 1,2 \dots , N \tag{4.2}$$

The HoQ identified the most important customer requirement to be land usage with an overall weighting of 14, followed by the capital cost with a weighting of 6.8. Ease of operation was found to be the least important customer requirement with a score of 1.8. The technical priorities revealed the cost per exergy to be the most important technical requirement with an 11% priority. With a priority of 7% the following technical requirements were ranked in second: reflectivity of the mirror elements, accurate tracking, half acceptance angle and concentration ratio.

		Customer Importance (g_m)	Exergy	Collection Efficiency	Optical Efficiency	Ideal Conversion Efficiency	Reflectivity of Concentrator Elements	Use of Standard Parts	Durable	Tolerance of External Loads	Accurate Tracking	Half Acceptance Angle (Secondary Concentrator)	Concentration Ratio	Efficient Use of Land	Average Daily Shadow Efficiency	Parasitic Loads	Temperature Tolerance	Heat Transfer Characteristics	High Absorption	Compatible with Heat Transfer Fluid	Pressure Tolerance (Fixed Receiver)	Cost per Exergy	Typical LFR Design (x_m)	Target Rating (a_m)	Improvement Factor (u_m)	Overall Weighting (f_m)
Improve	Ease of Operation/Set-up	3						9	1	3	9	9				3				9	9		5	3	0.6	1.8
	Reliability	9	3					9	9	9	9	9				1	1			9	9	3	3	2	0.7	6
	Quality of Heat	3	9	9	9	9	9		3	1	9	9	9		9	1	9	9	9			9	2	4	2	6
Reduce	Capital Cost	9		3	9	3	9	9	9		9	9	3	9			9	9	9	3		9	4	3	0.8	6.8
	Cost of O&M	9		3	3	1	9		3		3	3				9	1	3	3	3	1	9	2	2	1	9
	Land Usage	9		1		1							9	9	9							9	2	3	1.5	14
Technical Evaluation	Target or Limit		<50W/m2	65%	70%	40%	90%	High	10 Years	High	0.5°	0.75°	30	70%	90%	10%	350 °C	6 W/m2.K	90%	High	50 bar	>5$/W				
	Technical Importance (t_n)		72	115	142	96.8	196	131	162	65	212	212	196	182	176	98	130	142	142	117	79	335				
	Technical Difficulty (0 = Easy to Accomplish, 10 = Extremely Hard)			6	5	5	5	7	8	6	8	7	7	5	9	3	6	4	2	9	3					
	Technical Priority		2%	4%	5%	3%	7%	4%	5%	2%	7%	7%	7%	6%	6%	3%	4%	5%	5%	4%	3%	11%				

Sample calculations:

Ease of Operation
fm = 3(3/5)=1.8*

Exergy
t_1 = (6x3)+(9x6) = 72
t_1 priority = 72/3000 = 2.4%

Figure 4.1: House of Quality constructed for the design of a novel LFR for India.

4.4 Concept development and selection

Three LFR concepts, Circular, Parabolic and Elevation, were consequently developed taking into account the customer and technical requirements and their weightings. Each LFR concept comprised a concentrator, formed from mirror elements, focusing on a fixed insulated target (the design traits typifying an LFR). Schematics of the three concepts and a standard LFR design (Horizontal) used as a baseline are shown in Figure 4.2a–d, which distinguishes the tracking method and element location in each case. A Pugh selection matrix, which in essence is a systematic process for the selection of a 'best' concept, was used to compare the novel LFR concepts in comparison to Horizontal. In the matrix concepts were scored against each technical requirement as better '1', even '0', or worse '-1'. Each score was then multiplied by the corresponding technical priority and totalled to provide a final weighted ranking. Among the alternatives the 'Elevation' concept, henceforth referred to concisely as the Elevation Linear Fresnel Reflector (ELFR), received the highest weighted ranking (see Table 4.2).

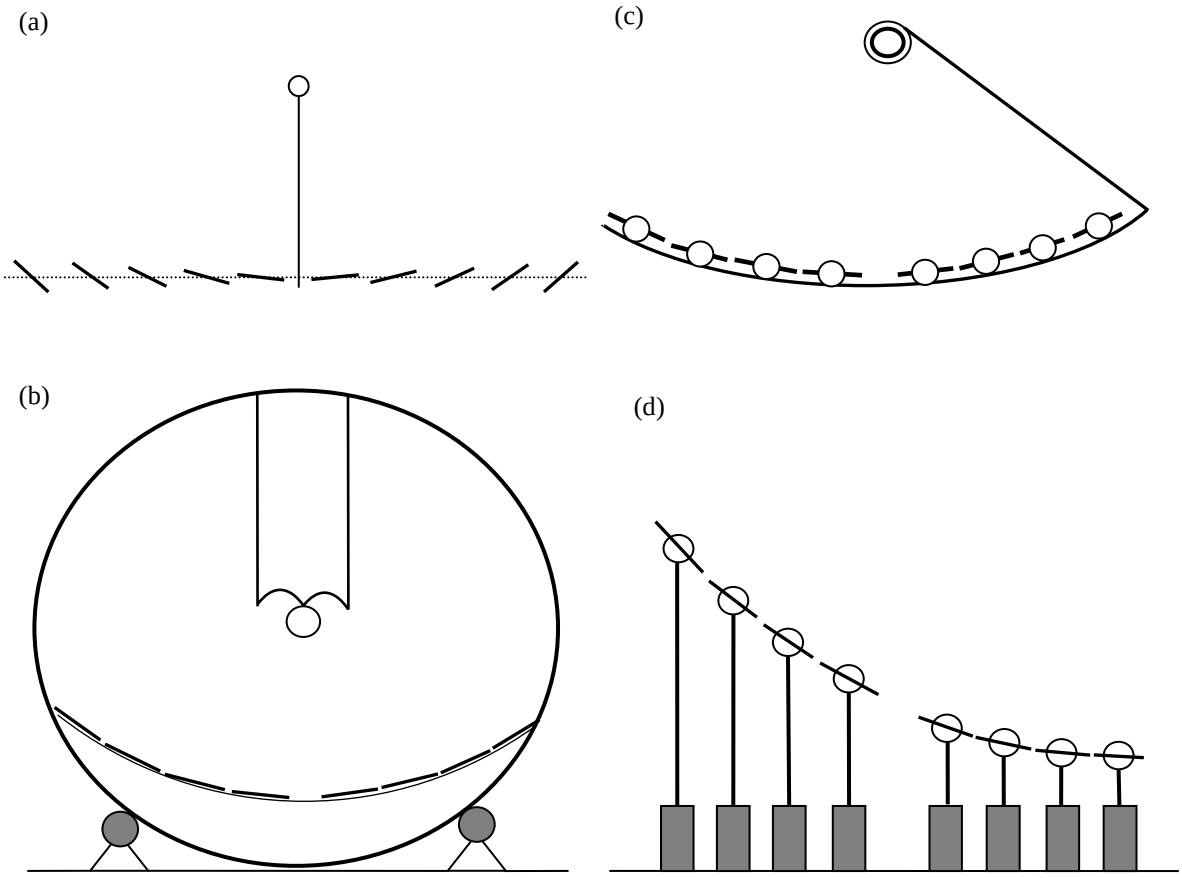

Figure 4.2a-d: Reference LFR concept (a) Horizontal - horizontal rotating elements. LFR concepts (b) Circular - elements located along parabola rotating in a circular wheel, (c) Parabolic - rotating elements placed along parabolic path and (d) Elevation - rotating and elevating elements.

Table 4.2: Pugh concept selection matrix for a novel LFR. The concept Elevation (ELFR) obtained the highest final weighted ranking.

Technical Requirements	**Technical Priorities**	**Horizontal (a)**	**Circular (b)**	**Parabolic (c)**	**Elevation (d)**
Exergy	2%	0	1	1	1
Collection Efficiency	4%	0	1	0	1
Optical Efficiency	5%	0	1	0	1
Ideal Conversion Efficiency	3%	0	1	0	1
Durable	7%	0	0	0	0
Concentration Ratio	4%	0	1	1	1
Use of Standard Parts	5%	0	-1	-1	-1
Parasitic Loads	2%	0	0	0	0
Efficient Use of Land	7%	0	1	0	1
Tolerance of External Loads	7%	0	-1	0	0
Reflectivity of Concentrator Elements	7%	0	0	0	0
Average Daily Shadow Efficiency	6%	0	1	0	1
Accurate Tracking	6%	0	1	0	1
Temperature Tolerance	3%	0	0	0	0
Heat Transfer Characteristics	4%	0	0	0	0
Specialist Coatings	5%	0	0	0	0
Compatible with Heat Transfer Fluid	5%	0	0	0	0
Pressure Tolerance (Fixed Receiver)	4%	0	0	0	0
Half Acceptance Angle	3%	0	1	-1	0
Cost per Exergy	11%	0	0	0	0
Total Score		0	7	0	7
Final Weighted Ranking		0	0.277	-0.013	0.322

4.5 Finalised design of selected concept.

A final ELFR design using 8 mirror elements, each 250 mm wide and spaced 260 mm apart (10 mm gap), was chosen to satisfy the specified targets and limits (Table 4.1). This formed a single LFR unit 4 m in length. A secondary compound parabolic concentrator (CPC) at the receiver aperture was also chosen to maintain the capture of rays from the collector extremity for changing element focal distances. Through the use of a CPC the width of the receiver's absorbing target was reduced, thus overcoming the disadvantage of using wide flat mirror elements as opposed to curved mirror elements. The target absorber was a 63.5 mm diameter pipe located at a height of 5 m, with a truncated CPC so the receiver was not oversized. This provided the target concentration ratio of 30 as specified in the HoQ. To simplify the construction of a prototype the receiver was positioned at the maximum practical height of 2.5 m, resulting in a receiver absorbing target width of 152.4 mm; thus, three 63.5 mm pipes were selected (see Figure 4.3). The detailed design method for the CPC receiver is given in the following chapter.

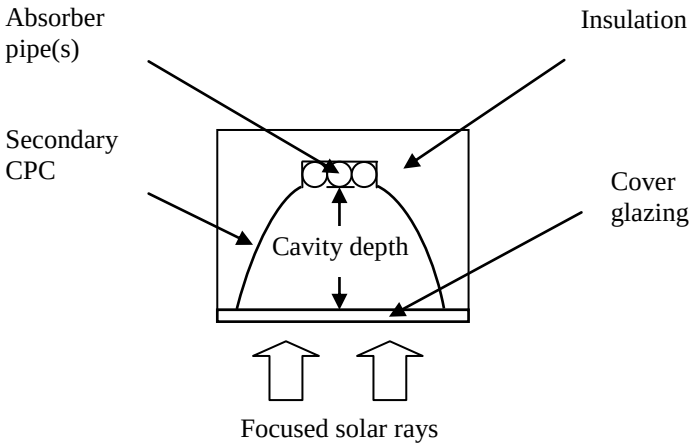

Figure 4.3: Schematic of an insulated receiver configuration with secondary CPC.

4.6 Detailed analysis of selected LFR against standard design

Technical and financial criteria of the finalised ELFR were evaluated with reference to two equivalent Horizontal LFR designs with different spacing arrangements; 'H-constant' having mirror elements with a horizontal-constant spacing of 260 mm (the same spacing as the ELFR design), and 'H-variable' having horizontal-variable spacing such that the onset of shadowing among adjacent elements occurred at a solar transversal angle of 45° (see Figure 4.4a-c). Note that the wider mirror spacing of H-variable required a redesigned CPC. The technical performance of each design was calculated from the maximum available power output (i.e. exergy) at the receiver's absorbing target surface. The financial factors considered were the land usage and the capital costs incurred from the LFR sub-components, which included the receiver, concentrator elements and frame.

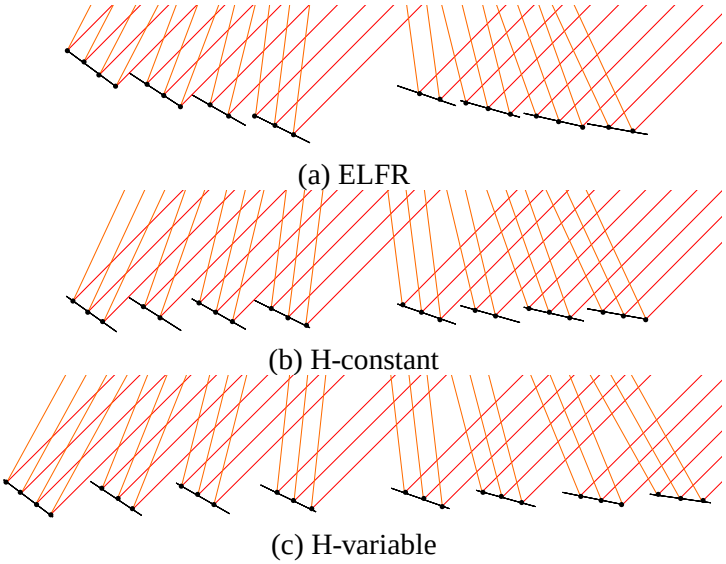

Figure 4.4a-c: Mirror spacing arrangement for an (a) ELFR, (b) H-constant and (c) H-variable design for solar rays approaching at a transversal angle of 45°.

4.6.1 Technical Analysis

Achievable performance was predicted for the ELFR operating with a north-south axis tracking orientation over a TMY for Gujarat. Since the focus of this study was on the collector design, the concept of exergy was again used to provide details on the maximum available power output for a given operating absorber pipe surface temperature and ambient temperature (see Section 3.5).

For the ELFR the individual mirror element elevation required throughout operation to remove shadowing, es_n, can be approximated from the solar profile angle and the element's width, slope angle and shift (see Figure 4.5).

$$es_n = \frac{W}{2}(sin\theta_n + sin\theta_{n+1}) - S_n Tan\theta_p \tag{4.3}$$

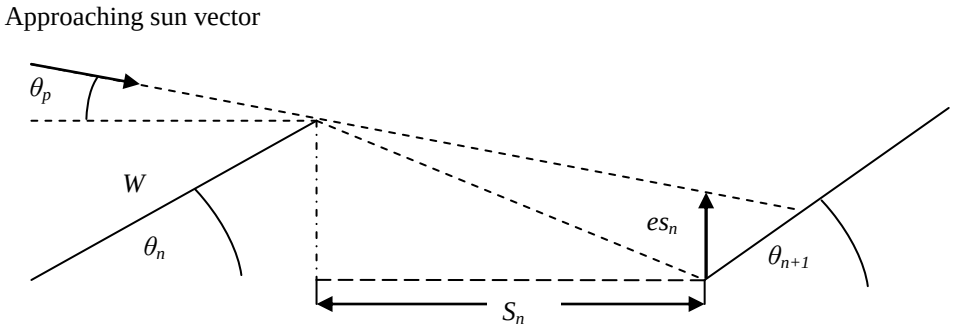

Figure 4.5: Elevation required to remove shadowing from an adjacent mirror element.

With a change in elevation an iterative process was required to calculate the correct slope angle. Depending upon the mirror element geometry a narrow spacing arrangement may result in blocking of reflected rays from adjacent mirrors (see Figure 4.6). The elevation to removing blocking was estimated from:

$$eb_n = \frac{W}{2}(sin\theta_{n+1} + sin\theta_n) - \frac{S_n h}{(Q_{n+1} + \left(\frac{W}{2}\right) Cos\theta_{n+1} + S_n)} \tag{4.4}$$

The tracking arrangement from sunrise to sunset for the ELFR is shown in Figure 4.7.

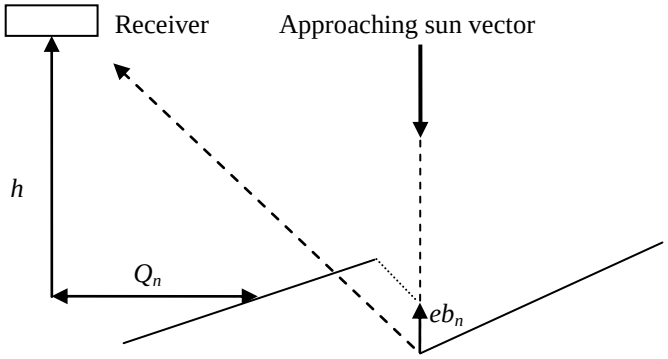

Figure 4.6: Elevation required to remove blocking from an adjacent mirror element.

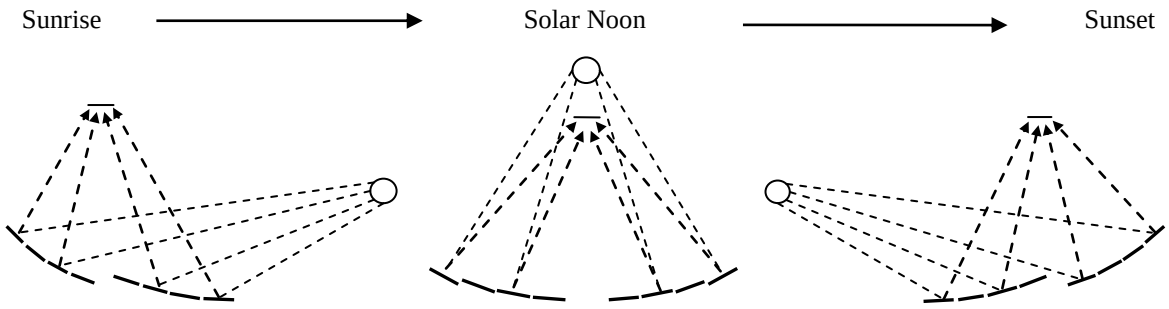

Figure 4.7: Tracking arrangement of the mirrors elements from sunrise to sunset for the ELFR.

4.6.2 Performance results

Performance characteristics of the three designs – ELFR, H-constant and H-variable – were evaluated for the Gujarat TMY. For each design the optical efficiency at normal incidence ($\theta=0$) and the incident angle modifiers IAM(θ_t) and IAM(θ_l) were determined using Optica. The IAM(θ_t) and IAM(θ_l) for each design are shown in Figure 4.8a–b. The average hourly exergy (per total mirror area) and the average daily number of operational hours (for a target operating temperature of 300 °C) for each month are shown in Figures 4.9 and 4.10 respectively. Exergy and operational hours were characteristically low during the Indian monsoon season, after reaching a peak in April-May.

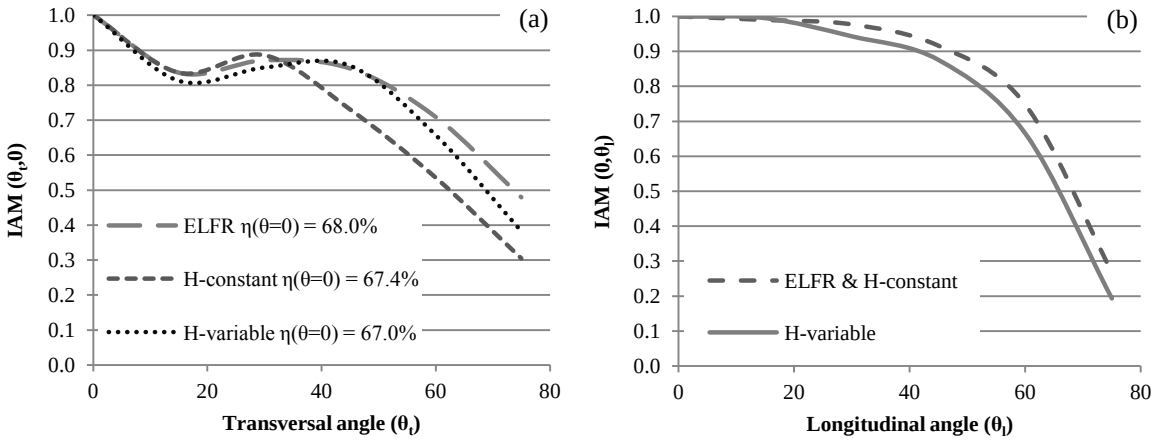

Figure 4.8a-b: IAMs for changing angles in the transversal plane (a) and longitudinal plane (b) for the ELFR, H-constant and H-variable. The optical efficiency at normal incidence is also shown for each design.

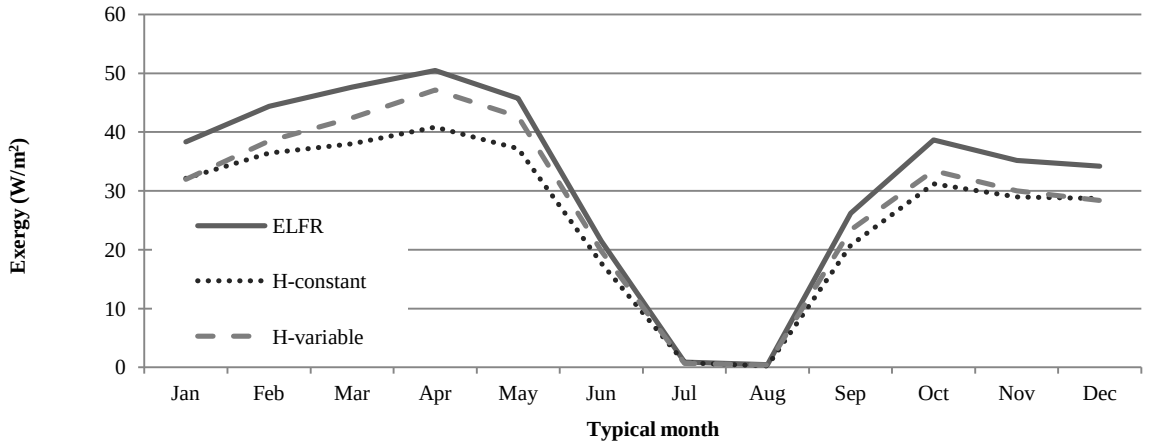

Figure 4.9: Average hourly exergy for each month in a TMY for Gujarat.

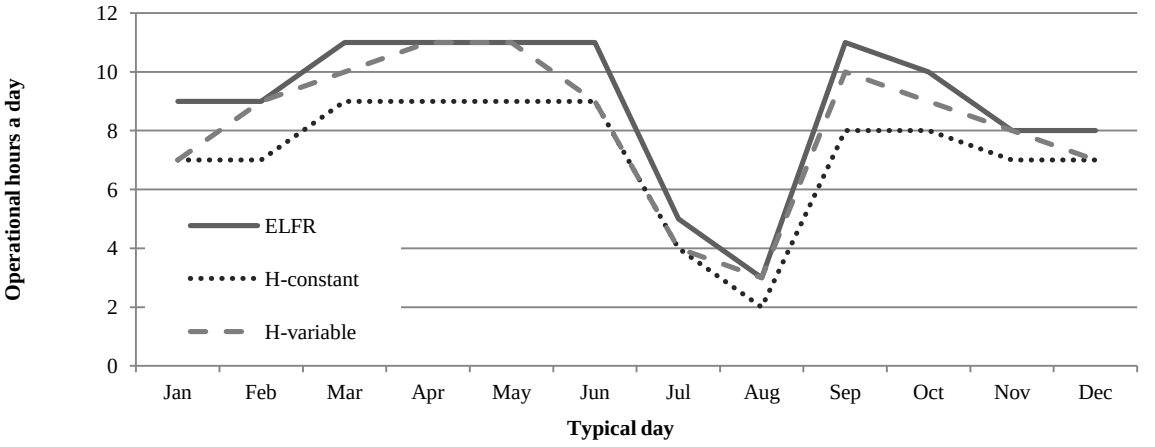

Figure 4.10: Average number of operational hours at a constant operating temperature of 300 °C for a typical day in each month for Gujarat.

The ELFR design achieved a 23% exergy increase over H-constant and a 13% increase over H-variable. A 24% and 9% increase in the operational hours was found to be achievable in comparison to H-constant and H-variable respectively. Exergy and operational hours were increased due to the ELFR's improved optical performance for low solar altitude angles. The improved optical performance resulted in a higher annual optical efficiency in comparison to a typical LFR. The annual optical efficiency was based on the average optical efficiency for daylight periods during a year. The average hourly exergy, total operational hours above an operating temperature of 300 °C, net heat transfer to the receiver target and annual optical efficiency are shown in Table 4.3.

Table 4.3: Annual performance for the ELFR, H-constant and H-variable; annual exergy, operational hours, net heat transfer to receiver, and annual optical efficiency.

LFR designs	Exergy per total mirror area	Operational hours per annum	Net heat transfer per unit length	Annual optical efficiency
	W/m^2	hrs/a	kWh/m.a	%
ELFR	32.0	3255	1192	49.0
H-constant	26.1	2616	972.3	39.3
H-variable	28.2	2981	1054	45.0

4.6.3 Financial results

Through the construction of a prototype ELFR, monetary values were gathered for the collector's receiver, concentrator, frame and additional costs for the elevating elements (see Figure 4.11). To provide sensitivity to the results, upper and lower land costs were researched for the region of Gujarat. A final capital cost per exergy was calculated to compare the design alternatives. Units of US dollars were used, converted from Indian national rupees (INR) and pound sterling (GBP) at 2011 rates (see Table 4.4).

Figure 4.11: The ELFR prototype, constructed on the roof of Aston University, UK.

Table 4.4: Prototype component costs and cost per exergy for each design alternative (units of US dollars were used here, with exchange rates: 0.02$/INR, 1.57$/GBP).

Design		ELFR	H-constant	H-variable
Exergy per total mirror area	W/m^2	32.0	26.1	28.2
Land usage per collector unit	m^2	9.6	9.6	11.6
Lower total land cost	$	145	145	175
Upper total land cost	$	2009	2009	2428
Frame	$	6040	6040	6112
Drives for elevation	$	3429	0	0
Concentrator elements	$	3932	3932	3932
Receiver	$	1887	1887	1887
Total lower cost	$	15433	12004	12107
Total upper cost	$	17298	13869	14360
Lower cost per exergy	$/W	60.3	57.6	53.6
Upper cost per exergy	$/W	67.6	66.5	63.6

The ELFR increased the cost per exergy by potentially 2–5% and 6–13% over H-constant and H-variable respectively. The additional cost for the elevating elements, achieved through the use of linear slides and parallel pair linear actuators, formed approximately 20% of the total capital cost.

4.7 Discussion

It was interesting to evaluate the methodology used in this study. The combination of QFD, AHP and the Pugh matrix was a relatively complex procedure. A simpler approach would be to use the Pugh matrix alone, but this would not have included the formulation of technical priorities as achieved through the complementary use of QFD and AHP. As a result, the more complex approach enabled the concepts to be differentiated. It highlighted the advantages of the Elevation concept with a 15% preference over the Circular concept.

A general criticism of systematic approaches to design decision and selection making, like QFD and AHP, is that the outcome can be rather dependent on the criteria fed into the process (i.e. the customer and technical requirements) [163, 164]. According to this initial choice a different concept may emerge as 'the best'. To address this concern, the investigation was taken a step further through a detailed technical and financial analysis, with comparisons made against two standard LFR designs (H-constant and H-variable).

The novel ELFR showed performance advantages. For a constant operating temperature of 300 °C, the ELFR gave a 13% increase in exergy, 274 additional operational hours per annum and a 17% reduction in land usage. This was compared to H-variable which referred to a horizontal mirror spacing arrangement specified for the onset of shadowing at a solar transversal angle of 45°. An even more significant increase in exergy of 23% was expected over a commonly employed narrow constant horizontal mirror spacing arrangement, H-constant. As regards annual optical efficiency, a value of 49% was predicted for the ELFR, compared to 45% and 39% for H-variable and H-constant respectively. It was interesting to note that these figures were comparable to an annual optical efficiency of 43% reported by Morin et al. for the Fresdemo LFR [64].

There were, however, some potential financial drawbacks to the ELFR. The cost per exergy was increased by 2–5% and 6–13% in comparison to H-constant and H-variable respectively, due to the additional expense of the elevating elements. However, costs for the prototype system were not a true reflection of the manufacturing costs to be expected with mass production. A 60% reduction in component costs would have resulted in the ELFR having a lower cost per exergy, for a high land cost scenario, in comparison to H-constant and H-variable.

The preferred choice of design will depend on the priorities at hand. The ELFR will be interesting for industrial process heat applications or roof installations where land is less available or more expensive. The efficient land usage will be of further benefit when considering additional factors such as ground preparation, piping requirements and pipe thermal losses. The higher obtainable temperatures for longer periods of the day will also be advantageous in solar thermal power plants for electricity generation, increasing full load hours and storage capabilities. However, with the ELFR system increasing capital cost and complexity, significant improvements will be required to make a commercial scale ELFR electricity power generating plant feasible. This is discussed further in the following chapter.

In future studies, the methodology could be improved by generation of more concepts to be combined and refined in the Pugh matrix. The Elevation design could also be applied to LFR systems employing wider mirrors with slight curvature, to the compact linear Fresnel reflector (CLFR) and to the etendue-matched CLFR [83, 97].

4.8 Conclusion

A novel Elevation LFR was selected and analysed with the aid of a multi-criteria decision-making methodology. Continuous reference to a standard LFR design was made throughout the design and decision processes. The performances of the novel design and two standard LFR designs (used as a baseline) were analysed through a technical study. Through the construction of a prototype, a financial assessment of the novel design was completed. With reference to the original chapter aims and objectives, the following conclusions were drawn:

1. The Elevation LFR design increased the annual exergy, optical efficiency and operational hours by 13–23%, 9–25% and 9–24% respectively.
2. Capital costs increased by 16–28% for the novel LFR over the standard LFR design. The cost per exergy increased by 2–13% depending upon land costs. The Elevation LFR also reduced land usage by as much as 17%.
3. The novel LFR improved land usage which was the highest overall weighted customer requirement (14). However, capital costs (weighting of 6.8) increased and reliability (6) and ease of operation (1.8) decreased due to the larger number of drives and mechanisms. The ELFR also improved the quality of heat (6). Operations and maintenance costs (9) were likely to remain similar to the

conventional LFR with the majority of costs coming from operating system pumps and fans. See Figure 4.1 for the development of the customer requirement weightings.

It was further concluded that the novel LFR is particularly suited for applications with low land availability and high land costs e.g. industrial locations and rooftops. For rural regions of India that have a greater abundance of land a standard LFR is preferred.

The methodology integrating AHP, QFD and Pugh helped to generate and select a novel design of a solar thermal collector and will have a wider potential in the field of solar thermal and renewable energy. Given the growing size and complexity of solar thermal projects, these methodologies or variants may have a role to play in co-ordinating decision activities among large teams.

4.9 Chapter summary

Three novel solar thermal collector concepts derived from the linear Fresnel reflector (LFR) were developed and evaluated through a multi-criteria decision-making methodology, comprising the following techniques: quality function deployment, the analytical hierarchy process and the Pugh selection matrix. Criteria were specified by technical and customer requirements gathered from Gujarat, India. The concepts were compared to a standard LFR for reference, and as a result, a novel 'Elevation Linear Fresnel Reflector' (ELFR) concept using elevating mirrors was selected. A detailed version of this concept was proposed and compared against two standard LFR configurations, one using constant and the other using variable horizontal mirror spacing. Annual performance was analysed for a typical meteorological year. Financial assessment was made through the construction of a prototype. The ELFR had an annual optical efficiency of 49% and increased exergy by 13−23%. Operational hours above a target temperature of 300 °C were increased by 9−24%. A 17% reduction in land usage was also achievable. However, the ELFR suffered from additional complexity and a 16−28% increase in capital cost. It was concluded that the novel design was particularly promising for industrial applications and locations with restricted land availability or high land costs. The decision analysis methodology adopted was considered to have a wider potential for applications in the field of solar thermal and renewable energy.

Chapter 5

Construction and experimentation of the Elevation Linear Fresnel Reflector (ELFR)

5.1 Introduction

This chapter discusses the construction and testing of the ELFR prototype. Whereas the previous chapter focused on concept development, this chapter addresses the detailed design and construction of the prototype ELFR, which has been installed on the roof of the South Wing of Aston University, Birmingham, UK. The purpose of the prototype was to perform experiments to verify theoretical models to predict the efficiencies of LFR systems, and to demonstrate the ELFR in operation in order to learn about its performance and ease of manufacture. An overview of the experiments performed to evaluate the performance of linear Fresnel reflector solar collectors is initially provided. The typical materials and components used in the construction of solar receivers are also outlined.

The performance of LFRs utilising cavity receivers, as described in Section 3.5, has been investigated by a number of authors. Singh et al. [84, 143] studied the thermal efficiency and heat loss coefficient for an LFR trapezoidal cavity receiver with varying concentration ratios. They tested different receiver absorber coatings: black paint, bright nickel and black nickel. Electrical heaters were used to heat water in a storage tank. The water was then pumped through the receiver, and the flow rate was controlled with a regulator value. The thermal efficiency was determined for different water inlet temperatures according to the ASHRAE standard-93 (1986), i.e. flow rate controlled to achieve a constant inlet and exit temperature for constant solar conditions. The heat loss coefficient was calculated by circulating Hytherm-500 oil at a constant flow rate for different inlet temperatures and measuring the difference in exit temperatures. An increase in mirror elements reduced the thermal efficiency and increased the settling time to reach stagnant temperature [85]. Khan [165] studied the heat loss coefficient and stagnation temperature for an electroplated selective copper oxide coated absorber. Absorption was measured with an alpha meter. Emittance was measured with a thermopile, calibrated against a black body at 100 °C. Khan measured the heat loss by circulating heated water into the absorber at different steady state temperatures and measuring the steady state exit temperature. Negi et al. [166] evaluated the optical performance of black paint, selective cobalt oxide and selective MAXORB foil as absorber coatings and also studied the heat loss coefficient for each

coating. Larsen et al. [167] also researched the heat loss characteristics of a trapezoidal cavity receiver, demonstrating a good correlation between experimental and theoretical results, and a good agreement with results reported by Singh et al, Khan and Negi et al. Yanhua et al. [168] analysed an LFR with secondary CPC receiver, finding the transmissivity of the cover glazing, reflectivity of the CPC and emissivity of the insulation to be the major influences on the receiver's thermal performance.

The thermal performance of receivers has also been characterised and optimised using Computational Fluid Dynamic (CFD) techniques. With the aim of maximising thermal efficiency, Reynolds et al. [169] theoretically modelled the flow patterns of air in a trapezoidal cavity receiver using CFD and validated the results experimentally by photographing smoke patterns highlighted by quartz-halogen lights. They used electrical heaters to maintain a receiver temperature of 300 °C, and measured the heat loss from the power consumption. The National Renewable Energy Laboratory (NREL), U.S., applied a similar approach for measuring the heat loss of the Schott PTR70 receiver, which is currently used in most commercial PTC and LFR power generating facilities. The heat loss coefficient in their experimental set-up was determined by heating the absorber pipe with electrical heaters placed inside a copper pipe centred in the absorber pipe. The power required to maintain the absorber pipe at a steady state temperature, measured with thermocouples, was then recorded [170]. Facão and Oliveira [86] also applied CFD and ray-tracing techniques to optimise a trapezoidal cavity receiver for an LFR.

The optical properties of a receiver's absorbing surface have been the focus of many studies reported in the solar literature. The surface of a receiver requires a high solar radiation absorptance and low thermal emittance, with these properties remaining stable at high temperatures. Selectively coated surfaces, such as black nickel (NiS-ZnS) and stable nickel (Ni)-pigmented alumina (Al_2O_3), produced through electrolytic or chemical treatments are commonly used to achieve these properties [146]. A thin upper layer which is highly absorbent to shortwave solar radiation and transparent to longwave thermal radiation is deposited on a reflective surface with a low emissivity. Substrates typically used include aluminium and stainless steel. Konttinen et al. [171] characterized mechanically manufactured selective absorber surfaces using electron microscopy to determine surface groove width and a spectrometer to measure surface absorption and emissivity. A detailed review of solar absorber coatings has been reported by NREL [172].

The affects of mirror slope deviation errors and wind loads on solar thermal collectors have been reported. Heimsath et al. [173] used the Fringe Reflection Technique (FRT), a method used for measuring surface gradients, to investigate the optical characteristics of mirror elements in an LFR system. The FRT method requires a camera to record reflected patterns from a mirror, evaluating surface normals for each camera by phase measurement. They investigated various mirror elements and found a 1.2–4.5 mrad slope error from the ideal transversal slope, with maximum slope errors occurring at the edges of the mirrors. In the longitudinal plane, deviations were characterised by waviness. Mirrors fabricated for the Fresdemo project were also examined, and it was found that slope deviations caused by torsion in mounting errors were greater than those caused by gluing. Heimsath et al. [173] concluded that the slope errors observed are a typical characterisation of the mirror elements in an LFR, and that a Gaussian error distribution underestimates the mirror's optical quality due to the small statistical deviations in central areas. Due to the surface shape of the PTC and PDR, these collectors, rather than the LFR, have been at the focus of wind force studies. Wind loads on PTCs, PDRs and ground based heliostats have been investigated by Peterka et al. [174-176]. NREL have also investigated peak lift and drag forces and pressure distribution on PTCs in a wind tunnel [177].

The reviewed literature identified the experimental procedures commonly applied for determining the performance of an LFR. Specific measured parameters included the heat loss coefficient, thermal efficiency and stagnation temperature. The experiments to determine these parameters can be summarised as: HTF heat loss for known mass flow (heat loss coefficient), HTF heat gain for known constant DNI and mass flow (thermal efficiency) and HTF maximum temperature for known DNI and zero mass flow (stagnation temperature).

The aim of this chapter was to outline and validate models to predict the energy gained by an HTF in an LFR system, thus enabling a CSP plant utilising LFR technology to be modelled and controlled. In addition to the optical efficiency models already described in Chapters 3 and 4, theoretical models were presented to estimate the heat loss coefficient, thermal efficiency and stagnation temperature. The summarised experimental procedures were performed to enable comparisons to be drawn between measured and estimated results, and subsequently the validity of the theoretical models were assessed. The design and construction of the ELFR has been described followed by the experimental test set-up and methods.

5.2 Theory

This section describes the theoretical models to estimate the heat loss coefficient, thermal efficiency and stagnation temperature. The equations required to measure these values are also presented. As a result of these and previous models for the optical efficiency, the useful heat gained by an HTF in an LFR system can be calculated. Knowledge of the useful heat gained for specified DNI and HTF mass flow, enables the exit HTF temperature from a solar thermal field to be predicted. The ability to model and control the exit temperature from a solar field is essential as downstream processes will require specific working temperatures.

5.2.1 Heat loss coefficient

The heat loss coefficient, U_L, for a cavity receiver can be estimated from the sum of the radiation and convection heat losses from an absorber pipe to cover glazing and the conduction losses from the insulated sides. One approach commonly adopted in the literature is to consider the losses between two horizontal plates, a method known as parallel plate correlation [143].

$$U_L = U_{L1} + U_{L2} \tag{5.1}$$

The heat loss from the bottom of the receiver through convection and radiation, U_{L1}, and conduction of the insulated sides, U_{L2}, is given by,

$$\frac{1}{U_{L1}} = \left[\frac{1}{h_{cp} + h_{rp}} + \left(\frac{A_r}{A_{cg}}\right)\left(\frac{1}{h_{co} + h_{ro}}\right)\right] \tag{5.2}$$

$$\frac{1}{U_{L2}} = \frac{1}{\left(\frac{k_{gw}}{A_r/L}\right)} \tag{5.3}$$

where the heat loss from absorber pipe to cover glazing, h_{cp}, is calculated from,

$$h_{cp} = Nu_{cp}.\frac{k_a}{d_c} \tag{5.4}$$

$$Nu_{cp} = 0.27\left(Gr.\mathrm{Pr_{cp}}\right)^{0.25} \tag{5.5}$$

$$Gr = \frac{\beta g (d_c)^3 (T_p - T_c)}{\nu^2} \tag{5.6}$$

$$Pr_{cp} = \frac{\mu C_{pa}}{k_a} \tag{5.7}$$

where *Nu*, *Gr* and *Pr* are the Nusselt, Grashof and Prandtl numbers. Other parameters include kinematic viscosity, υ, specific heat, C_{pa}, thermal conductivity, k_a, and expansion coefficient, β, which are taken for the average absorber pipe temperature, T_p. Eq.(5.7) is calculated using values for the average cover glazing temperature, T_c. The heat loss from the outer cover glazing, h_{co}, is given by,

$$h_{co} = Nu_{co}.k_a/L_{co} \tag{5.8}$$

where,

$$Nu_{co} = 0.664 Re^{0.5} (Pr_{co})^{0.33} \quad (10^3 < Re < 2.6x10^5) \tag{5.9}$$

$$Re = \rho v L/\mu \tag{5.10}$$

$$Pr_{co} = \mu C_{pa}/k_a \tag{5.11}$$

Parameters including the Reynold number, *Re*, density, ρ, and dynamic viscosity, μ, are determined for T_c and T_a. The radiation losses from the receiver, h_{ro}, and between the absorber pipe and cover glazing, h_{rp}, are determined from,

$$h_{ro} = \sigma \varepsilon_c (T_c^2 + T_a)(T_c + T_a) \tag{5.12}$$

$$h_{rp} = \frac{\left[\sigma\left(T_p^2 + T_c^2\right)\left(T_p + T_c\right)\right]}{\left[\left(\frac{1}{\varepsilon_c}\right) + \left(\frac{1}{\varepsilon_p}\right) - 1\right]} \tag{5.13}$$

Therefore, the heat loss coefficient can be estimated using assumptions or measurements for T_p, T_c, T_a, and the emissivity of the cover glazing, ε_c, and absorber pipe, ε_p.

The heat loss coefficient can be measured from an HTF losing energy to the ambient (temperature drop from receiver inlet, T_{in}, to exit T_{exit}) and travelling at a known mass flow.

$$U_L = \frac{m_{sol} C_p (T_{in} - T_{exit})}{A_r (T_{avg} - T_a)} \tag{5.14}$$

The average fluid temperature, T_{avg}, is determined from,

$$T_{avg} = \frac{T_{in} + T_{exit}}{2} \tag{5.15}$$

5.2.2 Thermal efficiency

To predict the thermal efficiency of a solar collector, the exit fluid temperature for a given flow rate, needs to be calculated. This requires knowledge of the collector's flow characteristics, which can be modelled using a series of equations for the heat exchange or collector efficiency factor, *F'*, collector flow factor, *F''*, and heat removal factor, F_R [31, 32].

$$F' = \frac{U_0}{U_L} \tag{5.16}$$

$$U_o = \left(\frac{1}{U_L} + \frac{D_o}{h_{fi} D_i} + \frac{D_o ln\left(\frac{D_o}{D_i}\right)}{2k_{pipe}} \right)^{-1} \tag{5.17}$$

$$F'' = \frac{m_{sol} C_p}{A_r U_L F'} \left[1 - exp - \left(\frac{A_r U_L F'}{m_{sol} C_p} \right) \right] \tag{5.18}$$

$$F_R = F''.F' \tag{5.19}$$

where D_{ri}, D_{ro} and k_{pipe} are respectively the inside diameter, outside diameter and thermal conductivity of the absorber pipe. The heat transfer coefficient inside the pipe is notated as h_{fi}. The useful heat gain, Q_u, is determined from,

$$Q_U = F_R A_a \left[Q_{in} - \frac{A_r}{A_a} U_L (T_{in} - T_a) \right] \tag{5.20}$$

The end loss efficiency of the ELFR, $\eta_{endloss}$, is considered as the collector prototype is only 4 metres in length, therefore:

$$Q_{in} = DNI.\eta_{(\theta=0)}IAM(\theta_t.\theta_l).\eta_{endloss} \tag{5.21}$$

The fluid temperature rise, ΔT, for a given mass flow rate is calculated from,

$$\Delta T = T_{in} - T_{exit} = \frac{Q_u}{m_{sol}C_p} \tag{5.22}$$

thus the exit temperature and subsequently the thermal efficiency can be predicted for a known useful heat gain and HTF mass flow rate. Moreover, the HTF mass flow rate can be controlled to achieve a desired exit temperature. Iterative calculations are required as the heat loss coefficient, mass flow rate and useful energy gain are dependent on each other. The thermal efficiency is determined from,

$$\eta_{thermal} = \frac{m_{sol}C_p(T_{exit} - T_{in})}{DNI.\eta_{endloss}A_a} \tag{5.23}$$

Measurement of the thermal efficiency enables the optical efficiency to be estimated for a predicted heat exchange efficiency factor as the thermal efficiency is also given by,

$$\eta_{thermal} = F'\left[\eta_{0(\theta=0)}IAM - \frac{U_L A_r(T_{avg} - T_a)}{DNI.\eta_{endloss}A_a}\right] \tag{5.24}$$

thus,

$$\eta_{0(\theta=0)}IAM = \frac{\eta_{thermal}}{F'} + \frac{U_L A_r(T_{avg} - T_a)}{DNI.\eta_{endloss}A_a} \tag{5.25}$$

5.2.3 Stagnation temperature

The stagnation temperature is a useful parameter as it can be measured to enable estimated heat loss coefficient and optical efficiency values to be evaluated. The stagnation temperature of the ELFR is estimated from:

$$T_{r,max} = T_a + \frac{DNI.A_m\eta_{0(\theta=0)}.IAM.\eta_{endloss}}{U_L A_r} \tag{5.26}$$

5.3 Development of the ELFR

Using data gathered from the literature on LFRs and the finalised ELFR concept (Section 4.5), the components and assembly of the ELFR were initially designed in SolidWorks®, which is a comprehensive 3D modelling packing used for Computer Aided Design (CAD). Figure 5.1 shows a visualisation of the final design. Engineering drawings were produced for each individual component that required manufacturing (see Appendix 5). The author, technicians at Aston University and external companies fabricated the parts. A number of components were bought in, including 6 black nickel coated absorber pipes (joined to form three 4 m pipes), 16 linear actuators, 16 rail systems, 8 microswitches, 8 WH0.8-1 worms, and M0.8-50 wheels, 8 die cast aluminium enclosures, 16 ECLM-08-02 clip bearings, 8 stepper motors, 8 stainless steel 8 mm diameter 250 mm shafts, 32 KBRM-08 rod end bearings, 16 250x1930 mm acrylic mirrors, 4 320x4000 mm stainless steel mirrors and a number of Item® MB System components. Exploded component assembly views with bill of materials are presented for the motor, receiver and element row sub-assemblies in Appendix 6. The details of the design and construction of the ELFR's frame, concentrator elements and receiver are now individually discussed. The software tools used for design modelling, simulation and control will also be described.

Figure 5.1: SolidWorks representation of the ELFR prototype.

5.3.1 The frame

The 4.0x2.5x3.2 m frame was constructed from the Item® Machine Building (MB) kit system [178], comprising high tensile aluminium profiles and fastening elements. The MB kit has been used in a wide range of applications for constructing machinery, jigs and complete assembly production lines. It was chosen for this project because of its assembly flexibility and modular nature, which overcame the problems of restricted access onto the roof and the unavailability of welding and heavy lifting equipment. While the MB kit was suitable for the development of a prototype, alternative more cost effective materials would be used for a final product.

Wind force calculations were performed to determine the weight required to secure the frame from lift and tipping forces under wind speeds of 80 mph (36 m/s) – the maximum gust wind speed recorded in The Midlands, UK [179], detailed calculations are presented in Appendix 7. Consequently the frame was secured onto 36 concrete paving slabs that had a combined weight of approximately 1 tonne. The receiver tower was tethered down to the frame extremities using 8 galvanised steel guy cables, which were sized according to the cable tension expected for wind speeds of 80 mph.

5.3.2 The concentrator elements

The mechanisms of the concentrator elements for the ELFR were designed to enable solar tracking by controlling the angle and height of the mirror elements. The mirror elements were made from acrylic mirror, rather than glass, for safety purposes. However drawbacks from using acrylic mirror arise as the surface can be wavy, scratched easily and degraded in ultraviolet light. To protect the mirror coating and increase rigidity, marine plywood and aluminium profiles were glued to the back using C.T.1 Sealant and Construction Adhesive [180]. The mirror elements were then secured to the aluminium frame with polymer bearings (Igubal® rod end and clip bearings [Igus]). Polymer bearings are ideal for solar applications as they are maintenance free and durable. Each element row was rotated by a low cost stepper motor [191-8356 RS Components] and worm wheel assembly [HPCGears], placed inside a die cast aluminium enclosure [517-3434 RS Components]. Elevation was achieved through the use of a parallel pair linear actuator system (LA35 actuators and TR-EM-239 parallel drive unit [Linak]) with Hall sensors for feedback positioning; a pair of linear rails were used to keep the frame rigid (DryLin® W linear guide system [Igus]), see Figure 5.2. Address communication control boards for the stepper motor and actuator system were designed and developed with the help of O.N.

Igobo, and were placed inside IP 66 rated enclosures (see Figure 5.3). Through the use of an encoder and decoders, a single signal cable was used to drive the stepper motors. Another signal cable was used to send forwards, backwards, stop and home commands to the TR-EM-239 actuator driver (see Figure 5.4). Appendix 8 shows the control board circuit schematics for the encoder, stepper motor decoder and driver, and the actuator decoder and controller. Power was supplied to the collector by means of a single 13 amp cable.

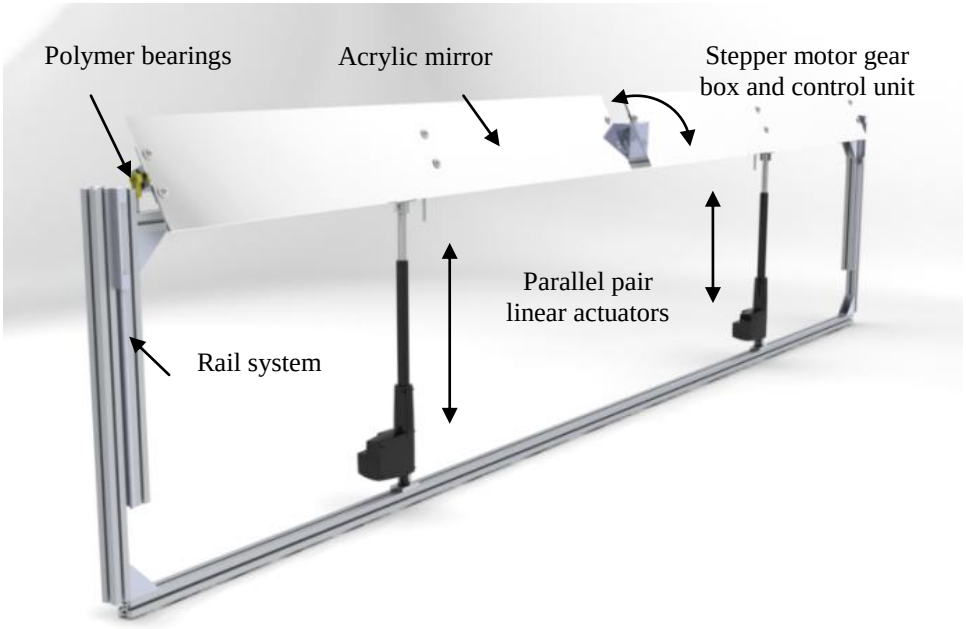

Figure 5.2: Concentrator row design details.

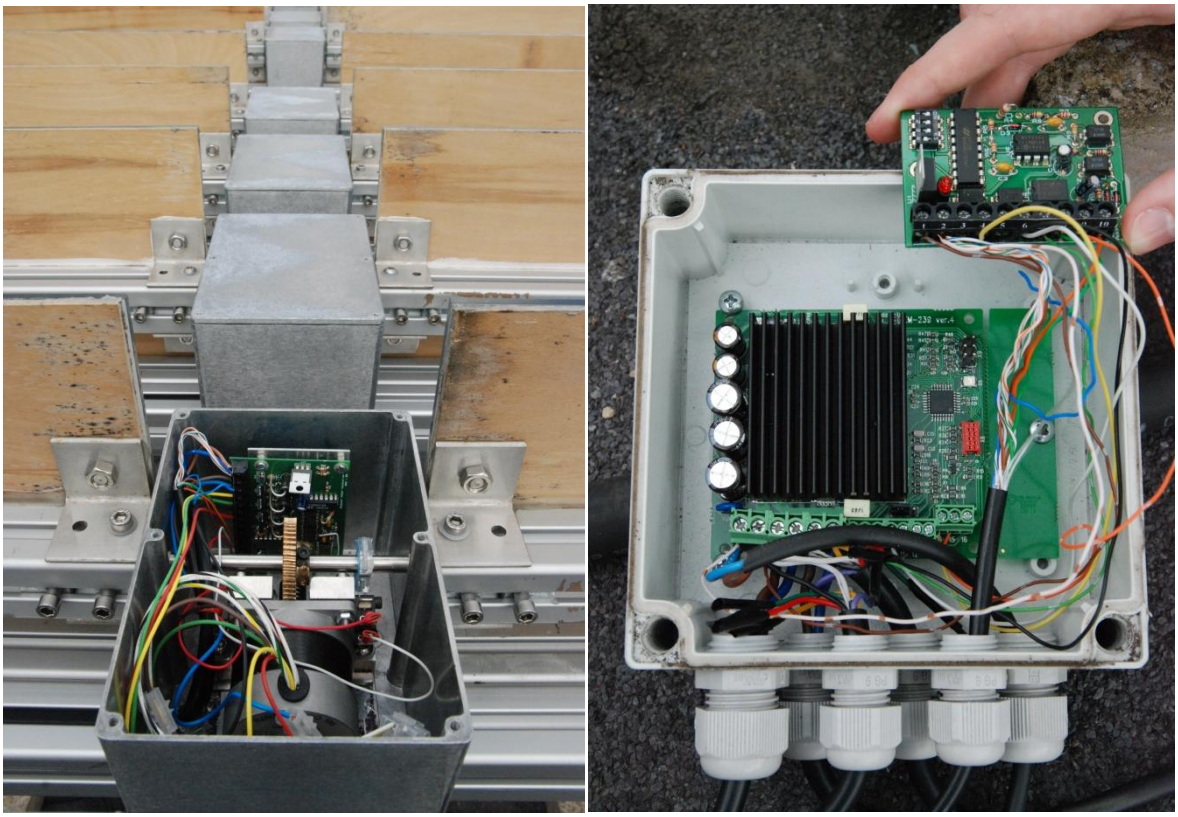

Figure 5.3: Address communication control boards placed inside the motor (left) and actuator (right) enclosures.

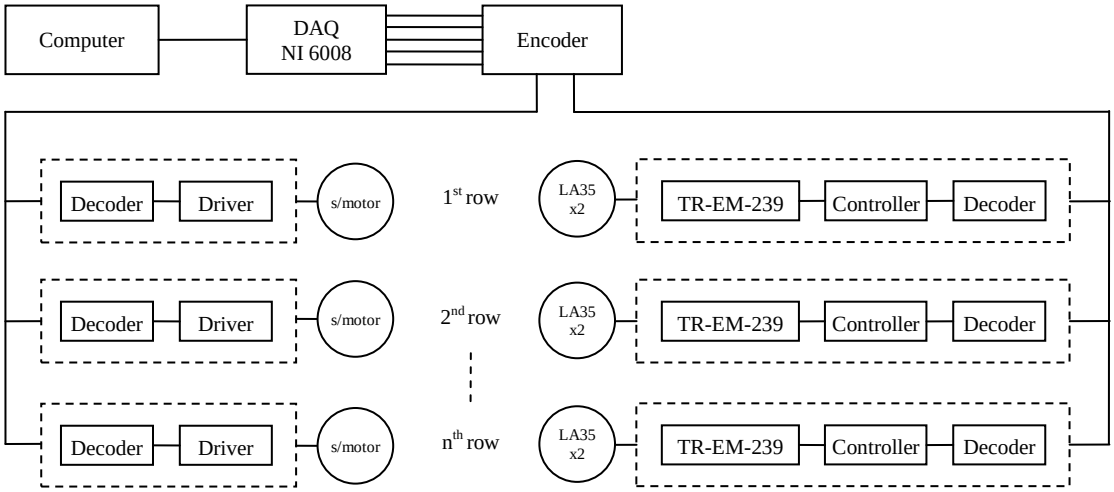

Figure 5.4: Control arrangement for the ELFR's stepper motors and linear actuators.

A tracking algorithm was developed by the author in LabVIEW to control the individual mirror element's angle and elevation. Each mirror element's slope angle and elevation height – to maintain focus on the receiver while avoiding shading and blocking – was determined sequentially from adjacent elements positions, geometrical position in respect to the receiver, site location (sun-earth geometry) and solar time. The flow logic of the control procedure is represented in Figure 5.5.

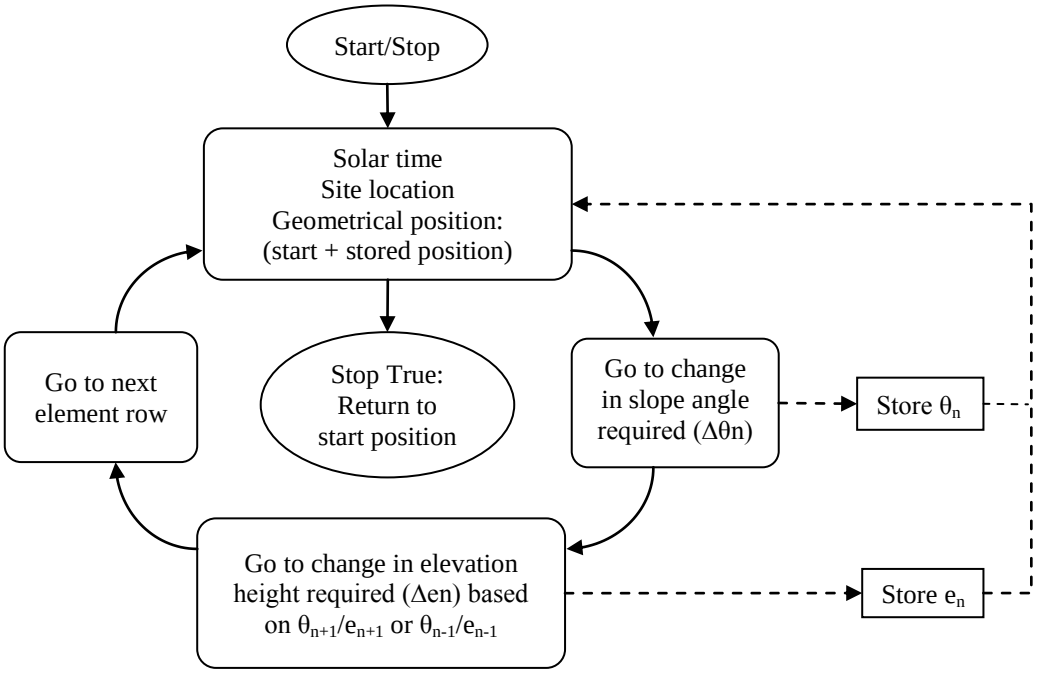

Figure 5.5: Element tracking control logical flow diagram.

The number and width of the mirror elements were chosen by analysing the potential cost per exergy. Eight to sixteen rows with mirror widths of 120 mm, 170 mm and 250 mm were considered (see Figure 5.6). With each additional mirror's contribution to the absorber surface decreasing (due to increased cosine losses, reduced effective aperture area, limited range of elevation to remove blocking and shadowing), the indicated number and width of the mirror elements were 8 and 250 mm. It was found that for mirror widths greater than 250 mm, curved mirrors would have been required to avoid an oversized CPC receiver.

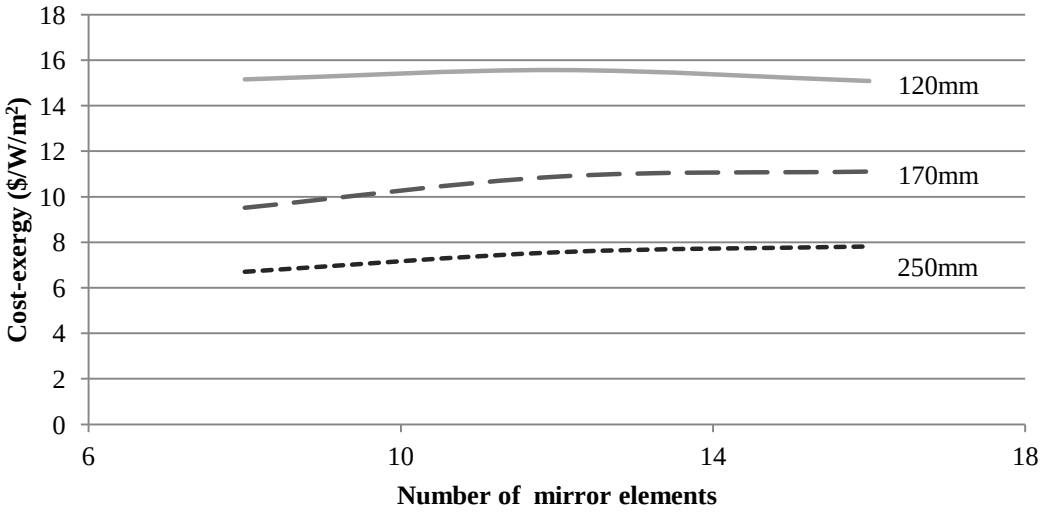

Figure 5.6: The cost per exergy of the ELFR with alternative number and width of mirror element cost per exergy.

5.3.3 The CPC cavity receiver

The cavity receiver designed and implement for the ELFR comprised a secondary CPC, 3 absorber pipes and a cover glazing. The CPC profile was formed from aluminium sections to support and shape a highly reflective stainless steel sheet (reflectivity ≈ 95%). Having reviewed the typical material properties and sizing of receivers, the absorber pipes were aluminium coated in a lacquered dull black nickel (absorption ≈ 90%, emissivity ≈ 0.17) and the cover glazing was made from 6 mm clear cast acrylic (transmittance ≈ 96%, emissivity ≈ 0.88). The absorber pipes were also insulated with a reflective insulation sheet and fibre glass wool. As mentioned in the previous chapter, the receiver tower's height was reduced for the prototype to 2.5 m, which resulted in a concentration ratio of 10, rather than 30. A cross section schematic of the CPC receiver is shown in Figure 5.7.

A secondary concentrator in the form of a compound elliptical non-imaging concentrator, typically referred to as a CPC, is often utilised for an LFR, due to the potential increased concentration ratio. The CPC is designed so that rays within a specified half acceptance

angle are focused onto a target area. A smaller half acceptance angle, θ_c, results in a greater CPC concentration ratio, C_i, where the ratio is given by the aperture entrance, a, to the target width, a'.

$$C_i = \frac{1}{\sin\theta_c} = \frac{2a}{2a'} \tag{5.27}$$

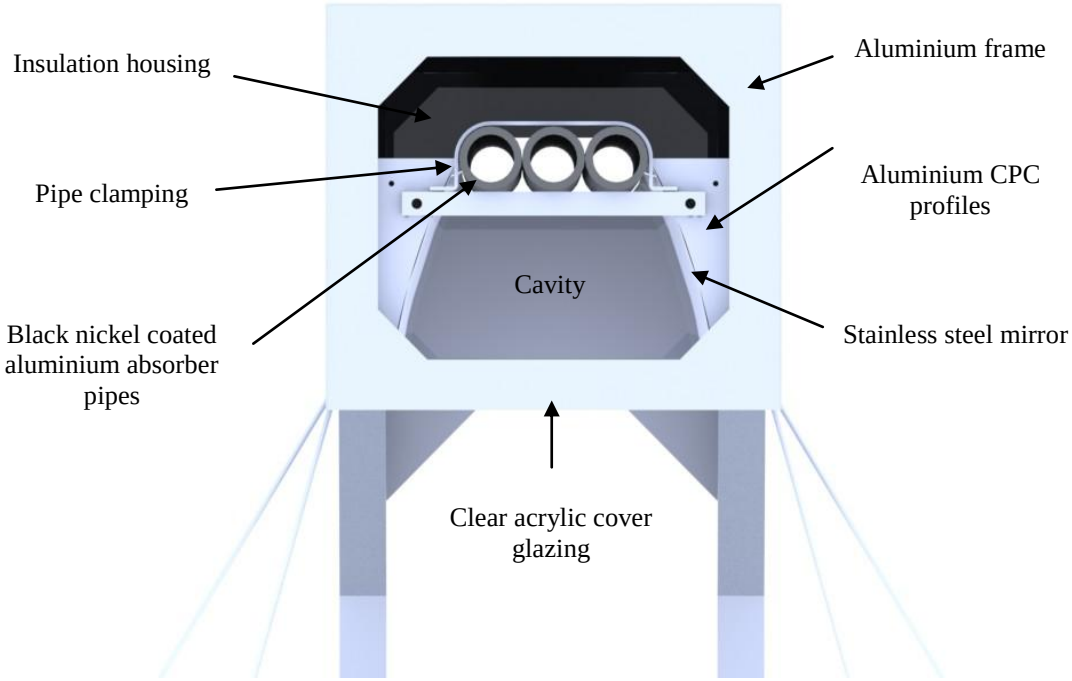

Figure 5.7: Section view of the CPC cavity receiver.

Increasing the height of the CPC from the concentrator decreases the approaching edge ray angle, thus increasing C_i. However, care needs to be taken when designing a CPC as geometrical factors, such as the depth, d, and surface area per unit depth, A_{RT}, can become unsuitably excessive. A truncated CPC is often employed as the truncated depth, d_T, can be as much as a half of the original depth with only a small reduction in C_i [32]. The equations for designing a truncated CPC, and determining the number of internal reflections, n_i, are given below, as specified by Welford and Winston (see Figure 5.8) [112].

$$f = a'(1 + \sin\theta_c) \tag{5.28}$$

$$a = \frac{a'}{\sin\theta_c} \tag{5.29}$$

$$d = \frac{f\cos\theta_c}{\sin^2\theta_c} \tag{5.30}$$

$$a_T = \frac{f\sin(\theta_T - \theta_c)}{\sin^2(\theta_T/2)} - a' \tag{5.31}$$

$$d_T = \frac{f\cos(\theta_T - \theta_c)}{\sin^2(\theta_T/2)} \tag{5.32}$$

$$\frac{A_{RT}}{2a_T} = \frac{f}{a_T}\left[\frac{\cos(\varphi/2)}{sin^2(\varphi/2)} + \ln\cot(\varphi/4)\right]\Bigg|_{\theta_c+\pi/2}^{\varphi_T} \tag{5.33}$$

$$n_i = max\left[C\frac{A_{RT}}{4a_T} - \frac{x^2 - cos^2\theta}{2(1+\sin\theta)}, 1 - \frac{1}{C}\right] \tag{5.34}$$

$$x = \left(\frac{1+\sin\theta}{\cos\theta}\right)\left(-\sin\theta + \left(1 + \frac{d_T}{d}cot^2\theta\right)^{1/2}\right) \tag{5.35}$$

The width of the focal point at the CPC aperture, termed the band of illumination, can be calculated for a known number of mirror rows with specified width and spacing. Mathur et al. [129] determined the band of illumination, r_n, from an LFR's mirror elements at solar noon by calculating a central band of light, r_c, from non-diverging rays and bands of light to the right, r_r, and left, r_l, from diverging rays.

Figure 5.8: Schematics of a secondary CPC [32].

$$r_n = r_c + r_y + r_l \tag{5.36}$$

$$r_c = W cos\theta_n sec2\theta_n \tag{5.37}$$

$$r_r = \left(\frac{Q_n + W cos\theta_n - \frac{W}{2} cos\theta_n sec2\theta_n}{sin2\theta_n} \right) \frac{sin0.27}{\cos\left(2\theta_n - 0.27\right)} \tag{5.38}$$

$$r_l = \left(\frac{Q_n + \frac{W}{2} cos\theta_n sec2\theta_n}{sin2\theta_n} \right) \frac{sin0.27}{\cos\left(2\theta_n - 0.27\right)} \tag{5.39}$$

By calculating the edge ray angle and band of illumination, which is dependent on the CPC's height from the concentrator, the CPC can be designed and positioned to achieve a target concentration ratio. As a design check, ray-tracing can be used to verify the CPC geometry; this is shown graphically for the CPC receiver designed for the ELFR (see Figure 5.9).

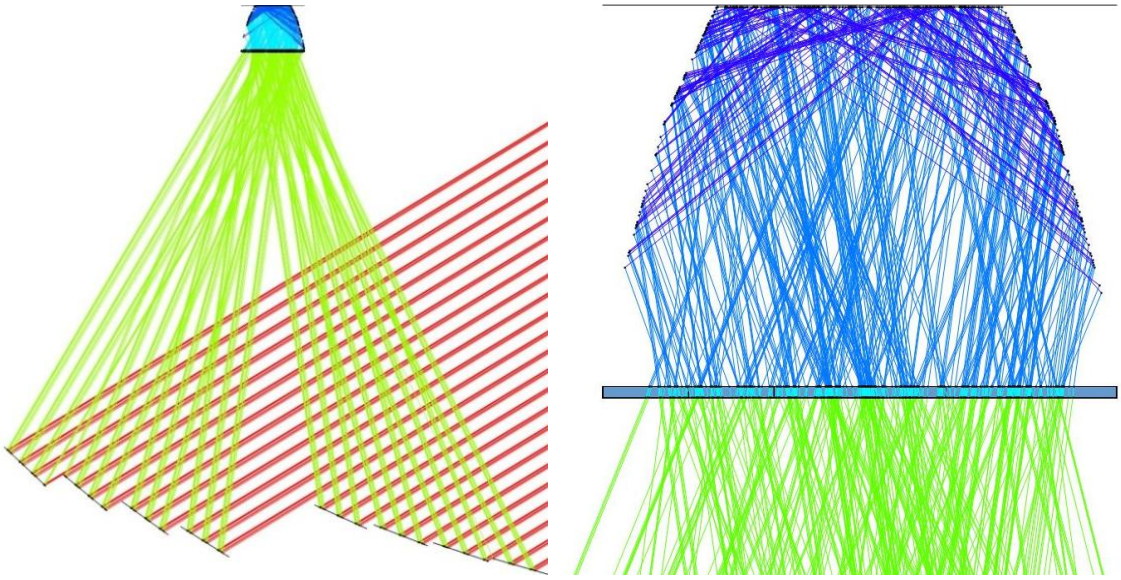

Figure 5.9: Rays being focused into a CPC cavity receiver by elevated mirror elements (Optica).

5.4 Experimental set-up

The ELFR was installed on the roof of Aston University (a shadow-free location) with a north-south axis east-west tracking orienting. Water was used for an HTF and was circulated through the three absorber pipe in series. The water circulation system included

a 145 litre stainless steel direct open vented cylinder fitted with a 3 kW immersion heater and thermostat, 115 litre cold water header tank, Grundfos 15-60 domestic circulating pump, G 3/8 2-30 l/min turbine flow metre (+/-3% accuracy), 5/8 OD steam hose, valves, copper pipes and pipe fittings. The receiver was fitted at the inlet and exit with pipe probe type K thermocouples (+/-1.0 °C accuracy). The set-up is delineated in Figure 5.10. Temperature values were logged using a National Instrument® (NI) 9178 chassis DAQ (data acquisition) with NI 9211 module. The mass flow rate was logged with a NI USB-6009 DAQ. Vents were located before and after the receiver so that air could be removed from the system and therefore the system was not pressurised (see Figure 5.11).

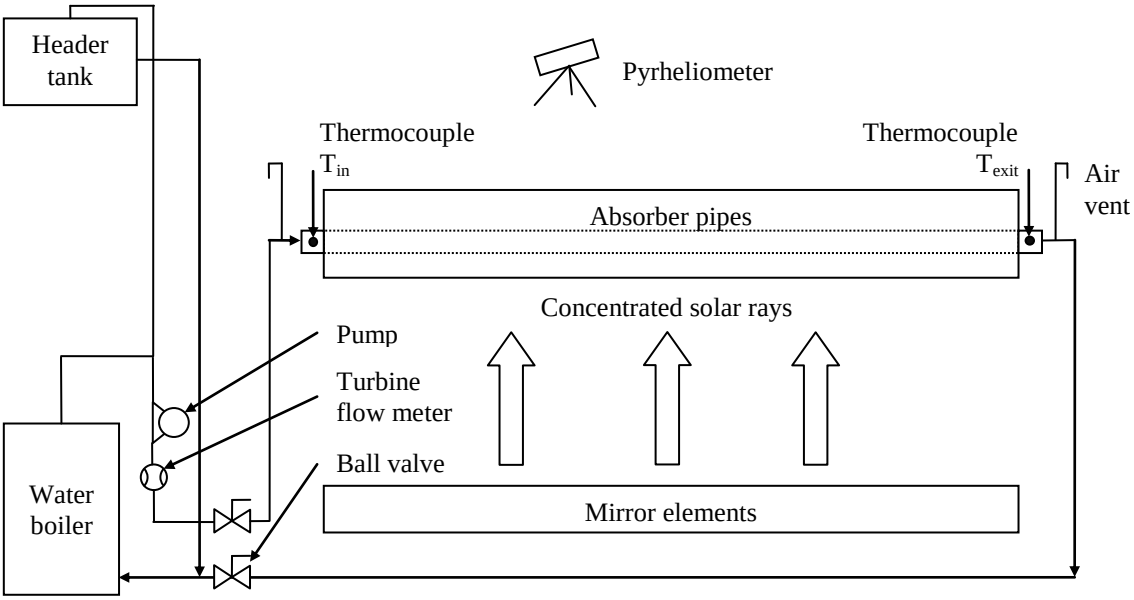

Figure 5.10: The ELFR experimental equipment set-up for measuring an HTF's inlet and exit temperature.

The DNI was measured using a pyrheliometer, which is the designated instrument by the International Standard ISO 9060 and the World Meteorological Organization (WMO) with which to measure direct solar radiation. The pyrheliometer used was Kipp and Zonen's CHP 1, and is an instrument compliant with ISO 9060, calibrated at the World Radiation Centre (WRC) in Switzerland (calibration certificate can be found in Appendix 9). The pyrheliometer works by providing a voltage, U_{emf}, which is proportional to the measured irradiance. A constant required in the measurement is the sensitivity, S, which is unique to each device. The DNI measurement is given by U_{emf}/S. The sensitivity of the pyrheliometer used was 8.06 μV/W/m^2. Irradiance values were logged using the NI 9211 as the module has a 24 bit resolution with +/-80mV range.

The tracking accuracy required for the CHP 1 pyrheliometer is within 0.75° of the normal. Therefore precise solar tracking is required. This was achieved through the use of a telescope tracker, the EQ3 Pro SynScan Computerised Go-To Equatorial Mounting System (see Figure 5.12). The stated positioning accuracy of the EQ3 is up to 1 arc minute, i.e. less than 0.02 degrees.

Figure 5.11: The ELFR connected to a water supply by means of a steam hose. The mirror elements were regularly cleaned using distilled water, as depicted.

Figure 5.12: Kipp and Zonen CHP 1 pyrheliometer (left) and the EQ3 equatorial mounting system (right).

Figure 5.13: An aerial view of the ELFR (left) and the illuminated receiver during operation (right).

5.5 Experimental procedure

Different HTF inlet temperatures were produced by preheating the water in the cylinder and controlling the thermostat; the inlet temperature was limited to a maximum temperature of 65 °C. The HTF flow rate was controlled and maintained by means of the ball valves and the pump's variable speed control. The flow rate was measured with the turbine flow metre (a Hall sensor) and recorded with a counter on the NI USB-6009 DAQ. The fluid inlet and exit temperatures were recorded with the NI 9211 to determine when the system had stabilised and achieved a steady state. Average fluid temperatures were determined from Eq.(5.15). To measure the heat loss coefficient, the ELFR was not focused, i.e. zero solar input, and the steady state temperature drop from inlet to exit was recorded. The cover glazing and pipe temperatures were also measured with type K thermocouples. The pyrheliometer was used to measure the ambient temperature.

The thermal efficiency was also measured for different HTF inlet temperatures. Steady state inlet and exit temperatures values were again recorded, this time with the ELFR focused (Figure 5.13) and experiments performed during approximately constant solar

conditions (DNI was measured with the pyrheliometer, attached to the EQ3 set to solar tracking). All experimental values were averaged over a period of steady state operation. The stagnation temperature was measured at solar noon with the pump turned off, valves closed and the collector having been focused for several hours to achieve a maximum stable receiver temperature. For safety reasons, the system was not pressurised; therefore, temperatures above 100 °C could not be achieved as at this point the HTF (water) boiled. To overcome this difficulty when it occurred, only one-half of the collector's mirrors were focused, resulting in a concentration ratio of 5 instead of 10.

5.6 Results: predictions and experimental measurements

5.6.1 Heat loss coefficient

On 19th – 23rd March 2012 a series of experiments were carried out to measure and estimate the ELFR's heat loss coefficient for average fluid temperatures in the range of 30–65 °C (see Figure 5.14a-c). In this temperature range, the difficulty with measuring the heat loss was evident by widely varying results, ranging from 8.6 – 18.8 W/m^2°C (see Figure 5.15). This is attributed the low receiver temperatures, as measurement inaccuracies of the type K thermocouples and flow meter will have had a significant effect of the measured heat loss, illustrated by the error bars of Figure 5.15. Using the ambient and cover glazing temperature measurements the receiver's heat loss coefficient was estimated to increase from 2.9 – 3.42 W/m^2°C, which was a 66.3% to 81.8% decrease in comparison to the measured heat loss values (8.6 – 18.8 W/m^2°C).

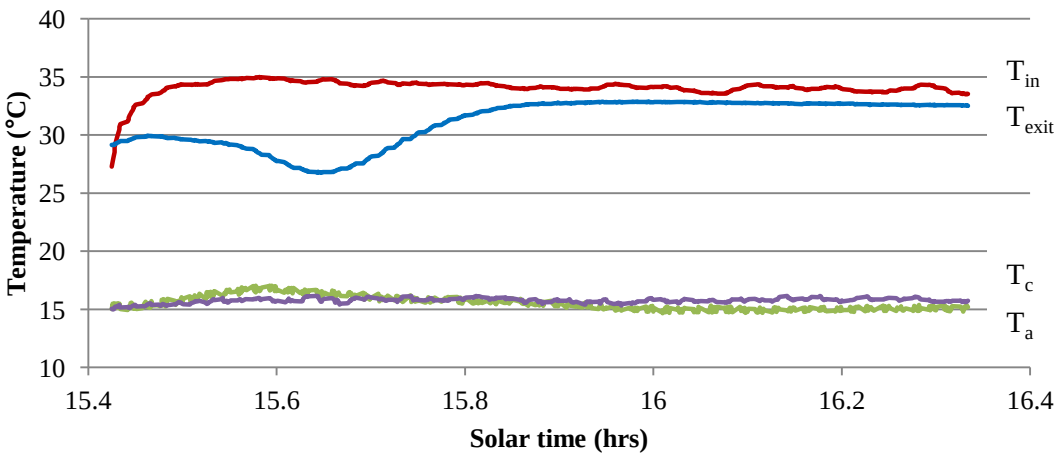

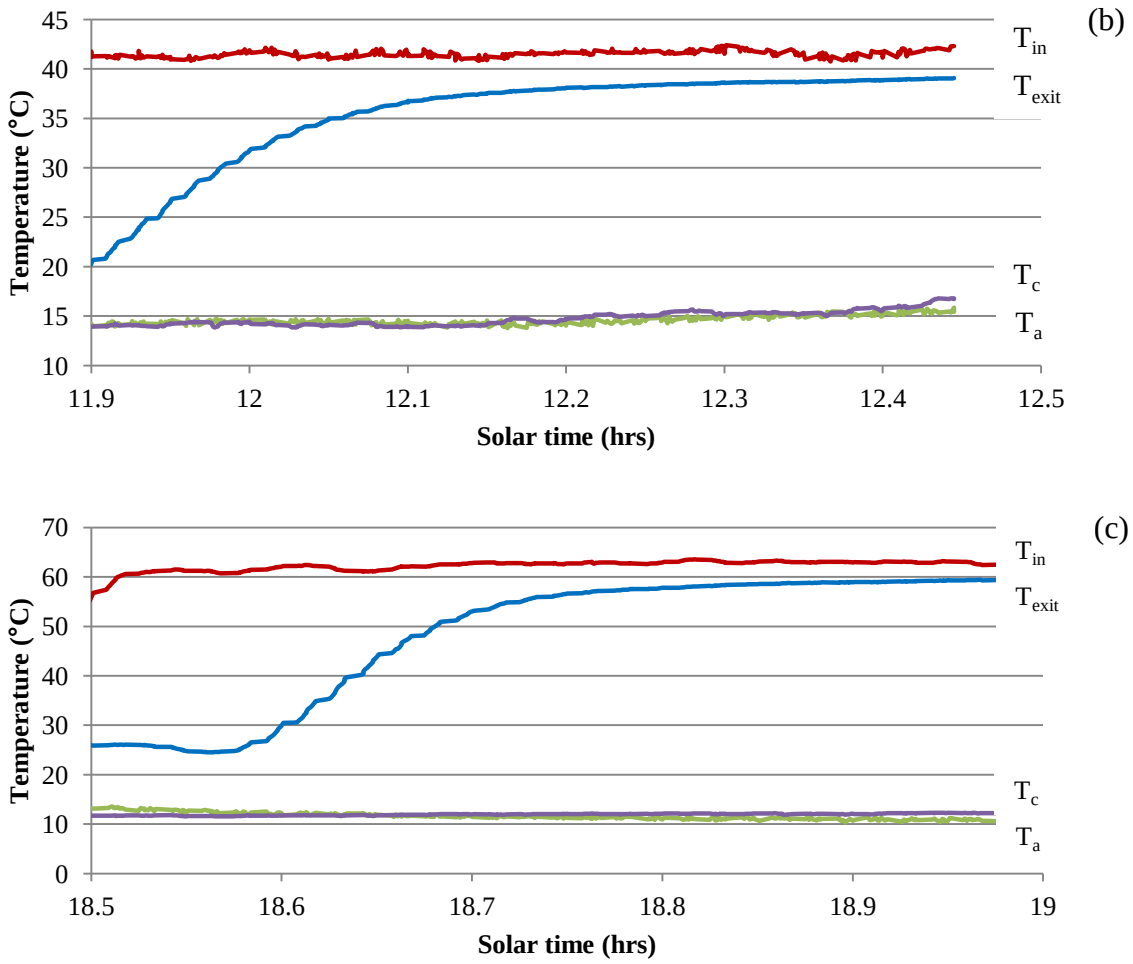

Figure 5.14a-c: Shows the ELFR receiver achieving a steady state inlet and exit temperature for an average fluid temperature of (a) 33 °C (b) 40 °C and (c) 60 °C. The ambient and average cover glazing temperatures are also plotted.

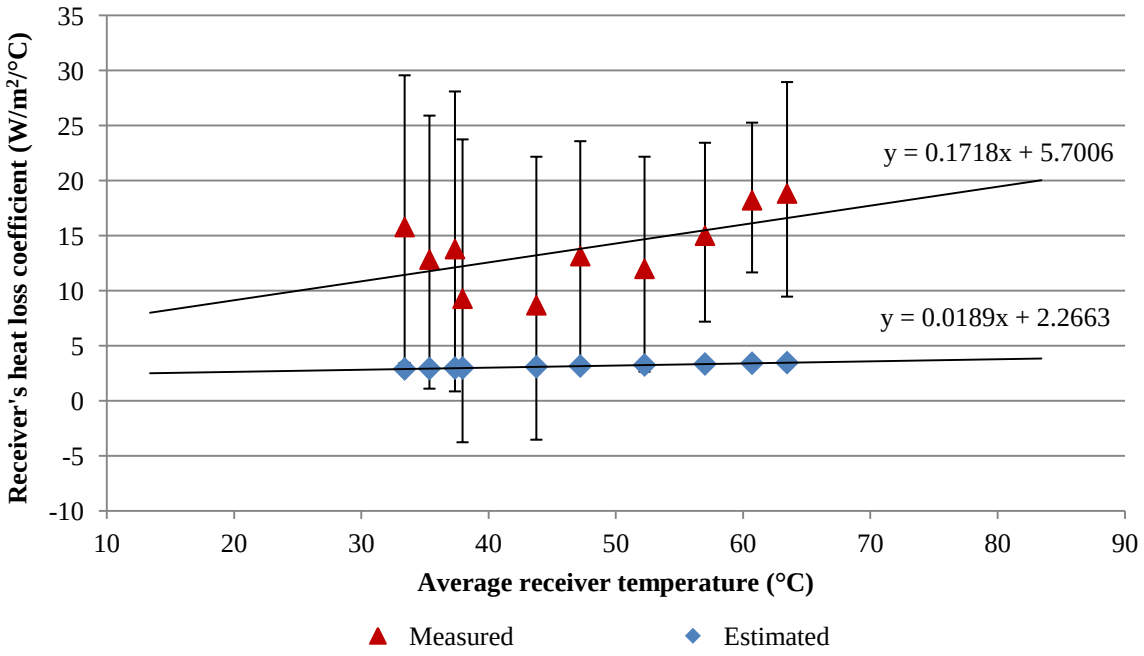

Figure 5.15: Shows the measured and estimated heat loss coefficient for the ELFR's receiver.

5.6.2 Thermal efficiency

On 27th March and 21st – 25th May 2012 at varying times of day, a series of experiments were performed during relatively constant solar conditions (DNI variation of less than 50 W/m^2) to measure the fluid temperature gain for different inlet temperatures. Measured values for the solar conditions, HTF mass flow, ambient, inlet and exit temperatures, thermal efficiency and derived optical efficiency are tabulated in Table 5.1. Figure 5.16a–c shows example results for average fluid temperatures of 38 °C, 45 °C and 55 °C. For the same solar and inlet temperature conditions, and using the ray-tracing model for an incident angle dependant optical efficiency (determined in the previous chapter, Figure 4.8a–b) and heat loss coefficient, the HTF exit temperature and consequently the thermal and optical efficiencies were predicted using the outlined flow characteristic equations presented in Section 5.2.2 (see Table 5.2).

Table 5.1: Measured HTF exit temperatures and resulting thermal efficiencies for the ELFR receiving varying DNI and HTF inlet temperatures. The IAM dependant optical efficiencies based on the measured thermal efficiencies and heat loss coefficients are also tabulated.

DNI	θ_t	θ_l	U_L	T_a	T_{in}	m_{sol}	T_{exit}	$\eta_{(\theta=0)}$.IAM	$\eta_{thermal}$
W/m^2	°	°	W/m^2°C	°C	°C	kg/s	°C	%	%
668	47.2	48.7	8.12	13.0	15.8	0.12	19.5	71	70
682	9.6	49.4	7.99	17.2	37.7	0.15	39.3	61	59
798	38.7	49.4	8.03	21.9	41.1	0.14	43.3	52	50
839	2.8	50.2	8.00	18.3	45.1	0.14	46.9	55	52
743	30.3	49.2	8.01	18.8	48.5	0.15	50.4	53	50
812	21.4	31.1	7.94	24.4	52.7	0.41	53.5	33	31
814	41.6	49.8	8.06	20.5	54.5	0.15	57.2	55	52
576	52.3	48.4	7.97	19.4	61.4	0.17	62.6	36	32
726	63.4	48.7	8.02	20.3	63.5	0.15	726	63	49

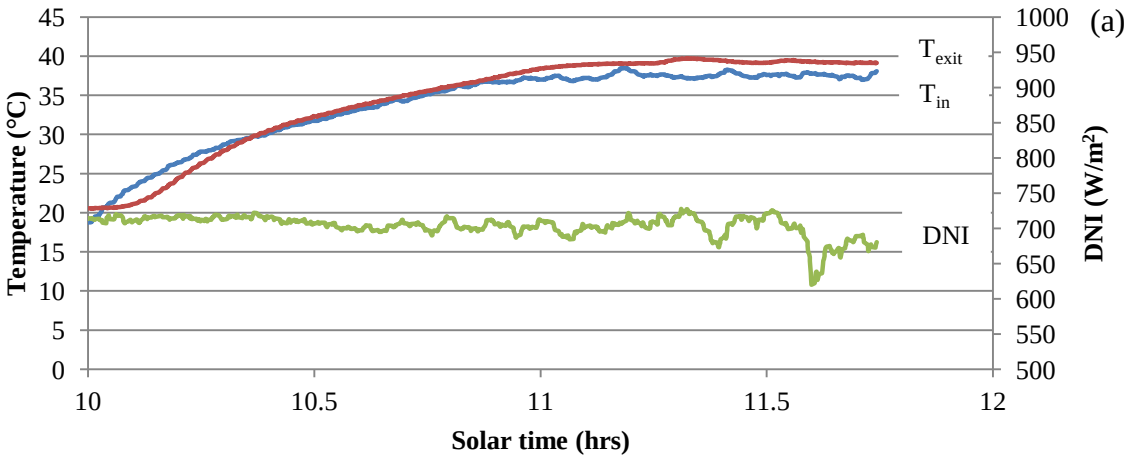

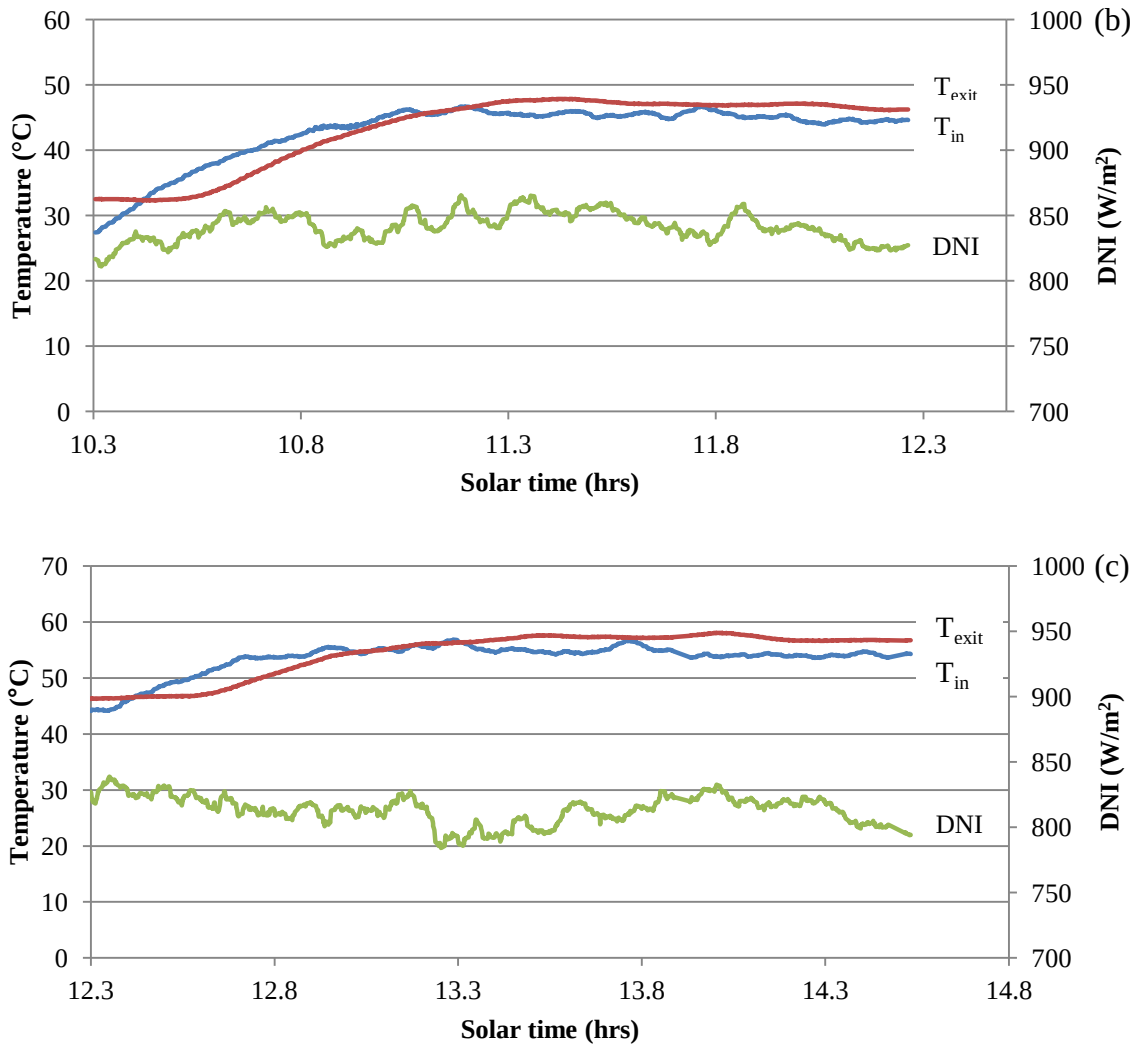

Figure 5.16a-c: Shows the ELFR receiving DNI and reaching a steady state exit temperature for an inlet temperature of (a) 38 °C (b) 45 °C and (c) 55 °C.

Table 5.2: Predicted HTF exit temperatures and resulting thermal efficiencies for the ELFR receiving varying DNI and HTF inlet temperatures. The IAM dependant optical efficiencies based on the ray-tracing model (Figure 4.8a-b) and estimated heat loss coefficients are also tabulated.

DNI	θ_t	θ_l	U_L	T_a	T_{in}	m_{sol}	T_{exit}	$\eta_{(\theta=0)}$.IAM	$\eta_{thermal}$
W/m^2	°	°	W/m^2°C	°C	°C	kg/s	°C	%	%
668	47.2	48.7	2.59	13.0	15.8	0.12	18.5	0.52	0.51
682	9.6	49.4	2.99	17.2	37.7	0.15	39.0	0.52	0.50
798	38.7	49.4	3.07	21.9	41.1	0.14	43.5	0.56	0.54
839	2.8	50.2	3.14	18.3	45.1	0.14	47.0	0.56	0.55
743	30.3	49.2	3.20	18.8	48.5	0.15	50.4	0.53	0.51
812	21.4	31.1	3.28	24.4	52.7	0.41	54.2	0.56	0.54
814	41.6	49.8	3.32	20.5	54.5	0.15	57.1	0.53	0.51
576	52.3	48.4	3.44	19.4	61.4	0.17	63.2	0.50	0.48
726	63.4	48.7	3.49	20.3	63.5	0.15	66.2	0.43	0.41

Predicted and measured HTF exit temperatures are compared in Figure 5.17, showing a strong correlation between results with a less than 5% deviation. The difference between the measured and predicted thermal efficiency values was more substantial (-38.8% to +31.0%). Figure 5.18 shows that in comparison to the ray-tracing model prediction the optical efficiency estimate (based on the thermal efficiency measurement) had a similar difference of -23.2% to +31.9%.

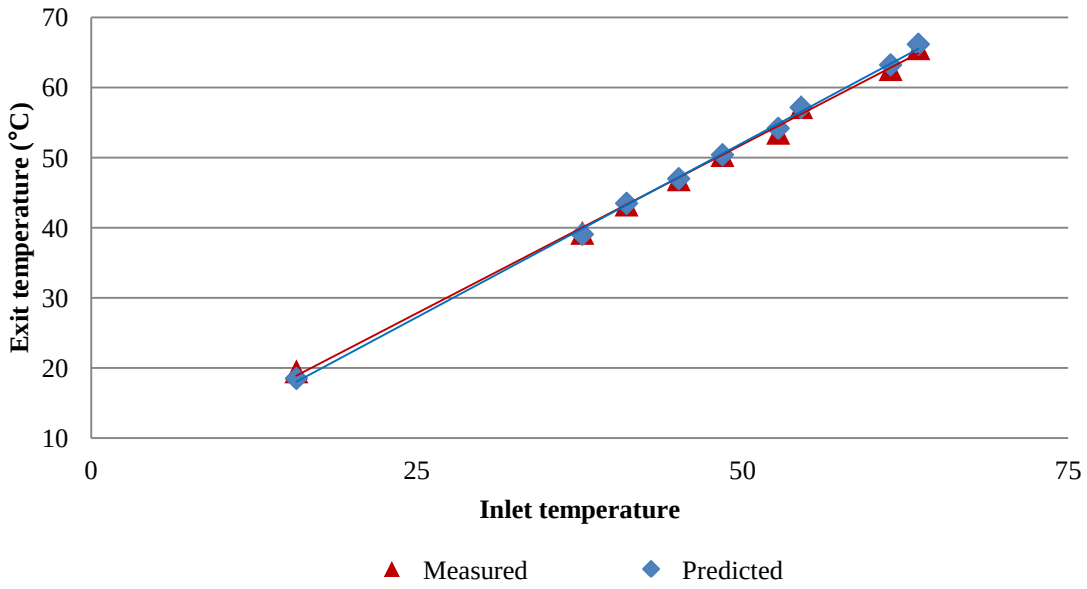

Figure 5.17: The measured and predicted exit temperatures for a range of inlet temperatures to the ELFR receiving DNI in the region of 750 W/m^2.

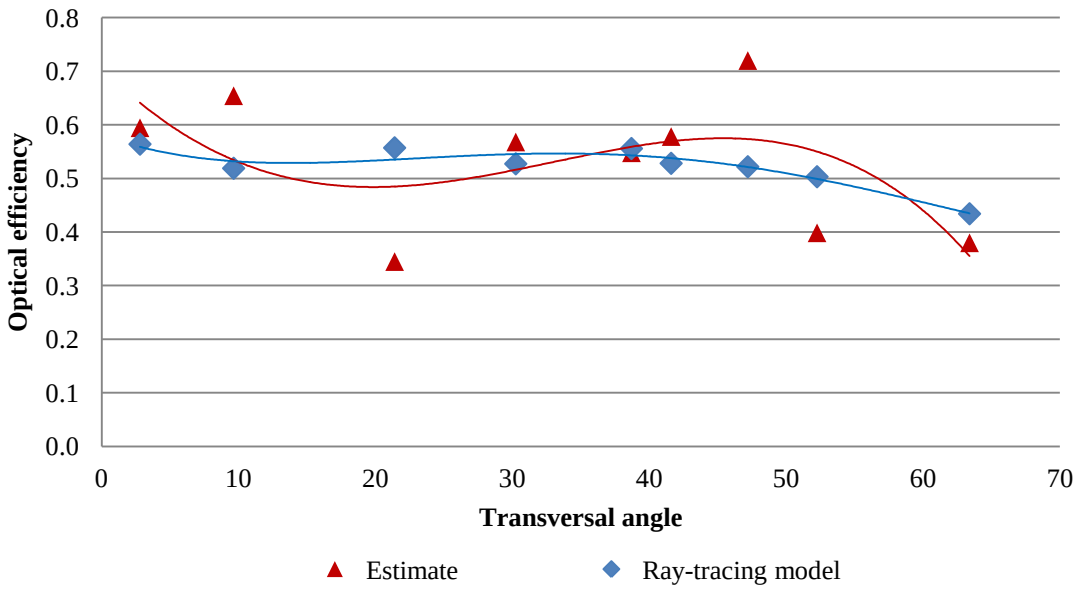

Figure 5.18: The optical efficiency estimate (based on measured thermal efficiency) and ray-tracing model prediction plotted against the transversal angle.

5.6.3 Stagnation temperature

On 25th May 2012 from 8 a.m. to solar noon, an experiment was carried out with one-half of the ELFR receiving around 760 W/m^2 of DNI and pipe, inlet and exit temperature measurements recorded. Maximum temperatures of 80–90 °C were achieved at solar noon, thus indicating the ELFR's stagnation temperatures (see Figure 5.19). The fluctuating results seen in Figure 5.19 were attributed to the temperature gradients between the bottom and top of the pipe, varying DNI, changing sun position (frame shadows and IAM) and the formation of bubbles as the water neared boiling point. In comparison, for the same solar conditions the predicted stagnation temperature was 110 °C, i.e. a 22–38% increase in comparison to the measured stagnation temperature.

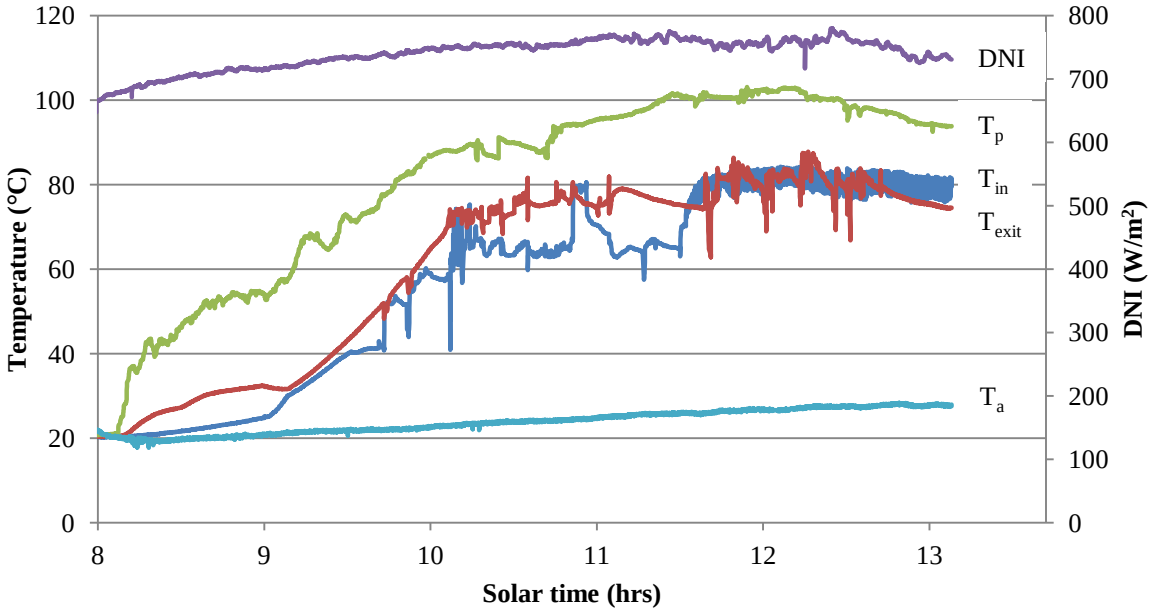

Figure 5.19: Measured inlet, exit, pipe and ambient temperature for determining the stagnation temperature at solar noon for a DNI of 760 W/m^2.

5.7 Discussion

Measured values for the heat loss coefficient indicated that the parallel plate correlation model underestimated the heat loss coefficient. This was not unexpected as the model did not take into account the receiver's end heat losses. Other authors have also reported that experimental values were higher than those predicted by parallel plate correlation, 27–37%, however these error margins have been considered as acceptable [143]. The estimated heat loss trend based on the average receiver, cover glazing and ambient temperatures demonstrated a good correlation (less than 10 % deviation) to those measured

and estimated for similar receiver types by Singh et al. [143], Khan [165], Negi et al. [166] and Larson et al. [167].

Experimental measurements for the thermal efficiency and stagnation temperature had a reasonable agreement with the theoretical predictions. The thermal efficiency was determined by modelling and measuring the HTF (water) exit temperature. Measured values for the collector's HTF exit temperature correlated strongly with model predictions, giving only a -1% to +5% difference. However, due to the low temperature range of the experiments, this small error in temperature measurement had a significant effect on the deviation between the measured and predicted thermal efficiency (-38.8% to +31.0%) and, therefore, also the optical efficiency (-23.22% to +31.9%). The measured stagnation temperature was 18% to 27% lower than predicted values. This was attributed to the underestimated heat loss coefficient and an overestimated optical efficiency as the ray-tracing model did not take into account mirror surface shape errors, mirror degradation, accumulation of dirt on the cover glazing and mirrors, and tracking and alignment errors.

From construction of the prototype it was learnt that one of the most difficult mechanics to achieve was a rigid and accurate method for rotating the mirror elements. The developed program and stepper motors used to drive the mirrors worked well; however backlash and movement occurred in the worm and wheel assembly and bearings. The linear rails and actuators used for elevating the mirror elements performed well; being precise (within +/- 0.4 mm) and rigid during high winds. The secondary CPC was shaped using multiple CPC profiled supports at 500 mm intervals; however the mirror was fractionally distorted between the profiles. An alternative approach will therefore be required to manufacture and shape the CPC to improve its effectiveness. The MB kit frame performed as expected being durable and rigid; however, a drawback was that assembly times were long at 2 – 3 weeks. Though the MB kit was ideal for the prototype, faster installation and lower cost solutions would be required for a final product. Careful handling of the custom absorber pipes was required to protect the absorber coating. For a final product with a concentration ratio in the region of 30, higher temperatures will be achieved and therefore a stable coating needs to be chosen. The best coating is still an open problem with a range of materials and manufacturing techniques available, including spluttering, and multi layer selective and cement coatings. This is therefore an interesting area for further research.

In future studies, thermal oil (to perform experiments above 100 °C) and high precision flow rate and temperature measurement equipment should be used. Alternative absorber coatings that achieve low emissivity and high absorption properties at the ELFR's expected operating temperatures should be researched. The cavity receiver's heat loss coefficient and thermal efficiency could be optimised using CFD. The mirror slope surface errors could be investigated to develop a more accurate ray-tracing model for LFR systems. The number and width of mirror elements in an ELFR system should also be studied further to develop an optimum geometrical design to improve the overall cost effectiveness of the ELFR.

Additional work is desirable to reduce the ELFR's drawbacks of increased cost and complexity. For the prototype, serial communication boards were developed to simplify control and reduce cabling and auxiliary electrical loads. Embedded control systems would be employed for large scale installations to further minimise complexity. Custom designed low cost mechanisms to achieve element elevation will significantly reduce costs as the prototype utilised expensive linear actuators of high power and precision. To determine the suitability of such mechanisms, further work needs to be carried out in order to evaluate the effect of elevation accuracies on the ELFR's optical efficiency. A final ELFR product for installation in a solar thermal field would be designed for mass production and therefore further cost reductions will be achievable.

5.8 Conclusion

An experimental set-up for measuring different performance parameters of an LFR system was described. Receiver temperatures were limited by the coupled tank-immersion heater and by the fact that the system was not pressurised. For receiver temperatures in the range of 30–65 °C, the estimated heat loss had a less than 10% deviation from results (estimated and measured) published by other authors on similar systems. Measured values for the HTF temperature gain, thermal efficiency (31–70%) and stagnation temperature (80–90 °C) had a difference from predicted values of -1% to 5%, -39% to +31% and 22% to 38% respectively. The estimated optical efficiency, based on the measured thermal efficiency and heat loss coefficient, had a percentage difference from the ray-tracing model developed in Chapter 4 of -23% to +32%.

It was concluded that the described theoretical models for determining the useful energy gained by an HTF were valid based on the experimental results for the heat loss

coefficient, thermal efficiency and stagnation temperature. The deviation between the measured and predicted results was considered to have arisen due to the low temperature range of the experiments and the prototype nature of the collector. Therefore, the theoretical models presented in this chapter were used to simulate a solar thermal field in a hybrid LFR-biomass power plant in the next chapter.

It was further thought that the experimental set-up described can be easily replicated by other researchers and manufacturers studying solar thermal collectors, however, temperatures greater than 100 °C should be used to more accurately profile the heat loss coefficient and thermal efficiency. As a result of the insights gained into the operating and design characteristics of the prototype ELFR, it was recommended that future LFR projects give careful consideration to the mirror elements design to avoid backlash and bearing movement, choice of selective absorber coating and the method for forming a secondary CPC.

5.9 Chapter summary

The aim of this chapter was to present and validate theoretical models defining the thermal performance of an LFR, specifically the energy gained by a heat transfer fluid. To validate the models a series of experiments were carried out for receiver temperatures in the range of 30–65 °C to measure the heat loss coefficient, gain in HTF temperature, thermal efficiency and stagnation temperature. The heat loss coefficient was underestimated due to the model exclusion of collector end heat losses. The measured HTF temperature gains were found to have a good correlation to the model predictions – less than 5% difference. Measured values for the thermal efficiency and stagnation temperature in comparison to model predictions had a difference of -39% to +31% and 22% to 38%. The difference between measured and predicted values was attributed to the low temperature region for the experiments. It was concluded that the theoretical models were valid and will be of significant value as they enable a solar thermal field's HTF exit temperature to be controlled.

Chapter 6

The feasibility of hybrid solar-biomass power plants in India

6.1 Introduction

In the previous chapters the design details of linear Fresnel reflector solar collectors for India have been investigated and specified. As described, the LFR uses multiple rows of low profile mirrors to focus solar radiation onto a fixed target pipe to generate steam directly. Such direct steam generation is an alternative to the more commonly employed heat transfer fluids – synthetic oil and molten salt – and has the potential to increase CSP plant efficiency and reduce costs [181]. However, thermal energy is difficult to store in DSG systems [72, 181, 182]. Auxiliary fossil/biomass boilers can therefore play a role in achieving temperature and load stability in LFR power plants. In this chapter the use of such collectors in hybrid solar-biomass power plants was to be evaluated.

Solar power plants benefit from hybridisation or effective energy storage due to the variable nature of solar energy, particularly in India's monsoon season. Constant base load or full load plants are typically implemented as plant efficiency is maximised and unit cost of energy is minimised. However, solar energy could be used to increase plant output during the day. In comparison to a biomass-only system, solar hybridisation reduces biomass demand, thus improving energy security and decreasing land required for farming and storage.

Hybrid solar systems have been investigated before. Kaushika et al. [183] studied a hybridised distillery waste-based co-generation plant with solar energy for India, with the bio-gas demand in relation to the amount of solar heat generated considered. Popov [184] modelled a Fresnel collector system for boiler preheating in a Rankine regenerative cycle for repowering fossil fuel power plants using Thermoflow's THERMOFLEX library [184]. Lerchenmüller et al. [185] at the Fraunhofer Institute evaluated various aspects of hybridising the LFR with biomass or gas co-firing for different solar shares, i.e. the percentage of electricity generated from solar energy as determined by the aperture area of the solar field. They calculated thermal and electrical outputs for constant base load operation using ColSim, an in-house simulation tool. Key economic indicators from the study included the Levelised Cost of Electricity (LCOE) and average annual profit after

interest rate repayments. The LCOE is the payment a plant must receive for each unit of electricity in order to meet operational costs.

Bermejo et al. [186] tested an LFR solar-gas cooling plant to identify design improvements that could be made on solar collector size, operation control and coupling to chiller. Cot et al. [187] presented the concept of 'Termosolar Borges' a hybrid CSP plant that will operate with a gas boiler during the day to respond to fast transients and a biomass boiler at night. Termosolar Borges will be the world's first hybrid CSP plant, and is expected to commence selling electricity to the Spanish grid in January 2013. A small scale demonstration project aiming for completion in June 2012 is TRESERT in Phitsanulok, Thailand. This is a hybrid power plant for tri-generation (electricity, heat and refrigeration) [188]. The Multipurpose Applications by Thermodynamic Solar (MATS) project by Agenzia Nazionale Per Le Nuove Tecnologie,l'energia E Lo Sviluppo Economico Sostenibile has recently outlined plans to develop small-mid scale CSP plants combined with biomass and biogas [189].

Several other studies have evaluated and optimised CSP power plants based on the criterion of LCOE [190, 191]. Considering LCOE and fossil-fuel demand, Montes et al. [181] assessed plant performance of a DSG hybrid solar thermal-fossil fuel plant as a function of Solar Multiple (SM), which is defined as the ratio of the solar field mirror aperture area to the size of the field aperture that produces sufficient energy, including thermal and optical losses, to drive a prime mover at its rated capacity at a design irradiance value. The SM therefore provides a measure of hybridisation. Frebourg et al. [192] studied the feasibility of a small scale grid connected hybrid solar-biomass power system in Thailand. Beerbaum et al. [193] have also estimated the LCOE for large CSP power plants in India.

Energy and exergy analyses (or first law and second law analyses) have been widely adopted to provide a comprehensive assessment of thermodynamic cycles. Exergy is particularly useful in assessing power generation systems to establish the maximum work potential and the true magnitude of losses and their locations. Bhattacharya et al. [194] performed an energy and exergy analysis of a hybrid gas-biomass system, and determined the optimum degree of supplementary firing to maximise exergetic efficiencies and the major sources of exergy losses in the cycle. Vidal et al. [195] established the exergy loss in each component of a combined power and refrigeration cycle, finding the highest

irreversibilities to occur in the heat exchanger. Singh et al. [134] performed an exergy analysis of a solar thermal power station finding the maximum energy loss to occur at the condenser, while the exergy analysis determined that the maximum losses occurred in the solar thermal field.

Exergetic analyses have also been combined with economic studies as exergy is the part of energy that is useful to society and therefore has economic value [196, 197]. Such exergoeconomic analyses are typically used for design optimisation, assessing feasibility, and comparing system operating conditions and technologies, by evaluating the cost associated with the exergy loss in system components [198]. Rosen and Dincer [199] identified the correlation of total or internal exergy loss and capital cost leading to an overall optimum design for coal, oil and nuclear power stations. Kaushik et al. [200] performed an exergoeconomic evaluation of a solar thermal power plant, identifying the system components that would benefit the most from an increased capital cost to reduce exergy loss. Hepbasli [201] provides a comprehensive review of exergetic studies of sustainable energy systems.

Hybrid plant studies in the literature have been primarily focused on the levelised energy cost with electricity as the sole output. As indicated, the concept of exergy has been widely adopted in the power generation sector, but no assessment of hybrid solar-biomass systems has been made. A range of hybrid solar-biomass applications and the resulting drawbacks and benefits for varying levels of hybridisation have also not been thoroughly investigated. In addition to generating electricity, hybrid systems can provide heat for industrial processes. As introduced in Chapter 1, a promising hybrid application in India is the tri-generation plant, producing electricity, ice and reject heat, through the use of a LFR solar field, biomass boiler, steam turbine and absorption chiller (see Figure 1.2). Many industries have a large demand for steam and, in food-processing facilities, requirements for thermal energy and ice may exceed that for electricity.

The aim of this Chapter was to assess the feasibility and prospects of hybrid solar-biomass power plants for various applications in India. Instead of optimising purely based on LCOE, a range of applications were considered including base and peak load demands for tri-generation, electricity generation and process heat. The following specific research questions were addressed:

Q1. What is the appropriate solar multiple for a hybrid solar-biomass power plant?
Q2. How does the ELFR compare to the conventional LFR for use in hybrid plants?
Q3. How do the levelised energy costs of alternative hybrid applications compare to other energy sources, renewable and conventional?
Q4. How does the hybrid plant compare to a biomass-only plant?
Q5. Which is the most feasible application for a hybrid solar-biomass power plant; tri-generation, electricity generation or industrial process heat?

The answers will enable the hybrid plant concept to be evaluated and recommendations to be made on the best applications of such plants. This will have implications for policymakers interested in incentivising biomass and solar energy and for plant designers and investors.

The methodology of this chapter was based on six case studies chosen to cover a range of scenarios for hybrid LFR-biomass power plants (Table 6.1). The data for the case studies was gathered from the field, background literature and in previous chapters. A simulation model was developed in TRNSYS® (Solar Energy Laboratory, University of Wisconsin-Madison) [202] for application to the case studies and this model will be described in detail. Each case study was analysed with variable sizes of solar field, as represented by the solar multiple. Evaluations and comparisons were made against technical, financial and environmental criteria, to provide answers to the research questions above. Technical performance was evaluated through an energy and exergy analysis. Financial assessment was made against the costs per exergy losses, similar to that in Chapter 3, along with calculated levelised energy costs and payback periods. Environmental impact was judged against biomass and land saving.

Table 6.1: The six case studies and their applications, operational conditions and financing.

Case study	(1) Gujarat LFR plant	(2) Gujarat ELFR plant	(3) College - peak load	(4) College - base load	(5) College - electricity	(6) Printing factory
Application	Tri-gen	Tri-gen	Tri-gen	Tri-gen	Electricity only	Process heat
Demand load	Peak	Peak	Peak	Base	Base	Base
Location	Gujarat	Gujarat	Tamilnadu	Tamilnadu	Tamilnadu	Tamilnadu
Peak capacity	5 $MW_{thermal}$	5 $MW_{thermal}$	10 $MW_{thermal}$	10 $MW_{thermal}$	10 $MW_{thermal}$	2 $MW_{thermal}$
Fixed charge rate	5%	5%	8%	8%	8%	8%
Capital subsidy	30%	30%	30%	30%	30%	30%
Feedstock	Rice husk	Rice husk	Coconut shell	Coconut shell	Coconut shell	Bio-brick
Feedstock LHV	14 MJ/kg	14 MJ/kg	16 MJ/kg	16 MJ/kg	16 MJ/kg	20 MJ/kg
Feedstock price	50 $/tonne	50 $/tonne	50 $/tonne	50 $/tonne	50 $/tonne	100 $/tonne

2. Evaluation criteria and assumptions

The evaluation required several criteria as used by other authors [64, 134, 181, 185-187, 190-193, 200]. These criteria fell into three categories:

1. Technical: energy efficiency (η_I) and exergetic efficiency (η_{II}).
2. Financial: cost per exergy loss (C_{pel}) Levelised Cost of Electricity (LCOE), Levelised Energy Cost (LEC), Payback Period on total capital cost (PP_{cap}) and Payback Period on cost of solar field (PP_{sol}).
3. Environmental: mass of biomass saved (B_{saved}) and resulting land saved (L_{saved}).

The assumptions and equations used for calculating these criteria will be defined.

6.2.1 Technical

The energy efficiencies (1st law efficiency, η_I) and exergetic efficiencies (2nd law efficiency, η_{II}) of the hybrid plants' components (solar field, biomass boiler, heat cycle and overall system) were studied to provide a quantitative and qualitative assessment of the energy conversion process at each stage in the system.

The hybrid plant's overall system energy efficiency is given by,

$$\eta_{I,os} = \frac{W_{net}}{\frac{Q_{boiler}}{\eta_{I,b}} + \frac{Q_u}{\eta_{I,c}}} \tag{6.1}$$

The net work, W_{net}, is a result of the annual work at the turbine, W_{turb}, and heat absorbed by the chiller, Q_e. The auxiliary load of the plant was assumed to be 1.25 times the auxiliary electrical requirement, $E_{el,aux}$.

$$W_{net} = W_{turb} + Q_e - (E_{el,aux}.1.25) \tag{6.2}$$

The useful energies transferred to the steam from the biomass boiler and solar thermal field are expressed as Q_{boiler} and Q_u respectively. The boiler efficiency, $\eta_{I,b}$, which varies for part loads, can be determined from the following equation:

$$\eta_{I,b} = \frac{Q_{boiler}}{M_{bio}.LHV} \tag{6.3}$$

The mass of the biomass feedstock consumed is given by M_{bio}. The Lower Heating Value (LHV) for fuels specifies the amount of energy released per mass of fuel during combustion.

The annual solar radiation rate on a solar thermal field, Q_{in}^{*} (GJ/a), is calculated from the solar insolation, Q^{year} (GJ/m^2/a), and the field's aperture area, A_{SF}:

$$Q_{in}^{*} = Q^{year}.A_{SF} \tag{6.4}$$

Thus, the energy efficiency of the solar field, $\eta_{I,c}$, is given by Q_u/Q_{in}.

Each case study was evaluated to determine the exergy received and delivered by each system component. The exergy received, Ex_c, and exergy delivered, Exu_c, by the solar thermal field are given by,

$$Ex_c = (Q_{in})\left[1 - \frac{T_a}{T_{sol}}\right] \tag{6.5}$$

$$Exu_c = Q_u\left[1 - \frac{T_a}{T_s}\right] \tag{6.6}$$

where T_{sol} is the apparent black body temperature of the sun (5600K) and T_s is the temperature of steam available to the heat cycle.

The exergy received, Ex_b, and delivered, Exu_b, by the biomass boiler are determined from,

$$Ex_b = e^{CH}.M_{bio} \tag{6.7}$$

$$Exu_b = Q_{boiler}\left[1 - \frac{T_a}{T_s}\right] \tag{6.8}$$

where e^{CH} is the chemical exergy of dry biomass; estimates for a variety of feedstocks are given in [203].

The exergy received by the heat cycle, Ex_{hc}, is the sum of the exergy delivered by the collector and boiler. The exergy delivered by the heat cycle and overall system are calculated from the net work. The exergetic efficiencies of the solar field, $\eta_{II,c}$, boiler, $\eta_{II,b}$, heat cycle, $\eta_{II,hc}$, and overall system, $\eta_{II,os}$, are calculated from the following equations.

$$\eta_{II,c} = \frac{Exu_c}{Ex_c} \tag{6.9}$$

$$\eta_{II,b} = \frac{Exu_b}{Ex_b} \tag{6.10}$$

$$\eta_{II,hc} = \frac{W_{net}}{Exu_c + Exu_b} \tag{6.11}$$

$$\eta_{II,os} = \frac{W_{net}}{Ex_c + Ex_b} \tag{6.12}$$

The main outputs from the plant include the electricity produced, E_{el}, mass of ice, M_{ice}, and low and high grade reject heat. Surplus heat from the solar thermal field was categorised as high grade reject heat, $Q_{reject,h}$, as temperatures will be the region of 300 °C. Low grade reject heat, $Q_{reject,l}$, temperatures less than 100 °C, will be produced from the chiller.

The total mass of ice produced can be estimated from the following [204],

$$Q_e = M_{water}C_{pw}T_a + M_{ice}L_{fw} + M_{ice}C_{pi}T_{ice} \tag{6.13}$$

where C_{pw} and C_{pi} are the specific heat capacity of water and ice, L_{fw} is the latent heat of fusion for water, and T_{ice} is the desired ice temperature.

6.2.2 Financial

The capital cost per exergy loss, $C_{pel,}$ for each plant component (solar field, $C_{pel,c}$, boiler, $C_{pel,b}$, heat cycle, $C_{pel,hc}$, and overall system, $C_{pel,os}$) was evaluated from:

$$C_{pel,c} = \frac{A_{SF}.c_{sf} + c_{land}.TA_{SF}}{Ex_c - Exu_c} \tag{6.14}$$

$$C_{pel,b} = \frac{c_{boiler} + c_{bio}}{Ex_b - Exu_b} \tag{6.15}$$

$$C_{pel,hc} = \frac{c_{turb} + c_{chill} + c_{pb}}{Ex_{hc} - W_{net}} \tag{6.16}$$

$$C_{pel,os} = \frac{C_{capital}}{Ex_c + Ex_b - W_{net}} \tag{6.17}$$

The capital cost of the plant, $C_{capital}$, and cost of operations and maintenance, $C_{O\&M}$, for the hybrid plant were calculated from:

$$C_{capital} = (A_{SF}.c_{sf} + c_{land}.TA_{SF} + c_{boiler} + c_{turb} + c_{chill} + c_{pb}) \tag{6.18}$$

$$C_{O\&M} = \left(f_{SFstaff}.TA_{SF} + f_{PBstaff}\right).c_{staff} + c_{ins} + c_{water} + c_{spare} + c_{bio} \tag{6.19}$$

It has been estimated that an LFR solar field, based on aperture area, must cost below 281 \$/m^2 (216 €/m^2) to be competitive with other CSP technologies [105]. Typical costs for an LFR system were researched in Chapter 2, and were found to cost around 235 \$/m^2. The Solar Mission proposed a 30% capital cost subsidy for solar energy technologies implemented in India, therefore, a value of 165 \$/m^2 was assumed for the cost of the solar field, c_{sf}. In addition, the Solar Mission outlined the availability of soft loans at a 5% interest rate for solar energy projects, and a 60% capital cost subsidy for un-electrified rural regions of India [10]. Therefore, depending upon the hybrid plant scenario, these financial incentives were or were not considered. Land usage for the solar field was assumed to be three times that of its aperture area. The cost of land procurement and preparation, average salary of a medium skilled employee and value of ice were taken to be 20 \$/m^2, \$2000 per annum and 40 \$/tonne respectively, which were values gathered by the author during site visitations with companies in Gujarat (2011). The cost of the biomass

boiler, c_{boiler}, was assumed to be \$54,000 per tonne of steam produced per hour. Depending upon the amount of ice produced in a year the cost of the chiller, c_{chill}, was taken to be \$25,000 per tonne of ice produced [44]. The cost of the turbine, c_{turb}, was highly variable and depends upon the steam turbine selected. The additional cost for the rest of the power block, c_{pb}, was assumed to be 40 \$/MWh$_e$. Other operational costs include the biomass, c_{bio}, which will depend on feedstock type and site location. The number of staff required for the solar field and rest of the plant was assumed to be 2 persons/hectare and 10 employees respectively (control, hauling ice, repairs, security, etc.). The cost of the water consumption was taken to be 1.73 \$/MWh [64]. And the annual part replacement and plant insurance cost were both assumed to be 1% of the total capital cost. The LCOE was used to determine the cost of the electricity produced. Levelised Energy Cost (LEC) was used to determine the unit cost of other energy outputs, i.e. cooling effect and electrical generation.

$$LCOE = \frac{(C_{capital} - c_{chiller}).FCR + C_{O\&M}}{E_{el} - E_{el,aux}} \tag{6.20}$$

$$LEC = \frac{C_{capital}.FCR + C_{O\&M}}{Q_{turb} + Q_e} \tag{6.21}$$

where the Fixed Charge Rate (FCR) was determined by the real debt interest, k_d, over an n number of years.

$$FCR = \frac{k_d.(1+k_d)^n}{(1+k_d)^n - 1} \tag{6.22}$$

In this study an FCR was determined from the rate of return to repay the capital cost of the plant over a 20 year period (e.g. for a 5% interest rate loan, FCR = 8%). The cash flow earned by the plant was determined from the value of ice, I_{val}, and electricity, $E_{el,val}$. Electricity generated from the solar and biomass input was assumed to be saleable at a different fixed tariff rate. Thus, the percentage of electricity produced from solar, $E_{el,\%sol}$, and biomass, $E_{el,\%bio}$, were calculated to determine a total electricity value. With tariff incentives for electricity generation from solar and biomass being dependent on a number of factors – state, capacity, year, etc. – a fixed value of 19 ¢/kWh was taken for solar, as solar projects commissioned after 31st December 2009 were eligible for this rate in India [205]. The assumption was made that electricity generated from biomass was sold, and electricity was bought, at an industry rate of 12 ¢/kWh. The fraction of the total useful energy from the solar input is termed the solar share, *FS*.

$$E_{el,val} = 19.E_{el,\%sol}.\left(E_{el}-E_{el,aux}\right) + 12.E_{el,\%bio}.\left(E_{el}-E_{el,aux}\right) \quad (6.23)$$

The annual profit of the plant after FCR repayments, P_{ar}, and with FCR repayments (e.g. loans), P_{wr}, was determined from:

$$P_{ar} = I_{val} + E_{el,val} - C_{O\&M} \quad (6.24)$$

$$P_{wr} = I_{val} + E_{el,val} - C_{O\&M} - C_{capital}.FCR \quad (6.25)$$

To investigate the benefit of a hybrid plant in comparison to a biomass-only plant it was useful to determine the payback period for the additional investment in solar energy, PP_{sol}, which is specified by the capital cost and profit of a hybrid plant for a given solar multiple (SM = m) and a biomass-only plant (SM = 0):

$$PP_{sol} = \frac{C_{capital}.(P_{wr}(SM=0) - P_{wr}(SM=m))}{P_{ar}(SM=m) - P_{ar}(SM=0)} + n \quad (6.26)$$

The payback period or breakeven time for the overall plant's capital cost, PP_{cap}, was also included as it is a key indicator for investors of whether a project is financially feasible. Tax rates and other financial incentives such as carbon credits were not considered. All monetary values in this chapter were again presented in US dollars, converted at an exchange rate of 1 Indian Rupee (INR) = 0.02 US Dollar (USD).

6.2.3 Environmental

The key environmental factors considered were the amount of biomass and land saved, B_{saved} and L_{saved}, relative to biomass-only operation. The land usage was calculated based on a crop yield assumption of 13 tonnes per hectare annum [206].

6.3 Simulation model of hybrid plant

Several software packages with the capability to enable users to model solar thermal and renewable energy based power plants were available on the market. Exemplary packages included: Thermoflex, Ebsilon, IPSEpro, TRNSYS, SAM, Greenius and ColSim. For the purposes of this study a hybrid LFR-biomass power plant model to determine the criteria values was developed in TRNSYS, a validated TRaNsient SYstem Simulation software tool. It is a graphical software environment, typically used to model the performance of

thermal and electrical energy generating systems, and has been previously applied in the field of CSP [207, 208]. Each component forming the hybrid plant model is now described. Mathematical models and assumptions used are explicitly provided.

6.3.1 Biomass boiler

A TRNSYS steam boiler component developed by Liebecq at the Solar Energy Laboratory was used to model the biomass boiler [209]. The model enables information on the composition of the fuel to be specified as a main parameter. Published fuel compositions for a variety of agricultural wastes are reported in the literature [210-213]. For a given steam demand, temperature and pressure, the boiler efficiency, flue gas temperature and biomass feed rate were calculated. Losses due to flue gas, blowdown, ash removal, radiation and convection were also considered. The boiler was considered as a counter flow heat exchanger with the flue gas exchanging heat to the supply water through an economizer, evaporator and superheater section.

6.3.2 Solar field operation

To model the solar field a custom component was developed in TRNSYS. The hourly performance of the solar field was modelled based on the typical parameters established in the previous chapters for an LFR or ELFR: Concentration ratio, *C*, Incident Angle Modifier, *IAM*, optical efficiency at normal incidence, $\eta_{(\theta=0)}$ and heat loss coefficient, U_L.

The receiver sections which act as a pre-heater, evaporator and boiler had to be treated individually. Thus, for a given inlet temperature the mass flow could be determined to achieve a specified exit temperature.

$$m_{sol} = \frac{Q_u}{\left[C_{pw}(100 - T_{in}) + L_{ew} + C_{ps}(T_{exit} - 100)\right]} \tag{6.27}$$

The solar field aperture area required to provide enough useful heat gain to achieve the maximum thermal requirement (mass flow and temperature) at the turbine, for peak cosine-adjusted DNI in a Typical Meteorological Year (TMY), i.e. S.M = 1, could then be determined. For SM > 1 the flow rate from the solar field can be too high to be utilised by the turbine, thus excess flow needed to be siphoned off. At night, flow bypassed the solar field. The field pipe losses were not considered.

6.3.3 Refrigeration plant

A single effect absorption chiller within the TRNSYS component files was used to model the heat absorbed from a chilled flow stream, heat rejected to a cooling flow stream and auxiliary electrical load. The chiller was assumed to operate with a constant COP of 0.5 and a calcium chloride ($CaCl_2$) brine solution with a specific heat capacity of 3.2 kJ/kg K for the chilled stream [43]. The aqueous $CaCl_2$ solution was chosen as it enables temperatures below 0 °C to be obtained in the chiller. An additional component had to be modelled to control the chilled stream to match the varying hot water flow rates (193–220 °C), so that a constant hot water exit temperature of 50 °C was achieved. Heat was rejected via the cooling stream entering at the ambient with a constant flow rate of 2.5 kg/s. The cooling stream flow rate could also be controlled to maintain a constant exit temperature for another process heat application; however, this was not considered. The desired chilled stream exit temperature from the chiller was specified as -20 °C. It was assumed that ice was produced in a perfectly insulated brine tank. Therefore, the energy absorbed by the brine to chill water-ice from the ambient to -5 °C was equivalent to the energy absorbed from the brine in the chiller.

6.3.4 Turbine selection

The steam turbine was modelled using data gathered on two back pressure turbines (IBL's BT-4, and Siemens' SST-060) and assumptions made for a condensing turbine. The BT-4 operates with an isentropic efficiency of 45%. The generator efficiency ranges from 82–89%. The SST-060 has an isentropic efficiency of around 39–53% with a generator efficiency of 79–92%. Monetary values were also been obtained through communications with IBL and Siemens in 2011, the capital cost of the BT-4 and SST-060 was $120,000 and $660,000 respectively. The operational range in terms of full and part load flow rates, mechanical outputs, pressures, temperatures, and efficiencies are given in Table 6.2. A cost of $800,000 was assumed for the condensing turbine.

Table 6.2: Specifications for the IBL BT-4, Siemens STT-060 and condensing steam turbine.

	m_{turb}	P_{inlet}	P_{exit}	T_1	T_2	W_{turb}	E_{el}	Is_{eff}	Gen_{eff}
Turbine	kg/s	bar	bar	°C	°C	kW	kWe	%	%
BT-4	0.83	8.5	2.5	280	215	95	78	44%	82%
BT-4	1.66	8.5	2.5	280	213	198	175	45%	89%
SST-060	1.18	8.5	1.5	300	220	170	135	39%	79%
SST-060	3	8.5	1.5	300	193	591	544	53%	92%
Condensing	3	8.5	0.1	300	50	1389	1320	59%	95%

6.4 Case studies

In this section, the key features of the six hybrid plant case studies are presented (as summarised in Table 6.1). Each case includes details on plant application, site location, sizing, operational parameters and assumptions. Results for the evaluation criteria defined in Section 6.2 are plotted against SM. Full simulation results can be found in Appendix 10.

6.4.1 Case study 1 – Gujarat LFR plant

The Gujarat hybrid plant is a pilot system to be implemented in Vapi, India. The project is part funded by research grants and therefore has a low FCR of 5%. The plant will provide electricity to the grid, and ice to nearby fisheries and chemical plants. In the future, surplus heat will be used for additional process steam applications. The plant will operate with a 3 tonne boiler and BT-4 steam turbine. Rice husk feedstock, with an LHV of 14 MJ/kg, will be sourced at a cost of 40 $/tonne.

The Gujarat plant was modelled using the following conditions. At the biomass boiler's full load, steam exited at 280 °C, 8.5 bar and 0.83 kg/s, thus providing the part load thermal requirement of the turbine. Additional steam was sent to the turbine from the solar field until the mass flow reached 0.415 kg/s; at this state the biomass boiler was switched to part load (i.e. the two flow streams were combined to achieve the part load of the turbine). If the solar field's mass flow reached 0.83 kg/s the boiler was shut down and hot banked; the fuel and energy requirement was not included. For an SM > 1, the steam mass flow rate from the field was limited to a maximum of 1.66 kg/s, hence, additional flow was siphoned off. Exhaust steam from the turbine was sent to the chiller where it exited at 50 °C. The TMY for the nearest weather station, Rajkot, was used. For the Gujarat plant a solar multiple of 1 required a solar field aperture area of 9350 m^2. Results for the Gujarat LFR plant are shown in Figure 6.1a–d.

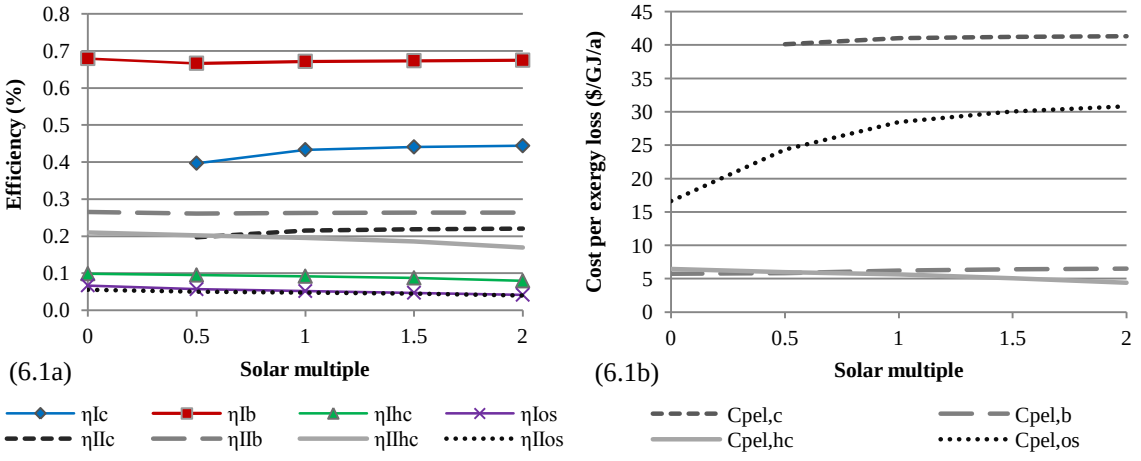

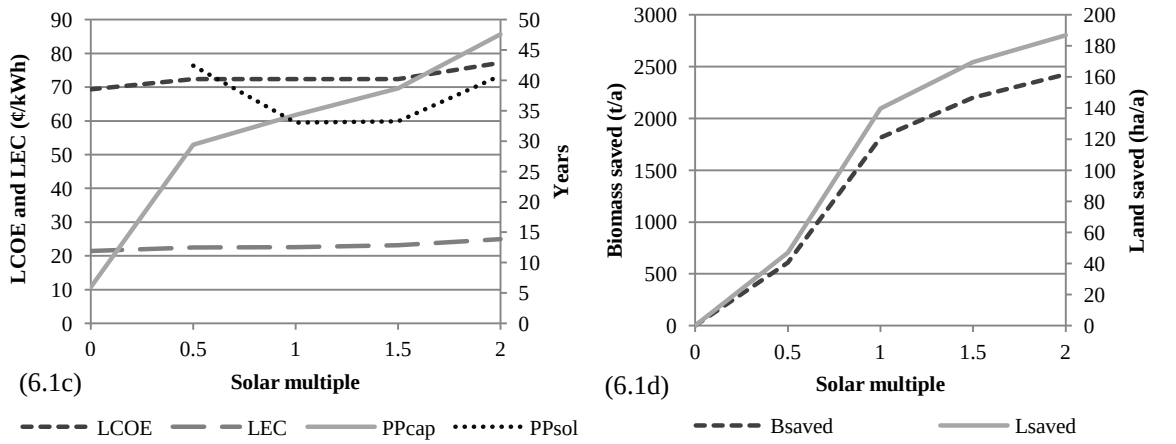

Figure 6.1a–d: Gujarat LFR plant (case study 1) shows: (a) the minimum energy and exergetic efficiencies occurred at the heat cycle, and the overall system energy and exergetic efficiencies decreased relatively constantly from 0.067 to 0.042 and 0.056 to 0.040 for SM = 0 – 2; (b) the overall system cost per exergy loss increased by hybridising with solar, but remained relatively constant for larger SMs; (c) the levelised costs of electricity and energy remained relatively constant among the SM alternatives, around 72 and 22 ¢/kWh respectively, and a solar multiple of 1 to 1.5 resulted in the minimum payback period for the solar investment (33 years) and a capital cost payback period of 34 to 39 years; (d) the biomass and land saving became less substantial for SM > 1, at SM = 1 the hybrid plant saved 1800 tonnes and 140 hectares per annum.

6.4.2 Case study 2 – Gujarat ELFR plant

The model parameters for the Gujarat ELFR plant were the same as those in case study 1, except that the ELFR technology was utilised. Therefore, a smaller sized solar field aperture area, 9000 m^2, achieved a solar multiple 1. Based on the ELFR's capital cost increase in comparison to a typical LFR, 16-28% found in Chapter 4, a value of 200 $/$m^2$ was assumed for the solar field.

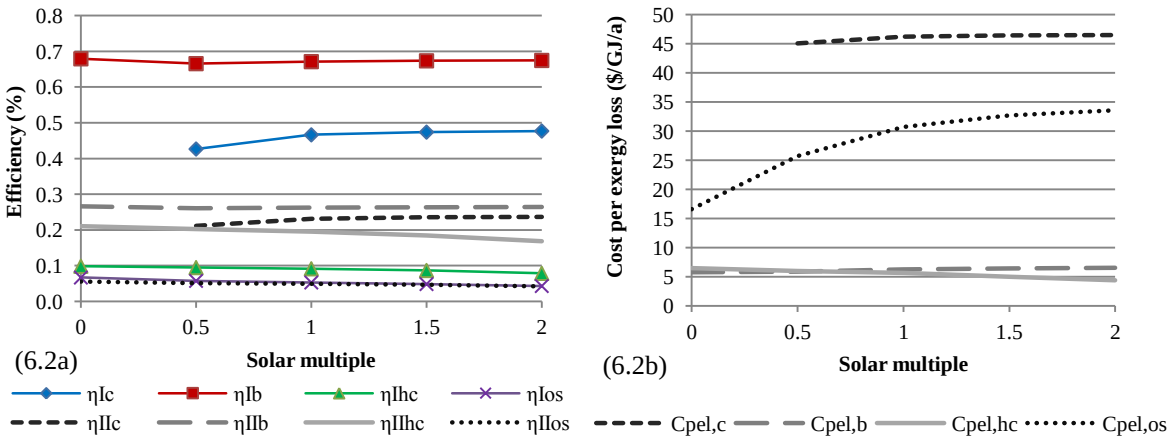

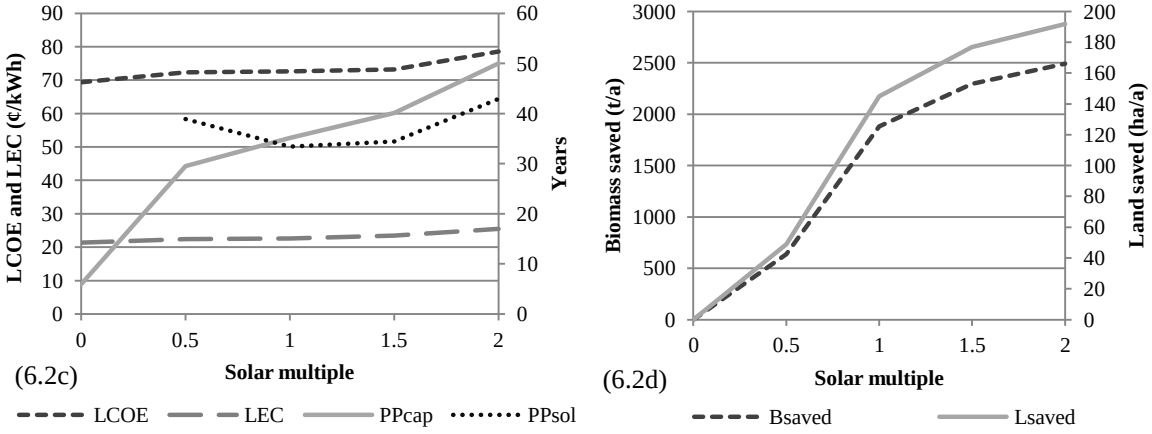

Figure 6.2a–d: Gujarat ELFR plant (case study 2) shows: (a) the minimum energy and exergetic efficiencies occurred at the heat cycle, and the overall system energy and exergetic efficiencies decreased relatively constantly from 0.067 to 0.043 and 0.056 to 0.042 for SM = 0 – 2; (b) the overall system cost per exergy loss increased by hybridising with solar, but remained relatively constant for larger SMs; (c) the levelised costs of electricity and energy remained relatively constant among the SM alternatives, around 73 and 23 ¢/kWh respectively, and a solar multiple of 1 resulted in the minimum payback period for the solar investment (33 years) and a capital cost payback period of 35 years; (d) the biomass and land saving became less substantial for SM > 1, at SM = 1 the hybrid plant saved 1880 tonnes and 145 hectares per annum.

6.4.3 Case studies 3, 4 and 5 – College-peak load, base load and electricity

An educational institution in Tamilnadu is aiming to improve their sustainability by combining solar and biomass energy to provide electricity and cooling, or electricity only, to their campus buildings. In addition, they are also interested in designing a system that best meets their demand. Three case studies were therefore modelled.

College-peak load and base load (cases 3 and 4) were modelled with a STT-060 turbine (requiring steam at 300 °C and 8.5 bar), a biomass boiler running on coconut shells and a chiller. For case 3 the mass flow from the solar field and biomass boiler was controlled as presented for case 1, i.e. peak demand during the day. For this case a 4 tonne boiler with a full load steam rate of 1.18 kg/s was chosen. Case 4 was controlled so that a constant base load was achieved. For this case a larger 10.8 tonne boiler (steam rate equal to 3 kg/s) was modelled. The boiler was assumed to complement the solar input with an ideal response in the range of 40–100% of its peak thermal requirement. Thus, steam at a flow rate of up to 1.8 kg/s from the solar field was added to the steam flow from the biomass boiler. Surplus flow was generated from the solar field for flow rates greater than 1.8 kg/s. However, if the solar field achieved a steam flow of 3 kg/s the biomass boiler was turned off and hot banked. Surplus flow was therefore produced for flow rates greater than 3 kg/s. For both

cases 3 and 4, the assumption was made that electricity and ice produced were sold at the fixed tariff rates outlined in section 2.2. In reality, the plant may provide electricity and cooling purely as amenities to the campus buildings. The key results for the College-peak and -base load case studies are plotted in Figures 6.3a–d and 6.4a–d.

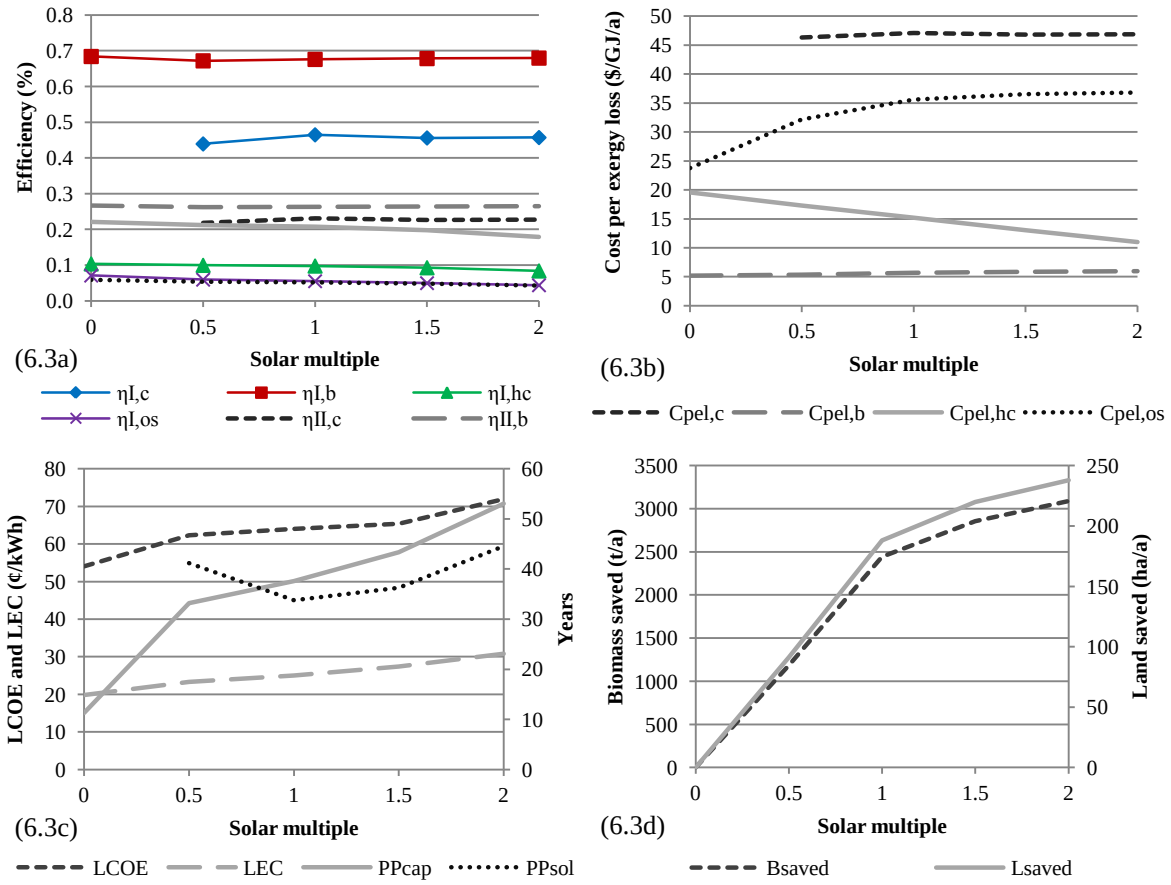

Figure 6.3a–d: College-peak load (case study 3) shows: (a) the minimum energy and exergetic efficiencies occurred at the heat cycle, and the overall system energy and exergetic efficiencies decreased relatively constantly from 0.071 to 0.044 and 0.059 to 0.043 for SM = 0 – 2; (b) the overall system's cost per exergy loss increased by hybridising with solar, but remained relatively constant for larger SMs. The heat cycle's cost per exergy loss decreased constantly for larger SMs; (c) the levelised electricity and energy costs increased relatively constantly for an increasing SM, and an SM = 1 resulted in the minimum solar payback period and a capital cost payback period of 38 years; (d) the biomass and land saving became less substantial for SM > 1, at SM = 1 the hybrid plant saved 2500 tonnes and 188 hectares per annum.

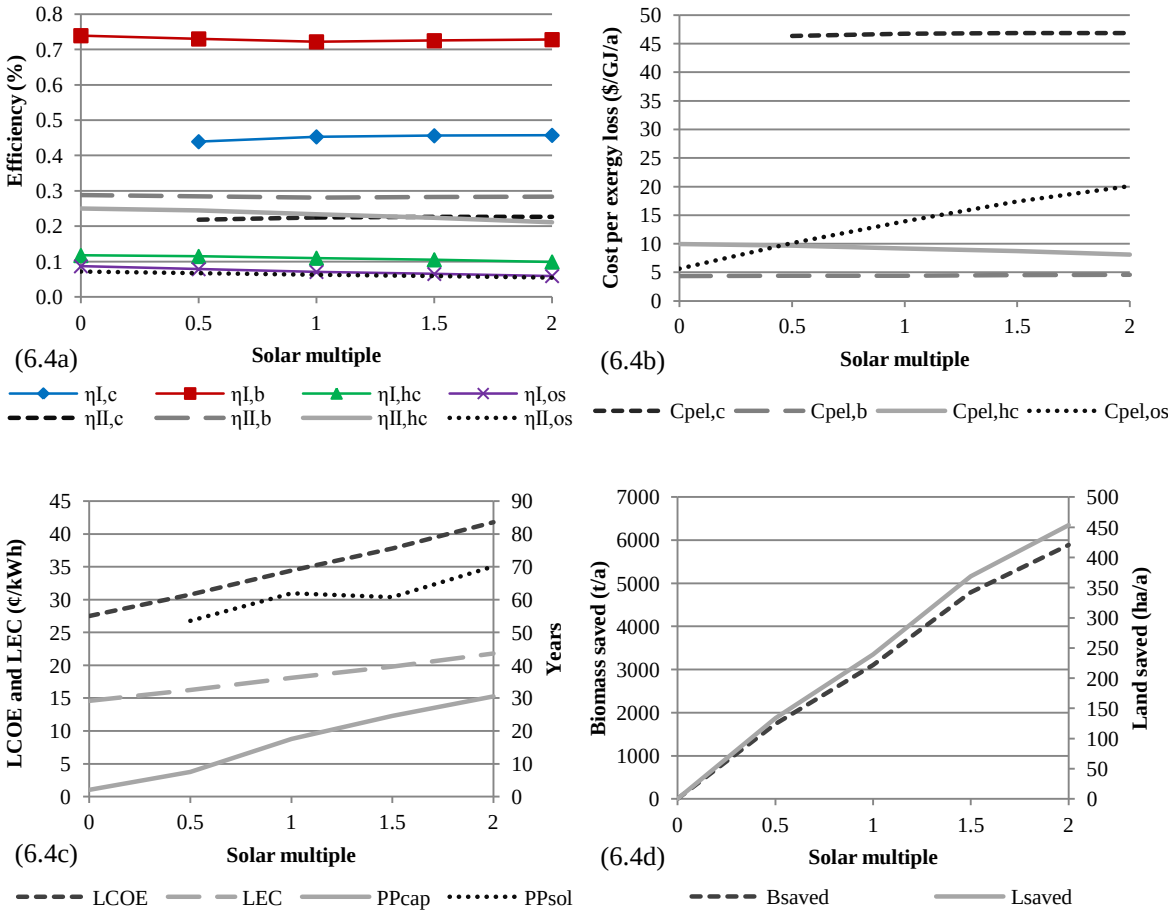

Figure 6.4a–d: College-base load (case study 4) shows: (a) the minimum energy efficiencies occurred at the heat cycle and solar field and minimum exergetic efficiencies occurred at the heat cycle. The overall system energy and exergetic efficiencies decreased relatively constantly from 0.087 to 0.049 and 0.072 to 0.055 for SM = 0 – 2; (b) the overall system cost per exergy loss increased constantly for larger SMs; (c) the levelised electricity and energy cost increased constantly for larger solar multiples, and an SM = 1 resulted in the minimum solar payback period (62 years) and a capital cost payback period of 18 years; (d) the biomass and land saving remained constant for an increasing SM, at SM = 1 the hybrid plant saved 3100 tonnes and 240 hectares per annum.

College-electricity (case 5) was modelled similarly to case 4, except that a condensing turbine was used rather than a back pressure turbine-chiller combination, this resulted in alternative technical and financial values only (see Figure 6.5a–d). In all cases the weather data from the Coimbatore weather station was used for the TMY. Cases were assumed to be funded by a government loan with a 5% interest rate, thus an FCR of 8% was modelled. For the College case studies a solar multiple of 1 required a solar field aperture area of 19500 m^2.

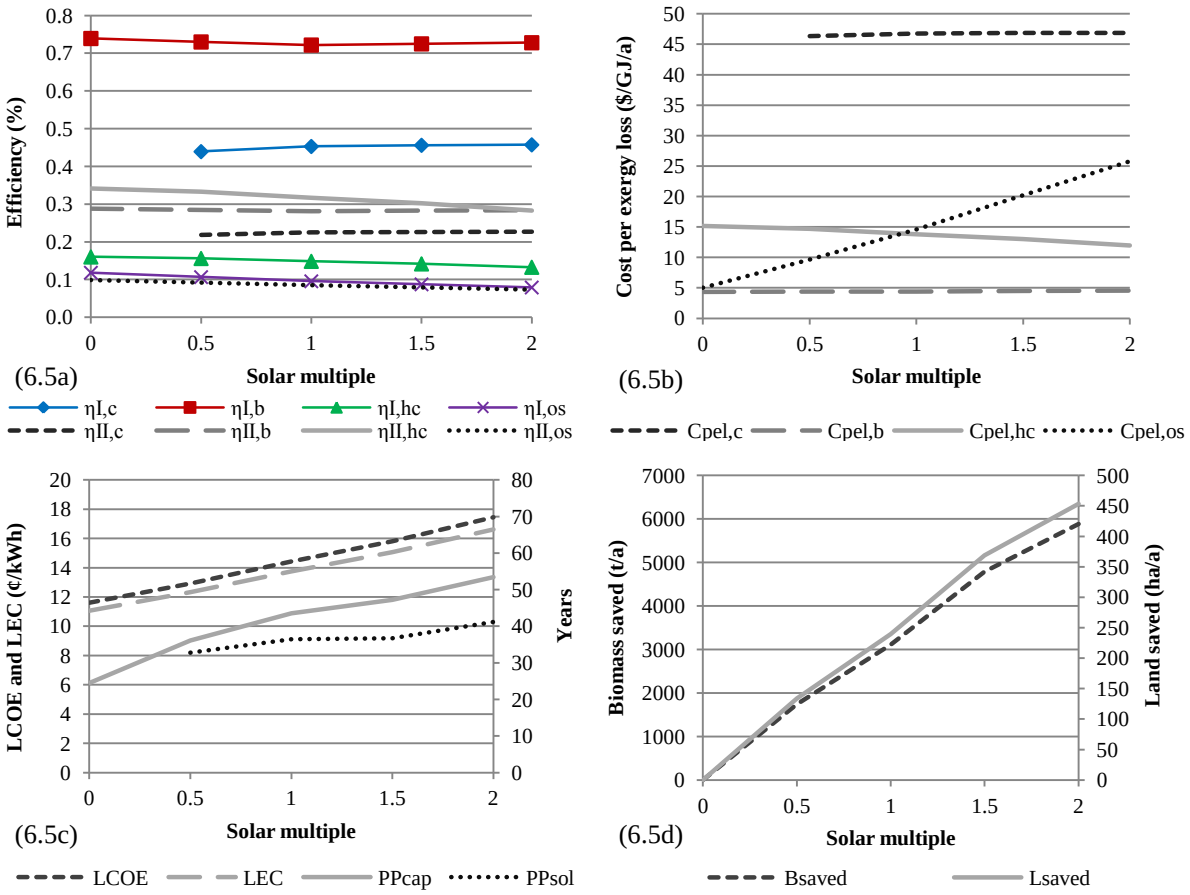

Figure 6.5a–d: College-electricity (case study 4) shows: (a) the minimum energy efficiencies occurred at the solar field and minimum exergetic efficiencies occurred at the heat cycle. The overall system energy and exergetic efficiencies decreased relatively constantly from 0.118 to 0.079 and 0.098 to 0.073 for SM = 0 – 2; (b) the overall system cost per exergy loss increased constantly for larger SMs; (c) the levelised electricity and energy costs increased constantly from around 11.5 to 17 ¢/kWh for an SM of 0 – 2, and a capital cost and solar investment payback period of 44 and 36 years respectively for an SM = 1; (d) the biomass and land saving remained constant for an increasing SM, at SM = 1 the hybrid plant saved 3100 tonnes and 240 hectares per annum.

6.4.4 Case study 6 – Printing factory

A printing factory, located in Tamilndadu, India, requires a large quantity of steam (2MW thermal yearly average) to dry textile printings. The factory currently operates on biomass alone (bio-bricks). The bio-bricks are made from sawdust, ground nut husk, coffee husk and tamarind husk, all provided by a farmer in Kerala, they are then transported to Dharapuram and made into the bio-bricks by a subsidiary company before being sent to the factory. From farmer to boiler the biomass is transported over 350 km. The printing factory reports that the cost of the bio-bricks has increased from 16 $/tonne in 2005 to a value of 100 $/tonne in 2011, and are suffering from an inconsistent feedstock supply. Thus, to reduce biomass dependency they are looking to integrate solar energy into their plant.

As the printing factory uses steam directly, the plant's performance was evaluated purely on the energy delivered by the solar field and biomass boiler. The hybrid plant for the printing factory was also modelled on the assumption that a constant steam flow rate of 0.4 kg/s, at 230 °C and 2 bar, was required. Bio-bricks were consumed at a rate of 0.081 kg/s. The fuel composition of birch bark was assumed to have comparable properties to the bio-bricks, i.e. an LHV of 20 MJ/kg. For S.M = 1, a field aperture of 2100 m^2 was required to achieve the 0.4 kg/s steam flow rate at peak solar irradiance over the TMY. The TMY for Coimbatore was again used. The biomass boiler was modelled as either on or off. Thus, the boiler was shut down when the solar field was able to produce the demanded steam rate. Flow below 0.4 kg/s from the solar field was therefore considered as surplus heat. At an SM>1, further surplus energy was created for steam flows greater than 0.4 kg/s. A solar field aperture of 4200 m^2 provided a solar multiple of 1 for the printing plant. The results for the plant are shown in Figure 6.6a–d.

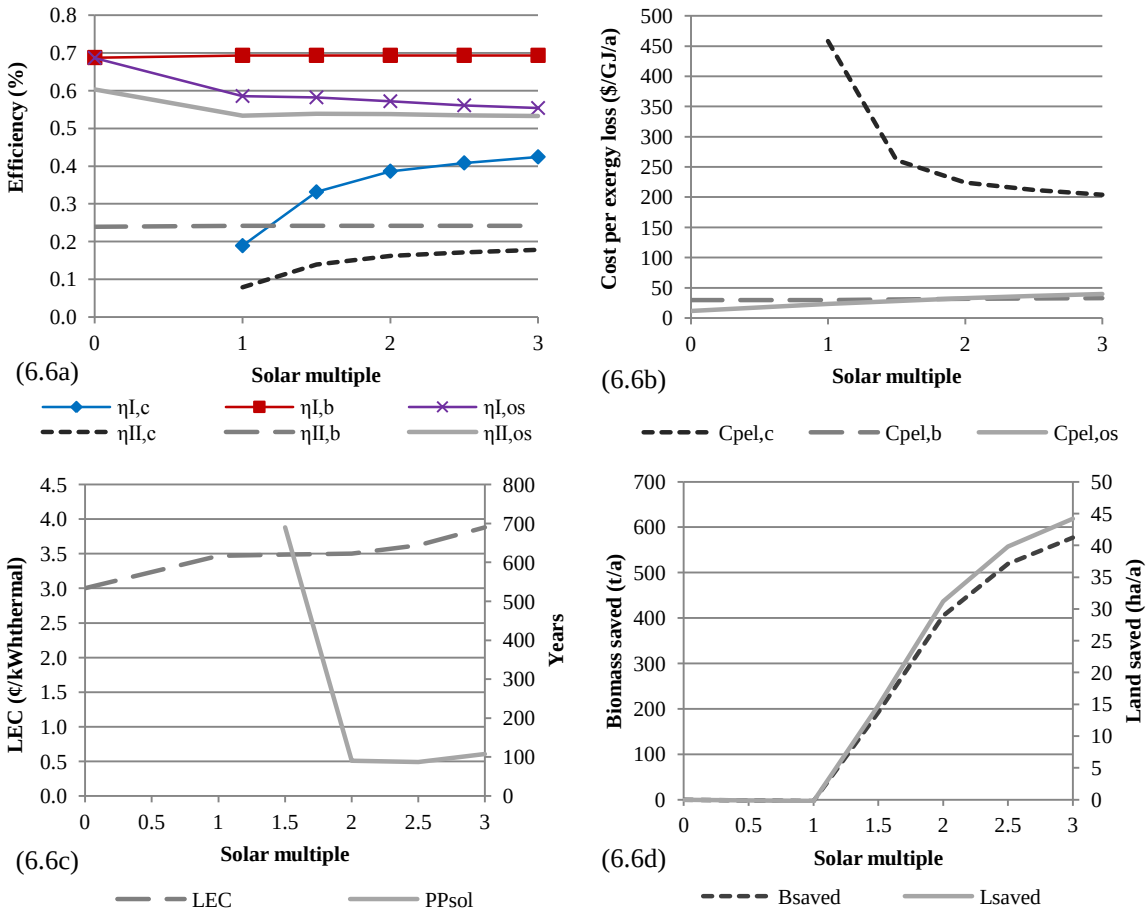

Figure 6.6a–d: Printing factory (case study 6) shows: (a) the minimum energy and exergetic efficiencies occurred at the solar field. The overall system energy and exergetic efficiencies decreased relatively constantly from 0.687 to 0.554 and 0.603 to 0.533 for SM = 0 – 2; (b) the cost per exergy loss of the overall system and solar field increased and decreased respectively for larger SMs; (c) the levelised energy cost

increased from 3.2 to 4 ¢/kWh$_t$ for an SM of 0 to 3, and a minimum payback period of 88 years for SM = 2.5; (d) the biomass and land saving remained constant for an increasing SM from 1 to 2, at SM = 2.5 the hybrid plant saved 500 tonnes and 40 hectares per annum.

6.5 Discussion

The results from the case studies will now be summarised and discussed thus providing answers to the five research questions outlined in this chapter's introduction:

Q1. What is the appropriate solar multiple for a hybrid plant?

A solar multiple varying from 1 (cases 2, 3 and 4) to 2.5 (case 5) was indicated (see Table 6.3) by consideration of a hybrid plant's energy and exergetic efficiencies, cost per exergy loss, levelised costs, payback periods, and biomass and land saved. The variation in the recommended SM was due to differing operating conditions and financial assumptions. For the tri-generation and electricity base load studies (cases 3 and 4), the cost per exergy loss and levelised costs increased constantly with SM (Figures 6.3 and 6.4). For the peak load studies (cases 1 and 2) the addition of solar energy increased the cost per exergy loss which remained relatively constant for an increasing SM. The peak load (cases 1 and 2) and process heat (case 5) studies had a less substantial levelised cost increase for an SM = 0.5–1.5 and 1–2 respectively, which resulted in a minimum payback period for the solar investment being indicated. As expected the capital cost payback period increased for larger solar multiples, but increased more gradually for an SM = 0.5–1.5. For a large SM the biomass and land saved also became less substantial in comparison to increased values for the financial criteria.

Table 6.3: Selected solar multiple for the six case studies (see Table 6.1) and the resulting energy and exergetic efficiencies, cost per exergy loss increase in comparison to a biomass only plant, levelised electricity and energy costs (including cost increase in comparison to a biomass-only plant), payback periods and biomass and land saved.

Case study	(1) Gujarat LFR plant	(2) Gujarat ELFR plant	(3) College - peak load	(4) College - base load	(5) College - electricity	(6) Printing factory
SM	1.5	1.5	1	1	1	2.5
$\eta_{I,os}$ (%)	4.7	4.9	5.5	6.3	9.6	56.1
$\eta_{II,os}$ (%)	4.5	4.6	5.2	7.1	8.5	53.4
$C_{pel,os}$ ($/GJ/a)	30.1	32.7	35.6	13.9	14.6	36.7
Increase in $C_{pel,os}$ ($/GJ/a)	14.1	16.1	11.9	8.3	9.6	24.8
Levelised costs						
Electricity (¢/kWh)	72.4	73.19	64.1	34.4	14.4	-
Energy (¢/kWh)	23.2	23.5	25	18.1	13.8	3.7
Increase in levelised costs						
Electricity (¢/kWh)	3.1	3.9	10	6.8	2.9	-
Energy (¢/kWh)	1.8	2.1	5.2	3.5	2.7	0.6
B_{saved} (t/a)	2200	2300	2442	3108	3108	192
L_{saved} (ha/a)	169	178	188	239	239	40
As a percentage (%)	28	30	26	14	14	20
PP_{cap} (years)	38.7	40.1	37.6	17.6	43.6	-
PP_{sol} (years)	33.3	34.4	33.8	61.9	36.4	87.5

Q2. How does the ELFR compare to the conventional LFR for use in hybrid plants?

The levelised energy costs and payback periods were only slightly increased for the ELFR plant (0.3 ¢/kWh and 1.4 years), even though the ELFR was considerably more expensive than the LFR. This was due to the ELFR improving the solar field's energy and exergetic efficiencies by 8% and 7%, which resulted in more biomass (100 t/a) and land (9 ha/a) being saved, thus reducing O&M costs. Both case studies were simulated using a low land cost estimate for India (720 INR/m^2). For a high land cost (10,000 INR/m^2) the LFR and ELFR plants with a solar multiple of 1.5 would have resulted in a levelised energy cost of 43.1 ¢/kWh and 38.8 ¢/kWh respectively. Therefore, the ELFR plant would have reduced levelised energy costs by 10%. While it was unlikely that a large power generating plant would be built in a location with such high land costs, the potential of the ELFR is evident; particularly as designing for mass manufacture could significantly reduce the solar field's capital costs. A 4% decrease in the cost of the ELFR solar field or a 15% increase in land cost would have resulted in the Gujarat ELFR plant (case 2) being cost competitive with the Gujarat LFR plant (case 1), with regards to levelised energy cost.

Q3. How do the levelised energy costs of alternative hybrid applications compare to other energy sources, renewable and conventional?

The levelised energy costs for hybrid solar-biomass power plants were competitive with other renewable energy systems in India. Energy costs for the six case studies modelled were lower than photovoltaic and comparable to wind turbines (see Figure 6.7). Furthermore, the levelised electricity costs for all the case studies were even more attractive in comparison to the costs researched for extending India's electrical grid to rural areas, which ranged from 6.4–462.3 ¢/kWh [214]. In comparison to the Gujarat LFR plant, the College case studies (cases 3-5), which had higher capital and operating costs, achieved lower electricity and energy cost values, due to the larger capacity of these plants. On a larger scale, the unit energy costs for the case studies were approximately two and four times what would be expected for a commercial CSP and coal fired power station in India respectively. Yet, in comparison to small scale decentralised system in India, the hybrid plants performed well with considerably lower electricity and energy cost values.

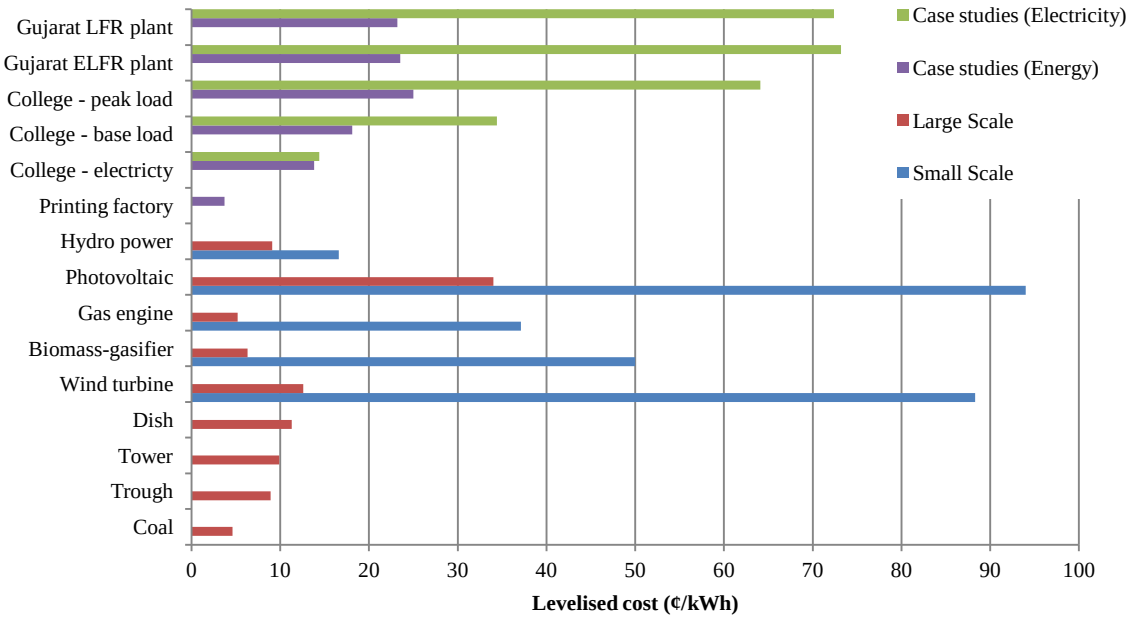

Figure 6.7: Levelised electricity and energy costs for the six case studies compared to the levelised cost of electricity for small and large scale energy systems in India, reported by Rangan [215], Nouni et al. [3] and Beerbaum and Weinrebe [193].

Q4. How does the hybrid plant compare to a biomass-only plant?

The hybrid plants' energy and exergetic efficiencies were largely insensitive to an increasing SM. For cases 1 – 3 the heat cycle had the lowest exergetic efficiency, however, exergetic efficiencies were comparable at around 20–30% for the solar field, biomass

boiler and heat cycle. In comparison to a biomass-only plant, the main drawbacks of the hybrid solar-biomass power plants were financial, however there were environmental advantages. For the selected SMs shown in Table 6.3 the cost per exergy loss and levelised energy cost increased from 8.3 to 24.8 $/GJ/a and 1.8 to 5.2 ¢/kWh respectively in comparison to biomass-only. A more significant drawback was the long payback periods for the hybrid plant. With a high solar share, the peak load studies (cases 1, 2 and 3) had the minimum solar investment payback period. College-base load (case 4) resulted in the lowest cost per exergy loss increase and capital cost payback period. Interestingly the College-electricity only plant (case 5, which had the lowest LCOE) had low profits without any ice production, and subsequently the payback periods for the capital and solar investment were high at 44 and 36 years respectively (see Table 6.3). However, payback periods for the capital cost would be decreased if larger subsidies, such as those for un-electrified rural areas of India were available, or larger facilities were built with higher performance turbines and chillers implemented. A solar field subsidy of 60% would have resulted in a capital cost payback period of 20 years for case 1 and 9 years for case 4.

An increase in feedstock price would have resulted in the solar payback periods being considerably reduced. Biomass feedstock prices for rice husk have increased significantly in recent years from 8 $/tonne to 50 $/tonne [18]. Kapur et al. in 1996 reported a rice husk cost of 4–20 $/tonne [216] and according to Afzal et al. the cost, in 2011, ranged from 30–60 $/tonne [217]. The printing factory reported an 84 $/tonne increase over a 6 years period for their bio-bricks. For the hybrid plant case studies it was observed that a 1.2 – 3.2 times cost increase in biomass would have resulted in comparable levelised energy costs with biomass-only operation. Likewise, a 47.7 – 98.5% capital subsidy or cost decrease, for the solar technology would have had similar results (see Table 6.4).

Table 6.4: Solar field subsidy and cost of biomass for the hybrid plants with selected SM to be cost competitive with biomass only-operation, i.e. same levelised energy costs.

Case study	(1) Gujarat LFR plant	(2) Gujarat ELFR Plant	(3) College -peak load	(4) College -base load	(5) College -electricity	(6) Printing factory
Solar field subsidy (%)	48	48	71	96	99	81
Cost of biomass ($/tonne)	62	62	90	155	165	200

In these case studies hybridisation reduced dependency on biomass and land by around 14–29%. Consequent amount of land saved will be highly dependent on biomass crop yield

and supply assumptions. Crop yield is highly variable. For example, rice paddy has an upper and lower yield of 2.5–7 t/ha.a, and wheat has a yield range of 1.5–9 t/ha.a [218]. With large amounts of agricultural waste produced in India, such as coconut shells, sawdust and rice husk, it could have been argued that there was no land requirement to grow these fuels. However, these agro-wastes still need to be prepared (dried), transported and stored, which accounts for the majority of the biomass cost. Furthermore, in certain regions of India, land is expensive and availability is low. Water shortage is also causing difficulties with growing biomass crops, especially as agricultural land is used for growing edible crops. Therefore, the reduced dependency on biomass in these hybrid plants was considered a significant benefit due to increasing feedstock prices, biomass exploitation and transportation and storage difficulties [17].

Q5. Which is the most feasible application for a hybrid solar-biomass power plant; tri-generation, electricity generation or industrial process heat?

The feasibility of alternative hybrid solar-biomass power plant applications will be highly dependent on regional energy policies. For the case studies presented, which assumed similar financing and key design priorities, the tri-generation and industrial process heat applications were considered to be feasible for a hybrid plant, providing a plant is carefully designed to maximise the efficient use of reject heat. Among the case studies, a tri-generation base load hybrid plant scenario (case 4) resulted in the lowest cost per exergy loss (13.9 $/GJ/a), levelised energy cost (18.1 ¢/kWh) and capital cost payback period (18 years). A constant base load mode of operation improved the viability of a hybrid system, increasing plant efficiencies and reducing the cost per exergy loss, levelised energy cost and capital cost payback period. Hybrid plants for off-grid applications in India, eligible for a 60% capital subsidy, presented an even more attractive option for investors. With the current technologies on the market, however, larger subsidies would be required for an electricity only plant at the less than 10MW scale. An off-grid tri-generation plant is recommended as the most feasible application for a hybrid solar-biomass power plant and should therefore be the focus for policymakers and renewable energy power plant developers in India.

6.5.1 Further work

The case studies covered alternative financial baseline values, e.g. feedstock price, fixed charge rate, component costs and capital subsidies. However, the monetary values assumed could be further varied to investigate the sensitivity of levelised energy/electricity costs

and payback periods. Additional factors could be considered such as inflation, tax, varying annual feedstock prices and alternative worldwide site locations with varying capital subsidies and tariffs. Further applications for the effective use of reject heat should also be modelled. For example, alternative refrigeration systems – air conditioning, multi-effect distillation and double effect absorption chillers – could be considered. Applications of the hybrid tri-gen plant to the food processing industry could also be investigated further, such as, plant integration with a rice mill, where the husk would provide some of the biomass fuel. Reject heat could be used for feed water pre-heating, which will improve plant efficiency and reduce costs as the solar thermal field size could be decreased due to a higher inlet temperature. Thermal storage options in DSG systems, will improve efficiencies, solar share, load stability and reduce costs and payback periods. One type of thermal storage, the steam accumulator, currently offers one of the best options to improve load stability, compensating for the fast transients in DSG. Accumulators act as a storage buffer and have been successfully integrated in several solar thermal projects [219, 220].

A more detailed energy and exergy analysis of a hybrid plant's components (pumps, turbine stages, chiller, feed-water heaters, fans, condenser, deaerator, storage tanks, etc.) could be carried out to investigate the major sources of irreversibilities and thus identify which components would benefit the most from technological improvements. Optimisation of a plant's operating temperature could also be achieved by extension of the energy-exergy analysis. Indeed, improvements can be made to hybrid plants and future case specific studies will require more detailed analysis. An interesting study would be a detailed comparison of hybrid ELFR-, LFR- and PTC-biomass power plants.

The modelling assumed several simplifications regarding the control of the plants. The mass flow in the solar field was controlled to achieve a constant temperature and pressure. However, in practice this is difficult as overshoot can occur. The concept of hybridising solar and biomass for steam generation to power directly a turbine raises numerous control challenges. There are a number of non-linear variables and steam turbines only tolerate temperature and load fluctuations of a few degrees and percent per minute [220]. Superheated steam generated directly in the solar field exhibits fast transients as a result of the variable solar input and demand changes at the boiler, and this can result in difficulties with maintaining drum pressure and water level. Thus, hybrid solar-biomass power plants will require high-quality control systems which should be the focus of further work. One manufacturer of an LFR system claims that they have already developed a predictive

control system that is capable of maintaining pressure, temperature and flow for varying solar inputs [100]. By implementing suitable control strategies a fast boiler response time, and constant pressure, temperature and flow should also be achievable. Kalogirou [221] presents a comprehensive review on artificial intelligence systems for combustion processes, including boilers and gas engines. However, the best control scheme for a steam boiler to attain a fast response remains an open problem.

The solar multiple could also have been selected using a decision-making technique. Multi-criteria decision-making procedures have been demonstrated in previous chapters to be effective approaches in renewable energy planning to rank alternatives for explicitly better and more informed decisions. To specify a suitable solar multiple for a hybrid plant, an MCDM strategy would be particularly useful as it is a multifaceted problem with a number of potential criteria to consider. Detailed design priorities for a hybrid plant application could also be established using MCDM methods to facilitate discussion among designers and stakeholders.

6.6 Conclusion

Having considered the answers to the research questions posed in this chapter, the future prospects for the use of the LFR and ELFR in hybrid solar-biomass power plants are now addressed.

For small-mid scale applications (2-10 MW thermal), hybrid solar-biomass power plants are a feasible option for tri-generation (electricity, cooling and heat) in India, providing solar capital subsidies remain in place (30% grid-connected, 60% off-grid). With these subsidies, both the LFR and ELFR are viable solar thermal technologies for hybrid plants. Hybrid plants for industrial process heat also present a viable option for applications with an effective utilisation of heat. At these scales there are better options for generating electricity only. The comparison between the LFR and ELFR for application to the hybrid plant in Gujarat, found that the ELFR increased a solar field's energy and exergetic efficiencies by 8% and 7% respectively, with only a 0.3 ¢/kWh and 1.4 years increase in levelised energy costs and capital cost payback period. The ELFR solar field also resulted in additional biomass (100 t/a) and land (9 ha/a) being saved. For hybrid plants located in isolated areas with high land costs the ELFR will significantly reduce levelised energy costs.

Hybrid solar-biomass power plants will become an increasingly attractive option as steam energy storage methods improve, solar thermal costs decrease and biomass feedstock and fossil fuel prices rise. Focus should be given to making technological improvements to the heat cycle of small scale hybrid plants due to low energy and exergetic efficiencies. While biomass-only systems are currently more economically viable, for a small levelised energy cost increase (1.8–5.2 ¢/kWh), hybrid systems can play an important role in tackling the biomass supply chain issues in India and worldwide (14–29% biomass and land reduction). Furthermore, the price of feedstock is rapidly rising and an additional 1.2 – 3.2 times increase will result in hybrid systems becoming cost competitive with biomass-only. It was concluded that energy policymakers in India should prioritise subsidies for hybrid tri-generation systems to promote the concept to potential investors and plant developers, thus establishing the technology in the market. Hybrid plants should be up-scaled in India for electricity generation; this would aid in keeping solar thermal a competitive option in comparison to alternative renewable energy technologies and establish India as a global leader on hybrid solar-biomass power systems.

6.7 Chapter summary

Assessment was made of the feasibility for hybrid solar-biomass power plants for use in India in various applications including tri-generation, electricity generation and industrial process heat. To cover this breadth of scenarios six case studies with peak thermal capacities ranging from 2–10 MW were analysed with the help of simulation models developed in TRNSYS. Evaluations were made against technical, financial and environmental criteria. Suitable solar multiples, based on the trade-offs among the various criteria, ranged from 1–2.5. Compared to conventional energy sources, levelised energy costs were high – but competitive in comparison to other renewables such as photovoltaic and wind. Long payback periods for the hybrid plants (ranging from 18–44 years) mean that they cannot compete directly with biomass-only systems. However, a 1.2 – 3.2 times increase in feedstock price would have resulted in the hybrid systems becoming cost competitive. Furthermore, in comparison to biomass-only, the hybrid plants saved up to 29% biomass and land with an 8.3–24.8 $/GJ/a and 1.8–5.2 ¢/kWh increase in cost per exergy loss and levelised energy cost. It was concluded that hybrid solar-biomass power plants will become an increasingly attractive option as the costs of solar thermal collectors fall and feedstock, fossil fuel and land prices continue to rise. In the foreseeable future, solar will continue to rely on subsidies and it was recommended to subsidise preferentially tri-generation plants.

Chapter 7

Conclusions

7.1 Introduction

This concluding chapter provides a summary of the whole thesis and evaluates the research outcomes, responding to the original aim and objectives outlined in Section 1.7. Each objective is recalled and a summary of the studies that were performed in order to answer them is provided. In addition, the original contributions to knowledge that this thesis provides to the fields of renewable and solar thermal energy, arising through these studies, are highlighted with reference to earlier studies. The extent to which the overall thesis aim has been achieved is assessed. Final remarks are made on the recommendations for further work.

7.2 Responses to objectives

Objective 1: Select solar thermal collector technology for power generation in India

Objective 1.1: *Review current solar thermal technology options*

To meet this objective a literature review of the primary concentrating solar thermal power technology options was performed in Chapter 2. The review identified the main technology alternatives to be the parabolic trough collector, heliostat field collector, linear Fresnel reflector, parabolic dish reflector, compound parabolic concentrator and linear Fresnel lens. The review also encompassed alternative receiver-heat transfer fluid configurations, including synthetic oil, direct steam generation, molten salt, air and the Stirling engine. As an output, the literature review revealed quantitative data for a series of technical, financial and environmental criteria, deemed necessary for the comparison of these CSP technologies.

Objective 1.2: *Establish method for evaluating and selecting a solar thermal collector for India*

This objective also was achieved in Chapter 2. The outputs of the literature study fed into a multi-criteria decision-making method known as the analytical hierarchy process, which was developed by Thomas. L. Saaty [50]. The AHP is a tool that provides a structured approach to the analysis of complex problems. It is particularly suited to multifaceted problems where there are both quantitative and qualitative data, as it incorporates factual information and expert opinion into the decision rationale. Thus, the AHP is suited for

indicating the best solar thermal technology option for a given region or country, as there is a large number of choices and variations in expert opinion. There are several MCDM managerial tools that have been implemented for a wide range of applications and the AHP is one of the most popular techniques. However, AHP has been relatively neglected in the field of solar thermal.

Qualitative data for the AHP study was gathered through a workshop, consisting of a panel convened at the Solar Energy Centre in Delhi, India, to obtain expert opinion. The AHP study indicated the preferred solar thermal technology option for north-west India to be the linear Fresnel lens or reflector type collector. Subsequently, the LFR was pursued in the subsequent chapters. It was concluded that while the AHP suffers from several known drawbacks – subjectivity never reduced to zero, no indication of poor judgements and result dependence on inclusion of irrelevant alternatives – it provides a strong and proven approach to decision-making, and should be used in the future for technology selection in the field of renewable energy.

The contributions to knowledge made under this first objective are:

- Comparative quantitative data for the technical, financial and environmental considerations for solar thermal collector technologies in India.
- Identification and application of an appropriate multi-criteria decision-making methodology for solar thermal technology selection, indicating the preferred technologies for Gujarat, India, to be the linear Fresnel lens and reflector.

The work contain within Chapter 1 has been published in the journal *Energy*:
J.D. Nixon, P.K. Dey and P.A. Davies: Which is the best solar thermal collection technology for electricity generation in north-west India? Evaluation of options using the analytical hierarchy process. Energy, 35(12), 5230–5240. (2010).

Objective 2: Improve selected solar thermal collector for applications in India

Objective 2.1: *Determine avenues of optimisation for the selected solar collector.*

This objective was accomplished in Chapter 3. The LFR was further investigated to determine the technology's current advantages and drawbacks. Existing research was reviewed and research gaps were identified. One particular disadvantage of the LFR was a low annual optical efficiency, due to shading and blocking caused by adjacent rows. Subsequently, a method was sought to optimise the LFR mirror spacing arrangement, and

apply it to a prototype LFR constructed by the author and project partners in Vapi, India. Building upon the work of Mathur at al. [129], a cost-exergy optimisation approach was developed that maximises the LFR's exergy and operational hours, and minimises capital costs. In addition, the ideal operating temperature of the collector was indicated. This was achieved by the detailed optical modelling of a series of alternative mirror spacing arrangements by means of ray-tracing to determine an incident angle dependant optical efficiency. Thus, annual performance could be modelled for a typical meteorological year. For a prototype collector developed in Vapi, Gujarat, the cost-exergy optimisation indicated an ideal operating temperature of 300 °C and a mirror arrangement spaced for the onset of shadowing to occur at a solar profile angle of 45°. In comparison to Mathur's conventional method for specifying the mirror spacing arrangement in an LFR system, the cost-exergy method was found to increase the annual exergy by 9 % with an additional 122 operational hours per annum predicted.

Objective 2.2: *Investigate new concepts based on the selected solar collector technology to further improve its design*

In Chapter 4 this objective was achieved through the development and application of a multi-criteria decision-making methodology comprising AHP, QFD and Pugh selection matrix. To establish design priorities for a novel solar thermal collector, the house of quality (the primary phase of QFD) was used. The customer requirements for this study were extracted from the AHP results in Chapter 2. With design priorities established, three novel LFR concepts were developed. A Pugh selection matrix was completed to make a weighed judgement based on the design priorities to select one concept to pursue. Consequently, an Elevation LFR design was chosen. To validate the selected concept a detailed technical and financial analysing was performed to compare the ELFR to a conventional LFR. The ELFR increased annual exergy, optical efficiency, operational hours and capital cost by 13–23%, 9–25%, 9–24% and 16–28% respectively. In comparison to an LFR with a horizontal variable mirror spacing arrangement, the ELFR reduced land usage by as much as 17%. It was concluded that the ELFR is particular suited for applications with low land availability and high land costs, and the methodology outlined has a wider potential for future design and decision activities in the field of solar thermal and renewable energy.

Objective 2.3: *Describe a model to simulate selected solar collector and build a prototype for demonstration and experimental verification.*

This objective was met in Chapter 5. Theoretical models were outlined that would enable the energy gained by a heat transfer fluid in an LFR system to be simulated. Modelled parameters included the heat loss coefficient, thermal efficiency, and stagnation temperature. Details of a prototype ELFR constructed on the roof of Aston University and an experimental set-up were also described. Measured and predicted HTF temperature gains demonstrated a good agreement with a maximum recorded deviation of 5%. A number of insights were gained by demonstrating the ELFR prototype and, as a result, design recommendations were made for a final ELFR product.

The following contributions to knowledge under the second objective are:

- Establishment of a new and improved method in comparison to the conventional technique reported in the literature for specifying the mirror spacing arrangement in an LFR system, leading to a recommended optimum mirror spacing arrangement specified for the onset of shadowing at a solar profile angle 45°.
- Development of a novel solar collector, termed the 'Elevation Linear Fresnel Reflector' (ELFR), improving an LFR's annual optical efficiency and land usage.

The study completed in Chapter 3 has been published in *Solar Energy*. The work contained within Chapter 4 is 'under review' by the journal *Energy Conversion and Management.*

J.D. Nixon and P.A. Davies: Cost-exergy optimisation of linear Fresnel reflectors. Solar Energy, 86(1), 147-156. (2012).

J.D. Nixon, P.K. Dey and P.A. Davies: Design of a novel solar thermal collector using a multi-criteria decision-making methodology. Energy Conversion and Management, 'Under Review' (2012).

Objective 3: Evaluate the feasibility of hybrid solar-biomass power plants in India

Objective 3.1: *Perform a technical, financial and environmental study of alternative hybrid plant applications in India*

This objective was met in Chapter 6. A model was developed in a transient simulation package to analyse a series of hybrid plant case studies for small-mid scale (2 – 10 MW thermal) applications, including: tri-generation (electricity, ice and heat), electricity generation and process heat. The case studies were evaluated by reviewing a series of technical, financial and environmental considerations. It was concluded that a tri-

generation hybrid plant was the most feasible application to improve India's energy issues – biomass availability, food perseveration and lack of rural electrification – at an acceptable levelised energy cost, providing financial incentives remain in place.

Objective 3.2: *Investigate the suitable sizing of the solar thermal field for hybrid operation with a biomass boiler for alternative plants, including the Gujarat hybrid plant*

This objective was also answered in Chapter 6. Alternative hybrid plant case studies, which included two versions of the Gujarat plant (one with an LFR solar field and the other with an ELFR solar field), a tri-gen and electricity-only plant for a College and an industrial process heat printing factory, were modelled for a range of solar inputs, specified by the solar multiple. As a result, a recommendation was provided on the most suitable solar multiple for each case study by considering the plants' energy and exergetic efficiencies, cost per exergy losses, levelised costs, payback periods and biomass and land saving. For the Gujarat plant operating with an LFR solar field, a solar multiple of 1.5, a solar field aperture area of 14,025 m^2, was recommended. In comparison to biomass-only operation, a solar multiple of 1.5 resulted in a biomass saving of 2200 tonnes per annum and a 1.8 ¢/kWh increase in the levelised energy cost. It was further predicted that 169 hectares of land would be saved and 12,450 tonnes of ice produced per annum. Depending on site location, an ELFR solar field may reduce levelised energy costs and increase plant performance, thus increasing biomass and land saving.

For the third and final objective the contributions to knowledge are:

- Characterisation of the key technical, financial and environmental considerations for specifying the solar multiple of hybrid solar-biomass power plants to be the energy efficiencies, exergetic efficiencies, cost per exergy losses, levelised cost of electricity, levelised energy cost, payback period on total capital cost, payback period on cost of solar field, mass of biomass saved and resulting land saved.
- It has been established that a suitable solar multiple for varying hybrid solar-biomass power plant applications ranges from 1 to 2.5.
- An off-grid tri-generation plant is the most feasible application for a hybrid solar-biomass power plant in India.

The study performed in Chapter 6 for the third objective has been published in *Energy*. Preliminary work was also published for the *World Renewable Energy Congress XI*.

J.D. Nixon, P.K. Dey and P.A. Davies: The feasibility of hybrid solar-biomass power plants in India. Energy, 46(1), 541–554. (2012).

J.D. Nixon, Z. Engineer, A. Hossain and P.A. Davies: A hybrid solar-biomass power plant for India, World Renewable Energy Congress XI, Abu Dhabi. 'Conference Proceedings' (2010).

7.3 Response to overall aim

The overall aim of this thesis is to specify the design details of a solar thermal collector and evaluate the feasibility of application to hybrid CSP-biomass power plants in India.

It is considered that the overall aim of the thesis was successfully achieved through the research outcomes for the aforementioned objectives. The philosophy implemented in this thesis was to combine engineering and management perspectives to advance solar thermal technologies for sustainable energy applications. In Chapter 2, the decision for which solar thermal technology to pursue was made using the analytical hierarchy process, a multi-criteria decision-making tool. As a result of the AHP and other practical constraints, the linear Fresnel reflector was chosen. Chapter 3 presented a techno-economic optimisation method for the LFR, improving performance and minimising costs. In Chapter 4 operational research techniques were used to formulate and select a novel Elevation Linear Fresnel Reflector concept. Chapter 5 outlined and validated theoretical models for the performance of LFR systems. Combining the studies contained within Chapters 3, 4 and 5, alternative case study applications for a hybrid plant operating with an LFR type solar thermal field were proposed and analysed. As a result, the mirror aperture area of the solar field was selected for each hybrid plant scenario. The feasibility of hybrid solar-biomass applications with a 2 – 10 MW thermal capacity will be case specific. However a general conclusion was that tri-generation systems have the greatest potential (considering energy and exergetic efficiencies, cost per exergy losses, levelised costs, payback periods and biomass and land saved) and should be the focus for policymakers, investors and plant developers in India.

The author considers that a key contribution of this thesis is the Elevation Linear Fresnel Reflector. In comparison to the conventional LFR, the ELFR increases capital costs (16–28%), however improves performance (9 –25% increase in optical efficiency), reduces auxiliary fuel/storage demand (13–23% increase in operational hours) and land usage (17%), and has the potential to decrease a power plants levelised energy costs (up to 10%).

Therefore the ELFR is thought to have considerable potential for solar thermal applications in India and elsewhere.

It is considered that the research performed using engineering and decision science methods has successfully specified the design details and methodologies for the Gujarat plant's solar collector and solar thermal field. The preliminary research performed on the hybrid LFR-biomass power plants in India highlights the feasibility of applications for tri-generation as well as electricity generation and industrial process heat. The overall thesis philosophy is considered to contribute towards promoting combined engineering and management methodologies in R&D, and enhancing the candidacy of solar thermal applications worldwide.

7.4 Final remarks

The solar thermal field for a hybrid solar-biomass power plant was thoroughly investigated in this thesis as it was considered the critical component for the feasibility of such plants. However, hybrid solar-biomass power plants would benefit from additional research covering the solar field and other components. Hybrid plants could be analysed for a range of alternative CSP technologies, e.g. parabolic trough and heliostat field collector. Bespoke components for the heat cycle of small-scale hybrid applications should be researched to improve the low energy and exergetic efficiencies. The control system for a case specific hybrid plant will also need to be optimised. The entire hybrid plant heat cycle was also not considered – piping layout, pump sizing, structure, etc. – and will need to be specified. Additional LFR prototypes will also need developing and finalising in India. This may include an LFR with curved mirror elements or an ELFR system to gather cost data.

The studies performed for the CSP technology and hybrid plant have been primarily theoretical. The next stage for the hybrid plant project in Gujarat will be the construction of the plant using the design recommendations from this thesis. The technical aspects of the system will be assessed during real operational conditions. Further recommendations are to perform site location measurements for the direct irradiance to validate the TMY model, as the effects of dust and haze in India can have major influence on the site specific insolation. The following phase for the plant will be the integration of a rice mill for concept demonstration. The commercial feasibility of the plant will then be addressed for the deployment of additional installations.

Sustainable energy systems are growing in complexity, as is managing the strategic decisions for technology selection, deployment, and research and development. Operations research is a fundamental area of business management and will play an important role in the future of decision-making in sustainable engineering. A review of multi-criteria decision-making analyses for technology selection and deployment in the field of sustainability will highlight areas for further research to make an impact and contribution in the renewable energy sector.

Appendices

Appendix 1: Analytical hierarchy process example calculation

Appendix 2: Pair-wise comparison matrices of solar collectors

Appendix 3: Analytical hierarchy process case scenarios

Appendix 4: Pair-wise comparison of criteria for Gujarat, Southern Spain, Mojave Desert and the Sahara Desert

Appendix 5: ELFR component engineering drawings

Appendix 6: Exploded sub-assemblies and bill of materials

Appendix 7: Wind force calculations

Appendix 8: Control board circuit schematics

Appendix 9: Pyrheliometer calibration certificate

Appendix 10: Hybrid plant case study results

Appendix 1

Analytical hierarchy process example calculation

A-1.1 AHP sample calculation

The criteria for the AHP were derived from the functional requirements and product characteristics. During the review process of solar collectors the technological alternatives were assessed in terms of their technical, financial and environmental viability, to develop a series of sub problems to be analysed (Table A-1.1).

Table A-1.1: Sub criteria selected for the AHP study.

TECHNICAL	
Efficiency	Ideal conversion efficiency
	Collector efficiency
	Stagnation temperature
	Optical efficiency
	Concentration Ratio
	Half acceptance angle
	Parasitic load
Compatibility with working fluid	Pressure Tolerance
	Temperature Tolerance
	Chemical compatibility of heat transfer medium
Reliability	Annual replacement of parts
Availability	Use of standard technologies or parts
FINANCIAL	
Affordability	Capital cost
	Total O&M cost
Environmental	
Resource usage	Land usage
	Slope tolerance
	Water usage
Scalability	Efficiency at different scales
	Suitable operating range

The following solar technologies were selected as the possible solution alternatives from the review (Table A-1.2).

Table A-1.2: List of the solar technology alternatives used in the AHP study.

Solar Technology Alternatives	Acronym
Parabolic Trough using Synthetic Oil	PTC – Oil
Parabolic Trough with Direct Steam Generation	PTC – DSG
Heliostat Field Collector with a Water/Steam Receiver	HFC – Water/Steam
Heliostat Field Collector with a Molten Salt Receiver	HFC – Salt
Heliostat Field Collector with a Volumetric Air Receiver	HFC – Air
Compact Linear Fresnel Reflector	CLFR
Linear Fresnel Reflector	LFR
Parabolic Dish Reflector	PDR
Compound Parabolic Collector	CPC
Fresnel Lens with a Secondary Compound Parabolic Collector	CPC – Fresnel lens

The method for the AHP analysis is discussed and partially demonstrated for the chemical compatibility criteria. The full analysis can be found in Appendix 2 - 4.

An order of preference for each criterion is first established, and a decision hierarchy tree is developed. Data obtained on each collector was used to determine the favoured order for the decision tree and judgment or expert opinion was used where data was unavailable (Figure A-1.1).

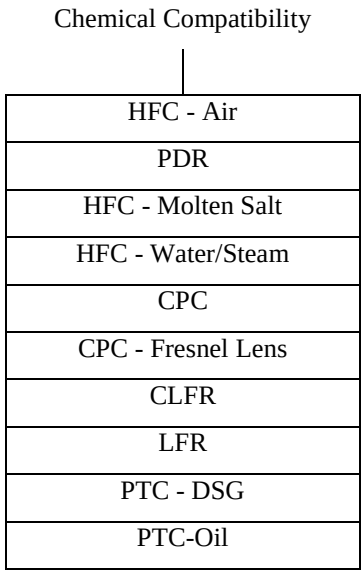

Figure A-1.1: The Decision Hierarchy Tree for sub criteria chemical compatibility.

To establish how much a certain collector was favoured over another for a given criteria, priorities were ascertained to develop the Pair-wise Comparison Matrix. Judgment of preference was selected on a scale of one to nine

The Pair-wise Comparison Matrix is a mathematical process which orders the decision tree into a matrix for the comparison scale to be applied.

A priority vector for each collector in terms of chemical compatibility was then calculated by dividing each cell by the total column value and averaging the row (see Tables A-1.4 and A-1.5).

Table A-1.3: Pair-wise comparison matrix showing how preferred each alternative is in terms of their chemical compatibility.

	HFC-air	PDR	HFC-salt	HFC-H20	CPC	CPC-fl	CLFR	LFR	PTC-dsg	PTC-oil
HFC-air	1	1	2	3	3	3	3	3	5	5
PDR	1.00	1	2	3	3	3	3	3	5	5
HFC-salt	0.50	0.50	1	2	2	2	2	2	4	4
HFC-H20	0.33	0.33	0.50	1	1	1	1	1	3	3
CPC	0.33	0.33	0.50	1.00	1	1	1	1	3	3
CPC-fl	0.33	0.33	0.50	1.00	1.00	1	1	1	3	3
CLFR	0.33	0.33	0.50	1.00	1.00	1.00	1	1	3	3
LFR	0.33	0.33	0.50	1.00	1.00	1.00	1.00	1	3	3
PTC-dsg	0.20	0.20	0.25	0.33	0.33	0.33	0.33	0.33	1	1
PTC-oil	0.20	0.20	0.25	0.33	0.33	0.33	0.33	0.33	1.00	1
Total	4.57	4.57	8.00	13.67	13.67	13.67	13.67	13.67	31.00	31.00

Table A-1.4: Priority vectors of each alternative for the chemical compatibility.

	HFC-air	PDR	HFC-salt	HFC-H20	CPC	CPC-fl	CLFR	LFR	PTC-dsg	PTC-oil	Priority Vector
HFC-air	0.22	0.22	0.25	0.22	0.22	0.22	0.22	0.22	0.16	0.16	0.211
PDR	0.22	0.22	0.25	0.22	0.22	0.22	0.22	0.22	0.16	0.16	0.211
HFC-salt	0.11	0.11	0.13	0.15	0.15	0.15	0.15	0.15	0.13	0.13	0.133
HFC-H20	0.07	0.07	0.06	0.07	0.07	0.07	0.07	0.07	0.10	0.10	0.077
CPC	0.07	0.07	0.06	0.07	0.07	0.07	0.07	0.07	0.10	0.10	0.077
CPC-fl	0.07	0.07	0.06	0.07	0.07	0.07	0.07	0.07	0.10	0.10	0.077
CLFR	0.07	0.07	0.06	0.07	0.07	0.07	0.07	0.07	0.10	0.10	0.077
LFR	0.07	0.07	0.06	0.07	0.07	0.07	0.07	0.07	0.10	0.10	0.077
PTC-dsg	0.04	0.04	0.03	0.02	0.02	0.02	0.02	0.02	0.03	0.03	0.031
PTC-oil	0.04	0.04	0.03	0.02	0.02	0.02	0.02	0.02	0.03	0.03	0.031
Total	1.00	1.00	1.00	1.00	1.00	1.00	1.00	1.00	1.00	1.00	

The consistency index Eq.(2.1) was calculated as 0.14. The random consistency index is stated as 1.45 for an *m* value of 9 (see Table 2.4). The consistency ratio Eq.(2.2) could then be calculated and there was an acceptable consistency of 0.097 or 9.7%.

Appendix 2

Pair-wise comparison matrices of solar collectors

A-2.1 Pair-wise comparison matrices for collector priority vectors

Table A-2.1: Pair-wise comparison matrix for Ideal Conversion Efficiency.

	PDR	HFC-air	HFC-H20	HFC-salt	PTC-dsg	PTC-oil	CLFR	LFR	CPC-fl	CPC	Priority Vector
PDR	0.30	0.36	0.32	0.32	0.32	0.27	0.21	0.19	0.19	0.17	0.266
HFC-air	0.15	0.18	0.21	0.21	0.21	0.20	0.18	0.16	0.16	0.15	0.183
HFC-H20	0.10	0.09	0.11	0.11	0.11	0.13	0.14	0.14	0.14	0.13	0.119
HFC-salt	0.10	0.09	0.11	0.11	0.11	0.13	0.14	0.14	0.14	0.13	0.119
PTC-dsg	0.10	0.09	0.11	0.11	0.11	0.13	0.14	0.14	0.14	0.13	0.119
PTC-oil	0.08	0.06	0.05	0.05	0.05	0.07	0.11	0.11	0.11	0.11	0.080
CLFR	0.05	0.04	0.03	0.03	0.03	0.02	0.04	0.05	0.05	0.07	0.040
LFR	0.04	0.03	0.02	0.02	0.02	0.02	0.02	0.03	0.03	0.04	0.027
CPC-fl	0.04	0.03	0.02	0.02	0.02	0.02	0.02	0.03	0.03	0.04	0.027
CPC	0.04	0.03	0.02	0.02	0.02	0.01	0.01	0.01	0.01	0.02	0.019
Total	1.00	1.00	1.00	1.00	1.00	1.00	1.00	1.00	1.00	1.00	

Table A-2.2: Pair-wise comparison matrix for Concentration Ratio.

	PDR	HFC-H20	HFC-salt	HFC-air	PTC-dsg	PTC-oil	CLFR	LFR	CPC-fl	CPC	Priority Vector
PDR	0.22	0.22	0.22	0.24	0.22	0.22	0.20	0.20	0.18	0.14	0.209
HFC-H20	0.22	0.22	0.22	0.24	0.22	0.22	0.20	0.20	0.18	0.14	0.209
HFC-salt	0.22	0.22	0.22	0.24	0.22	0.22	0.20	0.20	0.18	0.14	0.209
HFC-air	0.11	0.11	0.11	0.12	0.18	0.18	0.17	0.17	0.16	0.14	0.145
PTC-dsg	0.04	0.04	0.04	0.03	0.04	0.04	0.07	0.07	0.08	0.10	0.056
PTC-oil	0.04	0.04	0.04	0.03	0.04	0.04	0.07	0.07	0.08	0.10	0.056
CLFR	0.04	0.04	0.04	0.02	0.02	0.02	0.03	0.03	0.05	0.08	0.038
LFR	0.04	0.04	0.04	0.02	0.02	0.02	0.03	0.03	0.05	0.08	0.038
CPC-fl	0.03	0.03	0.03	0.02	0.01	0.01	0.02	0.02	0.03	0.06	0.027
CPC	0.02	0.02	0.02	0.01	0.01	0.01	0.01	0.01	0.01	0.02	0.014
Total	1.00	1.00	1.00	1.00	1.00	1.00	1.00	1.00	1.00	1.00	

Table A-2.3: Pair-wise comparison matrix for Collector Efficiency.

	HFC-air	HFC-H20	HFC-salt	PDR	PTC-dsg	PTC-oil	CLFR	LFR	CPC-fl	CPC	Priority Vector
HFC-air	0.21	0.21	0.21	0.23	0.21	0.21	0.17	0.17	0.17	0.17	0.196
HFC-H20	0.21	0.21	0.21	0.23	0.21	0.21	0.17	0.17	0.17	0.17	0.196
HFC-salt	0.21	0.21	0.21	0.23	0.21	0.21	0.17	0.17	0.17	0.17	0.196
PDR	0.10	0.10	0.10	0.11	0.14	0.14	0.14	0.14	0.14	0.14	0.128
PTC-dsg	0.07	0.07	0.07	0.06	0.07	0.07	0.11	0.11	0.11	0.11	0.086
PTC-oil	0.07	0.07	0.07	0.06	0.07	0.07	0.11	0.11	0.11	0.11	0.086
CLFR	0.03	0.03	0.03	0.02	0.02	0.02	0.03	0.03	0.03	0.03	0.028
LFR	0.03	0.03	0.03	0.02	0.02	0.02	0.03	0.03	0.03	0.03	0.028
CPC-fl	0.03	0.03	0.03	0.02	0.02	0.02	0.03	0.03	0.03	0.03	0.028
CPC	0.03	0.03	0.03	0.02	0.02	0.02	0.03	0.03	0.03	0.03	0.028
Total	1.00	1.00	1.00	1.00	1.00	1.00	1.00	1.00	1.00	1.00	

Table A-2.4: Pair-wise comparison matrix for Half-Acceptance Angle.

	CPC	CPC-fl	HFC-air	HFC-salt	HFC-H20	LFR	CLFR	PTC-dsg	PTC-oil	PDR	Priority Vector
CPC	0.31	0.38	0.36	0.31	0.31	0.26	0.26	0.22	0.22	0.16	0.279
CPC-fl	0.16	0.19	0.24	0.23	0.23	0.21	0.21	0.18	0.18	0.16	0.199
HFC-air	0.10	0.10	0.12	0.16	0.16	0.16	0.16	0.15	0.15	0.13	0.137
HFC-salt	0.08	0.06	0.06	0.08	0.08	0.10	0.10	0.11	0.11	0.11	0.090
HFC-H20	0.08	0.06	0.06	0.08	0.08	0.10	0.10	0.11	0.11	0.11	0.090
LFR	0.06	0.05	0.04	0.04	0.04	0.05	0.05	0.07	0.07	0.09	0.057
CLFR	0.06	0.05	0.04	0.04	0.04	0.05	0.05	0.07	0.07	0.09	0.057
PTC-dsg	0.05	0.04	0.03	0.03	0.03	0.03	0.03	0.04	0.04	0.07	0.036
PTC-oil	0.05	0.04	0.03	0.03	0.03	0.03	0.03	0.04	0.04	0.07	0.036
PDR	0.04	0.03	0.02	0.02	0.02	0.01	0.01	0.01	0.01	0.02	0.020
Total	1.00	1.00	1.00	1.00	1.00	1.00	1.00	1.00	1.00	1.00	

Table A-2.5: Pair-wise comparison matrix for Parasitic Load.

	CPC	CPC-fl	LFR	CLFR	PDR	PTC-oil	HFC-air	PTC-dsg	HFC-salt	HFC-H20	Priority Vector
CPC	0.34	0.42	0.39	0.35	0.31	0.25	0.25	0.22	0.20	0.20	0.292
CPC-fl	0.17	0.21	0.26	0.26	0.25	0.21	0.21	0.19	0.18	0.18	0.212
LFR	0.11	0.10	0.13	0.17	0.18	0.18	0.18	0.17	0.16	0.16	0.154
CLFR	0.09	0.07	0.07	0.09	0.12	0.14	0.14	0.14	0.13	0.13	0.112
PDR	0.07	0.05	0.04	0.04	0.06	0.11	0.11	0.11	0.11	0.11	0.081
PTC-oil	0.05	0.03	0.03	0.02	0.02	0.04	0.04	0.06	0.07	0.07	0.041
HFC-air	0.05	0.03	0.03	0.02	0.02	0.04	0.04	0.06	0.07	0.07	0.041
PTC-dsg	0.04	0.03	0.02	0.02	0.02	0.02	0.02	0.03	0.04	0.04	0.028
HFC-salt	0.04	0.03	0.02	0.01	0.01	0.01	0.01	0.01	0.02	0.02	0.019
HFC-H20	0.04	0.03	0.02	0.01	0.01	0.01	0.01	0.01	0.02	0.02	0.019
Total	1.00	1.00	1.00	1.00	1.00	1.00	1.00	1.00	1.00	1.00	

Table A-2.6: Pair-wise comparison matrix for Pressure Tolerance.

	CPC	HFC-air	PDR	LFR	CLFR	HFC-salt	HFC-H20	CPC-fl	PTC-oil	PTC-dsg	Priority Vector
CPC	0.19	0.19	0.19	0.20	0.20	0.19	0.19	0.17	0.15	0.15	0.181
HFC-air	0.19	0.19	0.19	0.20	0.20	0.19	0.19	0.17	0.15	0.15	0.181
PDR	0.19	0.19	0.19	0.20	0.20	0.19	0.19	0.17	0.15	0.15	0.181
LFR	0.09	0.09	0.09	0.10	0.10	0.12	0.12	0.13	0.12	0.12	0.110
CLFR	0.09	0.09	0.09	0.10	0.10	0.12	0.12	0.13	0.12	0.12	0.110
HFC-salt	0.06	0.06	0.06	0.05	0.05	0.06	0.06	0.08	0.09	0.09	0.068
HFC-H20	0.06	0.06	0.06	0.05	0.05	0.06	0.06	0.08	0.09	0.09	0.068
CPC-fl	0.05	0.05	0.05	0.03	0.03	0.03	0.03	0.04	0.06	0.06	0.043
PTC-oil	0.04	0.04	0.04	0.03	0.03	0.02	0.02	0.02	0.03	0.03	0.029
PTC-dsg	0.04	0.04	0.04	0.03	0.03	0.02	0.02	0.02	0.03	0.03	0.029
Total	1.00	1.00	1.00	1.00	1.00	1.00	1.00	1.00	1.00	1.00	

Table A-2.7: Pair-wise comparison matrix for Temperature Tolerance.

	PDR	HFC-air	HFC-salt	HFC-H20	PTC-dsg	PTC-oil	CLFR	LFR	CPC-fl	CPC	Priority Vector
PDR	0.25	0.26	0.30	0.22	0.25	0.21	0.20	0.20	0.16	0.15	0.218
HFC-air	0.25	0.26	0.30	0.32	0.25	0.21	0.20	0.20	0.16	0.15	0.229
HFC-salt	0.12	0.13	0.15	0.22	0.19	0.17	0.16	0.16	0.14	0.13	0.157
HFC-H20	0.12	0.09	0.07	0.11	0.19	0.17	0.16	0.16	0.14	0.13	0.134
PTC-dsg	0.06	0.06	0.05	0.04	0.06	0.13	0.13	0.13	0.12	0.11	0.089
PTC-oil	0.05	0.05	0.04	0.03	0.02	0.04	0.07	0.07	0.12	0.11	0.059
CLFR	0.04	0.04	0.03	0.02	0.02	0.02	0.03	0.03	0.07	0.08	0.039
LFR	0.04	0.04	0.03	0.02	0.02	0.02	0.03	0.03	0.07	0.08	0.039
CPC-fl	0.04	0.04	0.02	0.02	0.01	0.01	0.01	0.01	0.02	0.05	0.023
CPC	0.03	0.03	0.02	0.01	0.01	0.01	0.01	0.01	0.01	0.02	0.014
Total	1.00	1.00	1.00	1.00	1.00	1.00	1.00	1.00	1.00	1.00	

Table A-2.8: Pair-wise comparison matrix for Chemical Compatibility.

	HFC-air	PDR	HFC-salt	HFC-H20	CPC	CPC-fl	CLFR	LFR	PTC-dsg	PTC-oil	Priority Vector
HFC-air	0.22	0.22	0.25	0.22	0.22	0.22	0.22	0.22	0.16	0.16	0.211
PDR	0.22	0.22	0.25	0.22	0.22	0.22	0.22	0.22	0.16	0.16	0.211
HFC-salt	0.11	0.11	0.13	0.15	0.15	0.15	0.15	0.15	0.13	0.13	0.133
HFC-H20	0.07	0.07	0.06	0.07	0.07	0.07	0.07	0.07	0.10	0.10	0.077
CPC	0.07	0.07	0.06	0.07	0.07	0.07	0.07	0.07	0.10	0.10	0.077
CPC-fl	0.07	0.07	0.06	0.07	0.07	0.07	0.07	0.07	0.10	0.10	0.077
CLFR	0.07	0.07	0.06	0.07	0.07	0.07	0.07	0.07	0.10	0.10	0.077
LFR	0.07	0.07	0.06	0.07	0.07	0.07	0.07	0.07	0.10	0.10	0.077
PTC-dsg	0.04	0.04	0.03	0.02	0.02	0.02	0.02	0.02	0.03	0.03	0.031
PTC-oil	0.04	0.04	0.03	0.02	0.02	0.02	0.02	0.02	0.03	0.03	0.031
Total	1.00	1.00	1.00	1.00	1.00	1.00	1.00	1.00	1.00	1.00	

Table A-2.9: Pair-wise comparison matrix for Annual Replacement of Parts.

	CPC-fl	LFR	CLFR	HFC-H20	HFC-salt	HFC-air	PDR	CPC	PTC-dsg	PTC-oil	Priority Vector
CPC-fl	0.38	0.50	0.50	0.35	0.35	0.29	0.25	0.25	0.25	0.25	0.337
LFR	0.09	0.12	0.12	0.18	0.18	0.17	0.16	0.16	0.16	0.16	0.149
CLFR	0.09	0.12	0.12	0.18	0.18	0.17	0.16	0.16	0.16	0.16	0.149
HFC-H20	0.09	0.06	0.06	0.09	0.09	0.13	0.13	0.13	0.13	0.13	0.102
HFC-salt	0.09	0.06	0.06	0.09	0.09	0.13	0.13	0.13	0.13	0.13	0.102
HFC-air	0.05	0.03	0.03	0.03	0.03	0.04	0.06	0.06	0.06	0.06	0.047
PDR	0.05	0.02	0.02	0.02	0.02	0.02	0.03	0.03	0.03	0.03	0.029
CPC	0.05	0.02	0.02	0.02	0.02	0.02	0.03	0.03	0.03	0.03	0.029
PTC-dsg	0.05	0.02	0.02	0.02	0.02	0.02	0.03	0.03	0.03	0.03	0.029
PTC-oil	0.05	0.02	0.02	0.02	0.02	0.02	0.03	0.03	0.03	0.03	0.029
Total	1.00	1.00	1.00	1.00	1.00	1.00	1.00	1.00	1.00	1.00	

Table A-2.10: Pair-wise comparison matrix for Use of Standard Technologies.

	CLFR	LFR	CPC	CPC-fl	HFC-H20	PTC-dsg	HFC-salt	PTC-oil	HFC-air	PDR	Priority Vector
CLFR	0.20	0.20	0.20	0.22	0.21	0.21	0.19	0.19	0.16	0.15	0.193
LFR	0.20	0.20	0.20	0.22	0.21	0.21	0.19	0.19	0.16	0.15	0.193
CPC	0.20	0.20	0.20	0.22	0.21	0.21	0.19	0.19	0.16	0.15	0.193
CPC-fl	0.10	0.10	0.10	0.11	0.14	0.14	0.14	0.14	0.14	0.13	0.124
HFC-H20	0.07	0.07	0.07	0.06	0.07	0.07	0.09	0.09	0.11	0.11	0.081
PTC-dsg	0.07	0.07	0.07	0.06	0.07	0.07	0.09	0.09	0.11	0.11	0.081
HFC-salt	0.05	0.05	0.05	0.04	0.03	0.03	0.05	0.05	0.07	0.08	0.050
PTC-oil	0.05	0.05	0.05	0.04	0.03	0.03	0.05	0.05	0.07	0.06	0.048
HFC-air	0.03	0.03	0.03	0.02	0.01	0.01	0.02	0.02	0.02	0.05	0.024
PDR	0.02	0.02	0.02	0.01	0.01	0.01	0.01	0.01	0.01	0.02	0.015
Total	1.00	1.00	1.00	1.00	1.00	1.00	1.00	1.00	1.00	1.00	

Table A-2.11: Pair-wise comparison matrix for Capital Cost.

	CLFR	LFR	CPC	CPC-fl	HFC-H20	PTC-dsg	HFC-salt	PTC-oil	HFC-air	PDR	Priority Vector
CLFR	0.20	0.20	0.20	0.22	0.22	0.20	0.17	0.17	0.17	0.14	0.190
LFR	0.20	0.20	0.20	0.22	0.22	0.20	0.17	0.17	0.17	0.14	0.190
CPC	0.20	0.20	0.20	0.22	0.22	0.20	0.17	0.17	0.17	0.14	0.190
CPC-fl	0.10	0.10	0.10	0.11	0.11	0.13	0.14	0.14	0.14	0.13	0.121
HFC-H20	0.10	0.10	0.10	0.11	0.11	0.13	0.14	0.14	0.14	0.13	0.121
PTC-dsg	0.07	0.07	0.07	0.05	0.05	0.07	0.11	0.11	0.11	0.11	0.083
HFC-salt	0.03	0.03	0.03	0.02	0.02	0.02	0.03	0.03	0.03	0.06	0.031
PTC-oil	0.03	0.03	0.03	0.02	0.02	0.02	0.03	0.03	0.03	0.06	0.031
HFC-air	0.03	0.03	0.03	0.02	0.02	0.02	0.03	0.03	0.03	0.06	0.031
PDR	0.02	0.02	0.02	0.01	0.01	0.01	0.01	0.01	0.01	0.02	0.014
Total	1.00	1.00	1.00	1.00	1.00	1.00	1.00	1.00	1.00	1.00	

Table A-2.12: Pair-wise comparison matrix for Operations and Maintenance Cost.

	CPC-fl	LFR	CLFR	CPC	PTC-dsg	PTC-oil	HFC-air	HFC-H20	HFC-salt	PDR	Priority Vector
CPC-fl	0.23	0.23	0.26	0.26	0.24	0.21	0.19	0.19	0.19	0.15	0.216
LFR	0.23	0.23	0.26	0.26	0.24	0.21	0.19	0.19	0.19	0.15	0.216
CLFR	0.12	0.12	0.13	0.13	0.16	0.16	0.15	0.15	0.15	0.13	0.140
CPC	0.12	0.12	0.13	0.13	0.16	0.16	0.15	0.15	0.15	0.13	0.140
PTC-dsg	0.08	0.08	0.06	0.06	0.08	0.11	0.11	0.11	0.11	0.12	0.093
PTC-oil	0.06	0.06	0.04	0.04	0.04	0.05	0.08	0.08	0.08	0.10	0.062
HFC-air	0.05	0.05	0.03	0.03	0.03	0.03	0.04	0.04	0.04	0.07	0.039
HFC-H20	0.05	0.05	0.03	0.03	0.03	0.03	0.04	0.04	0.04	0.07	0.039
HFC-salt	0.05	0.05	0.03	0.03	0.03	0.03	0.04	0.04	0.04	0.07	0.039
PDR	0.03	0.03	0.02	0.02	0.01	0.01	0.01	0.01	0.01	0.02	0.015
Total	1.00	1.00	1.00	1.00	1.00	1.00	1.00	1.00	1.00	1.00	

Table A-2.13: Pair-wise comparison matrix for Land Usage.

	CLFR	PTC-dsg	CPC-fl	LFR	PTC-oil	HFC-air	HFC-H20	HFC-salt	PDR	CPC	Priority Vector
CLFR	0.31	0.36	0.36	0.36	0.36	0.24	0.24	0.24	0.19	0.16	0.283
PTC-dsg	0.10	0.12	0.12	0.12	0.12	0.15	0.15	0.15	0.13	0.13	0.128
CPC-fl	0.10	0.12	0.12	0.12	0.12	0.15	0.15	0.15	0.13	0.13	0.128
LFR	0.10	0.12	0.12	0.12	0.12	0.15	0.15	0.15	0.13	0.13	0.128
PTC-oil	0.10	0.12	0.12	0.12	0.12	0.15	0.15	0.15	0.13	0.13	0.128
HFC-air	0.06	0.04	0.04	0.04	0.04	0.05	0.05	0.05	0.08	0.09	0.054
HFC-H20	0.06	0.04	0.04	0.04	0.04	0.05	0.05	0.05	0.08	0.09	0.054
HFC-salt	0.06	0.04	0.04	0.04	0.04	0.05	0.05	0.05	0.08	0.09	0.054
PDR	0.04	0.02	0.02	0.02	0.02	0.02	0.02	0.02	0.03	0.05	0.027
CPC	0.03	0.02	0.02	0.02	0.02	0.01	0.01	0.01	0.01	0.02	0.016
Total	1.00	1.00	1.00	1.00	1.00	1.00	1.00	1.00	1.00	1.00	

Table A-2.14: Pair-wise comparison matrix for Slope Tolerance.

	PDR	HFC-air	HFC-H20	HFC-salt	PTC-oil	PTC-dsg	CLFR	LFR	CPC	CPC-fl	Priority Vector
PDR	0.19	0.19	0.19	0.19	0.19	0.19	0.19	0.19	0.19	0.19	0.192
HFC-air	0.19	0.19	0.19	0.19	0.19	0.19	0.19	0.19	0.19	0.19	0.192
HFC-H20	0.19	0.19	0.19	0.19	0.19	0.19	0.19	0.19	0.19	0.19	0.192
HFC-salt	0.19	0.19	0.19	0.19	0.19	0.19	0.19	0.19	0.19	0.19	0.192
PTC-oil	0.04	0.04	0.04	0.04	0.04	0.04	0.04	0.04	0.04	0.04	0.038
PTC-dsg	0.04	0.04	0.04	0.04	0.04	0.04	0.04	0.04	0.04	0.04	0.038
CLFR	0.04	0.04	0.04	0.04	0.04	0.04	0.04	0.04	0.04	0.04	0.038
LFR	0.04	0.04	0.04	0.04	0.04	0.04	0.04	0.04	0.04	0.04	0.038
CPC	0.04	0.04	0.04	0.04	0.04	0.04	0.04	0.04	0.04	0.04	0.038
CPC-fl	0.04	0.04	0.04	0.04	0.04	0.04	0.04	0.04	0.04	0.04	0.038
Total	1.00	1.00	1.00	1.00	1.00	1.00	1.00	1.00	1.00	1.00	

Table A-2.15: Pair-wise comparison matrix for Water Usage.

	PDR	CPC	HFC-air	HFC-salt	CPC-fl	CLFR	LFR	HFC-H20	PTC-dsg	PTC-oil	Priority Vector
PDR	0.30	0.36	0.33	0.33	0.27	0.27	0.27	0.18	0.18	0.18	0.269
CPC	0.15	0.18	0.22	0.22	0.20	0.20	0.20	0.16	0.16	0.16	0.185
HFC-air	0.10	0.09	0.11	0.11	0.14	0.14	0.14	0.13	0.13	0.13	0.121
HFC-salt	0.10	0.09	0.11	0.11	0.14	0.14	0.14	0.13	0.13	0.13	0.121
CPC-fl	0.07	0.06	0.05	0.05	0.07	0.07	0.07	0.11	0.11	0.11	0.076
CLFR	0.07	0.06	0.05	0.05	0.07	0.07	0.07	0.11	0.11	0.11	0.076
LFR	0.07	0.06	0.05	0.05	0.07	0.07	0.07	0.11	0.11	0.11	0.076
HFC-H20	0.04	0.03	0.02	0.02	0.02	0.02	0.02	0.03	0.03	0.03	0.025
PTC-dsg	0.04	0.03	0.02	0.02	0.02	0.02	0.02	0.03	0.03	0.03	0.025
PTC-oil	0.04	0.03	0.02	0.02	0.02	0.02	0.02	0.03	0.03	0.03	0.025
Total	1.00	1.00	1.00	1.00	1.00	1.00	1.00	1.00	1.00	1.00	

Table A-2.16: Pair-wise comparison matrix for the suitability to operate at the proposed scale for Southern Spain (100MW).

	PDR	HFC-air	HFC-salt	HFC-H20	PTC-dsg	PTC-oil	CLFR	LFR	CPC-fl	CPC	Priority Vector
PDR	0.18	0.18	0.18	0.18	0.19	0.19	0.18	0.18	0.16	0.13	0.176
HFC-air	0.18	0.18	0.18	0.18	0.19	0.19	0.18	0.18	0.16	0.13	0.176
HFC-salt	0.18	0.18	0.18	0.18	0.19	0.19	0.18	0.18	0.16	0.13	0.176
HFC-H20	0.18	0.18	0.18	0.18	0.19	0.19	0.18	0.18	0.16	0.13	0.176
PTC-dsg	0.06	0.06	0.06	0.06	0.06	0.06	0.09	0.09	0.10	0.10	0.075
PTC-oil	0.06	0.06	0.06	0.06	0.06	0.06	0.09	0.09	0.10	0.10	0.075
CLFR	0.05	0.05	0.05	0.05	0.03	0.03	0.04	0.04	0.06	0.09	0.049
LFR	0.05	0.05	0.05	0.05	0.03	0.03	0.04	0.04	0.06	0.09	0.049
CPC-fl	0.04	0.04	0.04	0.04	0.02	0.02	0.02	0.02	0.03	0.07	0.034
CPC	0.02	0.02	0.02	0.02	0.01	0.01	0.01	0.01	0.01	0.01	0.014
Total	1.00	1.00	1.00	1.00	1.00	1.00	1.00	1.00	1.00	1.00	

Table A-2.17: Pair-wise comparison matrix for the suitability to operate at the proposed scale for India (1MW).

	CLFR	LFR	CPC-fl	PDR	PTC-dsg	PTC-oil	HFC-air	HFC-salt	HFC-H20	CPC	Priority Vector
CLFR	0.17	0.17	0.17	0.17	0.17	0.17	0.17	0.17	0.17	0.15	0.166
LFR	0.17	0.17	0.17	0.17	0.17	0.17	0.17	0.17	0.17	0.15	0.166
CPC-fl	0.17	0.17	0.17	0.17	0.17	0.17	0.17	0.17	0.17	0.15	0.166
PDR	0.17	0.17	0.17	0.17	0.17	0.17	0.17	0.17	0.17	0.15	0.166
PTC-dsg	0.17	0.17	0.17	0.17	0.17	0.17	0.17	0.17	0.17	0.15	0.166
PTC-oil	0.06	0.06	0.06	0.06	0.06	0.06	0.08	0.08	0.08	0.10	0.068
HFC-air	0.03	0.03	0.03	0.03	0.03	0.02	0.03	0.03	0.03	0.05	0.029
HFC-salt	0.03	0.03	0.03	0.03	0.03	0.02	0.03	0.03	0.03	0.05	0.029
HFC-H20	0.03	0.03	0.03	0.03	0.03	0.02	0.03	0.03	0.03	0.05	0.029
CPC	0.02	0.02	0.02	0.02	0.02	0.01	0.01	0.01	0.01	0.02	0.015
Total	1.00	1.00	1.00	1.00	1.00	1.00	1.00	1.00	1.00	1.00	

Table A-2.18: Pair-wise comparison matrix for the suitability to operate at the proposed scale for California (500MW).

	HFC-air	HFC-salt	HFC-H20	PDR	PTC-dsg	PTC-oil	CLFR	LFR	CPC-fl	CPC	Priority Vector
HFC-air	0.19	0.19	0.19	0.19	0.21	0.21	0.17	0.17	0.16	0.12	0.182
HFC-salt	0.19	0.19	0.19	0.19	0.21	0.21	0.17	0.17	0.16	0.12	0.182
HFC-H20	0.19	0.19	0.19	0.19	0.21	0.21	0.17	0.17	0.16	0.12	0.182
PDR	0.19	0.19	0.19	0.19	0.21	0.21	0.17	0.17	0.16	0.12	0.182
PTC-dsg	0.05	0.05	0.05	0.05	0.05	0.05	0.10	0.10	0.11	0.11	0.072
PTC-oil	0.05	0.05	0.05	0.05	0.05	0.05	0.10	0.10	0.11	0.11	0.072
CLFR	0.04	0.04	0.04	0.04	0.02	0.02	0.03	0.03	0.05	0.11	0.042
LFR	0.04	0.04	0.04	0.04	0.02	0.02	0.03	0.03	0.05	0.11	0.042
CPC-fl	0.03	0.03	0.03	0.03	0.01	0.01	0.02	0.02	0.03	0.09	0.031
CPC	0.02	0.02	0.02	0.02	0.01	0.01	0.00	0.00	0.00	0.01	0.012
Total	1.00	1.00	1.00	1.00	1.00	1.00	1.00	1.00	1.00	1.00	

Table A-2.19: Pair-wise comparison matrix for the suitability to operate at the proposed scale for The Sahara Desert (2000MW).

	HFC-air	HFC-salt	HFC-H20	PDR	PTC-dsg	PTC-oil	CLFR	LFR	CPC-fl	CPC	Priority Vector
HFC-air	0.22	0.22	0.22	0.24	0.23	0.23	0.19	0.19	0.17	0.15	0.207
HFC-salt	0.22	0.22	0.22	0.24	0.23	0.23	0.19	0.19	0.17	0.15	0.207
HFC-H20	0.22	0.22	0.22	0.24	0.23	0.23	0.19	0.19	0.17	0.15	0.207
PDR	0.11	0.11	0.11	0.12	0.18	0.18	0.16	0.16	0.15	0.14	0.142
PTC-dsg	0.04	0.04	0.04	0.03	0.05	0.05	0.09	0.09	0.10	0.10	0.064
PTC-oil	0.04	0.04	0.04	0.03	0.05	0.05	0.09	0.09	0.10	0.10	0.064
CLFR	0.04	0.04	0.04	0.02	0.02	0.02	0.03	0.03	0.05	0.07	0.035
LFR	0.04	0.04	0.04	0.02	0.02	0.02	0.03	0.03	0.05	0.07	0.035
CPC-fl	0.03	0.03	0.03	0.02	0.01	0.01	0.02	0.02	0.02	0.05	0.025
CPC	0.02	0.02	0.02	0.02	0.01	0.01	0.01	0.01	0.01	0.02	0.015
Total	1.00	1.00	1.00	1.00	1.00	1.00	1.00	1.00	1.00	1.00	

Appendix 3

Analytical hierarchy process case scenarios

A-3.1 AHP scenarios

Gujarat, Southern Spain, California and The Sahara Desert, have been selected for the implementation of a solar thermal system. Each location's climate is determined along with their political standings in terms of government legislation that exists to promote renewable projects. The land and local population has also been considered as well as the likely scale for a solar thermal power plant in these areas. Using this information, four suitable case study scenarios have been developed for the AHP analysis.

A-3.1.1 Gujarat

The weather conditions across the whole of India, as well as Gujarat, are very variable. While coastal regions have a humid, mild climate with moderate amounts of rainfall in the monsoon period, inland areas experience a far more extreme climate. On average summers are very hot and dry, with temperatures reaching as high as 46 ºC during the day and 34 ºC at night. The winters are still very warm at 29 ºC during daylight and 12 ºC at night. The monsoon season can extend from the middle of June to September with extremely hot humid conditions before its arrival brings temperatures down to 38 ºC.

India has also recently announced feed-in tariffs to the maximum of Rs. 15/kWh (25 ¢/kWh) for grid connected systems in March 2008, and states are now starting to take this up with West Bengal being the first.

Gujarat, as well as numerous other places in India, may well be more suited to smaller off grid CSP systems with a number of smaller communities not being on a large national grid system. For the Indian case study, the following proposals are made:

Indian businesses have collaborated with European investors to develop a local small marketable solar thermal system to power local communities that are away from a grid network, while some states have yet to adopt the relatively new governments plans for feed-in tariffs, these should be utilised were possible. Suggested scales range from 100 kW – 1 MW. Weather conditions to contend with in India are the monsoon season bringing with it high winds, however freezing temperatures are likely to be infrequent.

A-3.1.2 Southern Spain

Spain's climate is very variable over the whole country. Southern Spain's climate or Mediterranean climate including the eastern coast has average temperatures of 11 ºC in the winter and 23 ºC in the summer. Annual rainfall ranges from 230 – 600 mm. Temperatures in the past have reached 47 ºC in Seville, which is home to Europe's first parabolic trough plant, Andasol 1. Spain ranks as one of the most suitable locations for solar power, receiving more sunshine than any other European country. Spain is also the fourth largest manufacturer of solar power technology.

Spain was the first country to implement feed-in tariffs for CSP, meaning that the regional or national electricity suppliers have to buy renewable generated electricity at a higher set market rate determined by the government for a guaranteed 25 year period. Another aspect that was crucial in developing the CSP industry in Spain was the granting of permission for solar plants to use natural gas as a back up to increase their operational capacity factor. The combination of these decrees meant that CSP technology could now compete with conventional power plants, however a limit of 500 MW of solar power generation in Spain has been set when the tariffs will be removed. The current amount of solar thermal generated energy, 183 MW, is hoped to rise substantially within the next couple of years.

Southern Spain seems suitable for large scale grid connected commercial generating power stations providing power to the local populous, which has been proven successfully in Seville. For this case study the following assumptions are made:

Financing for the initial development has been easy to come by with many enthusiastic investors keen to take advantage of the political incentives while they remain in place. Initial proposals are for a mid to large scale 100MW plant. Conditions for the selected region are seen to be very good, with few extreme weather conditions such as high winds and temperatures below freezing.

A-3.1.3 California – Mojave Desert

The Mojave Desert occupies a significant area in south-eastern California. The summer season in the Mojave brings with it temperatures as high as 50 ºC in some of its basins, as well as other weather extremes such as the North American Monsoon. While the Desert receives less than 250 mm of rain a year, windy days are common across the region. While solar collectors can re-orientate to protect themselves, wind is a major factor in damaging

CSP systems, particularly the receivers which are expensive as well as the mirrors; around 3000 mirrors are replaced every year at the SEGS plant. Autumn is mainly dry with temperatures between 21 – 32 ºC. Winter can see extreme colds of -7 ºC on the valley floor and far lower in higher elevations. Storms from across the Pacific bring rain and snow but with long gaps between storms, temperatures can rise up to 27 ºC. Spring temperatures are often above 38 ºC with some storms influencing these temperatures.

The Mojave Desert was once the location for the main developments of solar power pushing the technology forward, but when tax credits and other subsidies were adjusted with a fall in oil prices, expansion plans for the world's largest solar power station fell through. This caused its developers, Luz Systems, to file for bankruptcy in 1991, which led to concerns for future developments of CSP technologies [33]. Luz Systems financial difficulties can be attributed to the unpredictable nature of the then existing policies, which were based on fossil fuel prices. Fossil fuel prices can be affected globally by many factors, emphasising why guaranteed fixed tariffs are so important [222].

California is aiming to achieve an ambitious 33% of their electricity sales to be served by renewable energy sources by 2020. To achieve this, a number of financial incentive plans have been put into place, once again starting a renewed enthusiasm in developing large solar power stations in this region. Further detail on all the financial incentive plans can be obtained from the US Department of Energy [223]**.**

The case study scenario for California assumes that the development of a 500MW plant has been initiated. Funding has however been difficult with some investors withdrawing due to fears caused by historical records in this region of further large scale solar thermal developments leading to financial difficulties. Extreme temperature highs can be reach, yet designers have also had to consider the problems faced with the below freezing temperatures and the North American monsoon. It has also been suggested that some of the hotter locations on the valley basins could be utilised as large available areas of suitable level land can be difficult to come by.

A-3.1.4 Sahara Desert

The Sahara is the world's largest hot desert at over 9 million kilometres squared. The region's climate can be categorised into two types; the north, a dry subtropical climate consisting of annually high temperatures with cold winters and hot summers with two

rainy seasons, and the south, a dry tropical climate forming dry mild winters, and a hot dry season before the rainy season. The rainy seasons in the north can cause potential flash flooding, usually around August. The dry tropical climate of the southern region, at high elevations, receives temperatures well below freezing. In the western regions the cold Canary current reduces rainfall and lowers the average temperature, increasing the humidity and the potential of fog.

The Sahara Desert has been linked with plans to establish huge scale solar thermal plants for electricity to be exported to the whole of Europe, and while financing plans have been initiated, it remains dubious as to how far the projected plans will go.

With Africa receiving 95% of the world's best winter sunlight and an abundance of other renewable resources to harness, it is well situated to develop the means of providing substantial amounts of energy for its own requirements and exportation. Around 50% of Africa's electricity is generated by *Eskom* who run mainly coal fired power stations, producing 45% of the country's greenhouse gases alone, and this is with the majority of South Africa being without power. The reluctance towards renewable energy in Africa can be linked to the lack of political legislation that has been pioneered in other countries. The success seen with feed-in tariffs could promote numerous industries to develop a greater interest in regions such as the Sahara Desert for renewable projects.

With the abundance of land unlike anywhere else, the Sahara stands out as a location with great potential for huge scale CSP systems. In this case study the following hypothesis is made:

African consortiums with large European investors with additional financial backing from the EU have begun plans for a multi-networked solar system totalling over 2000MW. While initial investments have been successful the total amount required for the project could be difficult to come by. Africa's lack of political incentives in the use and development of renewables has also made the long term payback period a concern for some parties.

Appendix 4

Pair-wise comparison of criteria for Gujarat, Southern Spain, Mojave Desert and the Sahara Desert

A-4.1 Criteria weighting vector results

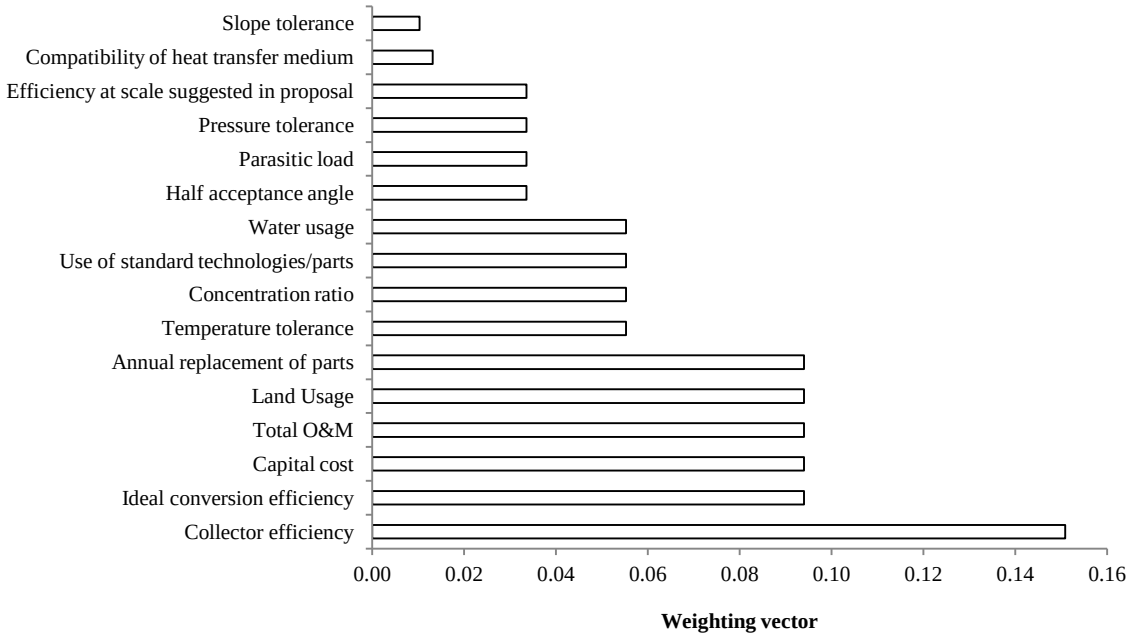

Figure A-4.1: Pair-wise comparison matrix criteria weighting vector results for Gujarat.

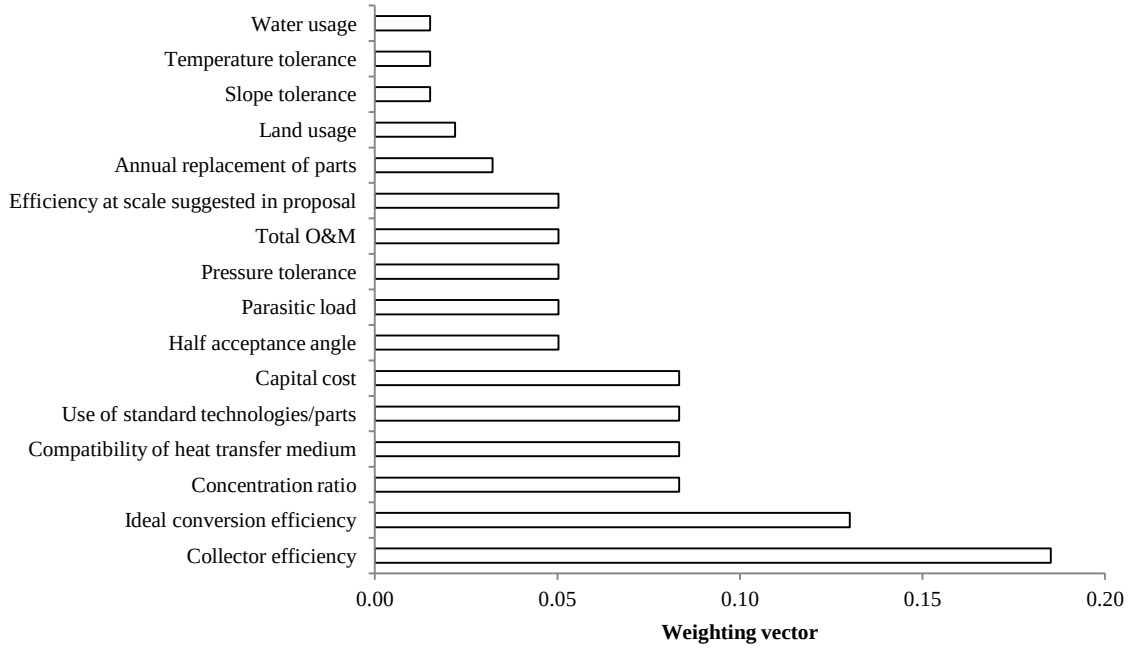

Figure A-4.2: Pair-wise comparison matrix criteria weighting vector results for Southern Spain.

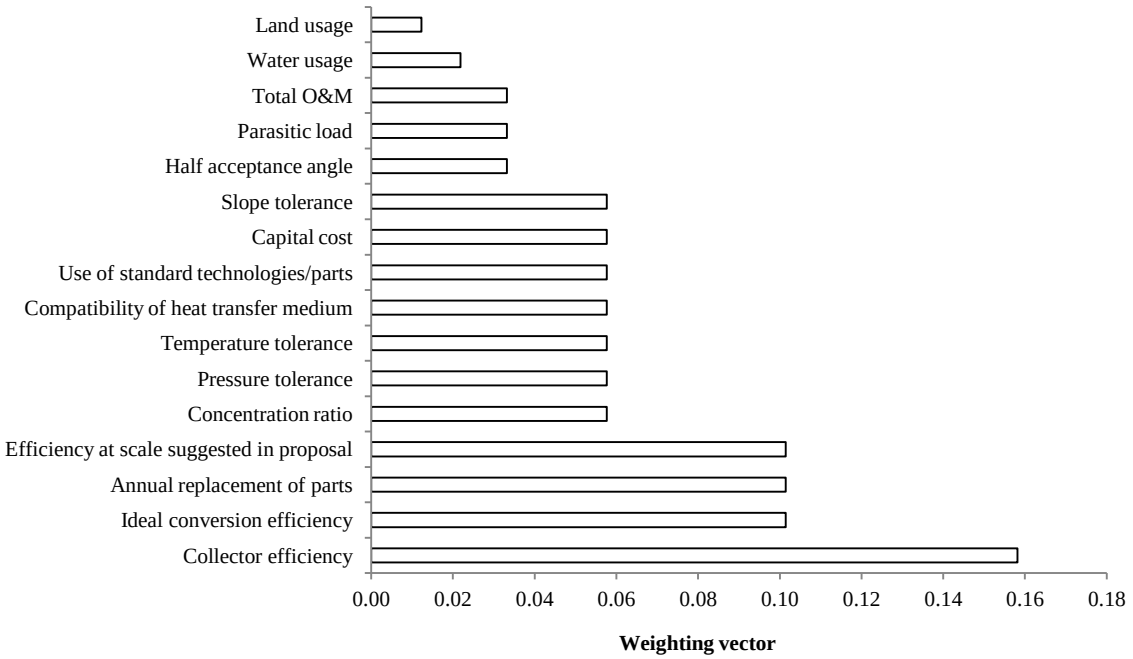

Figure A-4.3: Pair-wise comparison matrix criteria weighting vector results for the Mojave Desert.

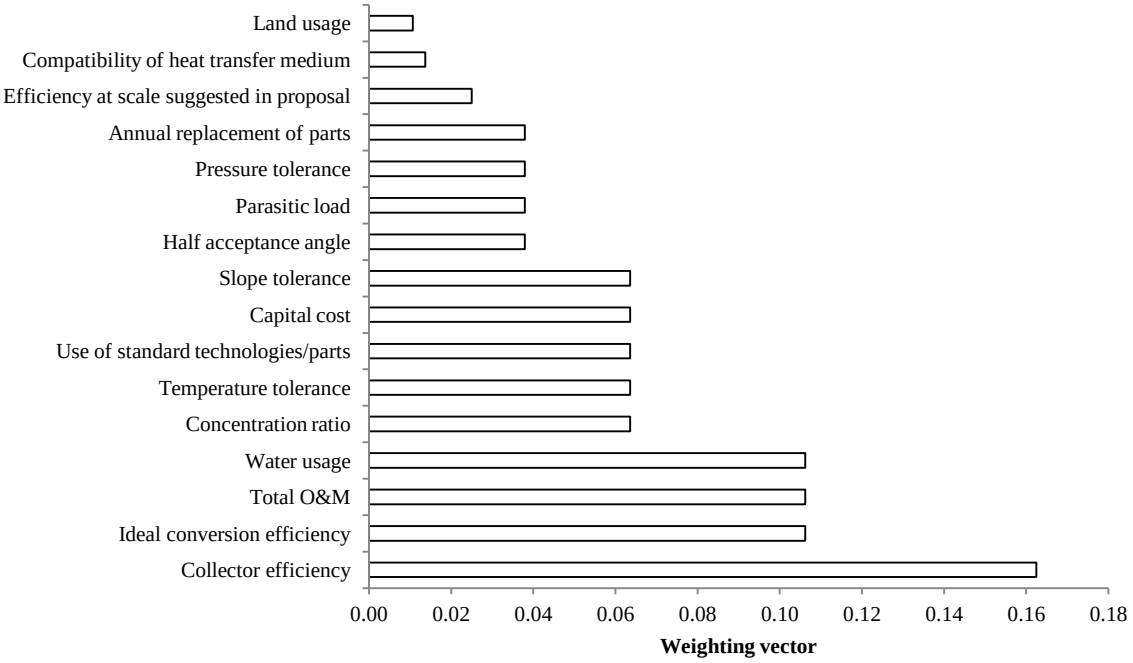

Figure A-4.4: Pair-wise comparison matrix criteria weighting vector results for the Sahara Desert.

Appendix 5

ELFR component engineering drawings

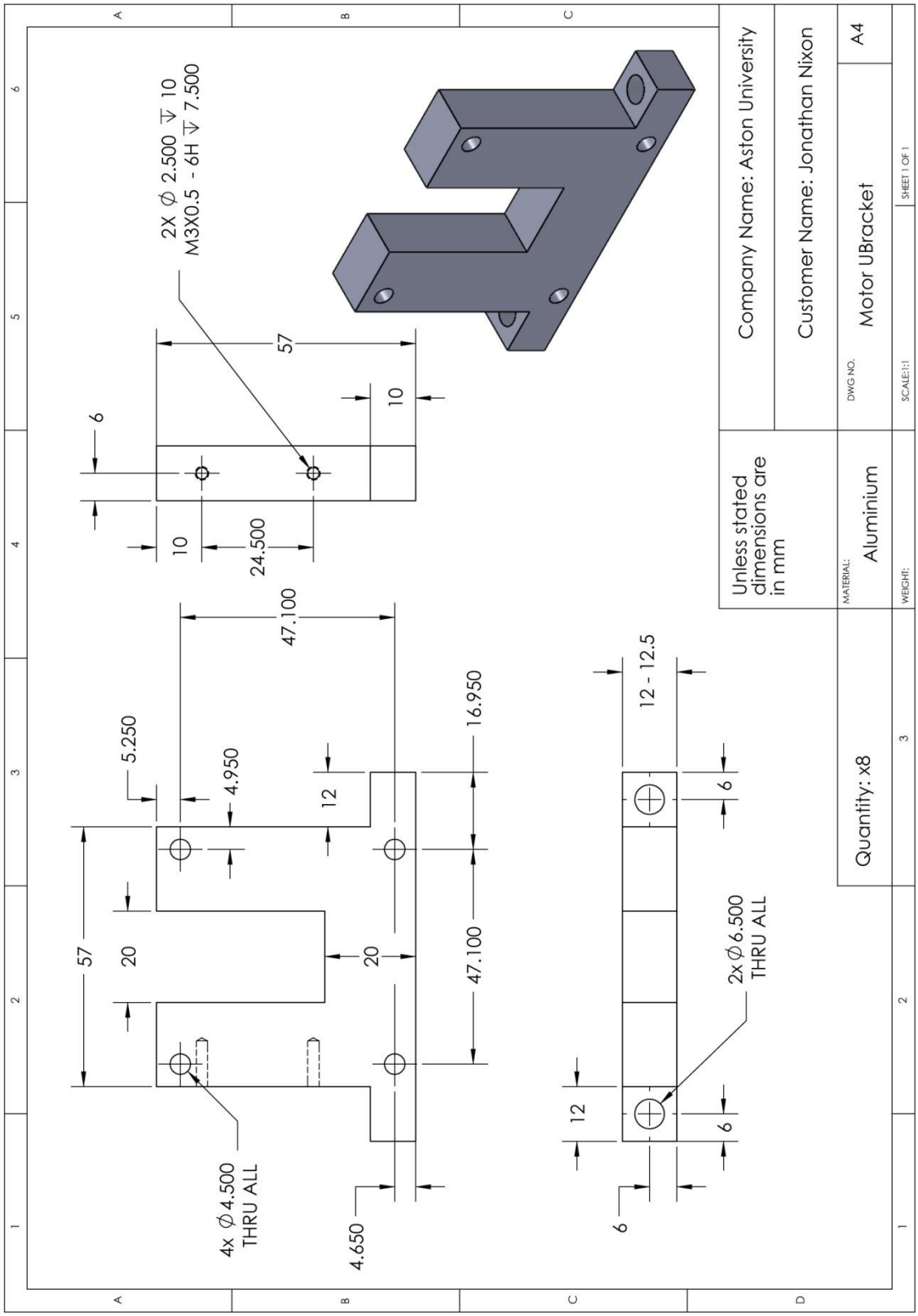

Figure A-5.1: Engineering drawing for the motor U-bracket.

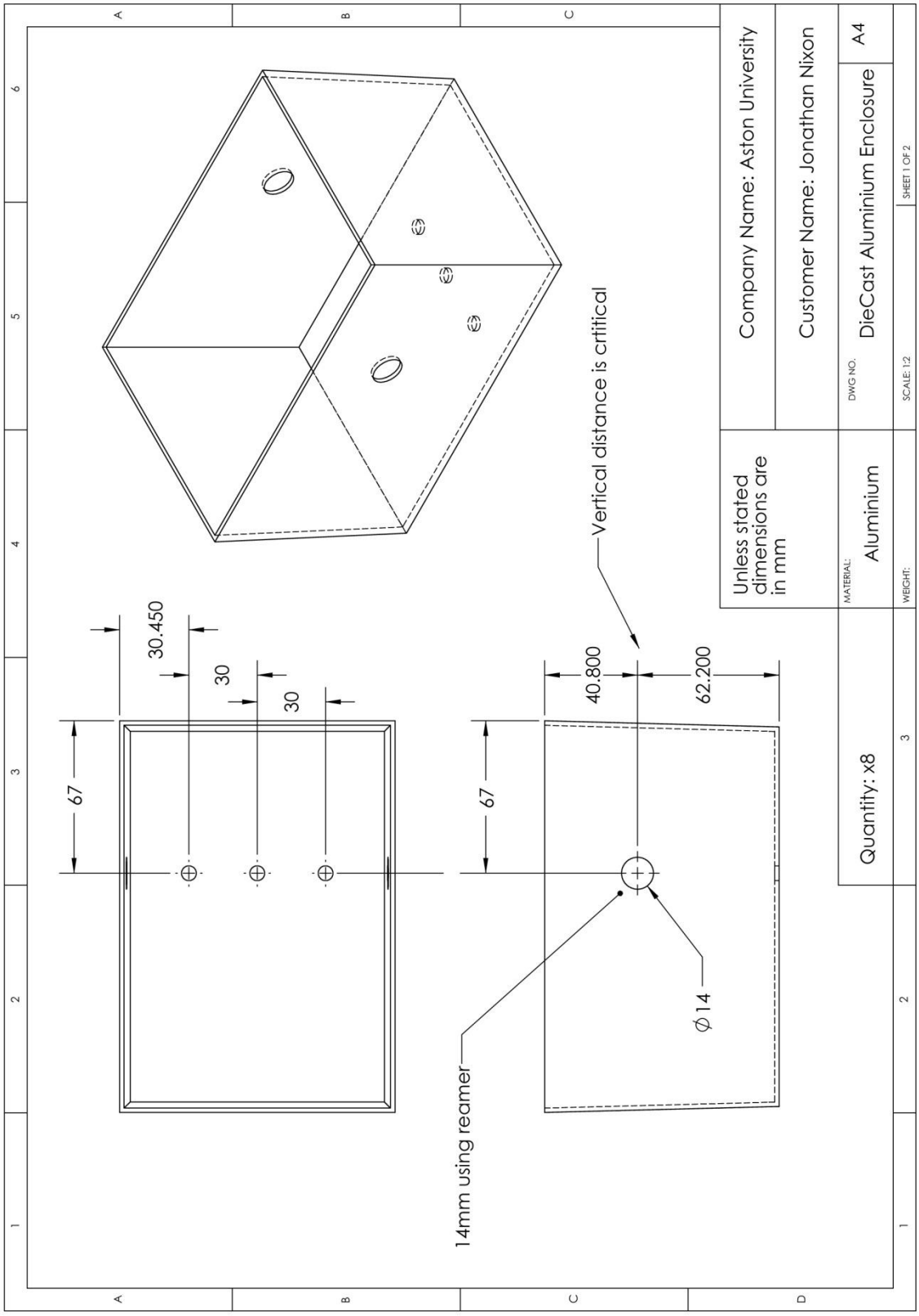

Figure A-5.2: Engineering drawing for the die cast aluminium enclosure.

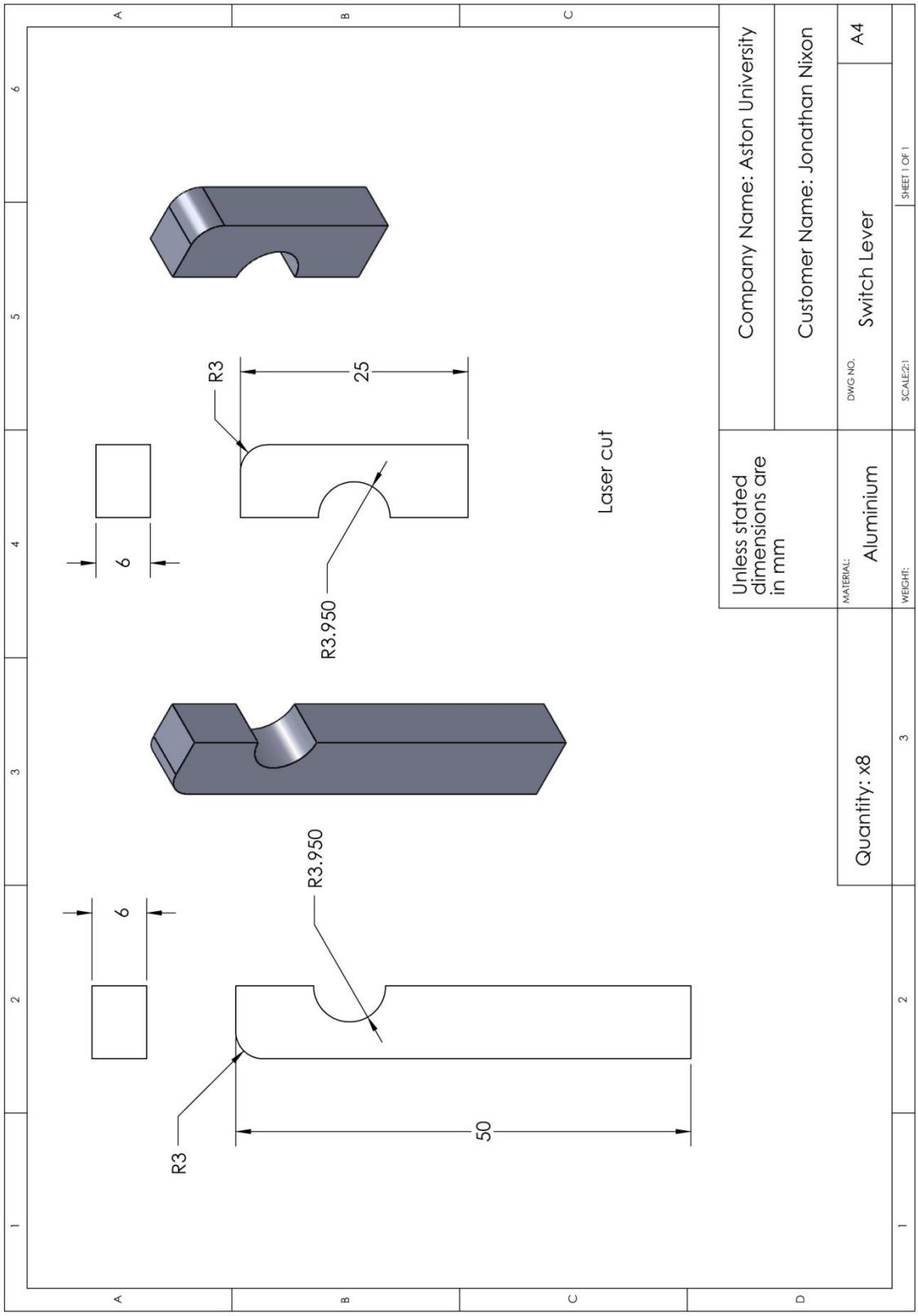

Figure A-5.3: Engineering drawing for the switch lever.

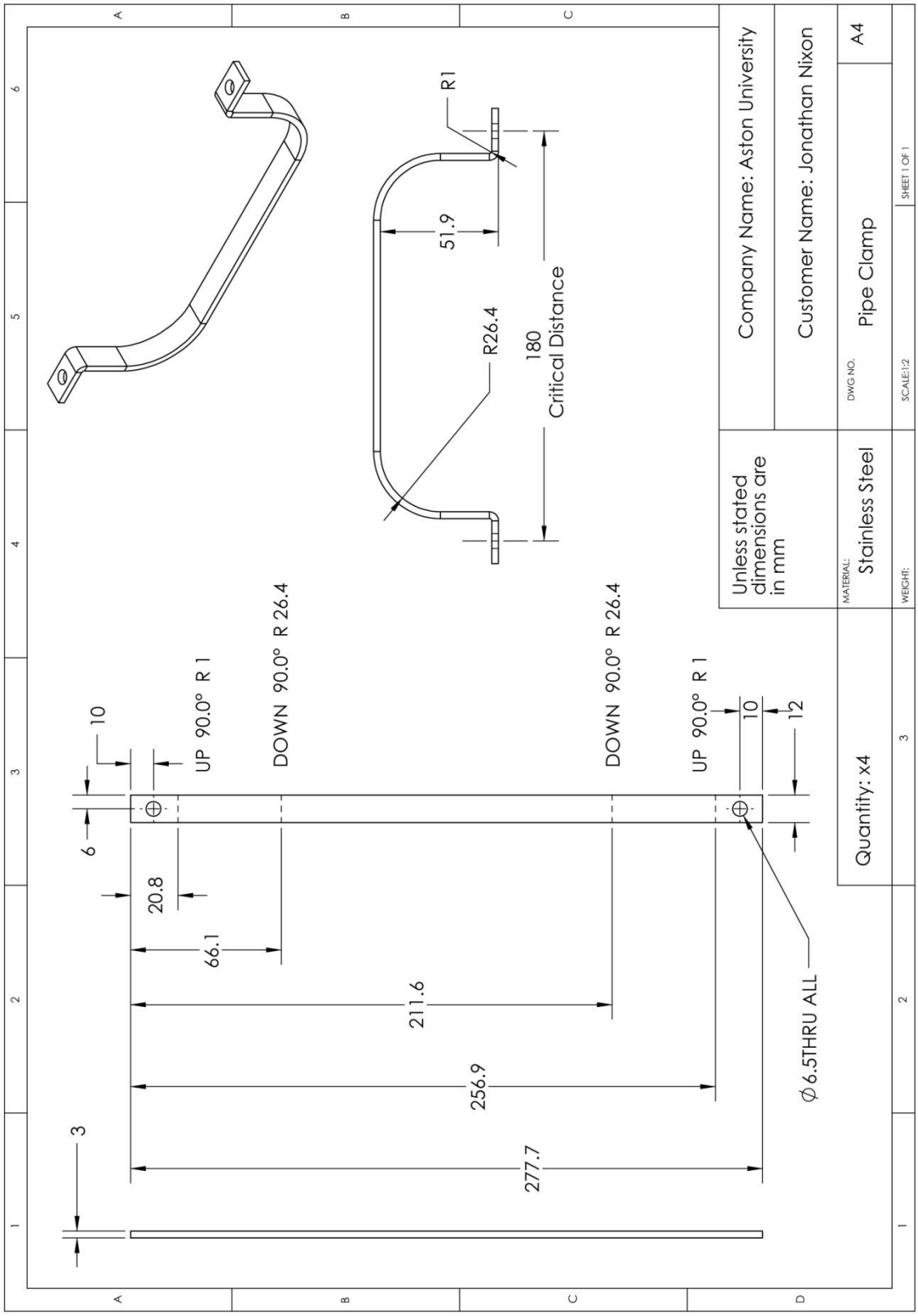

Figure A-5.4: Engineering drawing for the switch lever.

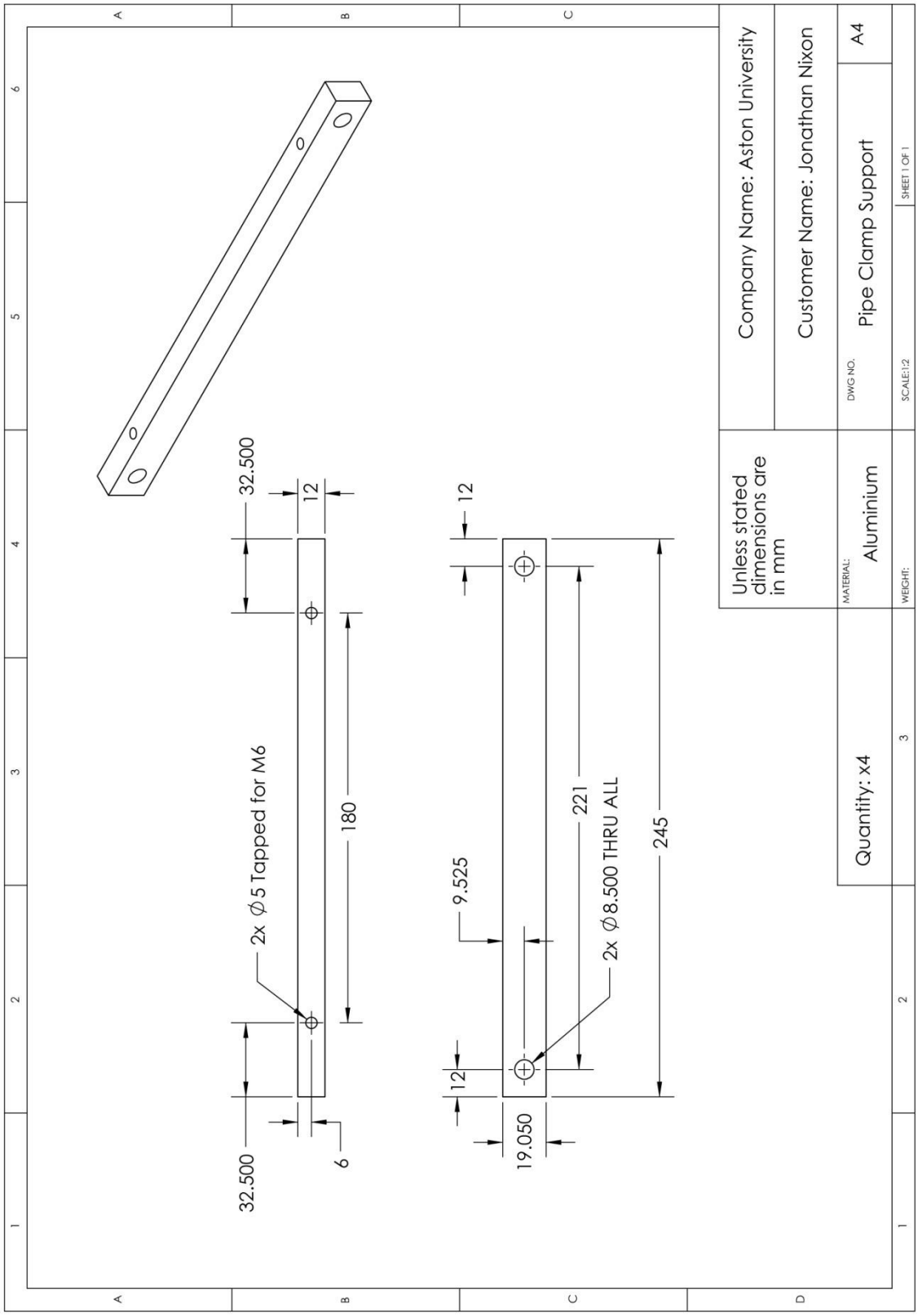

Figure A-5.5: Engineering drawing for the pipe clamp support.

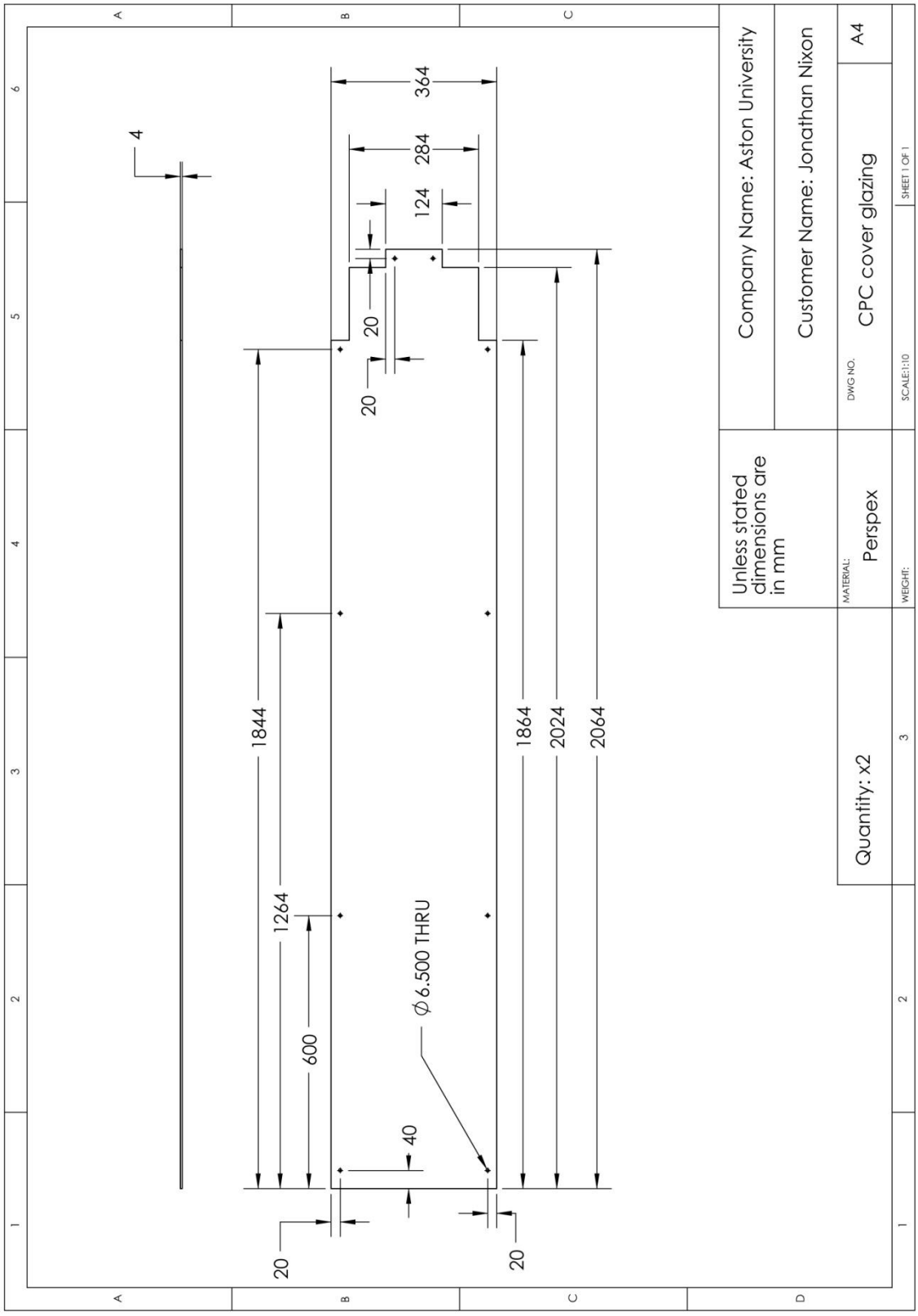

Figure A-5.6: Engineering drawing for the CPC cover glazing.

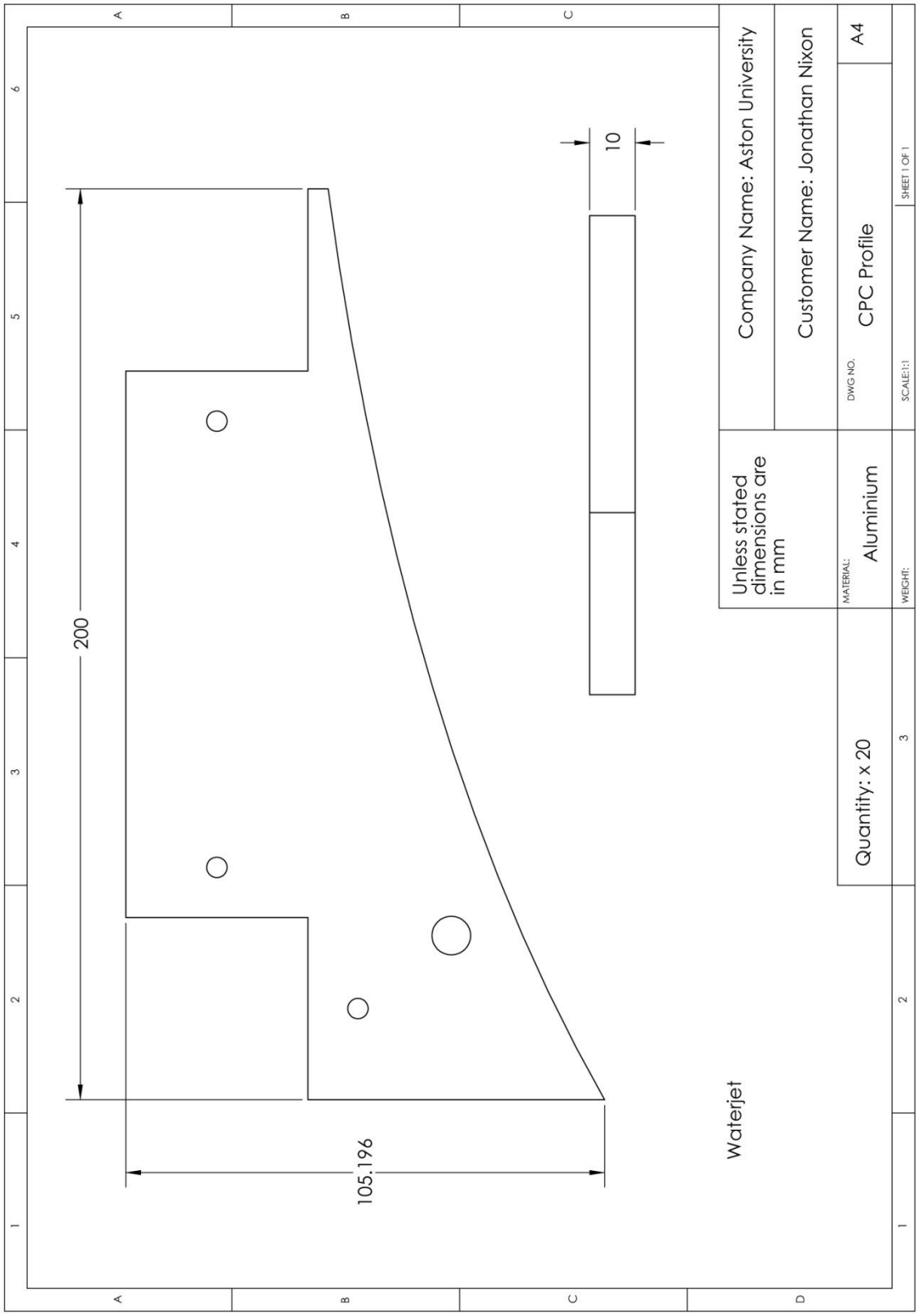

Figure A-5.7: Engineering drawing for the CPC profile.

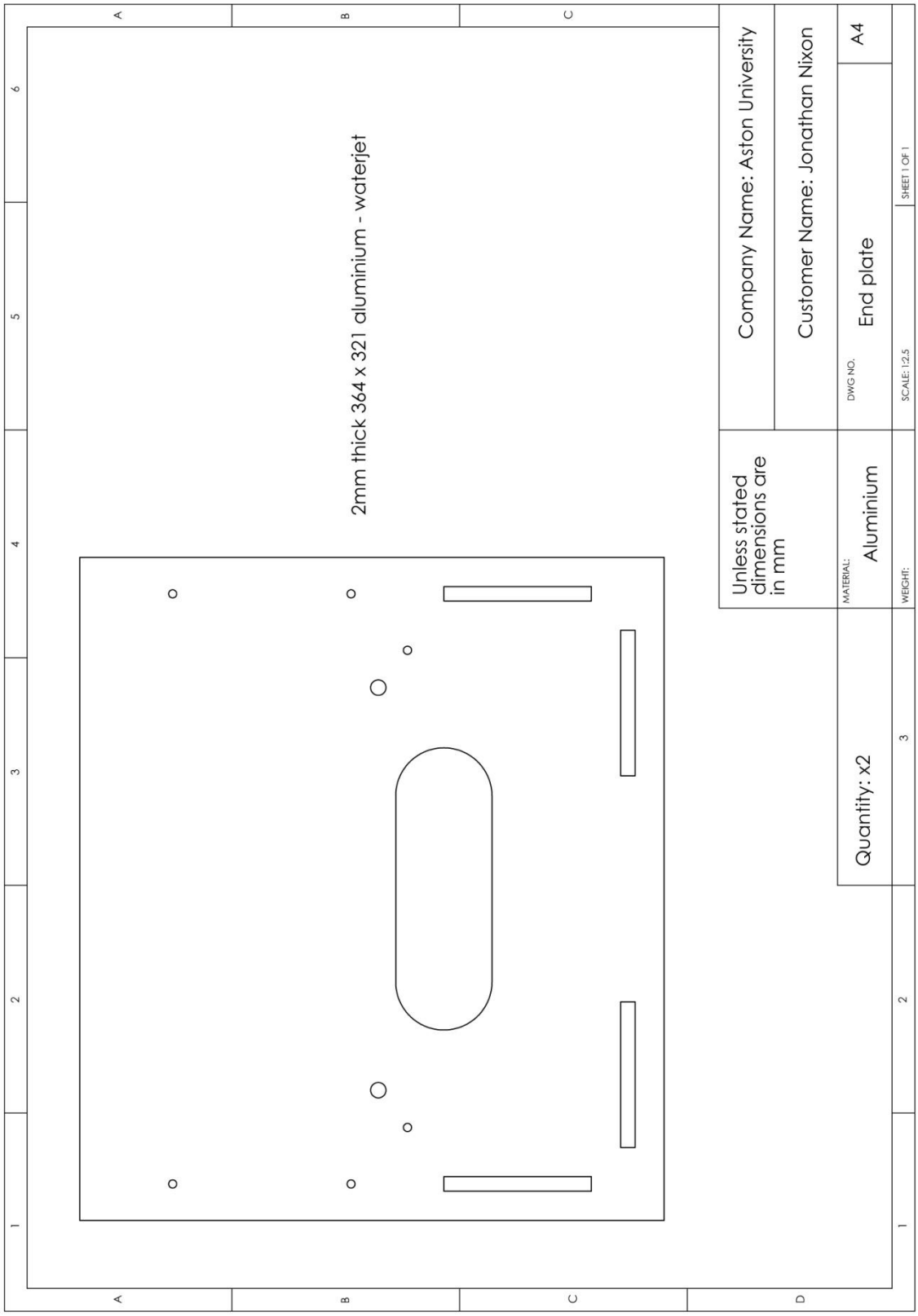

Figure A-5.8: Engineering drawing for the end plate.

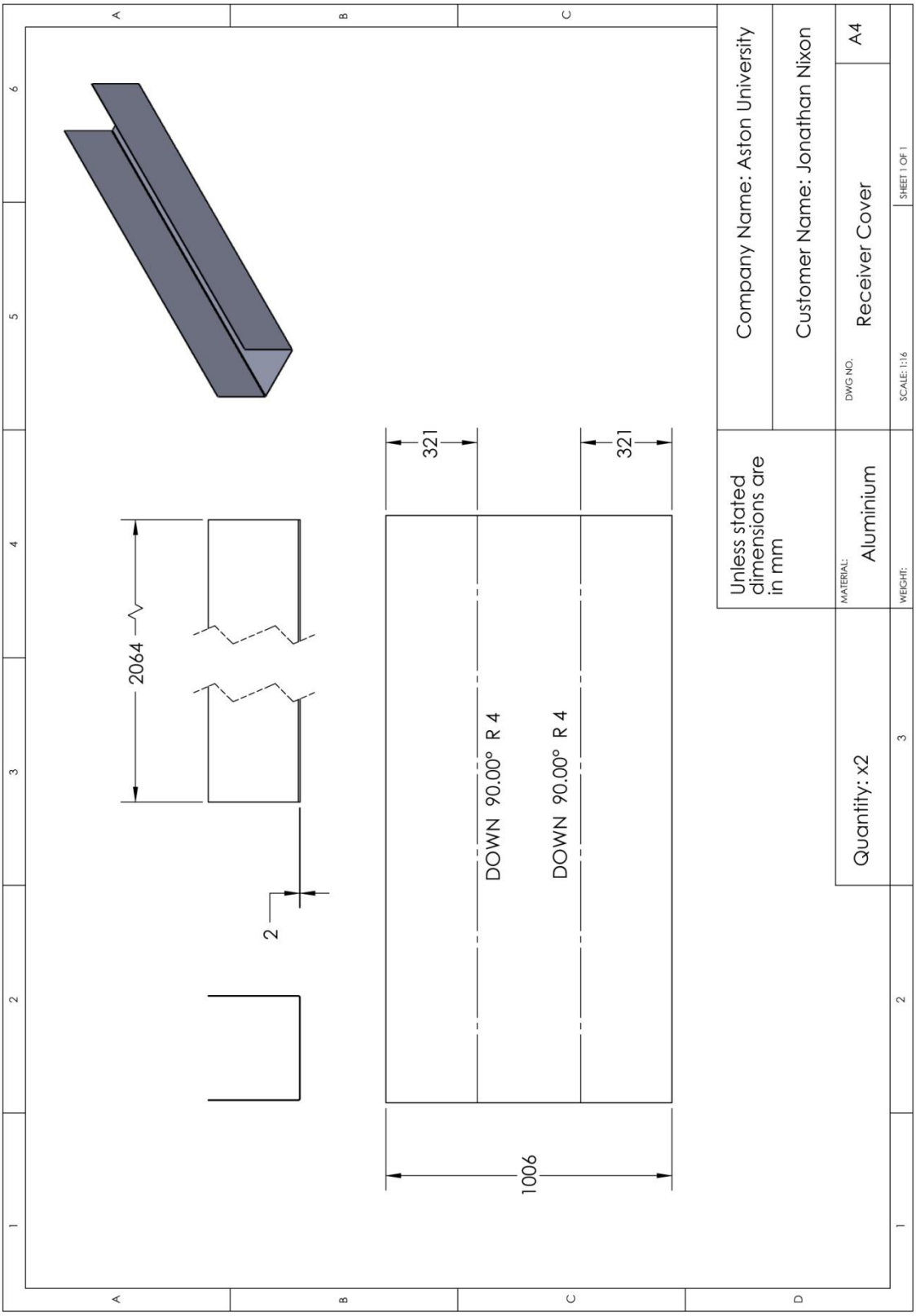

Figure A-5.9: Engineering drawing for the receiver cover.

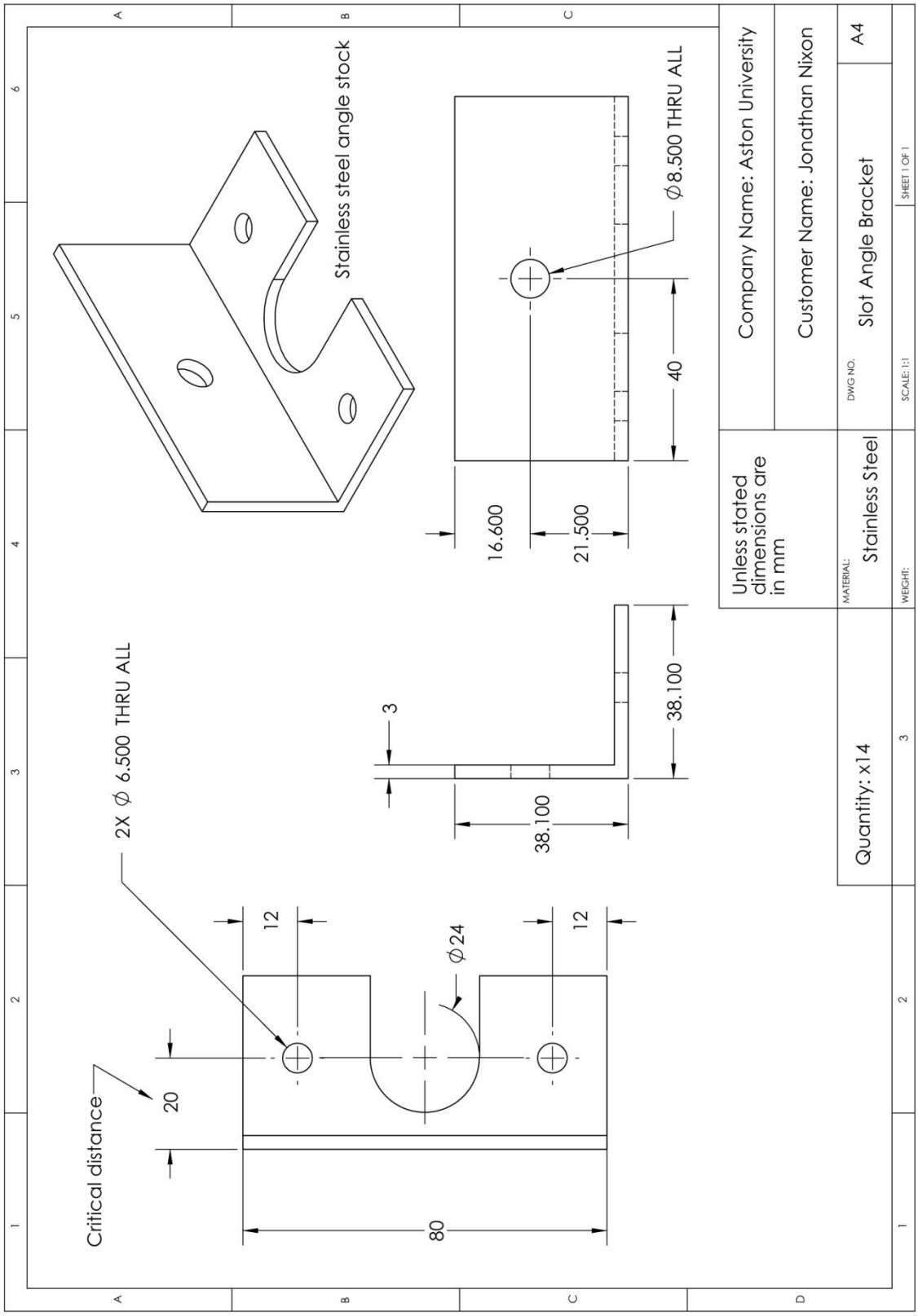

Figure A-5.10: Engineering drawing for the slot angle bracket.

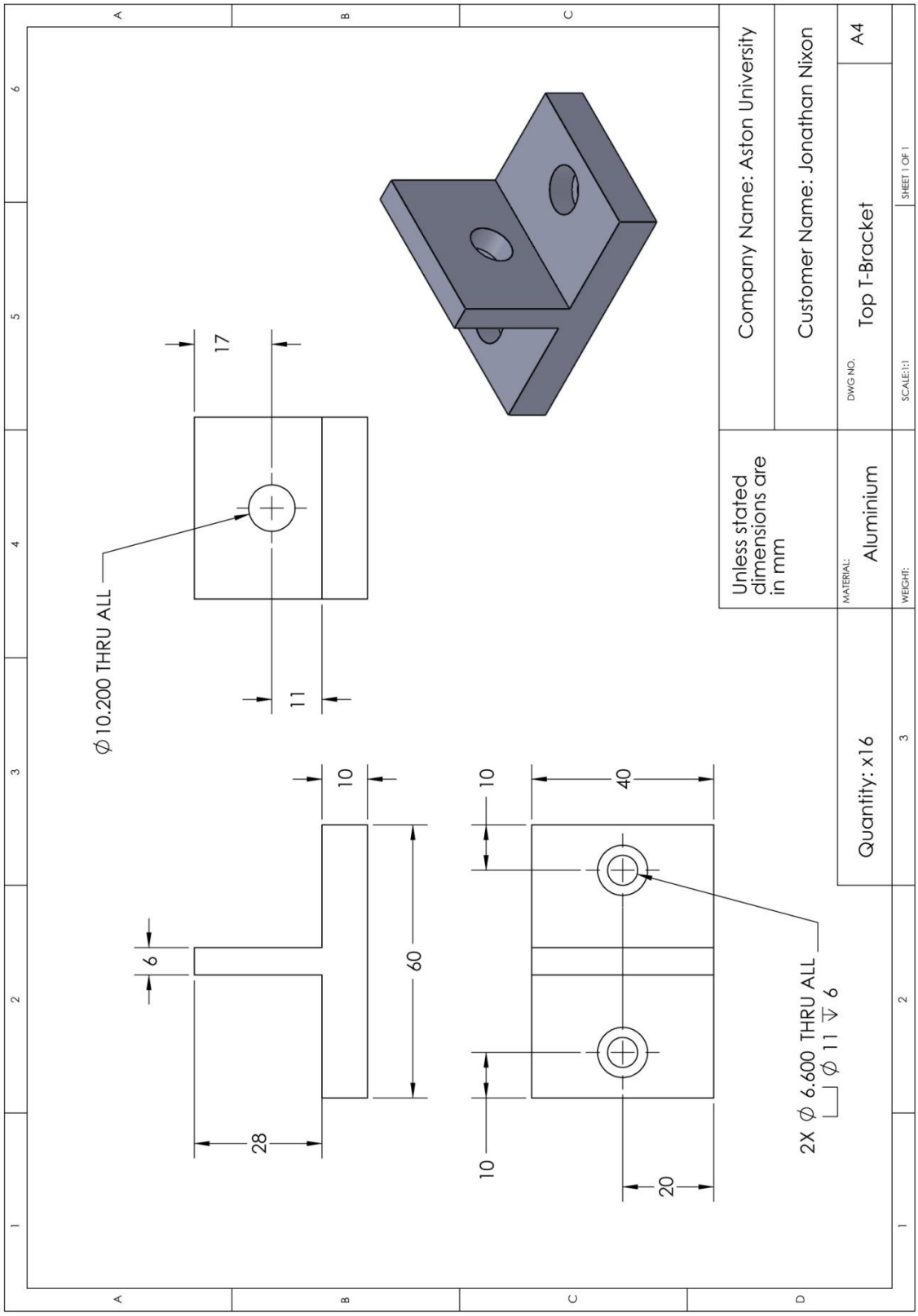

Figure A-5.11: Engineering drawing for the top T-bracket.

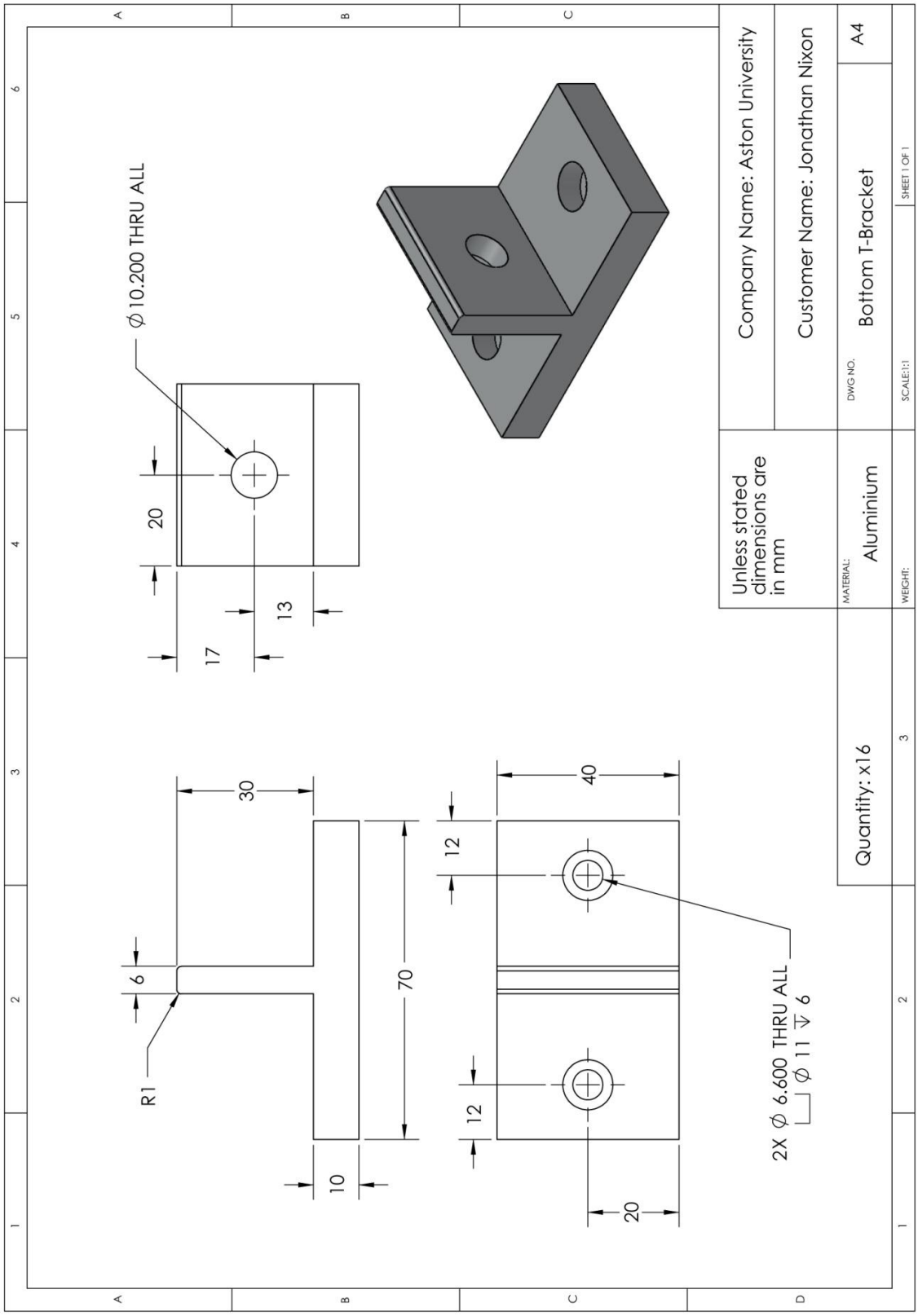

Figure A-5.12: Engineering drawing for the bottom T-bracket.

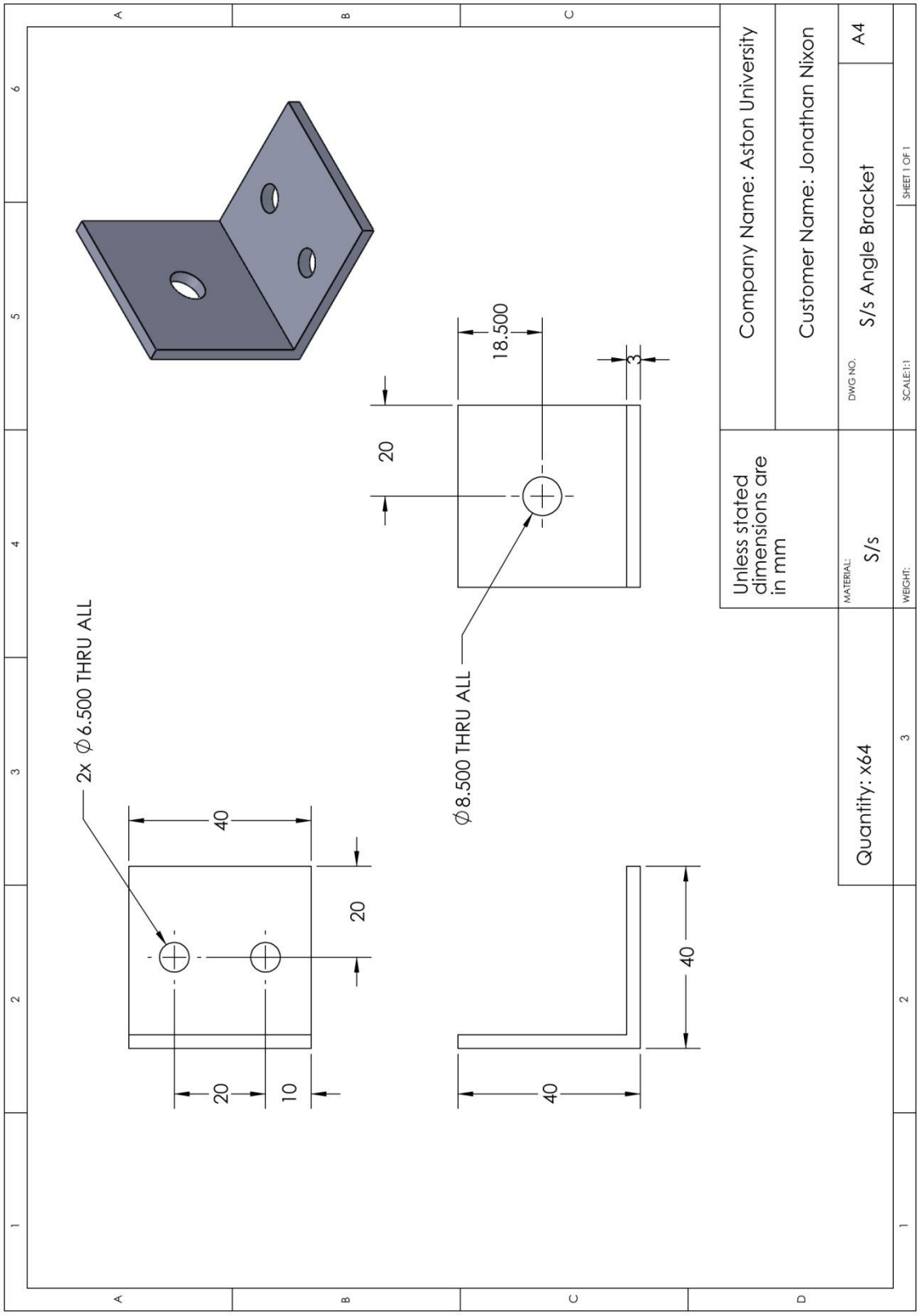

Figure A-5.13: Engineering drawing for the angle bracket.

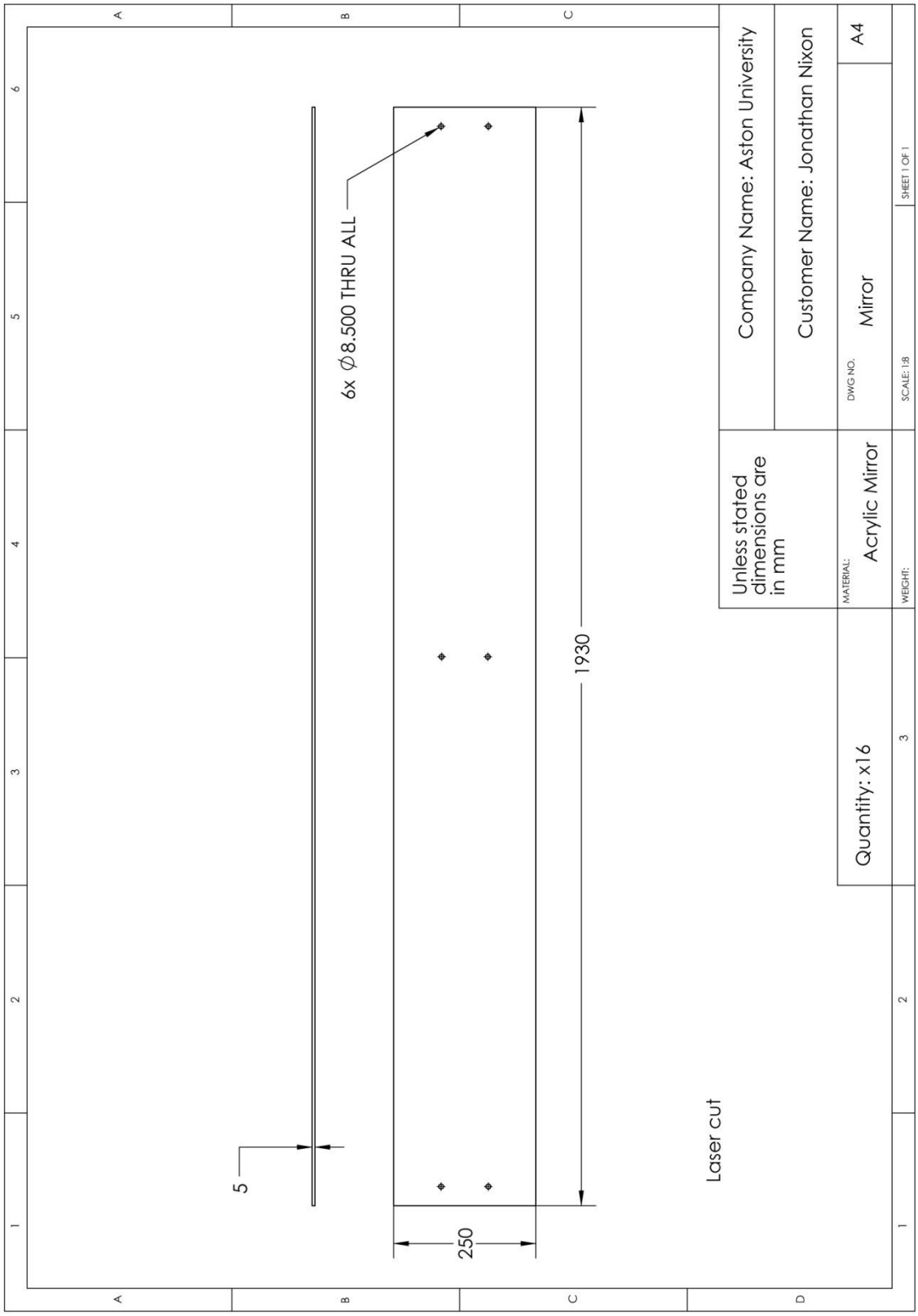

Figure A-5.14: Engineering drawing for the mirror.

Appendix 6

Exploded sub-assemblies and bill of materials

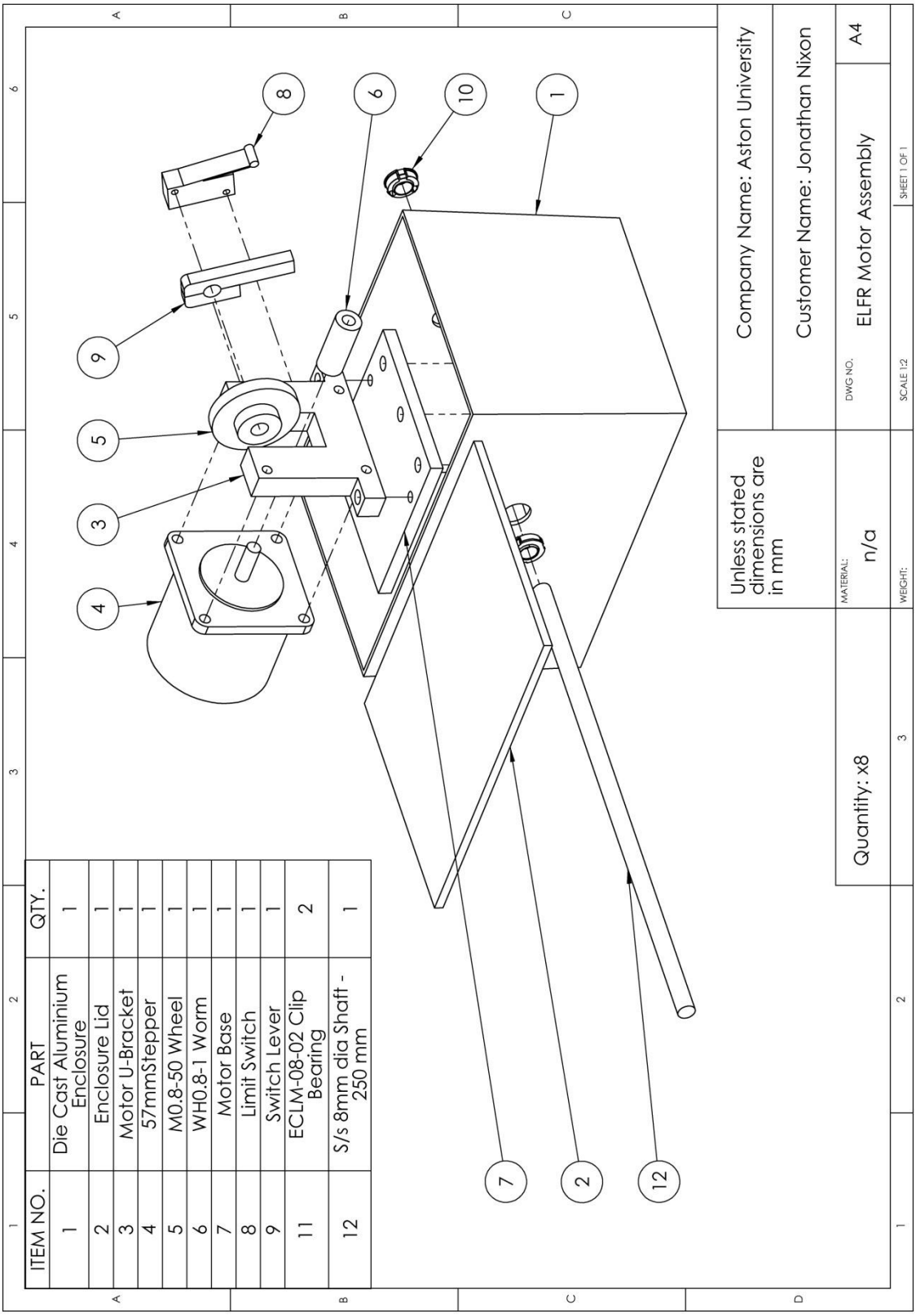

Figure A-6.1: Exploded sub-assembly and BOM for the ELFR motor assembly.

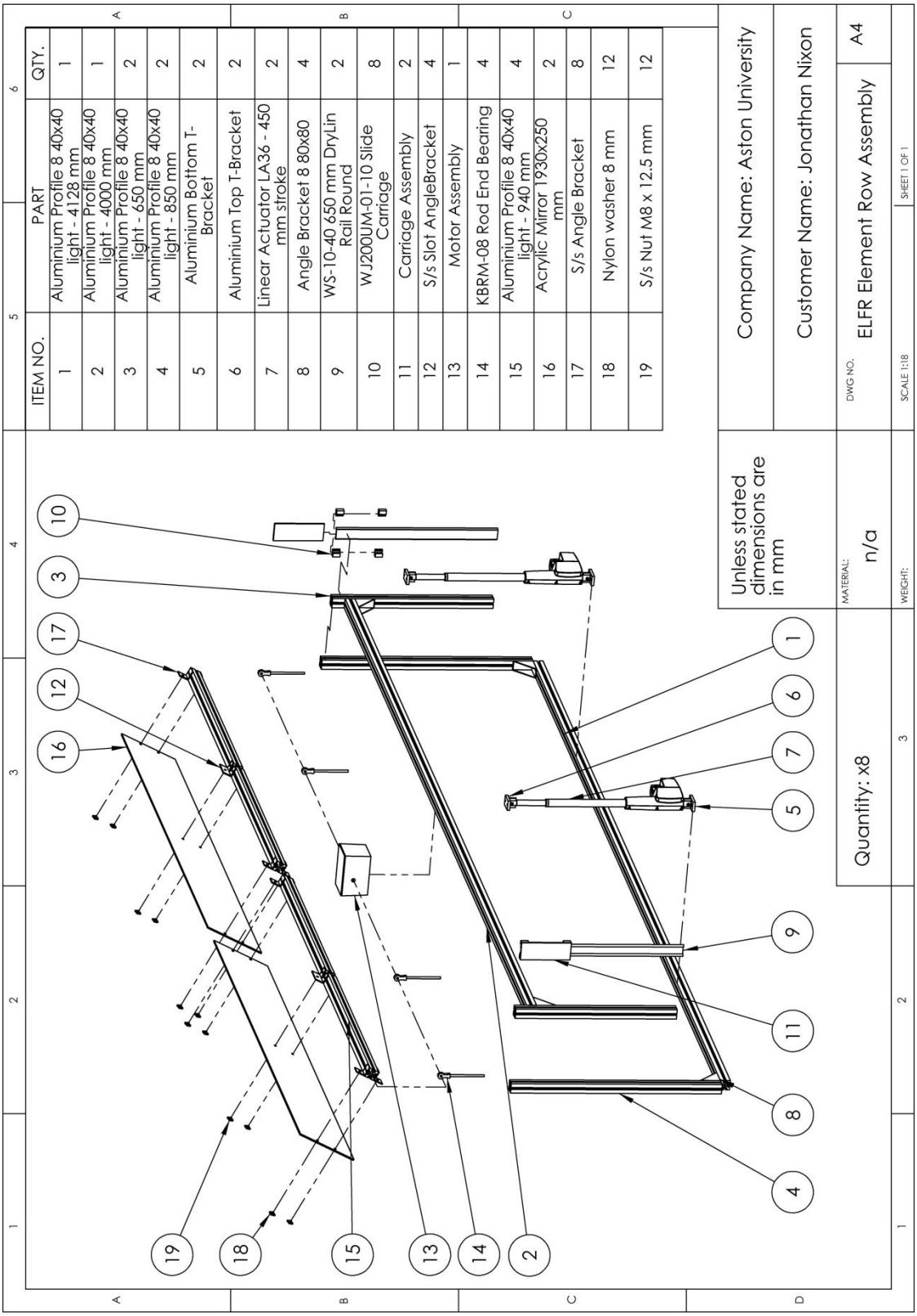

Figure A-6.2: Exploded sub-assembly and BOM for the ELFR element row assembly.

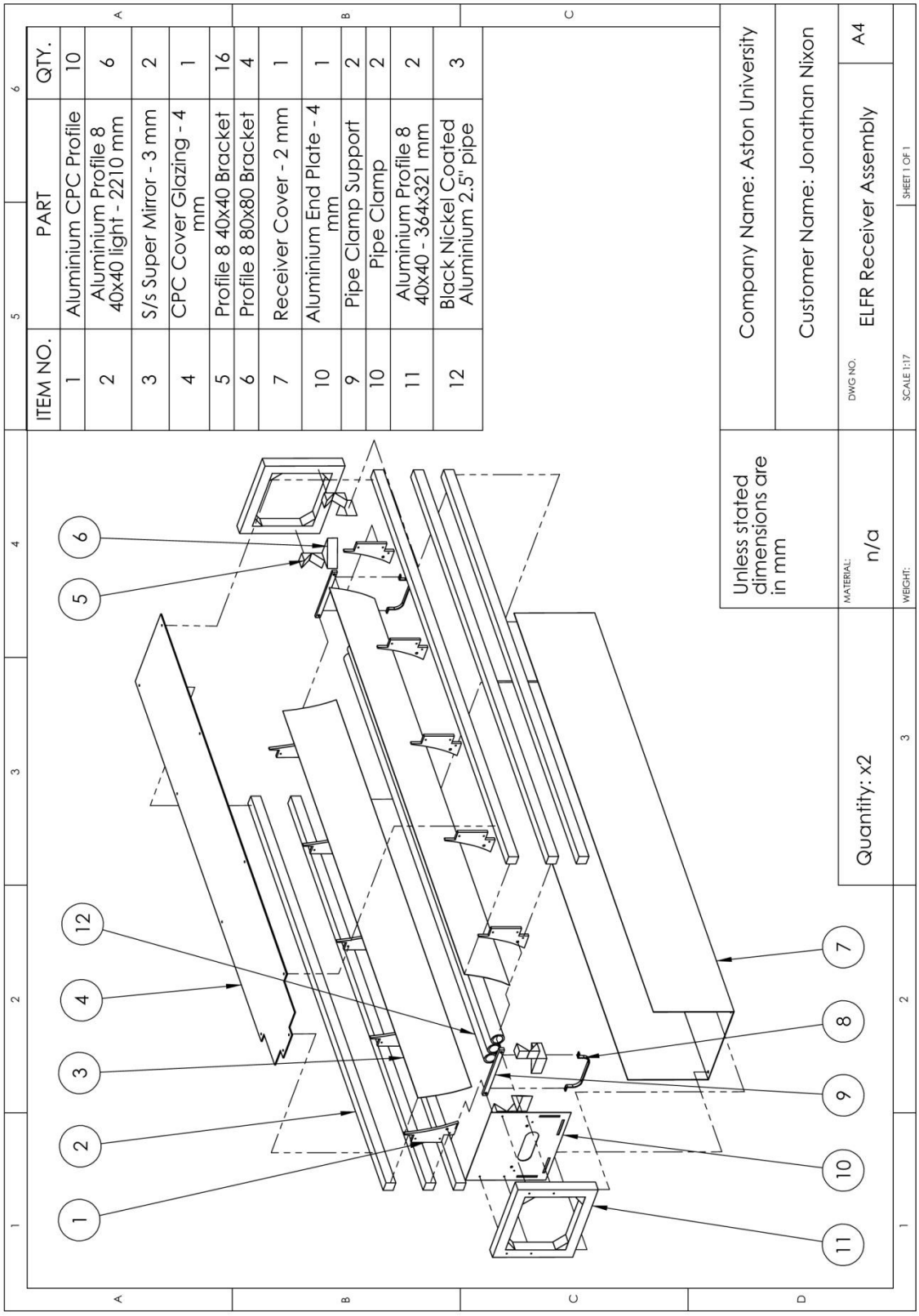

Figure A-6.3: Exploded sub-assembly and BOM for the ELFR receiver assembly.

Appendix 7

Wind force calculations

A-6.1 Drag force

The wind force acting on an object, a solar collector in this case, can be calculated from the drag, *Fd*, or air/fluid resistance, which is given by:

$$Fd = 1/2\rho ve^2 ACd \quad \text{(A-6.1)}$$

where ρ is the density of the fluid, *ve* the speed of the object relative to the fluid, *Cd* is the drag coefficient and *A* is the reference area of the object perpendicular to the wind direction.

In a worst case scenario, the wind could act vertically over the ELFR's total mirror area, which was 8 m^2. For this scenario, the weight required to keep the collector grounded for an 80mph wind was 1000 kg. The weight of a single concrete slab was 27 kg; therefore 36 slabs were attached to the ELFR's frame.

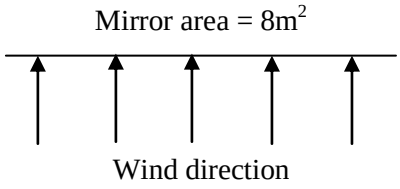

Figure A-6.1: Wind direction relative to the orthographic projection of the ELFR.

A-6.2 Tipping force

In addition to the drag force, the tipping force, F_T, which is the force just large enough to tip the collector over, was calculated. The weight was assumed to be at the bottom of the collector, i.e the concrete slabs. Using moments about a corner, the clockwise and counter clockwise force (Fcw and Fccw) was calculated from, Fcw = 1000 x 9.81 x 2, and, Fccw = F_R x 3.5.

At the onset of tipping, Fcw equals Fccw, therefore, $F_{T,}$ equals 5700 N. For wind speeds of 80 mph, the maximum force, F_T, exerted on the receiver tower area (1.36m^2) equals 2000 N.

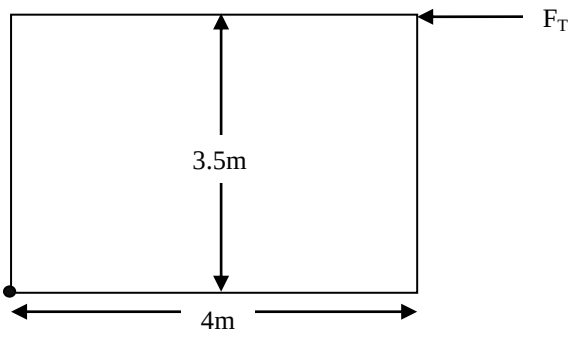

Figure A-6.2: Force diagram for the ELFR tipping calculations.

Drag and tipping forces were also calculated for the water header tank, however these are not shown.

A-6.3 Tension force

The tension force is the force transmitted through a cable or rope being pulled. The number and size of steel guy cables for the receiver tower were determined for the maximum tension expected for wind speeds of 80 mph, i.e 2000 N on the receiver tower

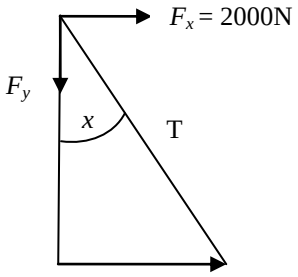

Figure A-6.3: Force diagram for the ELFR tension force calculations.

$$Tcosx = F_x \qquad \text{(A-6.2)}$$

As a result, eight cables (four to take 342 kg per cable and four more to take 271 kg per rope) were used.

Appendix 8

Control board circuit schematics

Figure A-7.1: Encoder circuit schematic in Proteus® by O. N. Igobo.

Figure A-7.2: Stepper motor decoder and driver circuit schematic in Proteus® by O. N. Igobo.

Figure A-7.3: Actuator decoder and controller circuit schematic in Proteus® by O. N. Igobo.

Appendix 9

Pyrheliometer calibration certificate

KIPP & ZONEN
SINCE 1830

CALIBRATION CERTIFICATE

CERTIFICATE NUMBER	005314110574
PYRHELIOMETER MODEL	CHP 1
SERIAL NUMBER	110574
SENSITIVITY	8.09 µV/W/m²
IMPEDANCE	26.4 Ohm
TEMPERATURE	22 ±2 °C
REFERENCE PYRHELIOMETER	Kipp & Zonen CHP 1 snREF1 active from January 3, 2011
CALIBRATION DATE	07-Jun-2011 (recalibration is recommended every two years)
IN CHARGE OF TEST	G. van der Wilt

Calibration procedure
Exact interchange of test pyrheliometer and reference pyrheliometer in a horizontal parallel beam of light from a Xenonlamp. Full collimation angle of beam is 1.0º. Irradiance 500 ± 50 W/m². Roomtemperature 22 ±2 ºC.

Hierarchy of traceability
This reference pyrheliometer was compared with the reference radiometer PMO2 of the World Radiation Center (WRC) using the sun as source. The reference radiometer is periodically calibrated against the World Standard Group (WSG), maintained at the WRC Davos. The readings are referred to the World Radiometric Reference (WRR) as stated in the WMO Technical Regulations. The originally estimated uncertainty of the WRR relative to SI is ±0.3%. The measurements were performed in Davos (latitude: 46.8143°, longitude: -9.8458°, altitude: 1588 m above sea level).

During the comparisons, the reference pyrheliometer received direct solar radiation with intensities ranging from 728 to 1029 W/m², with a mean of 944 Wm⁻². The ambient air temperature ranged from +13.6 to +26.6 ºC with a mean of +21.5 ºC. The sensitivity calculation is based on 1662 individual measurements. The sensitivity and its expanded uncertainty (95% level of confidence) are only valid for similar environmental conditions and amount: 7.92 ± 0.04 µVW⁻¹m².
WRR- factor of PMO2: 0.998618 (from the last International Pyrheliometer Comparison, IPC-2005).
Date of measurements: 2010, July 8, 9, 12, 14 - 16, 19 - 21, 31, August 1

Correction applied 0.0 %
No correction to the Davos sensitivity figure has been applied.

Justification of total instrument calibration uncertainty
The combined uncertainty of the result of the calibration is the positive "root sum square" of two uncertainties.
1. The expanded uncertainty due to random effects and instrumental errors during the calibration of the reference CHP 1 as given by the World Radiation Center in Davos is ±0.04/7.92= ±0.51%. (See traceability text).
2. Based on experience the expanded uncertainty of the transfer procedure (calibration by non-simultaneous comparison) is estimated to be ±1%.
The estimated combined expanded uncertainty is the positive "root sum square" of these two uncertainties: √(0.51^2 + 1^2)= ±1.1%.

Notice
The calibration certificate supplied with the instrument is at the date of first use. Even though the calibration certificate is dated relative to manufacture, or recalibration, the instrument does not undergo any sensitivity changes when kept in the original packing. From the moment the instrument is taken from its packaging and exposed to irradiance the sensitivity may deviate with time. See the 'non-stability' value (% change in sensitivity per year) given in the radiometer specifications.

Page 1/1
Kipp & Zonen B.V.
Delftechpark 36, 2628 XH Delft
P.O. Box 507, 2600 AM Delft
The Netherlands
T: +31 (0) 15 2755 210
F: +31 (0) 15 2620 351
info@kippzonen.com
www.kippzonen.com
VAT no.: NL0055.74.857.B.01
Trade Register no.: 27239004
Member of HMEI

Figure A-9.1: CHP 1 pyrheliometer calibration certificate.

Appendix 10

Hybrid plant case study results

Table A-10.1: Results for the Gujarat LFR plant case study.

Symbol	Units	SM = 0	SM = 0.5	SM = 1	SM = 1.5	SM = 2
Q_{boiler}	GJ/a	73382	66299	55481	51983	49952
M_{bio}	tonnes	7715	7105	5901	5514	5288
Q_{in}	GJ/a	0	34502	69003	103505	138006
A_{SF}	m^2	0	4675	9350	14025	18700
Q_u	GJ/a	0	13693	29901	45623	61271
$Q_{heat,h}$	GJ/a	0	0	0	1903	10089
W_{turb}	GJ/a	2986	3169	3294	3625	3775
E_{el}	MWh/a	647	692	724	814	855
Q_e	GJ/a	4456	4671	4819	5209	5386
M_{ice}	tonnes/a	10649	11163	11517	12449	12872
$Q_{heat,l}$	GJ/a	13454	14094	14535	15698	16225
$E_{el,aux}$	MWh/a	56	65	76	87	92
Exc	GJ/a	0	32655	65311	97966	130622
Exb	GJ/a	129659	119419	99172	92673	88872
Exhc	GJ/a	34458	37562	40092	45833	52227
Exos	GJ/a	50715	79365	104101	134214	165383
Exuc	GJ/a	0	6430	14040	21423	28771
Exub	GJ/a	34458	31132	26052	24410	23456
Wnet	GJ/a	7240	7604	7840	8521	8832
Cpel,c	$/GJ/a	0.00	40.11	41.03	41.23	41.31
Cpel,b	$/GJ/a	5.73	5.84	6.22	6.38	6.49
Cpel,hc	$/GJ/a	6.48	5.99	5.64	5.04	4.40
Cpel,os	$/GJ/a	16.61	24.34	28.47	30.07	30.81
$\eta_{I,c}$	%	-	0.40	0.43	0.44	0.44
$\eta_{I,b}$	%	0.68	0.67	0.67	0.67	0.67
$\eta_{I,hc}$	%	0.10	0.10	0.09	0.09	0.08
$\eta_{I,os}$	%	0.067	0.057	0.052	0.047	0.042
$\eta_{II,c}$	%	-	0.1969	0.2150	0.2187	0.22
$\eta_{II,b}$	%	0.27	0.26	0.26	0.26	0.26
$\eta_{II,hc}$	%	0.21	0.20	0.20	0.19	0.17
$\eta_{II,os}$	%	0.056	0.050	0.048	0.045	0.040
LEC	¢/kWh	21.40	22.52	22.56	23.15	24.96
LCOE	¢/kWh	69.33	72.43	72.39	72.40	77.20
FS	%	0	0.17	0.35	0.47	0.55
$C_{capital}$	million$	336270	1391424	2445595	3503697	4558425
c_{sf}	million$	0	771375	1542750	2314125	3085500
c_{land}	million$	0	280500	561000	841500	1122000
c_{boiler}	million$	160000	160000	160000	160000	160000
c_{turb}	million$	120000	120000	120000	120000	120000
$c_{chiller}$	$	30392	31857	32868	35529	36736
c_{PB}	$	25878	27692	28977	32543	34189
$C_{O\&M}$	$/a	413574	406162	368937	372789	384517
$f_{SFstaff}$	-	0	1	2	3	4
$f_{PBstaff}$	-	10	10	10	10	10
c_{staff}	$/a	20000	21870	23740	25610	27480
c_{water}	$/a	1119	1198	1253	1407	1479
c_{spare}	$/a	3363	13914	24456	35037	45584
c_{ins}	$/a	3363	13914	24456	35037	45584

c_{bio}	$/a	385730	355266	295032	275698	264390
c_{elec}	$/a	-	-	-	-	-
P_{wr}	$/a	56395	11764	-10192	-44676	-115692
P_{ar}	$/a	83297	123078	185456	235620	248982
FCR	%	0.05	0.05	0.05	0.05	0.05
I_{val}	$/a	425970	446510	460674	497978	514887
$E_{el,val}$	$/a	70901	82731	93718	110431	118612
n	years	20	20	20	20	20
PP_{cap}	years	6.0	29.4	34.3	38.7	47.6
PP_{sol}	years	-	42.4	33.0	33.3	40.8
B_{saved}	tonnes/a	0	609	1814	2201	2427
L_{saved}	ha	0	47	140	169	187

Table A-10.2: Results for the Gujarat ELFR plant case study.

Symbol	**Units**	**SM = 0**	**SM = 0.5**	**SM = 1**	**SM = 1.5**	**SM = 2**
Q_{boiler}	GJ/a	73382	65989.39	54831.29	51107.00	49331.83
M_{bio}	tonnes	7715	7078.35	5832.79	5418.00	5221.83
Q_{in}	GJ/a	0	33210	66420	99630	132840
A_{SF}	m^2	0	4500	9000	13500	18000
Q_u	GJ/a	0	14175.75	30986.56	47241.00	63378.10
$Q_{heat,h}$	GJ/a	0	0.00	0.00	2090.46	10601.94
W_{turb}	GJ/a	2986	3175.71	3305.33	3625	3803.83
E_{el}	MWh/a	647	694.06	727.29	817.00	862.25
Q_e	GJ/a	4456	4679.13	4832.00	5224.00	5419.32
M_{ice}	tonnes/a	10649	11182.86	11548.00	12487.00	12951.86
$Q_{heat,l}$	GJ/a	13454	13978.86	14434.14	15698	16184.61
$E_{el,aux}$	MWh/a	56	68	77	87	92
Exc	GJ/a	0	31433	62866	94299	125732
Exb	GJ/a	129659	118966	98032	91060	87763
Exhc	GJ/a	34458	37643	40297	46181	52925
Exos	GJ/a	50715	77965	101210	129916	160060
Exuc	GJ/a	0	6656	14550	22183	29760
Exub	GJ/a	34458	30986	25747	23998	23165
Wnet	GJ/a	7240	7612	7862	8536	8892
Cpel,c	$/GJ/a	0.00	45.04	46.20	46.43	46.51
Cpel,b	$/GJ/a	5.73	5.84	6.25	6.43	6.52
Cpel,hc	$/GJ/a	6.48	5.98	5.61	5.00	4.35
Cpel,os	$/GJ/a	16.61	25.72	30.70	32.68	33.58
$\eta_{I,c}$	%	-	0.43	0.47	0.47	0.48
$\eta_{I,b}$	%	0.68	0.67	0.67	0.67	0.67
$\eta_{I,hc}$	%	0.10	0.09	0.09	0.09	0.08
$\eta_{I,os}$	%	0.067	0.058	0.053	0.049	0.043
$\eta_{II,c}$	%	-	0.2118	0.2314	0.2352	0.24
$\eta_{II,b}$	%	0.27	0.26	0.26	0.26	0.26
$\eta_{II,hc}$	%	0.21	0.20	0.20	0.18	0.17
$\eta_{II,os}$	%	0.056	0.051	0.049	0.046	0.042
LEC	¢/kWh	21.40	22.46	22.65	23.47	25.46
LCOE	¢/kWh	69.33	72.33	72.66	73.19	78.58
FS	%	0	0.18	0.36	0.48	0.56
$C_{capital}$	million$	336270	1455677	2574048	3696316	4815453
c_{sf}	million$	0	900000	1800000	2700000	3600000
c_{land}	million$	0	216000	432000	648000	864000
c_{boiler}	million$	160000	160000	160000	160000	160000
c_{turb}	million$	120000	120000	120000	120000	120000
$c_{chiller}$	$	30392	31915	32957	35636	36963
c_{PB}	$	25878	27762	29092	32680	34490

$C_{O\&M}$	$/a	413574	402032	365979	371640	388092
$f_{SFstaff}$	-	0	1	2	3	4
$f_{PBstaff}$	-	10	8	9	10	11
c_{staff}	$/a	20000	17800	21600	25400	29200
c_{water}	$/a	1119	1201	1258	1413	1492
c_{spare}	$/a	3363	14557	25740	36963	48155
c_{ins}	$/a	3363	14557	25740	36963	48155
c_{bio}	$/a	385730	353918	291640	270900	261091
c_{elec}	$/a	-	-	-	-	-
P_{wr}	$/a	56395	11764	-15445	-56286	-134967
P_{ar}	$/a	83297	128219	190479	239419	250269
FCR	%	0.05	0.05	0.05	0.05	0.05
I_{val}	$/a	425970	447315	461920	499480	518074
$E_{el,val}$	$/a	70901	82936	94538	111579	120287
n	years	20	19	20	20	20
PP_{cap}	years	6.0	29.5	35.1	40.1	50.0
PP_{sol}	years	-	38.9	33.4	34.4	42.9
B_{saved}	tonnes/a	0	636	1882	2297	2493
L_{saved}	ha	0	49	145	177	192

Table A-10.3: Results for the College-peak load plant case study.

Symbol	**Units**	**SM = 0**	**SM = 0.5**	**SM = 1**	**SM = 1.5**	**SM = 2**
Q_{boiler}	GJ/a	104107	89519	76458	72245	69815
M_{bio}	tonnes	9508	8324	7067	6655	6418
Q_{in}	GJ/a	0	63960	127920	191880	255840
A_{SF}	m^2	0	9750	19500	29250	39000
Q_u	GJ/a	0	28109	59481	87537	117015
$Q_{heat,h}$	GJ/a	0	0	0	7184	23759
W_{turb}	GJ/a	5182	5776	6812	7894	8486
E_{el}	MWh/a	1135	1280	1531	1851	2016
Q_e	GJ/a	5855	6282	6913	7515	7844
M_{ice}	tonnes/a	13791	14799	16284	17703	18477
$Q_{heat,l}$	GJ/a	17482	18757	20635	22430	23409
$E_{el,aux}$	MWh/a	70	95	126	159	182
Exc	GJ/a	0.00	60537.58	121075.16	181612.74	242150.32
Exb	GJ/a	183341.65	160502.09	136262.04	128313.18	123753.10
Exhc	GJ/a	48885.10	55233.85	63832.38	75028.00	87728.79
Exos	GJ/a	71437.29	123075.65	174168.33	231608.72	290369.51
Exuc	GJ/a	0.00	13198.80	27930.29	41104.19	54946.19
Exub	GJ/a	48885.10	42035.05	35902.09	33923.81	32782.60
Wnet	GJ/a	10784.69	11715.41	13270.25	14838.38	15674.51
Cpel,c	$/GJ/a	0.00	46.34	47.10	46.84	46.87
Cpel,b	$/GJ/a	5.17	5.37	5.71	5.86	5.95
Cpel,hc	$/GJ/a	19.55	17.31	15.18	13.03	11.01
Cpel,os	$/GJ/a	23.74	32.18	35.60	36.53	36.80
$\eta_{I,c}$	%	-	0.44	0.46	0.46	0.46
$\eta_{I,b}$	%	0.68	0.67	0.68	0.68	0.68
$\eta_{I,hc}$	%	0.10	0.10	0.10	0.09	0.08
$\eta_{I,os}$	%	0.071	0.059	0.055	0.050	0.044
$\eta_{II,c}$	%	-	0.2180	0.2307	0.2263	0.23
$\eta_{II,b}$	%	0.27	0.26	0.26	0.26	0.26
$\eta_{II,hc}$	%	0.22	0.21	0.21	0.20	0.18
$\eta_{II,os}$	%	0.059	0.053	0.052	0.048	0.043
LEC	¢/kWh	19.82	23.32	24.99	27.37	30.84
LCOE	¢/kWh	54.06	62.32	64.05	65.35	71.91
FS	%	0.00	0.24	0.44	0.55	0.63

$C_{capital}$	million$	964759	3167185	5375214	7585811	9788367
c_{sf}	million$	0	1608750	3217500	4826250	6435000
c_{land}	million$	0	585000	1170000	1755000	2340000
c_{boiler}	million$	220000	220000	220000	220000	220000
c_{turb}	million$	660000	660000	660000	660000	660000
$c_{chiller}$	$	39359	42235	46474	50521	52731
c_{PB}	$	45400	51200	61240	74040	80635
$C_{O\&M}$	$/a	516681	505655	491293	521346	559758
$f_{SFstaff}$	-	0	2	4	6	8
$f_{PBstaff}$	-	10	10	10	11	12
c_{staff}	$/a	20000	23900	27800	33700	39600
c_{water}	$/a	1964	2214	2649	3202	3487
c_{spare}	$/a	9648	31672	53752	75858	97884
c_{ins}	$/a	9648	31672	53752	75858	97884
c_{bio}	$/a	475422	416197	353340	332728	320903
c_{elec}	$/a	-	-	-	-	-
P_{wr}	$/a	85590	-5083	-58327	-152116	-303294
P_{ar}	$/a	162771	248292	371690	454749	479775
FCR	%	0.08	0.08	0.08	0.08	0.08
I_{val}	$/a	551651	591967	651373	708109	739080
$E_{el,val}$	$/a	127800	161980	211610	267986	300453
n	years	20	20	20	20	20
PP_{cap}	years	11.3	33.2	37.6	43.4	53.0
PP_{sol}	years	-	41.2	33.8	36.3	44.5
B_{saved}	tonnes/a	0	1185	2442	2854	3090
L_{saved}	ha	0	91	188	220	238

Table A-10.4: Results for the College-base load plant case study.

Symbol	**Units**	**SM = 0**	**SM = 0.5**	**SM = 1**	**SM = 1.5**	**SM = 2**
Q_{boiler}	GJ/a	269243	245560	227000	208491	196562
M_{bio}	tonnes	22759	21019	19652	17971	16873
Q_{in}	GJ/a	0	63960	127920	191880	255840
A_{SF}	m^2	0	9750	19500	29250	39000
Q_u	GJ/a	0	28109	57958	87537	117015
$Q_{heat,h}$	GJ/a	0	0	7066	13931	27777
W_{turb}	GJ/a	18534	18502	18511	18517	18521
E_{el}	MWh/a	4736	4728	4730	4731	4733
Q_e	GJ/a	13653	13649	13650	13651	13651
M_{ice}	tonnes/a	32162	32151	32154	32156	32158
$Q_{heat,l}$	GJ/a	40711	40708	40711	40714	40716
$E_{el,aux}$	MWh/a	157	197	235	275	307
Exc	GJ/a	0	60538	121075	181613	242150
Exb	GJ/a	438844	405283	378922	346512	325343
Exhc	GJ/a	126427	128505	133807	139004	147245
Exos	GJ/a	438844	465820	499997	528124	567493
Exuc	GJ/a	0	13199	27215	41104	54946
Exub	GJ/a	126427	115307	106591	97900	92299
Wnet	GJ/a	31623	31440	31314	31177	31067
Cpel,c	$/GJ/a	0.00	46.34	46.75	46.84	46.87
Cpel,b	$/GJ/a	4.35	4.38	4.42	4.50	4.56
Cpel,hc	$/GJ/a	9.93	9.69	9.18	8.73	8.10
Cpel,os	$/GJ/a	5.65	10.14	13.93	17.39	20.10
$\eta_{I,c}$	%	-	0.44	0.45	0.46	0.46
$\eta_{I,b}$	%	0.74	0.73	0.72	0.73	0.73
$\eta_{I,hc}$	%	0.12	0.11	0.11	0.11	0.10
$\eta_{I,os}$	%	0.087	0.079	0.071	0.065	0.059

$\eta_{II,c}$	%	-	0.2180	0.2248	0.2263	0.23
$\eta_{II,b}$	%	0.29	0.28	0.28	0.28	0.28
$\eta_{II,hc}$	%	0.25	0.24	0.23	0.22	0.21
$\eta_{II,os}$	%	0.072	0.067	0.063	0.059	0.055
LEC	¢/kWh	14.60	16.24	18.09	19.78	21.80
LCOE	¢/kWh	27.51	30.77	34.42	37.80	41.81
FS	%	0.00	0.10	0.20	0.30	0.37
$C_{capital}$	million$	1161221	3354607	5548456	7742274	9936077
c_{sf}	million$	0	1608750	3217500	4826250	6435000
c_{land}	million$	0	585000	1170000	1755000	2340000
c_{boiler}	million$	220000	220000	220000	220000	220000
c_{turb}	million$	660000	660000	660000	660000	660000
$c_{chiller}$	$	91788	91756	91763	91770	91775
c_{PB}	$	189433	189102	189193	189254	189302
$C_{O\&M}$	$/a	1189380	1150107	1129532	1093267	1086152
$f_{SFstaff}$	-	0	2	4	6	8
$f_{PBstaff}$	-	10	10	10	10	10
c_{staff}	$/a	20000	23900	27800	31700	35600
c_{water}	$/a	8193	8179	8183	8185	8187
c_{spare}	$/a	11612	33546	55485	77423	99361
c_{ins}	$/a	11612	33546	55485	77423	99361
c_{bio}	$/a	1137962	1050936	982580	898536	843643
c_{elec}	$/a	-	-	-	-	-
P_{wr}	$/a	553719	443754	316108	200579	51924
P_{ar}	$/a	646617	712123	759985	819961	846811
FCR	%	0.08	0.08	0.08	0.08	0.08
I_{val}	$/a	1286497	1286048	1286156	1286250	1286317
$E_{el,val}$	$/a	549500	576181	603361	626979	646646
n	years	20	20	20	20	20
PP_{cap}	years	2.1	7.6	17.6	24.5	30.5
PP_{sol}	years	-	53.6	61.9	60.7	70.1
B_{saved}	tonnes/a	-	1741	3108	4789	5886
L_{saved}	ha	0	134	239	369	453

Table A-10.5: Results for the College-electricity plant case study.

Symbol	**Units**	**SM = 0**	**SM = 0.5**	**SM = 1**	**SM = 1.5**	**SM = 2**
Q_{boiler}	GJ/a	269243	245560	227000	208491	196562
M_{bio}	tonnes	22759	21019	19652	17971	16873
Q_{in}	GJ/a	0	63960	127920	191880	255840
A_{SF}	m^2	0	9750	19500	29250	39000
Q_u	GJ/a	0	28109	57958	87537	117015
$Q_{heat,h}$	GJ/a	0	0	7066	13931	27777
W_{turb}	GJ/a	43700	43700	43700	43700	43700
E_{el}	MWh/a	11533	11533	11533	11533	11533
Q_e	GJ/a	0	0	0	0	0
M_{ice}	tonnes/a	0	0	0	0	0
$Q_{heat,l}$	GJ/a	0	0	0	0	0
$E_{el,aux}$	MWh/a	157	267	373	476	561
Exc	GJ/a	0	60538	121075	181613	242150
Exb	GJ/a	438844	405283	378922	346512	325343
Exhc	GJ/a	126427	128505	133807	139004	147245
Exos	GJ/a	565271	533788	512729	485516	472588
Exuc	GJ/a	0	13199	27215	41104	54946
Exub	GJ/a	126427	115307	106591	97900	92299
Wnet	GJ/a	43136	42738	42356	41985	41681
Cpel,c	$/GJ/a	0.00	46.34	46.75	46.84	46.87

Cpel,b	$/GJ/a	4.35	4.38	4.42	4.50	4.56
Cpel,hc	$/GJ/a	15.14	14.71	13.79	13.00	11.95
Cpel,os	$/GJ/a	5.02	9.62	14.57	20.20	25.76
$\eta_{I,c}$	%	-	0.44	0.45	0.46	0.46
$\eta_{I,b}$	%	0.74	0.73	0.72	0.73	0.73
$\eta_{I,hc}$	%	0.16	0.16	0.15	0.14	0.13
$\eta_{I,os}$	%	0.118	0.107	0.096	0.088	0.079
$\eta_{II,c}$	%	-	0.2180	0.2248	0.2263	0.23
$\eta_{II,b}$	%	0.29	0.28	0.28	0.28	0.28
$\eta_{II,hc}$	%	0.34	0.33	0.32	0.30	0.28
$\eta_{II,os}$	%	0.098	0.092	0.085	0.079	0.073
LEC	¢/kWh	11.07	12.32	13.75	15.06	16.62
LCOE	¢/kWh	11.60	12.92	14.42	15.81	17.45
FS	%	0.00	0.10	0.20	0.30	0.37
$C_{capital}$	million$	1481320	3675070	5868820	8062570	10256320
c_{sf}	million$	0	1608750	3217500	4826250	6435000
c_{land}	million$	0	585000	1170000	1755000	2340000
c_{boiler}	million$	220000	220000	220000	220000	220000
c_{turb}	million$	800000	800000	800000	800000	800000
$c_{chiller}$	$	0	0	0	0	0
c_{PB}	$	461320	461320	461320	461320	461320
$C_{O\&M}$	$/a	1207541	1168289	1147709	1111440	1104322
$f_{SFstaff}$	-	0	2	4	6	8
$f_{PBstaff}$	-	10	10	10	10	10
c_{staff}	$/a	20000	23900	27800	31700	35600
c_{water}	$/a	19952	19952	19952	19952	19952
c_{spare}	$/a	14813	36751	58688	80626	102563
c_{ins}	$/a	14813	36751	58688	80626	102563
c_{bio}	$/a	1137962	1050936	982580	898536	843643
c_{elec}	$/a	-	-	-	-	-
P_{wr}	$/a	39114	-29419	-119186	-200777	-321573
P_{ar}	$/a	157619	264586	350319	444228	498933
FCR	%	0.08	0.08	0.08	0.08	0.08
I_{val}	$/a	0	0	0	0	0
$E_{el,val}$	$/a	1365160	1432875	1498028	1555668	1603255
n	years	20	20	20	20	20
PP_{cap}	years	24.4	36.1	43.6	47.2	53.4
PP_{sol}	years	-	32.8	36.4	36.7	41.1
B_{saved}	tonnes/a	-	1741	3108	4789	5886
L_{saved}	ha	0	134	239	369	453

Table A-10.6: Results for the Printing factory plant case study.

Symbol	**Units**	**SM = 0**	**SM = 1**	**SM = 1.5**	**SM = 2.0**	**SM = 2.5**
Q_{boiler}	GJ/a	35313	35648	32942	29992	28441
M_{bio}	tonnes	2567	2570	2375	2162	2051
Q_{in}	GJ/a	0	13773	20659	27546	34432
A_{SF}	m^2	0	2100	3150	4200	5250
Q_u	GJ/a	0	2603	6848	10643	14064
$Q_{heat,h}$	GJ/a	0	2603	3743	4313	5977
W_{turb}	GJ/a	-	-	-	-	-
E_{el}	MWh/a	-	-	-	-	-
Q_e	GJ/a	-	-	-	-	-
M_{ice}	tonnes/a	-	-	-	-	-
$Q_{heat,l}$	GJ/a	-	-	-	-	-
$E_{el,aux}$	MWh/a	14	21	32	42	50
Exc	GJ/a	0.00	13022.65	19533.97	26045.29	32556.62

Exb	GJ/a	58434.32	58498.69	54057.87	49216.36	46672.07
Exhc	GJ/a	16581.86	17961.39	18683.97	19080.61	19958.74
Exos	GJ/a	58434.32	71521.34	73591.84	75261.66	79228.69
Exuc	GJ/a	0.00	1030.87	2712.06	4215.04	5569.71
Exub	GJ/a	13985.44	14118.08	13046.33	11877.88	11263.84
Wnet	GJ/a	35262.23	38174.07	39674.45	40485.21	42323.09
Cpel,c	$/GJ/a	0.00	458.35	261.33	224.20	212.08
Cpel,b	$/GJ/a	29.80	29.54	30.47	31.67	32.41
Cpel,hc	$/GJ/a	-	-	-	-	-
Cpel,os	$/GJ/a	11.87	23.37	27.98	32.76	36.68
$\eta_{I,c}$	%	-	0.19	0.33	0.39	0.41
$\eta_{I,b}$	%	0.69	0.69	0.69	0.69	0.69
$\eta_{I,hc}$	%	-	-	-	-	-
$\eta_{I,os}$	%	0.687	0.586	0.582	0.572	0.561
$\eta_{II,c}$	%	-	0.0792	0.1388	0.1618	0.17
$\eta_{II,b}$	%	0.24	0.24	0.24	0.24	0.24
$\eta_{II,hc}$	%	-	-	-	-	-
$\eta_{II,os}$	%	0.603	0.534	0.539	0.538	0.534
LEC	¢/kWh	3.002	3.471	3.490	3.503	3.620
LCOE	¢/kWh	-	-	-	-	-
FS	%	0.00	0.07	0.17	0.26	0.33
$C_{capital}$	million$	160000	632500	868750	1105000	1341250
c_{sf}	million$	0	346500	519750	693000	866250
c_{land}	million$	0	126000	189000	252000	315000
c_{boiler}	million$	160000	160000	160000	160000	160000
c_{turb}	million$	-	-	-	-	-
$c_{chiller}$	$	-	-	-	-	-
c_{PB}	$	-	-	-	-	-
$C_{O\&M}$	$/a	281630	293070	279986	264992	260032
$f_{SFstaff}$	-	0	0	1	1	1
$f_{PBstaff}$	-	10	10	10	10	10
c_{staff}	$/a	20000	20840	21260	21680	22100
c_{water}	$/a	-	-	-	-	-
c_{spare}	$/a	1600	6325	8688	11050	13413
c_{ins}	$/a	1600	6325	8688	11050	13413
c_{bio}	$/a	256730	257013	237502	216231	205053
c_{elec}	$/a	1700	2568	3849	4981	6055
P_{wr}	$/a	-294430	-343670	-349486	-353392	-367332
P_{ar}	$/a	-281630	-293070	-279986	-264992	-260032
FCR	%	0.08	0.08	0.08	0.08	0.08
I_{val}	$/a	0	0	0	0	0
$E_{el,val}$	$/a	0	0	0	0	0
n	years	20	20	20	20	20
PP_{cap}	years	-	-	-	-	-
PP_{sol}	years	-	-66	690	91	88
B_{saved}	tonnes/a	0	-3	192	405	520
L_{saved}	ha	0	0	15	31	40

References

1. Census of India, provisional population totals, 2011. [cited 2011 1st November]; Available from: http://censusindia.gov.in/2011census/censusinfodashboard/index.html.
2. Legros, G., et al., The Energy Access Situation in Developing Countries, A Review Focusing on the Least Developed Countries and Sub-Saharan Africa, in World Health Organization, U.N.D. Programme, Editor. 2009.
3. Nouni, M.R., S.C. Mullick, and T.C. Kandpal, Providing electricity access to remote areas in India: Niche areas for decentralized electricity supply. Renewable Energy, 2009. 34(2): p. 430-434.
4. Electrical energy. United nations statistics division [cited 2011 12th July]; Available from: unstats.un.org.
5. Grover, R.B. and S. Chandra, Scenario for growth of electricity in India. Energy Policy, 2006. 34(17): p. 2834-2847.
6. bp, BP Statistical Review of World Energy June 2011.
7. Buragohain, B., P. Mahanta, and V.S. Moholkar, Biomass gasification for decentralized power generation: The Indian perspective. Renewable and Sustainable Energy Reviews, 2010. 14(1): p. 73-92.
8. (2008) Government of India, National Action Plan on Climate Change.
9. MNRE, Resolution: Jawaharlal Nehru National Solar Mission. 2010.
10. MNRE, Guidelines for off-grid and decentralised solar applications. 2010.
11. Wolff, G. Clean Power from Deserts, Desertec Foundation. Oct 2009. Seminar at the London Energy Institute.
12. Franz, T. (2006) German Aerospace Centre (DLR), Trans-Mediterranean Interconnection for Concentrating Solar Power. Final Report.
13. Government of India, Ministry of New and Renewable Energy, Annual Report, 2004-2005.
14. Government of India, Ministry of New and Renewable Energy, Annual Report, 2005-2006.
15. Suresh, C., Biomass resources assessment for power generation: A case study from Haryana state, India. Biomass and Bioenergy, 2010. 34(9): p. 1300-1308.
16. Ravindranath, N.H. and D.O. Hall, Biomass, energy, and environment : a developing country perspective from India. 1995, Oxford; New York: Oxford University Press.

17. Rentizelas, A.A., A.J. Tolis, and I.P. Tatsiopoulos, Logistics issues of biomass: The storage problem and the multi-biomass supply chain. Renewable and Sustainable Energy Reviews, 2009. 13(4): p. 887-894.
18. Mohan, B., K. Rising fuel costs make biomass energy unattractive. 2009 [cited 2011 25th November]; Available from: http://www.business-standard.com/india/news/rising-fuel-costs-make-biomass-energy-unattractive/373664/.
19. Ravindranath, N.H., et al., Assessment of sustainable non-plantation biomass resources potential for energy in India. Biomass and Bioenergy, 2005. 29(3): p. 178-190.
20. Ravindranath, N.H., et al., Sustainable biomass power for rural India: Case study of biomass gasifier for village electrification. Current Science, 2004. 87(7): p. 932-941.
21. Hall, D.O. and J.I. Scrase, Will biomass be the environmentally friendly fuel of the future? Biomass and Bioenergy, 1998. 15(4-5): p. 357-367.
22. RCUK. Science Bridges Awards, in Awards in innovation for UK links at Institutional level with USA, China and India.
23. EPSRC. Standard Proposal. RCUK-DST India Science Bridge. Bioenergy: Technology and Business Solutions for the UK and India. (EP/G039992/1). 2008.
24. (USTDA), U.S.T.a.D.A., Building capacity in India's cold chain infrastructure, in U.S. - Inida Agriculture Knowledge Initiative Program.
25. Chasapis, D., et al., Monitoring and operational results of a hybrid solar-biomass heating system. Renewable Energy, 2008. 33(8): p. 1759-1767.
26. Bhattacharya, S., T. Ruangrungchaikul, and H. Pham, Design and performance of a hybrid solar/biomass energy powered dryer for fruits and vegetables. A research report of energy research program, Asian Institute of Technology, Pathumthani. 12120.
27. Sharma, A., C. Chen, and N. Vu Lan, Solar-energy drying systems: A review. Renewable and Sustainable Energy Reviews, 2009. 13(6-7): p. 1185-1210.
28. Fehrenbacher, K. (05/05/2010) eSolar to Launch Hybrid Solar Biomass Tech in China.
29. Biopact (2006) Biomass-solar hybrid power for the developing world.
30. Hybrid solar-biomass refinery - New Mexico, in Solar Thermal magazine. 12/02/2010, Solar Thermal magazine.

31. Kalogirou, S.A., Solar thermal collectors and applications. Progress in Energy and Combustion Science, 2004. 30(3): p. 231-295.
32. Duffie, J.A. and W.A. Beckman, Solar engineering of thermal processes. 3rd ed. 2006, New York: John Wiley & Sons.
33. Johansson, T.B. and L. Burnham, Renewable energy : sources for fuels and electricity. 1993, Washington, D.C.: Island Press.
34. Steingress, F.M., Low pressure boilers. 1970, Chicago: American Technical Society.
35. Industrial Boilers Ltd. [cited 2012 29th June]; Available from: http://www.indboilers.com/.
36. Rathore, M.M., Thermal engineering. 2010, New Delhi: Tata McGraw-Hill Education.
37. Baumeister, T., A.M. Sadegh, and E.A. Avallone, Marks' standard handbook for mechanical engineers. 2007, New York; London: McGraw-Hill.
38. Bahadori, A. and H.B. Vuthaluru, Estimation of performance of steam turbines using a simple predictive tool. Applied Thermal Engineering, 2010. 30(13): p. 1832-1838.
39. Zachary, J., P. Kochis, and R. Narula, Steam Turbine Design Considerations for Supercritical Cycles, in Coal Gen. 2007.
40. Viswanathan, R. and W. Bakker, Materials for ultrasupercritical coal power plants—Turbine materials: Part II. Journal of Materials Engineering and Performance, 2001. 10(1): p. 96-101.
41. Woodward, Industrial Steam Turbine Control, in Application Note 83403. 2011.
42. Çengel, Y.A. and M.A. Boles, Thermodynamics : an engineering approach. 2001, Boston: McGraw-Hill.
43. Melinder, Å., Thermophysical Properties of Aqueous Solutions Used as Secondary Working Fluids. 2007, Royal Institute of Technology, KTH: Stockholm, Sweden.
44. Graham, J., Icemaking plant. 1975, Aberdeen: Torry Research Station.
45. Boubakri, A., J.J. Guilleminot, and F. Meunier, Adsorptive solar powered ice maker: experiments and model. Solar Energy, 2000. 69(3): p. 249-263.
46. Leite, A.P.F. and M. Daguenet, Performance of a new solid adsorption ice maker with solar energy regeneration. Energy Conversion and Management, 2000. 41(15): p. 1625-1647.
47. Li, M. and R.Z. Wang, Heat and mass transfer in a flat plate solar solid adsorption refrigeration ice maker. Renewable Energy, 2003. 28(4): p. 613-622.

48. R.E, C., Rapid cycling solar/biomass powered adsorption refrigeration system. Renewable Energy. 16(1-4): p. 673-678.
49. Saaty, T., Decision making with the Analytic Hierarchy Process. International Journal of Services Sciences, 2008. 1(1): p. 83-98.
50. Saaty, T.L., The analytic hierarchy process : planning, priority setting, resource allocation. 1980, New York; London: McGraw-Hill International Book Co.
51. Pohekar, S.D. and M. Ramachandran, Application of multi-criteria decision making to sustainable energy planning--A review. Renewable and Sustainable Energy Reviews, 2004. 8(4): p. 365-381.
52. Dey, P., Decision support system for inspection and maintenance: a case study of oil pipelines. IEEE transactions on engineering management, 2004. 51(1): p. 47-56.
53. Dey, P., Integrated project evaluation and selection using multiple-attribute decision-making technique. International Journal of Production Economics, 2006. 103(1): p. 90-103.
54. Ramanathan, R. and L.S. Ganesh, Energy resource allocation incorporating qualitative and quantitative criteria: An integrated model using goal programming and AHP. Socio-Economic Planning Sciences, 1995. 29(3): p. 197-218.
55. Marttunen, M. and R.P. Hämäläinen, Decision analysis interviews in environmental impact assessment. European Journal of Operational Research, 1995. 87(3): p. 551-563.
56. Bhattacharyya, S. and P. Dey, Selection of power market structure using the analytic hierarchy process. International Journal of Global Energy Issues, 2003. 20(1): p. 36-57.
57. Kaya, T. and C. Kahraman, Multicriteria renewable energy planning using an integrated fuzzy VIKOR & AHP methodology: The case of Istanbul. Energy, 2010. 35(6): p. 2517-2527.
58. Ramanathan, R. and L.S. Ganesh, Energy alternatives for lighting in households: An evaluation using an integrated goal programming-AHP model. Energy, 1995. 20(1): p. 63-72.
59. Kaltschmitt, M., W. Streicher, and A. Wiese, Renewable energy : technology, economics, and environment. 2007, Berlin; New York: Springer.
60. Technology Characterization Solar Parabolic Trough. [cited 2009 27th July]; Available from: http://www.solarpaces.org/CSP_Technology/docs/solar_trough.pdf.

61. Price, H., A Parabolic Trough Solar Power Plant Simulation Model, in Internation Solar Energy Confrence Hawaii Island. 2003, National Renewable Energy Laboratory: Hawaii. p. 5.
62. Weiss, W. and M. Rommel (2008) Process Heat Collectors.
63. (2003) National Renewable Energy Laboratory, Assessment of Parabolic Trough and Power Tower Solar Technology Cost and Performance Forecasts.
64. Morin, G., et al., Comparison of Linear Fresnel and Parabolic Trough Collector power plants. Solar Energy, 2012. 86(1): p. 1-12.
65. Goswami, D.Y. and F. Kreith, Energy conversion. 2008, Boca Raton: CRC Press.
66. Valenzuela, L., et al., Control scheme for direct steam generation in parabolic troughs under recirculation operation mode. Solar Energy, 2006. 80(1): p. 1-17.
67. Flores, V. and R. Almanza, Direct steam generation in parabolic trough concentrators with bimetallic receivers. Energy, 2003. 29(5-6): p. 645-651.
68. Eck, M. and W. Steinmann, D, Direct Steam Generation in Parabolic Troughs, First Results of the DISS Project. Journal of Solar Energy Engineering, 2002. 124: p. 134-140.
69. Zarza, E., et al., Direct steam generation in parabolic troughs: Final results and conclusions of the DISS project. Energy, 2003. 29(5-6): p. 635-644.
70. Mills, D., Advances in solar thermal electricity technology. Solar Energy, 2003. 76(1-3): p. 19-31.
71. Camacho, E.F., M. Berenguel, and F.R. Rubio, Advanced control of solar plants. 1997, Berlin; New York: Springer.
72. Birnbaum, J., et al., A Direct Steam Generation Solar Power Plant With Integrated Thermal Storage. Journal of Solar Energy Engineering, 2010. 132(3): p. 031014.
73. Boyle, G., Renewable energy, power for a sustainable future. 2004, Oxford: Oxford University Press, in association with the Open University.
74. Solar Central Power Towers. [cited 2012 29th June]; Available from: http://www.global-greenhouse-warming.com/solar-central-power-towers.html.
75. Dunn, R.I., P.J. Hearps, and M.N. Wright, Molten-Salt Power Towers: Newly Commercial Concentrating Solar Storage. Proceedings of the IEEE, 2011. PP(99): p. 1-12.
76. Energy Information Administration Official Energy Statistics from the U.S Government, Solar Thermal. 2008.
77. Pacheco, J., E, et al., Summary of the Solar Two: Test and Evaluation Program. 2000, SANDIA Labs: Alburquerque.

78. Technology Characterization Solar Power Towers. [cited 2009 27th July]; Available from: http://www.solarpaces.org/CSP_Technology/docs/solar_tower.pdf.
79. Kolb, G., J et al. (2007) Heliostat Cost Reduction, Sandia National Laboratories.
80. Collado, F.J., Quick evaluation of the annual heliostat field efficiency. Solar Energy, 2008. 82(4): p. 379-384.
81. Wei, L., Area utilization efficiency of a sloping heliostat system for solar concentration. Applied Optics, 1983. 22(4): p. 568-572.
82. Feuermann, D. and J. Gordon, Analysis of a two-stage linear Fresnel reflector solar concentrator. Journal of Solar Energy Engineering, 1991. 113: p. 272.
83. Mills, D. and G. Morrison, Compact linear Fresnel reflector solar thermal powerplants. Solar Energy, 2000. 68(3): p. 263-283.
84. Singh, P.L., R.M. Sarviya, and J.L. Bhagoria, Thermal performance of linear Fresnel reflecting solar concentrator with trapezoidal cavity absorbers. Applied Energy, 2010. 87(2): p. 541-550.
85. Singh, P., S. Ganesan, and G. Yadav, Technical note-Performance study of a linear Fresnel concentrating solar device. Renewable Energy, 1999. 18(3): p. 409-416.
86. Facão, J. and A.C. Oliveira, Numerical simulation of a trapezoidal cavity receiver for a linear Fresnel solar collector concentrator. Renewable Energy, 2011. 36(1): p. 90-96.
87. Baum, V.A., R.R. Aparasi, and B.A. Garf, High-power solar installations. Solar Energy, 1957. 1(1): p. 6-12.
88. Francia, G., Pilot plants of solar steam generating stations. Solar Energy, 1968. 12(1): p. 51-58, IN3-IN5, 59-62, IN7-IN13, 63-64.
89. Kalogirou, S. and Knovel. Solar energy engineering processes and systems. 2009.
90. Feuermann, D., Experimental evaluation of the PAZ solar thermal collector at the Ben-Gurion centre for solar thermal electricity generating technologies, in Final report, prepared for the Ministry of Energy and Infrastructure, State of Israel. 1993.
91. Plataforma Solar de Almería (P.S.A), in Annual Report. 2007.
92. Bernhard, R., et al., Linear Fresnel Collector Demonstration on the PSA Part I – Design; Construction and Quality Control, in SolarPACES. 2008.
93. Bernhard, R., et al., Linear Fresnel Collector Demonstration on the PSA Part II – Commissioning and First Performance Tests, in SolarPACES. 2008: Las Vegas.
94. HelioDynamics. [cited 2010 13th September]; Available from: http://www.heliodynamics.com/index.htm.

95. International Energy Agency (IEA), Solar Power and Chemical Energy Systems, in SolarPACES Annual Report, C. Richter, Editor. 2008.
96. Novatec Biosol. 06/09/10]; Available from: http://www.novatec-biosol.com/.
97. Chaves, J. and M. Collares-Pereira, Etendue-matched two-stage concentrators with multiple receivers. Solar Energy, 2010. 84(2): p. 196-207.
98. Zahler, C., N. Berger, and J. Louw, Mirroxx Fresnel Collectors Powering the Largest Solar Cooling System in the Middle East for a Showcase Football Stadium in Qater, in SolarPACES. 2011: Granada, Spain.
99. Mertins, M., M. Selig, and G. Morin, Supernova - Construction, Control and Performance of Steam Superheating Linear Fresnel Collector, in SolarPACES 2011. 2011: Granada, Spain.
100. Conlon, W., Superheated Steam from CLFR Solar, in SolarPACES. 2011: Granada, Spain.
101. AREVA to build Asia's largest concentrating solar power installation in Rajasthan, India. 2012 [cited 2012 7th December]; Available from: http://www.solarserver.com/solar-magazine/solar-news/current/2012/kw15/areva-to-build-asias-largest-concentrating-solar-power-installation-in-rajasthan-india.html.
102. Compact Linear Fresnel Reflector (CLFR) Solar. 2008 [cited 2009 27 July]; Available from: http://www.energy.ca.gov/reti/steering/2008-06-18_meeting/SOLAR_FS-Compact_Linear_Fresnel_Reflector.pdf.
103. Stalix. 5¢ / KWh Electricity from Concentrated Solar Power (CSP) – Finally a Reality. [cited 2009 31 July]; Available from: http://stalix.com/CSP%20White%20paper.pdf.
104. Mills, D., P. Le Lievre, and G. Morrison, First Results from Compact Linear Fresnel Reflector Installation. Proceedings of ANZSES Solar2004, 2004.
105. Morin, G., et al., Techno-Economic System Simulation and Optimisation of Solar Thermal Power Plants, in SolarPaces. 2008: Las Vegas, USA.
106. Taggart, S., CSP: dish projects inch forward. Renewable Energy Focus, 2008. 9(4): p. 52-54.
107. Stirling Energy Systems. [cited 2009 10th November]; Available from: http://www.stirlingenergy.com/.
108. Technology Characterization Solar Dish Systems. [cited 2009 22nd July]; Available from: http://www.solarpaces.org/CSP_Technology/docs/solar_tower.pdf.

109. Jogi, K.S., Encyclopaedia of energy resource management : (priorities for 21st century). 2000, Lucknow; New Delhi: Institute of Environmental Development Studies ; Sarup.
110. García-Rodríguez, L., A. Palmero-Marrero, and C. Gómez-Camacho, Comparison of solar thermal technologies for applications in seawater desalination. Desalination, 2002. 142(2): p. 135-142.
111. Collares-Pereira, M., High temperature solar collector with optimal concentration-Non-focusing Fresnel lens with secondary concentrator. Solar Energy, 1979. 23(5): p. 409-420.
112. Welford, W.T. and R. Winston, High collection nonimaging optics. 1989, San Diego: Academic Press.
113. Winston, R., Principles of solar concentrators of a novel design (from Solar Energy 1974). SPIE milestone series., 1995. 106: p. 18.
114. Kritchman, E., A. Friesem, and G. Yekutieli, Efficient Fresnel lens for solar concentration. Solar Energy, 1979. 22: p. 119-123.
115. Leutz, R., et al., Developments and Designs of Solar Engineering Fresnel Lenses. Tokyo University of Agriculture and Technology, Department of Mechanical Systems Engineering.
116. Kritchman, E., A. Friesem, and G. Yekutieli, Highly concentrating Fresnel lenses. Applied Optics, 1979. 18(15): p. 2688-2695.
117. Leutz, R. and A. Suzuki, Nonimaging Fresnel lenses : design and performance of solar concentrators. 2001, Berlin; New York: Springer.
118. Nelson, D., D. Evans, and R. Bansal, Linear Fresnel lens concentrators. Solar Energy, 1975. 17: p. 285-289.
119. Nixon, J.D., P.K. Dey, and P.A. Davies, Which is the best solar thermal collection technology for electricity generation in north-west India? Evaluation of options using the analytical hierarchy process. Energy, 2010. 35(12): p. 5230-5240.
120. Singh, D., Solar Energy Centre in India, in Alternative Energy eMagazine. Apr 2009.
121. Anderson, D.R., et al., An introduction to management science quantitative approaches to decision making. 2000, Cincinnati, Ohio: South-Western College Pub.
122. Dey, P., Analytic hierarchy process helps evaluate project in Indian oil pipelines industry. International Journal of Operations and Production Management, 2004. 24: p. 588-604.

123. Belton, V. and T. Gear, On a short-coming of Saaty's method of analytic hierarchies. Omega, 1983. 11(3): p. 228-230.
124. Sniezek, J.A. and R.A. Henry, Accuracy and confidence in group judgment. Organizational Behavior and Human Decision Processes, 1989. 43(1): p. 1-28.
125. Van Den Honert, R.C. and F.A. Lootsma, Group preference aggregation in the multiplicative AHP The model of the group decision process and Pareto optimality. European Journal of Operational Research, 1997. 96(2): p. 363-370.
126. Wallenius, J., et al., Multiple criteria decision making, multiattribute utility theory: recent accomplishments and what lies ahead. Management Science, 2008. 54(7): p. 1336–1349.
127. Sootha, G.D. and B.S. Negi, A comparative study of optical designs and solar flux concentrating characteristics of a linear fresnel reflector solar concentrator with tubular absorber. Solar Energy Materials and Solar Cells, 1994. 32(2): p. 169-186.
128. Velázquez, N., et al., Numerical simulation of a Linear Fresnel Reflector Concentrator used as direct generator in a Solar-GAX cycle. Energy Conversion and Management, 2010. 51(3): p. 434-445.
129. Mathur, S., T. Kandpal, and B. Negi, Optical design and concentration characteristics of linear Fresnel reflector solar concentrators--II. Mirror elements of equal width. Energy Conversion and Management, 1991. 31(3): p. 221-232.
130. Mathur, S., B. Negi, and T. Kandpal, Geometrical designs and performance analysis of a linear fresnel reflector solar concentrator with a flat horizontal absorber. International Journal of Energy Research, 2007. 14(1): p. 107-124.
131. Häberle, A., Geometry Optimization of Fresnel-Collectors with economic assessment, in EuroSun. 2004: Freiburg (Germany).
132. Barale, G., et al., Optical Design of a Linear Fresnel Collector for Sicily, in SolarPACES. 2010: Perpignan, France.
133. Häberle, A., et al., The Solarmundo line focussing Fresnel collector. Optical and thermal performance and cost calculations., in SolarPACES. 2002: Zurich, Switzerland.
134. Singh, N., S. Kaushik, and R. Misra, Exergetic analysis of a solar thermal power system. Renewable Energy, 2000. 19(1-2): p. 135-143.
135. Tyagi, S.K., et al., Exergy analysis and parametric study of concentrating type solar collectors. International Journal of Thermal Sciences, 2007. 46(12): p. 1304-1310.

136. Gupta, M.K. and S.C. Kaushik, Exergy analysis and investigation for various feed water heaters of direct steam generation solar-thermal power plant. Renewable Energy, 2010. 35(6): p. 1228-1235.
137. Koroneos, C., T. Spachos, and N. Moussiopoulos, Exergy analysis of renewable energy sources. Renewable Energy, 2003. 28(2): p. 295-310.
138. Dincer, I. and M.A. Rosen, Exergy analysis of renewable energy systems, in EXERGY. 2007, Elsevier: Amsterdam. p. 163-228.
139. Meteotest. Meteonorm. Available from: www.meteonorm.com.
140. William, B., S. Geyer, and M. Geyer, Power from the Sun. 2001.
141. Muneer, T., C. Gueymard, and H. Kambezidis, Solar radiation and daylight models. 2004, Amsterdam; Boston; London: Elsevier Butterworth Heinemann.
142. Woolf, H.M., Report NASA TM-X -164, in On the Computation of Solar Evaluation Angles and the Determination of Sunrise and Sunset Times,. (1986).
143. Singh, P.L., R.M. Sarviya, and J.L. Bhagoria, Heat loss study of trapezoidal cavity absorbers for linear solar concentrating collector. Energy Conversion and Management, 2010. 51(2): p. 329-337.
144. McIntire, W.R., Factored approximations for biaxial incident angle modifiers. Solar Energy, 1982. 29(4): p. 315-322.
145. Buie, D. and A.G. Monger, The effect of circumsolar radiation on a solar concentrating system. Solar Energy. 76(1-3): p. 181-185.
146. Tesfamichael, T. and E. Wäckelgård, Angular solar absorptance and incident angle modifier of selective absorbers for solar thermal collectors. Solar Energy, 2000. 68(4): p. 335-341.
147. Akao, Y., Quality function deployment: integrating customer requirements into product design. 2004: Productivity Pr.
148. Chan, L.-K. and M.-L. Wu, Quality function deployment: A literature review. European Journal of Operational Research, 2002. 143(3): p. 463-497.
149. Paul, D., et al. Artificial Neural Network Modeling for Efficient Photovoltaic System Design. in Advanced Computer Theory and Engineering, 2008. ICACTE '08. International Conference on. 2008.
150. Chan, L.-K. and M.-L. Wu, A systematic approach to quality function deployment with a full illustrative example. Omega, 2005. 33(2): p. 119-139.
151. Karsak, E.E., S. Sozer, and S.E. Alptekin, Product planning in quality function deployment using a combined analytic network process and goal programming approach. Computers & Industrial Engineering, 2003. 44(1): p. 171-190.

152. Min Hua Lu, C.N.M., Chu-hua Kuei, Dena Winokur, Integrating QFD, AHP and Benchmarking in Strategic Marketing. Journal of Business & Industrial Marketing, 1994. Vol. 9(Iss: 1): p. pp.41 - 50.
153. Butler, K.N., Rocket engine development, in Aerospace America. 1993. p. pp28-31.
154. Hsiao, S.-W., Concurrent design method for developing a new product. International Journal of Industrial Ergonomics, 2002. 29(1): p. 41-55.
155. Ho, W., Integrated analytic hierarchy process and its applications - A literature review. European Journal of Operational Research, 2008. 186(1): p. 211-228.
156. Lozano-Minguez, E., A.J. Kolios, and F.P. Brennan, Multi-criteria assessment of offshore wind turbine support structures. Renewable Energy, 2011. 36(11): p. 2831-2837.
157. Lee, A.H.I., H.H. Chen, and H.-Y. Kang, Multi-criteria decision making on strategic selection of wind farms. Renewable Energy, 2009. 34(1): p. 120-126.
158. Nobre, A., et al., Geo-spatial multi-criteria analysis for wave energy conversion system deployment. Renewable Energy, 2009. 34(1): p. 97-111.
159. Fausto, C., Multi-criteria decision aid to assess concentrated solar thermal technologies. Renewable Energy, 2009. 34(7): p. 1678-1685.
160. Kosoric, V., S. Wittkopf, and Y. Huang, Testing a design methodology for building integration of photovoltaics (PV) using a PV demonstration site in Singapore. Architectural Science Review, 2011. 54(3): p. 192-205.
161. Cavallaro, F., A comparative assessment of thin-film photovoltaic production processes using the ELECTRE III method. Energy Policy, 2010. 38(1): p. 463-474.
162. Pugh, S., Total design : integrated methods for successful product engineering. 1991, Wokingham, England; Reading, Mass.: Addison-Wesley Pub. Co.
163. Hazelrigg, G.A., Validation of engineering design alternative selection methods. Engineering Optimization, 2003. 35(2): p. 103 - 120.
164. Olewnik, A.T. and K. Lewis, On Validating Engineering Design Decision Support Tools. Concurrent Engineering, 2005. 13(2): p. 111-122.
165. Khan, M.K.A., Technical note Copper oxide coatings for use in a linear solar Fresnel reflecting concentrating collector. Renewable Energy, 1999. 17(4): p. 603-608.
166. Negi, B.S., S.S. Mathur, and T.C. Kandpal, Optical and thermal performance evaluation of a linear fresnel reflector solar concentrator. Solar & Wind Technology, 1989. 6(5): p. 589-593.

167. Flores Larsen, S., M. Altamirano, and A. Hernández, Heat loss of a trapezoidal cavity absorber for a linear Fresnel reflecting solar concentrator. Renewable Energy, 2012. 39(1): p. 198-206.
168. Yanhua, L., et al. Thermal performance analysis of linear fresnel reflector concentrator with a compound parabolic cavity absorber. in Materials for Renewable Energy & Environment (ICMREE), 2011 International Conference on. 2011.
169. Reynolds, D.J., et al., An experimental and computational study of the heat loss characteristics of a trapezoidal cavity absorber. Solar Energy. 76(1-3): p. 229-234.
170. Burkholder, F. and C. Kutscher, Heat Loss Testing of Schott's 2008 PTR70 Parabolic Trough Receiver. 2009, NREL.
171. Konttinen, P., P.D. Lund, and R.J. Kilpi, Mechanically manufactured selective solar absorber surfaces. Solar Energy Materials and Solar Cells, 2003. 79(3): p. 273-283.
172. Kennedy, C., E., Review of Mid- to High-Temperature Solar Selective Absorber Materials. 2002, NREL.
173. Heimsath, A., et al., Characterization of Optical Components for Linear Fresnel Collectors by Fringe Reflection Method, in SolarPACES. 2008, Fraunhofer Institute of Solar Energy Systems: Las Vegas, USA.
174. Peterka, J.A., J.M. Sinou, and J.E. Cerrnak, Mean Wind Forces on Parabolic - Trough Solar Collectors. 1980, Sandia National Laboratories: Albuquerque, New Mexico.
175. Peterka, J.A., et al., Wind loads on heliostats and parabolic dish collectors. 1988, Fort Collins, CO: Colorado State University.
176. Peterka, J.A., R.G. Derickson, and L. Sandia National, Wind load design methods for ground-based heliostats and parabolic dish collectors. 1992, Albuquerque, N.M.: Sandia National Laboratories;.
177. Hosoya, N., et al. Wind tunnel tests of parabolic trough solar collectors, March 2001- August 2003. 2008.
178. Machine Building Systems Ltd. [cited 2012 5th December]; Available from: http://www.mbsitem.co.uk/.
179. Met office. Midlands: climate. [cited 2012 1st December]; Available from: http://www.metoffice.gov.uk/climate/uk/mi/print.html.
180. C.T.1 Ltd. [cited 2012 28th September]; Available from: http://www.ct1ltd.com/.

181. Montes, M.J., A. Abánades, and J.M. Martínez-Val, Performance of a direct steam generation solar thermal power plant for electricity production as a function of the solar multiple. Solar Energy, 2009. 83(5): p. 679-689.
182. Hoshi, A., et al., Screening of high melting point phase change materials (PCM) in solar thermal concentrating technology based on CLFR. Solar Energy, 2005. 79(3): p. 332-339.
183. Kaushika, N., A. Mishra, and M. Chakravarty, Thermal analysis of solar biomass hybrid co-generation plants. International Journal of Sustainable Energy, 2005. 24(4): p. 175-186.
184. Dimityr, P., An option for solar thermal repowering of fossil fuel fired power plants. Solar Energy, 2011. 85(2): p. 344-349.
185. Lerchenmüller, H., M. Mertins, and G. Morin, Fresnel-Collectors in hybrid Solar Thermal Power Plants with high Solar Shares. 2004, Fraunhofer Institute for Solar Energy Systems.
186. Bermejo, P., F.J. Pino, and F. Rosa, Solar absorption cooling plant in Seville. Solar Energy, 2010. 84(8): p. 1503-1512.
187. Cot, A., et al., Termosolar Borges: A Thermosolar Hybrid Plant with Biomass, in Third International Symposium on Energy from Biomass and Waste. 2010: Venice, Italy.
188. Solarlite. TRESERT Phitsanulok, Thailand. [cited 2012 2nd December]; Available from: http://www.solarlite.de/en/project_phitsanulok.cfm.
189. Fabrizi, F. Multipurpose Applications by Thermodynamic Solar. Agenzia Nazionale Per Le Nuove Tecnologie,l'energia E Lo Sviluppo Economico Sostenibile [cited 2012 29th June]; Available from: http://cordis.europa.eu/search/index.cfm?fuseaction=proj.document&PJ_RCN=12271129.
190. Cost Reduction Study for Solar Thermal Power Plants. 1999, The World Bank Washington, D.C.
191. Kosugi, T. and P.S. Pak, Economic evaluation of solar thermal hybrid H2O turbine power generation systems. Energy, 2003. 28(3): p. 185-198.
192. Frebourg, P., et al., Feasibility Study of a Small-Scale Grid-Connected Solar Parabolic Biomass Hybrid Power Plant in Thailand.
193. Beerbaum, S. and G. Weinrebe, Solar thermal power generation in India—a techno–economic analysis. Renewable Energy, 2000. 21(2): p. 153-174.

194. Bhattacharya, A., et al., Biomass integrated gasification combined cycle power generation with supplementary biomass firing: Energy and exergy based performance analysis. Energy, 2011. 36(5): p. 2599-2610.
195. Vidal, A., et al., Analysis of a combined power and refrigeration cycle by the exergy method. Energy, 2006. 31(15): p. 3401-3414.
196. Rosen, M.A. A concise review of exergy-based economic methods. 2008: World Scientific and Engineering Academy and Society (WSEAS).
197. Kanoglu, M., I. Dincer, and M.A. Rosen, Understanding energy and exergy efficiencies for improved energy management in power plants. Energy Policy, 2007. 35(7): p. 3967-3978.
198. Baghernejad, A. and M. Yaghoubi, Exergoeconomic Analysis and Optimization of Solar Thermal Power Plants.
199. Rosen, M.A. and I. Dincer, Exergoeconomic analysis of power plants operating on various fuels. Applied Thermal Engineering, 2003. 23(6): p. 643-658.
200. Kaushik, S.C., et al., Exergoeconomic Evaluation of a Solar Thermal Power Plant. International Journal of Solar Energy, 2001. 21(4): p. 293-314.
201. Hepbasli, A., A key review on exergetic analysis and assessment of renewable energy resources for a sustainable future. Renewable and Sustainable Energy Reviews, 2008. 12(3): p. 593-661.
202. TRNSYS17. A TRaNsient SYstems Simulation Program. [cited 2011 10th Novermber].
203. Song, G., L. Shen, and J. Xiao, Estimating Specific Chemical Exergy of Biomass from Basic Analysis Data. Industrial & Engineering Chemistry Research, 2011. 50(16): p. 9758-9766.
204. Luo, H.L., et al., Year round test of a solar adsorption ice maker in Kunming, China. Energy Conversion and Management, 2005. 46(13-14): p. 2032-2041.
205. MinistryofNewandRenewableEnergy, Guidelines for Generation Based Incentive, Grid Interactive Solar Thermal Power Generation Projects. 2008.
206. Potential outputs of biofuels per hectare, per annum. 2008 [cited 2010 1st June]; Available from: http://www.biomassenergycentre.org.uk/portal/page?_pageid=75,163231&_dad=portal&_schema=PORTAL.
207. Jones S.A., B.N., Pitz-Paal R., Schwarzboezl P. and Cable B. TRNSYS Modeling of the SEGS VI Parabolic Trough Solar Electric Generating System. in ASME International Solar Energy Conference. 2001. Washington, DC.

208. Stuetzle T., B.N., Mitchell J.W., Beckman W.A. Automatic Control of a 30 MWe SEGS VI Parabolic Trough Plant. in SES 2001 Solar World Congress. 2001.
209. TRNLIB - Libraries of User-Written Components for TRNSYS. [cited 2011 24th October]; Available from: http://sel.me.wisc.edu/trnsys/trnlib/library16.htm.
210. Werther, J., et al., Combustion of agricultural residues. Progress in Energy and Combustion Science, 2000. 26(1): p. 1-27.
211. Thipwimon, C., H. Gheewala Shabbir, and P. Suthum, Environmental assessment of electricity production from Rice Husk: A case study in Thailand. Electricity supply industry in transition: issues and prospect for Asia, 2004. 20: p. 51–62.
212. Ayhan, D., Calculation of higher heating values of biomass fuels. Fuel, 1997. 76(5): p. 431-434.
213. Ayhan, D., Combustion characteristics of different biomass fuels. Progress in Energy and Combustion Science, 2004. 30(2): p. 219-230.
214. Nouni, M.R., S.C. Mullick, and T.C. Kandpal, Providing electricity access to remote areas in India: An approach towards identifying potential areas for decentralized electricity supply. Renewable and Sustainable Energy Reviews, 2008. 12(5): p. 1187-1220.
215. Rangan, B., Comparison of options for distributed generation in India. Energy Policy, 2006. 34(1): p. 101-111.
216. Kapur, T., T.C. Kandpal, and H.P. Garg, Electricity generation from rice husk in Indian rice mills: Potential and financial viability. Biomass and Bioenergy, 1996. 10(5-6): p. 393-403.
217. Afzal, A., M. Mohibullah, and V.K. Sharma, Performance analysis of a rice husk power generating system: a case study. International Journal of Sustainable Energy, 2011. 30(1): p. 1-10.
218. Fischer, G., et al., Biofuel production potentials in Europe: Sustainable use of cultivated land and pastures, Part II: Land use scenarios. Biomass and Bioenergy, 2010. 34(2): p. 173-187.
219. Medrano, M., et al., State of the art on high-temperature thermal energy storage for power generation. Part 2—Case studies. Renewable and Sustainable Energy Reviews, 2010. 14(1): p. 56-72.
220. Raphael, A., Superheated Direct Steam Generation, in SolarPACES. 2011: Granada, Spain.

221. Kalogirou, S.A., Artificial intelligence for the modeling and control of combustion processes: a review. Progress in Energy and Combustion Science, 2003. 29(6): p. 515-566.

222. Ahmed, K. and D. Anderson (1994) Renewable Energy Technologies, A Review of the Status and Costs of Selected Technologies, Annex 5 The Luz Experience.

223. California, Incentives/Polices for Renewables and Efficiency, Database of State Incentives for Renewables and Efficiency (DSIRE). [cited 2009 8th September]; Available from: http://www.dsireusa.org/incentives/incentive.cfm?Incentive_Code=CA25R&state=CA&CurrentPageID=1.